Generation and control of high-harmonic radiation

vorgelegt von

Carsten Winterfeldt

aus Würzburg

Würzburg 2006

Eingereicht am 7. September 2006
bei der Fakultät für Physik und Astronomie

Gutachter der Dissertation:
1. Gutachter: Prof. Dr. G. Gerber
2. Gutachter: Prof. Dr. V. Dyakonov

Prüfer im Promotionskolloquium:
1. Prüfer: Prof. Dr. G. Gerber
2. Prüfer: Prof. Dr. V. Dyakonov
3. Prüfer: Prof. Dr. H. Hinrichsen

Tag der mündlichen Prüfung (Promotionskolloquium): 14. November 2006

Doktorurkunde ausgehängt am: _____

List of publications

Parts of this work have been published in the following references:

Journal articles

1. C. Winterfeldt, C. Spielmann, and G. Gerber, *Colloquium: Adaptive temporal and spatial control of high-harmonic generation*, Rev. Mod. Phys., in preparation, solicited (2006).

2. T. Pfeifer, R. Spitzenpfeil, D. Walter, C. Winterfeldt, F. Dimler, G. Gerber, and C. Spielmann, *Towards optimal control with shaped soft-x-ray light*, in preparation.

3. C. Winterfeldt, T. Pfeifer, D. Walter, R. Kemmer, A. Paulus, R. Spitzenpfeil, G. Gerber, and C. Spielmann, *Adaptive temporal and spatial shaping of coherent soft x-rays,* Proc. SPIE Vol. 6187, Photon Management II, eds. J. T. Sheridan, F. Wyrowski, ISBN 0-8194-6243-8, 61870F (2006).

4. D. Walter, T. Pfeifer, C. Winterfeldt, R. Kemmer, R. Spitzenpfeil, G. Gerber, and C. Spielmann, *Adaptive spatial control of fiber modes and their excitation for high-harmonic generation,* Opt. Expr. **14**, 3433 (2006).

5. A. Paulus, C. Winterfeldt, T. Pfeifer, D. Walter, G. Gerber, and C. Spielmann, *A novel time-of-flight electron spectrometer optimized for time-resolved soft-X-ray photoelectron spectroscopy,* Rev. Sci. Instr. **77** (4), 043105 (2006).

6. T. Pfeifer, R. Kemmer, R. Spitzenpfeil, D. Walter, C. Winterfeldt, G. Gerber, and C. Spielmann, *Spatial control of high-harmonic generation in hollow fibers,* Opt. Lett. **30**, 1497 (2005).

7. T. Pfeifer, D. Walter, C. Winterfeldt, C. Spielmann, and G. Gerber, *Controlling the spectral shape of coherent soft X-rays,* Appl. Phys. B **80**, 277 (2005).

8. A. Flettner, T. Pfeifer, D. Walter, C. Winterfeldt, C. Spielmann, and G. Gerber, *High-harmonic generation and plasma radiation from water microdroplets,* Appl. Phys. B **77**, 747 (2003).

Book chapters

1. C. Winterfeldt, J. Lohbreier, A. Paulus, T. Pfeifer, R. Spitzenpfeil, D. Walter, G. Gerber, and C. Spielmann, *Adaptive Spatial Control of High-Harmonic Generation,* in *Ultrafast Phe-*

nomena XV, (eds. R. J. D. Miller, A. M. Weiner, P. Corkum, D. Jonas), (Springer, Berlin, 2006), Springer Series in Chemical Physics, accepted (2006).

2. T. Brixner, C. Dietl, G. Krampert, P. Niklaus, E. Papastathopoulos, T. Pfeifer, R. Selle, G. Vogt, D. Walter, C. Winterfeldt, and G. Gerber, *Adaptive femtosecond quantum control,* in *Ultrafast Optics IV*, (eds. F. Krausz, G. Korn, P. Corkum, and I. A. Walmsley) (Springer, Berlin, 2004), vol. 95 of Springer Series in Optical Sciences, pp. 117–126.

3. T. Pfeifer, D. Walter, C. Winterfeldt, C. Spielmann, and G. Gerber, *Adaptive engineering of coherent soft x-rays,* in *Ultrafast Phenomena XIV*, (eds. T. Kobayashi, T. Okada, T. Kobayashi, K. A. Nelson, and S. de Silvestri) (Springer, Berlin, 2004), vol. 79 of Springer Series in Chemical Physics, pp. 178–180.

Own conference and seminar contributions

Invited talks

1. C. Winterfeldt, *Adaptive temporal and spatial shaping of coherent soft x-rays,* (Physikalisches Seminar, Universität Bielefeld, July 2006), invited talk.

2. C. Winterfeldt, A. Paulus, T. Pfeifer, T. Sokollik, R. Spitzenpfeil, D. Walter, G. Gerber, and C. Spielmann, *Engineered Coherent Soft-X-Ray Spectra,* (CLEO/Europe-EQEC Conference, World of Photonics Congress 2005, 2005), invited talk.

Contributed talks

3. C. Winterfeldt, *Control of high-harmonic radiation,* (Special AMO–Plasma Physics Seminar, University of Texas at Austin, USA, August 2006), contributed talk.

4. C. Winterfeldt, T. Pfeifer, D. Walter, R. Kemmer, A. Paulus, R. Spitzenpfeil, G. Gerber, and C. Spielmann, *Adaptive temporal and spatial shaping of coherent soft x-rays,* (Photonics Europe 2006, Strasbourg, 2006, Photon Management II, talk 6187-56), contributed talk.

5. C. Winterfeldt, A. Paulus, T. Pfeifer, R. Spitzenpfeil, D. Walter, G. Gerber, and C. Spielmann, *Adaptive zeitliche und räumliche Formung Hoher Harmonischer,* (DPG Frühjahrstagung, Frankfurt, 2006), contributed talk.

6. C. Winterfeldt, *Adaptive temporal and spatial shaping of coherent soft x-rays,* (Doktorandentreffen im Rahmen des Schwerpunktprogramms 1134 der DFG, Physikalisches Institut, Uni Würzburg, 2005), contributed talk.

7. C. Winterfeldt, J. Lohbreier, A. Paulus, T. Pfeifer, T. Sokollik, R. Spitzenpfeil, D. Walter, G. Gerber, and C. Spielmann, *Adaptive spektrale Formung kohärenter weicher Röntgenstrahlung zur Realisierung eines Attosekundenpulsformers,* (DPG Frühjahrstagung, Berlin, 2005), contributed talk.

8. C. Winterfeldt, T. Pfeifer, D. Walter, C. Spielmann, and G. Gerber, *Neuartiges Phasenanpassungsschema für die Erzeugung von Hohen Harmonischen in einer glatten Hohlfaser,* (DPG Frühjahrstagung, München, 2004), contributed talk.

9. C. Winterfeldt, T. Pfeifer, D. Walter, C. Spielmann, and G. Gerber, *Fourier meets Taylor in Physics: Adaptive Shaping of Ultrashort Laser Pulses,* (Echange Würzburg-Caen, Université de Caen, Basse-Normandie, France, 2003), contributed talk.

Posters

10. C. Winterfeldt, J. Lohbreier, A. Paulus, T. Pfeifer, R. Spitzenpfeil, D. Walter, G. Gerber, and C. Spielmann, *Adaptive spatial control of high-harmonic generation,* (15th International Conference on Ultrafast Phenomena, Pacific Grove, California, USA, 2006), poster.

11. C. Winterfeldt, A. Paulus, T. Pfeifer, T. Sokollik, R. Spitzenpfeil, D. Walter, C. Spielmann, and G. Gerber, *Controlling the spectral shape of coherent soft x-rays,* (340th Wilhelm und Else Heraeus-Seminar, High-Field Attosecond Physics (HIFAT 2005), Universitätszentrum, Obergurgl, Austria, 2005), poster.

12. C. Winterfeldt, T. Pfeifer, D. Walter, C. Spielmann, and G. Gerber, *Adaptive engineering of coherent soft x-rays,* (ECAMP VIII, 8th European Conference on Atomic and Molecular Physics, Rennes, France, 2004), poster.

13. C. Winterfeldt, T. Pfeifer, D. Walter, C. Spielmann, and G. Gerber, *High-Harmonic Generation from Water Microdroplets,* (Applications of High Field and Short Wavelenght Sources X, Biarritz, France, 2003), poster.

14. C. Winterfeldt, T. Pfeifer, D. Walter, C. Spielmann, and G. Gerber, *High-Harmonic Generation from Water Microdroplets,* (Summer School, Cargèse, Corsica, France, 2003), poster.

Other

1. C. Winterfeldt, *Optical Parametric Amplifier for Nonlinear Optical Spectroscopy,* Master's Thesis, The University of Texas at Austin, 2002.

Contents

List of Figures

Chapter 1

Introduction

Femtosecond laser technology has enabled us to follow atomic motion in real time [1, 2] and to control molecular processes [3–9] with tailored femtosecond laser pulses [3, 10–13], leading to the development of femtochemistry. The vibrational periods of atoms in molecules, which reflect the intramolecular *atomic* dynamics, lie in the range of tens to hundreds of femtoseconds. Laser pulses with durations of this order of magnitude can therefore efficiently measure and control molecular dynamics.

However, the natural time scale of *electrons* falls into the sub-femtosecond or attosecond regime. Important electronic processes include charge transfer after excitation or atomic inner-shell transitions. In order to explore electronic motion in real time as well as to control electronic dynamics, it is therefore desirable to develop new light sources with energies in the XUV region and pulse durations of the order of attoseconds to be able to directly access core-level electrons easily with one-photon transitions and with laboratory-scale experimental setups.

State-of-the-art femtosecond laser systems are usually based on Ti:sapphire technology, implying an operational laser wavelength of 800 nm in the near infrared, limiting the shortest attainable laser pulse duration to about 2.6 fs (one complete oscillation cycle), almost reached by recent experiments [14]. For shorter pulse durations in the sub-femtosecond regime, shorter wavelengths have to be used. The energetic scale of core electronic transitions also necessitate photons in the XUV.

Several techniques can be used to reach this wavelength range. Laser-produced plasmas (LPP) [15–17] are created by the interaction of a high-intensity laser pulse with high-density materials, leading to the emission of both bremsstrahlung and characteristic line radiation. This radiation has durations on the sub-picosecond to femtosecond scale and is intrinsically synchronized to the external laser source that generated the plasma. As a drawback, the radiation is incoherent and is emitted into a 4π solid angle, so that only a small fraction of the generated light can be used.

This problem is resolved in undulator-based free-electron lasers (FEL) [18], where the build-up of the x-ray pulses is coherent, leading to much higher fluxes in the forward direction. Photons at 12.7 eV from the TTF-FEL at DESY have already been used to examine the multiple ionization of atom clusters [19]. Recently, the operation of the free-electron laser at 32 nm has been demonstrated [20].

To perform the far-reaching step towards attosecond laser pulse production and application

(labeled "the transition from femtochemistry to attophysics" by Silberberg [21]), a different approach is needed. Based on highly nonlinear effects accessible with high-power femtosecond laser systems, this can be realized by the generation of high-order harmonics of the driving laser [22–24], leading to coherent emission in the soft-x-ray range.

Since the invention of the laser in 1960 by Theodore Maiman [25], attainable laser pulse durations have decreased from several hundreds of microseconds in this Ruby laser down to less than ten femtoseconds at very high peak powers and intensities in modern femtosecond Ti:Sapphire laser systems [26]. This allows the use of nonlinear optical techniques to convert existing laser light frequencies to different frequencies where standard light sources with the desired properties (e.g. wavelength, pulse duration, intensity) do not exist. The first application of the red Ruby laser at 694.3 nm successfully produced blue 347.2 nm radiation through the process of second-harmonic generation [27]. When a strong electric field (as from this pulsed laser) is applied to a medium, the polarization in the medium exhibits contributions not only at the original frequency (linear response) but terms of second, third, or higher order in the driving electric field appear, resulting in the generation of light at the corresponding integer multiples of the frequency of the incident light.

Further advances in femtosecond laser technology do not only allow for these low-order nonlinear processes (second-harmonic generation, third-harmonic generation (THG), optical parametric amplification (OPA), stimulated Raman scattering (SRS)), but they make it possible to exploit the highly nonlinear response of atoms and other media in high-intensity laser fields to generate very-high-order harmonics of the fundamental laser frequency (high-harmonic generation). This new electromagnetic radiation at much shorter wavelengths than the original optical pulse (at visible and short infrared wavelengths) was found inadvertently over a decade ago when researchers used intense femtosecond laser pulses to ionize rare gases [22–24].

High-harmonic generation provides a powerful source of ultrashort coherent radiation in the XUV and soft-x-ray range and has the inherent advantage to be realizable on a laboratory scale (so-called table-top systems) as opposed to large free-electron-laser facilities. Recent experiments have proven the existence of high-harmonic-based attosecond laser pulses by characterizing the temporal structure of the high-order harmonics [28–34]. Several groups [35–39] have already exploited the unique temporal properties of this new radiation to examine electronic dynamics, for example the Auger decay of inner-shell electrons. The attosecond time domain had not been directly accessible before due to the lack of such extremely short light pulses. It is now up to the researchers to make further use of this novel light source which has the potential for a large number of seminal discoveries. Since the exploration and observation of processes in turn are accompanied with the desire to control them, it is the scope of this work to demonstrate ways to manipulate the properties of these soft-x-ray pulses.

In general, for multi-cycle linearly polarized femtosecond laser pulses in a centrosymmetric medium conventionally used, high harmonics are produced at each half-cycle of the electric field of a laser pulse and are therefore emitted as light bursts with a periodicity of half a laser period. Combined analysis of the reciprocity properties of the Fourier transform and of the observation of the sign flip between consecutive bursts shows that the full harmonic spectrum usually consists of the odd harmonics of the fundamental laser frequency [40, 41] (this fact and possible exceptions will be discussed later in this work). For spectroscopic applications, it is desirable to use a single harmonic to facilitate the interpretation of the acquired data. The

selection of single harmonics with a grating is accompanied with a loss of time resolution due to dispersion and with a substantial intensity reduction due to low reflectivities. As a superior alternative, existing laser pulse shaping techniques can be used to control the high-harmonic spectrum and engineer harmonics as needed. A number of experiments have already been performed with the goal to influence the harmonic spectra, which will be summarized in this work in order to cover the field of the control of high-harmonic radiation to a certain level of completeness.

Our own results demonstrate the comprehensive control of high harmonics [42–44], including both the enhancement and suppression of single or multiple selected harmonic orders by temporal pulse shaping. These tunable quasi-monochromatic high-harmonic spectra allow for time-resolved spectroscopy in the soft-x-ray region and are therefore of great importance to a broad field of scientific disciplines. Arbitrarily shaped soft-x-ray spectra will also allow for major modifications of the resulting harmonic pulses in the temporal domain which paves the way towards direct attosecond pulse shaping and optimal control in the soft-x-ray domain.

In addition to the temporal shaping of the electric field of the driving laser pulse, the influence of spatial properties such as propagation effects is examined using a feedback-controlled adaptive two-dimensional spatial light modulator. High-harmonic generation in a hollow-core fiber can be enhanced by coupling into a single fiber mode. These results resolve the long-standing issue about the limited controllability of high-harmonic generation in free-focusing geometries such as gas jets [45–47] as compared to geometries where the laser is guided [48, 49]. Complete control over the shape of the soft-x-ray spectrum has a major impact on ultrafast energy-resolved spectroscopy and on the temporal structure of high harmonics.

This work is organized as follows: Chapter 2 lays the physical and mathematical foundations of ultrashort laser pulses. Ultrashort laser pulses provide the high intensities required for nonlinear optics. Nonlinear frequency conversion, including low-order processes (such as second-harmonic generation), phase matching, and high-harmonic generation, is discussed in Chapter 3. Emphasis is put on the different aspects of high harmonics, such as their unique generation mechanism, the atomic phase, the harmonic spectrum and attosecond pulse generation, coherence, and high-harmonic phase matching. The following Chapter (Chapter 4) summarizes our experimental progress on the control of high harmonic radiation. (Adaptive) temporal shaping of the driving laser field allows engineering of harmonic spectra, while our results on spatial pulse front shaping confirm the influence of propagation effects on the emerging harmonic spectra. The contents of this Chapter is also partly contained in a recent review article [50]. Chapter 5 describes the zoo of available techniques for the characterization of both optical laser pulses and high-harmonic femtosecond and attosecond laser pulses. It also summarizes our results towards the temporal characterization of our shaped high harmonics using two-photon two-color ionization of noble gases. A summary of this work including an outlook is given in Chapter 6. The Appendix contains supplementary material such as details on the generation of high harmonics from water micro-droplets and information on the computer program used to record the photoelectron spectra, completing the presentation of the achievements and progress made in this dissertation.

Chapter 2

Ultrashort light pulses: femtoseconds and attoseconds

Contents

High-intensity lasers emit their radiation in ultrashort pulses, that is very short bunches of a high number of photons. When a laser runs in continuous-wave (cw) mode, the power is more or less evenly distributed over the whole time, making the instantaneous number of available photons very low. Bunching the photons in shorter and shorter pulses leads to the necessary increase in intensity (Fig. 2.1). We therefore need to understand the basic properties of ultrashort light pulses, both in the femtosecond and the attosecond regime. After a short overview over state-of-the-art chirped-pulse amplification systems including the laser system used for the present work, the fundamentals of mode-locking and the mathematical description of ultrashort laser pulses and dispersion will follow. These introductory remarks form the basis for nonlinear processes, including low-order processes such as second-harmonic generation (SHG) as well as high-harmonic generation (HHG).

2.1 Chirped-pulse amplification laser system

The generation of high-intensity ultrashort laser pulses [51] is based on a mode-locked laser oscillator [52]. Pulses from this oscillator are very weak and are therefore amplified in a regenerative or multi-pass amplifier to obtain the desired intensities. A schematic view of the laser system used for the experiments presented in this work is displayed in Fig. 2.2. In both the oscillator and the amplifier it relies on a titanium-doped sapphire crystal as the laser gain medium. The maximum of the gain curve is located in the near-infrared at 800 nm, while the absorption band is centered around 490 nm. Therefore both laser rods are pumped by frequency-doubled pump lasers with neodymium-doped laser crystals. These crystals allow
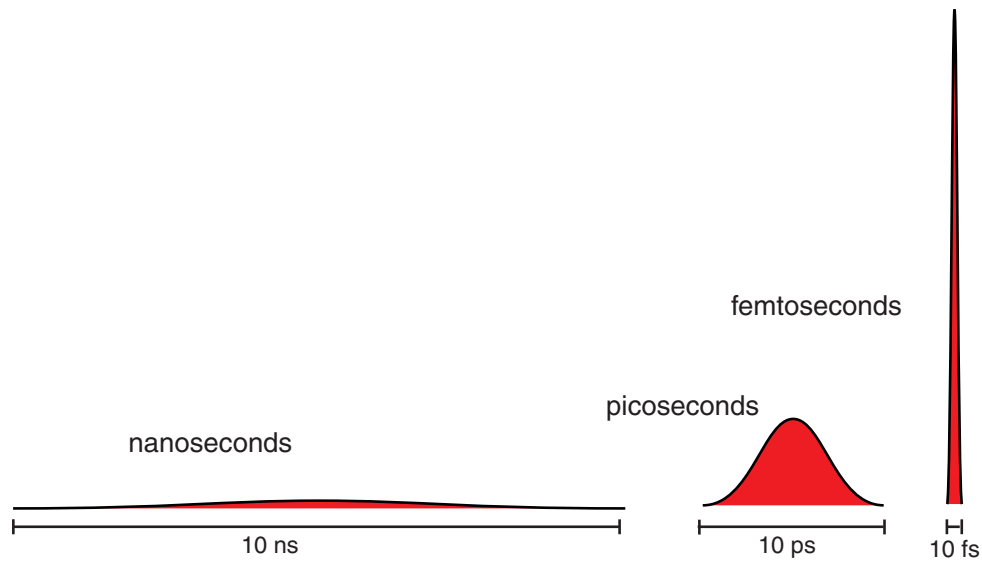
Figure 2.1 – Schematical view (not to scale) of the high potential of ultrashort laser pulses. For nanosecond lasers, the peak intensity is moderate. Compressing the number of available photons into shorter bunches (picoseconds) increases the peak intensity considerably. Going down to 10 femtoseconds which are relatively easy to achieve in state-of-the-art laser systems, highest peak intensities can be obtained, enabling the study of high-order nonlinear processes and of relativistic effects. In addition, the ultrashort time duration allows for the examination of ultrafast dynamics using pump-probe techniques.

for laser operation in the infrared around 1064 nm/1054 nm so that the frequency-doubled green photons have enough energy to be absorbed in the higher-energy absorption band.

In detail (Fig. 2.2), the Ti:sapphire oscillator (Spectra-Physics Tsunami) is pumped by a continuous-wave (cw) frequency-doubled Nd:YVO$_4$ laser (Spectra-Physics Millennia). This oscillator emits a pulse train of short 60-fs laser pulses with a spacing given by the round-trip time in the oscillator. This corresponds to a repetition rate of ≈ 80 MHz. The ultrashort light pulses are generated by phase-locking a large number of longitudinal cavity modes of the laser within the gain bandwidth of the laser medium (see Sec. 2.2). However, these pulses only have nJ energies. While this is sufficient for a number of low-order processes, usually much higher energies of at least hundreds of microjoules up to millijoules are required to obtain very high intensities such as needed for high-order processes. However, direct amplification of the pulses up to this level would result in nonlinear processes in the amplifier optics and could cause damage. A way to circumvent this problem was proposed by Strickland and Mourou [53] and has become a quasi-standard: *Chirped-pulse amplification* (CPA). The amplification of the pulses is accomplished by using chirped pulses instead of bandwidth-limited pulses from an oscillator.

The ultrashort pulses are first stretched in time by using some type of dispersive delay line [54]. In our system this is realized with a grating stretcher [55]. The difference in optical path lengths for the red and blue components due to the different diffraction angles of different wavelengths causes a chirp of the pulse, reducing its peak intensity considerably. The pulses are temporally stretched while they are spatially unchirped after the complete passage through the stretcher. Other devices for the purposes of stretching the pulse include optical
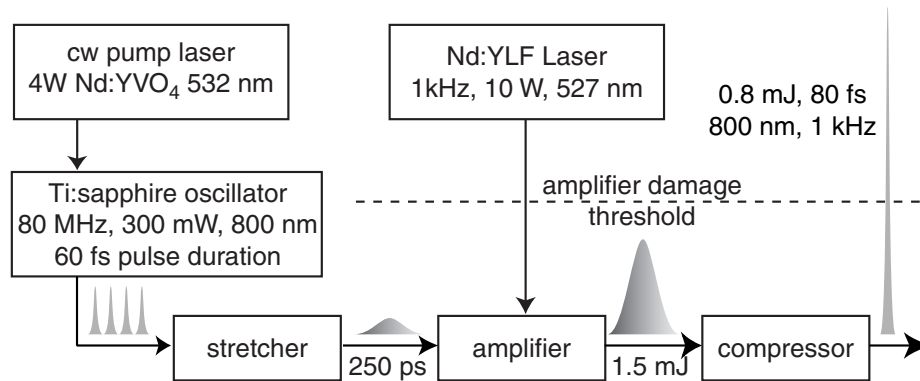
Figure 2.2 – Block diagram of our chirped-pulse amplification laser system. The Ti:sapphire oscillator, pumped by a cw Nd:YVO$_4$ pump laser at 4 W at 532 nm, produces ultrashort femtosecond laser pulses at 800 nm with a repetition rate of $\approx$ 80 MHz given by the cavity round-trip time. Before the amplification in a regenerative amplifier, these pulses are stretched in time to several picoseconds to avoid nonlinear effects and damage. The Ti:sapphire crystal in the amplifier is pumped by a green Q-switched Nd:YLF laser with a repetition rate of 1 kHz. The seed pulses from the oscillator are coupled into the cavity with a Pockels cell locked to the repetition rate of the pump laser. The amplified pulses are coupled out using a Pockels cell after saturation has been reached. They are subsequently compressed back to 80 fs to yield high-intensity ultrashort pulses.

fibers (both positive and negative chirp depending on the sign of the material dispersion, $\partial^2 n / \partial \omega^2$), diffraction grating pairs [55], prism pairs [56, 57], and chirped mirrors [58, 59]. As mentioned above, temporal stretching is the decisive first step in the chirped-pulse amplification scheme and is necessary to reduce the peak intensity for the successive amplifier to prevent damage and nonlinear responses by the optical components.

The stretched pulses are injected as seed pulses into the amplifier, in our case a Ti:sapphire laser cavity pumped by a Q-switched intra-cavity doubled Nd:YLF laser at 527 nm (Spectra-Physics Merlin). The pump pulse builds up a population inversion in the crystal which is then used for the amplification of the seed pulses by stimulated emission. After $\approx$ 12 round-trips, the highly amplified pulses are released from the cavity. Seed pulse injection and release of the amplified pulse (cavity dumping) are controlled by Pockels cells [60]. The frequency of the Q-switched pump laser and of the Pockels cells is 1 kHz, leading to a repetition rate of 1 kHz for the amplified pulses.

The highly amplified long laser pulses (about 1 ps) are then recompressed using a dispersive delay line of the opposite sign, which in our laser is a grating compressor. The energy of our pulses after the compressor is about 0.8 mJ which is higher by a factor of about 10^5 as compared to the seed pulses from the oscillator.

We are using a so-called regenerative amplifier which consists of a real laser cavity that can be operated in a free-running mode without being seeded by the oscillator pulses. When seeded at a level above amplified spontaneous emission (ASE), well-defined pulses are amplified at each pass through the laser crystal until they are coupled out.

The use of a laser cavity has the advantage of high stability (also pointing stability) and a good beam profile. However, for the amplification of large-bandwidth pulses such as needed for 30 fs laser systems, a multipass amplifier with typically less than ten passes must be used due to gain-narrowing issues.

Our amplifier system consisting of stretcher, regenerative amplifier, and compressor is a commercial Spectra-Physics Spitfire Chirped Pulse Amplifier [61]. State-of-the-art laser systems are all-solid-state systems. All laser media are solid materials, gas lasers such as the Ar^+ laser used in the past are no longer incorporated. If the pump lasers themselves are pumped by laser diodes instead of flash lamps, we speak of a DPSS (diode-pumped solid state) system. This very stable combination of lasers is nearly realized in our setup, only the Q-switched pump laser for the amplifier is based on flash lamp technology.

In order to increase the attainable pulse energy and thereby the maximum peak intensities, a home-made multipass amplifier [62] is incorporated into the housing of the regenerative amplifier. The amplifier is set up in a 4-pass bow-tie configuration [63, 64]. The uncompressed beam from the regenerative amplifier is sent through the bow-tie amplifier and is recompressed afterwards using the original compressor. However, the pump laser for the bow-tie amplifier (Coherent Infinity) had a repetition rate of only 100 Hz as opposed to 1 kHz of the regenerative amplifier in order to be able to deliver the necessary pump pulse energy of 100 mJ. This low repetition rate makes it necessary to increase integration times for experimental signals (high-harmonic optical spectra, electron spectra etc.) by a factor of ten.

We therefore used the theory developed by Lowdermilk and Murray [62, Eqs. (14) and (15)] in order to determine the pump fluence that would be needed if an available 15-mJ 1-kHz pump laser was used. The equations calculate the total gain depending on the number of round-trips and the small-signal gain. The small-signal gain is a function of parameters such as the saturation fluence of the crystal, the wavelength ratio between the pump laser and the seed laser, and of course the pump fluence. However, for seed energies of 1.3 mJ and pump energies of 15 mJ the required pump fluence is about $2 \, J/cm^2$ which exceeds the damage threshold of the mirrors in the bow-tie amplifier. In this case curved mirrors would have to be used in order to create the required fluences in the laser crystal while keeping the beam radius on the mirrors themselves at a safe level. Therefore the bow-tie amplifier was not used for the present experiments but can be redesigned in the future to deliver higher-energy pulses.

It is, of course, desirable to obtain high peak powers directly from passively mode-locked femtosecond oscillators to avoid external amplification stages. However, as stated above, the major challenge in scaling these oscillators to ever-higher peak powers is to prevent nonlinear effects in the system itself. Chirped-pulse oscillators with small net intracavity group-delay dispersion [65] present a possible way towards reaching this goal.

2.2 Mode locking

Ti:Sapphire laser oscillators are today being used as sources for ultrashort femtosecond pulses and as seed for high-energy chirped pulse amplification (CPA) laser systems. Ti:Sapphire has a very broad fluorescence spectrum [66, 67], thus being capable of delivering femtosecond pulses in mode-locked operation. At the same time the sapphire host crystal serves as the nonlinear Kerr medium required for passive mode-locking without any additional nonlinear elements.
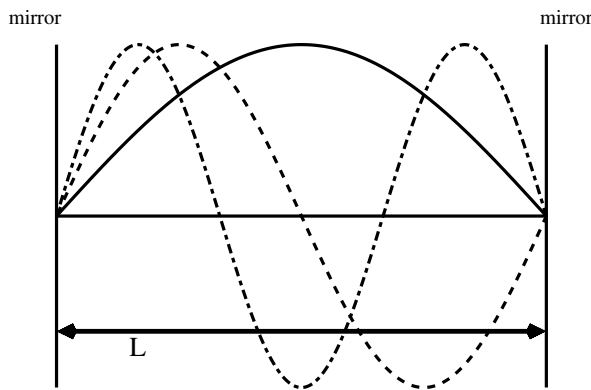
Figure 2.3 – Longitudinal modes (standing waves) in a cavity. The end mirrors are separated by the distance L, determining the longest wavelength from the condition $\lambda/2 = L$. The frequency spacing between the possible resonator modes is given by $\Delta \nu = c/2nL$.

Mode-locking [54, 68] works as the basic mechanism to provide femtosecond laser pulses. Based on this idea, an early consideration by Farkas and Tóth [69] shows that, similar to mode-locking in a femtosecond oscillator, high harmonics can be superimposed to yield attosecond pulses. This will be discussed later in the course of this work.

In order to better understand the physics behind mode-locking [66, 67], we briefly recap the concept of longitudinal resonator modes.

In an optical resonator such as a laser cavity electromagnetic fields can exist whose distributions of amplitudes and phases reproduce themselves upon repeated reflections between the mirrors. These electromagnetic field distributions are called *resonator modes* and can be divided into transverse modes (see Sec. 2.3) and longitudinal modes.

Fig. 2.3 schematically shows these longitudinal modes in a cavity. Since the electric field must be zero on the two mirrors we have to meet the condition

$$m\frac{\lambda}{2} = L \tag{2.1}$$

where $m = 1, 2, \ldots$, λ is the wavelength and L the length of the cavity. From Eq. (2.1) we get the resonant frequencies of our laser:

$$\nu = m \cdot \frac{c}{2L} \tag{2.2}$$

where c is the speed of light. The frequencies given by Eq. (2.2) are the allowed frequencies of a free-running laser when there are no wavelength-selective elements like prisms, gratings or etalons. The difference in frequency $\Delta\nu$ between two consecutive resonator modes simply is $\Delta\nu = \nu(m+1) - \nu(m)$ and we get:

$$\Delta\nu = \frac{c}{2L} \tag{2.3}$$

In the general case when the refractive index is not equal to unity one has, of course, to replace the cavity length L with the optical path length nL. This is, of course, the case in a semiconductor laser.

Now assume that the laser is lasing at a large number of different frequencies simultaneously. The electric field of a single mode l at frequency ω_l can be written as

$$E_l(t) = E_{l0}\exp[i\omega_l t + \phi_l] \tag{2.4}$$

where E_{l0} is its amplitude and ϕ_l is its phase. The resulting electric field is a linear superposition of these single modes. However, since the phases are totally random, the output (which

Figure 2.4 – Output of a free-running laser in multi-mode operation with random phases. If the phases of the single modes are stable, the pattern is repeated after τ_p but shows no distinct peaks. Pulse formation is random and has a low contrast.
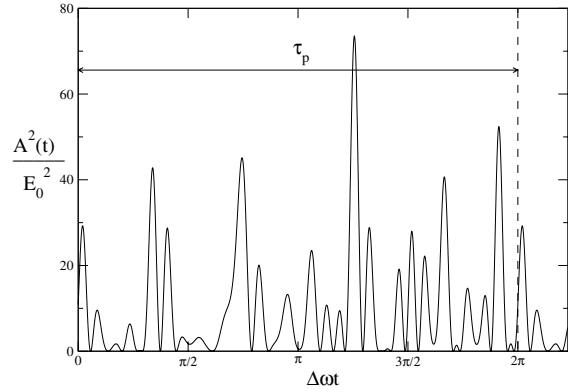
is proportional to the square of the electric field) is a random pattern as shown in Fig. 2.4. This is the continuous-wave (cw) output of a free-running laser with a large number of active laser modes.

The technique of *mode-locking* locks all the phases such that the phase difference between two consecutive modes has a constant value. This enables us to achieve pulses with a duration of the order of femtoseconds.

In order to understand the mathematics behind mode-locking, consider $2n + 1$ longitudinal modes which all have the same amplitude E_0 and are separated in frequency by $\Delta\omega = 2\pi\Delta\nu$ (Eq. (2.3)). This is a simplification as the amplitudes of the modes normally follow a Gaussian distribution according to the gain profile of the laser. The results of our approximation, however, are very similar to the real case and clearly show the emergence of light pulses. Let now the phases of the longitudinal modes have a fixed relationship as mentioned above, that is

$$\phi_l - \phi_{l-1} = \phi \tag{2.5}$$

where ϕ is a constant. The resulting electric field $E(t)$ then takes the form

$$E(t) = \sum_{l=-n}^{+n} E_0 \exp[i(\omega_0 + l\Delta\omega)t + l\phi]. \tag{2.6}$$

This can be rewritten as

$$E(t) = A(t)\exp(i\omega_0 t), \tag{2.7}$$

where

$$A(t) = \sum_{l=-n}^{+n} E_0 \exp[il(\Delta\omega t + \phi)]. \tag{2.8}$$

If we now switch to a new time reference $\Delta\omega t' = \Delta\omega t + \phi$ we have

$$A(t) = \sum_{l=-n}^{+n} E_0 \exp(il\Delta\omega t'), \tag{2.9}$$

which is a geometric progression and yields

$$A(t') = E_0 \frac{\sin[(2n+1)\Delta\omega t'/2]}{\sin(\Delta\omega t'/2)}. \tag{2.10}$$

The time-dependence of the output according to Eq. (2.10) can be seen in Fig. 2.5.
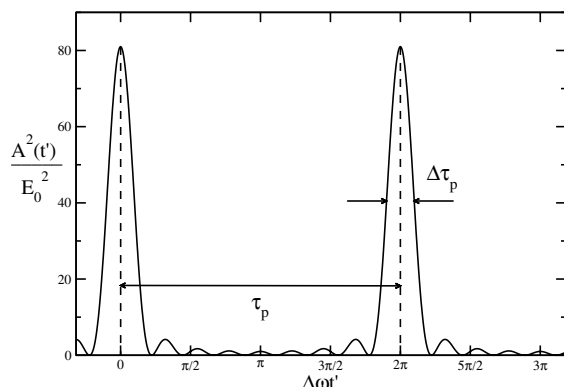
Figure 2.5 – Output of a mode-locked laser. The spacing τ_p between two pulses is given by the round-trip time in the laser cavity. The pulse duration $\Delta\tau_p$ is determined by the inverse of the available bandwidth.

The pulse maxima occur when the denominator vanishes (as well as numerator). This is the case for $t' = 0$, $\Delta\omega t'/2 = \pi$ etc. So the time τ_p between two pulses is $\tau_p = 2\pi/\Delta\omega$ or

$$\tau_p = \frac{1}{\Delta\nu}. \tag{2.11}$$

To calculate the pulse width $\Delta\tau_p$ we have to find the first zero of $A^2(t')$ (for $t' > 0$) which is at t'_p determined by

$$[(2n+1)\Delta\omega t'_p/2] = \pi. \tag{2.12}$$

Since the pulse width $\Delta\tau_p$ (FWHM) of $A^2(t') \approx t'_p$ we obtain the following expression for the pulse width of our mode-locked laser:

$$\Delta\tau_p \approx \frac{2\pi}{(2n+1)\Delta\omega} = \frac{1}{\Delta\nu_L}, \tag{2.13}$$

where $\Delta\nu_L = (2n+1)\Delta\nu$ is the total laser bandwidth. The frequency difference and the total bandwidth of the laser therefore determine the separation and width of the pulses, respectively.

As we will see later, the high-harmonic spectrum also consists of discrete "modes" (harmonic peaks) that are phase-locked [31]. The coherent superposition can be treated similarly to mode-locking in the oscillator and creates an attosecond pulse train, which is, in first approximation, a train of regularly spaced ultrashort pulses with durations on the attosecond time scale. This was first proposed by Farkas and Tóth [69] who considered the coherent sum of high harmonics 5 to 21 from a Nd laser (Fig. 2.6). The attosecond pulse train in Fig. 2.6 is essentially the same result as for the locking of the longitudinal modes in the laser oscillator in Fig. 2.5.

In order to drive the laser oscillator into mode-locking (instead of cw output) several approaches and techniques can be used. The main distinction is made between active mode-locking, where the mode-locking element is driven by an external source (AM mode-locking, FM mode-locking, synchronous pumping), and passive mode-locking, where the element that induces mode-locking is not driven externally but instead exploits some nonlinear optical effects, such as the saturation of a saturable absorber or a nonlinear refractive index change in a suitable material (fast saturable absorber, slow saturable absorber, Kerr-lens mode-locking (KLM), additive pulse mode-locking).

Let us now review amplitude modulation (AM) mode-locking which can be achieved with a modulator such as an acousto-optic modulator or electro-optic modulator which is placed
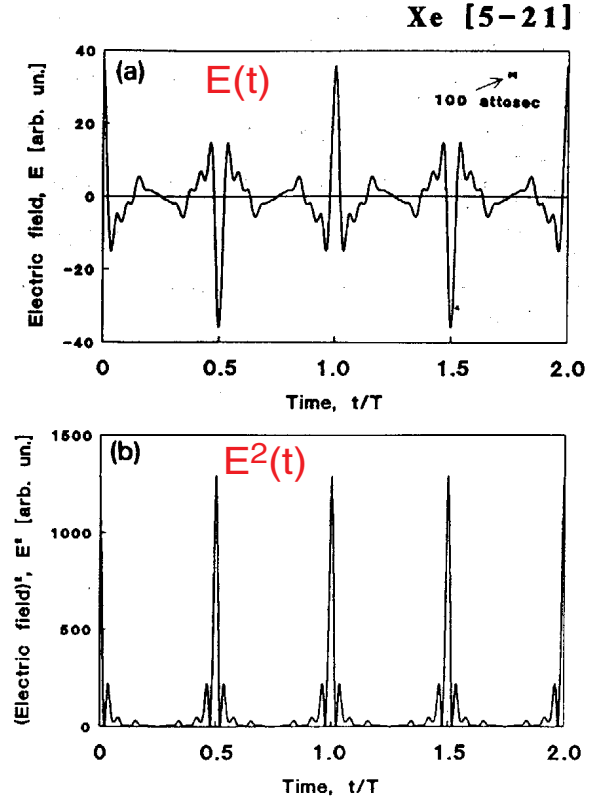
Figure 2.6 – Proposal for attosecond light pulse generation using laser induced multiple-harmonic conversion processes in rare gases. The high harmonics 5 to 21 of a Nd laser are coherently summarized. Panel a) shows the resulting electric field while panel b) displays the intensity of the short attosecond bursts (Figure adapted from Farkas and Tóth [69]).

inside the cavity of a conventional laser or by modulating the driving current of a semiconductor laser. Both methods introduce a time-varying loss at the frequency ω_m. The amplitude of the electric field of the l-th mode therefore has to be modified by a modulation factor:

$$E_l(t) = E_0\{1 - (\delta/2)[1 - \cos(\omega_m t)]\} \cos(\omega_l t + \phi_l). \tag{2.14}$$

The field amplitude is modulated from E_0 to $E_0(1 - \delta)$. If we note that

$$E_0(\delta/2) \cos(\omega_m t) \cos(\omega_l t + \phi_l) = \tag{2.15}$$
$$= (E_0\delta/4)\{\cos[(\omega_l + \omega_m)t + \phi_l] + \cos[(\omega_l - \omega_m)t + \phi_l]\}$$

we see that we obtain modulation sidebands at the frequencies $\omega_l \pm \omega_m$. If the frequency of the modulation is equal to the difference in frequency between two consecutive modes, $\omega_m = \Delta\omega$, these sidebands coincide with the adjacent mode frequencies of the modes $l + 1$ and $l - 1$. The electric field of one mode contributes to the electric fields of the adjacent modes and thus gives a contribution to the field equations which become coupled.

Passive mode-locking techniques can be realized by introducing an optical element with an intensity-dependent transmission into the laser cavity. The transmission must be higher for higher intensities (such as provided e. g. by a saturable absorber). Taking into account Fig. 2.4 we see that the time-dependent output of a free-running laser consists of a random sequence of some sort of pulses with higher and lower intensities. Low peaks now experience higher losses while passing through the special element with intensity-dependent transmission so that they fall below the lasing threshold and thus do not lase any more. The peak with the highest intensity, however, experiences the least losses and therefore the highest net gain. It will be amplified and thus be even higher upon return after one round-trip through the cavity

than it was. Gradually, an ultrashort pulse is shaped and gains more and more intensity until eventually a pulse train as in Fig. 2.5 results.

Kerr-lens mode-locking as an example for passive mode-locking will be covered in Sec. 3.3.2 after the introduction of Gaussian laser beams and nonlinear optics.

2.3   Gaussian laser beams

In addition to the longitudinal resonator modes described in Sec. 2.2, the resonator modes inside an optical resonator can be described based on the transverse distribution of the electromagnetic field. The lowest-order transverse electromagnetic mode is the *fundamental mode* or TEM$_{00}$ mode, with no nodes of intensity transverse to the beam axis in the vertical and horizontal directions [66] and the lowest losses compared to higher-order modes. The intensity profile has a Gaussian spatial shape with its maximum on the beam axis [70]:

$$I(r) \propto I_0 e^{-\frac{2r^2}{w^2}} \tag{2.16}$$

where r is the radial coordinate and w is the radial distance at which the field amplitude drops to $1/e$ of its value on the axis. The intensity accordingly drops to $1/e^2$ at this point. The quantity w is therefore called the beam radius or *spot size* of the laser beam. The TEM$_{00}$ is the most common and most desirable mode of a laser since all the power is contained in one small spot. Also, it can be well focused, yielding a Gaussian intensity distribution in the focus since the profile at focus is determined through a Fourier transform of the far-field distribution.

As this Gaussian beam propagates, the width of the intensity profile changes along the axis, although it remains Gaussian. The Gaussian beam contracts to a minimum spot size w_0 at the beam waist where the phase front is planar. The spot size w in Eq. (2.16) depends on the propagation coordinate z in the following way [66–68, 71]:

$$w^2(z) = w_0^2 \left[1 + \frac{z^2}{z_R^2} \right] \tag{2.17}$$

where $z = 0$ at the position of the beam waist.

The *Rayleigh range* z_R is defined by

$$z_R = \frac{\pi w_0^2 n}{\lambda}, \tag{2.18}$$

where w_0 is again the minimum spot size or beam waist, n is the index of refraction of the medium, and λ is the wavelength of the beam in vacuum. Eq. (2.18) denotes the distance after which the spot size of a beam has increased by a factor of $\sqrt{2}$ from the original beam waist w_0. In the literature, the Rayleigh range is sometimes replaced by the *confocal parameter b* given by

$$b = \frac{2\pi w_0^2 n}{\lambda} = 2z_R, \tag{2.19}$$

which is simply twice the Rayleigh range.

For a laser beam containing higher-order modes, the spot size w_0 in Eq. (2.17) must be corrected by the so-called M^2 value:

$$w_{\text{corrected}} = M^2 \, w_{0,\text{TEM00}}. \tag{2.20}$$

The wave front of a Gaussian beam is spherical, which is linked to the evolution of the spotsize $w(z)$ (Eq. (2.17)) as a function of the distance z. The radius of curvature of this spherical wavefront at a distance z from the waist is given by a similar expression [66, 71]:

$$R(z) = z \left[1 + \frac{z_R^2}{z^2} \right].$$
(2.21)

As can be seen from this Equation, radius of curvature becomes infinite at the position of the beam waist, which simply constitutes a planar wave front at focus.

The full form of the electric field of a Gaussian TEM_{00} mode can be derived mathematically using Maxwell's equations in an isotropic charge-free medium [71]. The result is

$$
\begin{aligned}
E(x,y,z) &= E_0 \frac{w_0}{w(z)} \exp \left\{ -i[kz - \eta(z)] - i\frac{kr^2}{2q(z)} \right\} = \\
&= E_0 \frac{w_0}{w(z)} \exp \left\{ -i[kz - \eta(z)] - r^2 \left[\frac{1}{w^2(z)} + \frac{ik}{2R(z)} \right] \right\}
\end{aligned}
$$
(2.22)

where

$$
\begin{aligned}
\eta(z) &= \arctan \left(\frac{z}{z_R} \right), \\
\frac{1}{q(z)} &= \frac{1}{R(z)} - i\frac{\lambda}{\pi n w^2(z)}.
\end{aligned}
$$
(2.23)
(2.24)

The parameter $\eta(z)$ describes the spatial phase of a laser beam. It can be clearly seen that it changes sign (acquires a value of π) along the propagation direction across a laser focus. This phase is called the *Gouy phase* and can be measured using the phase-selective detection of few-cycle-pulse-generated photoelectrons in a stereo-TOF arrangement [72].

The quantity $q(z)$ is also called the *Gaussian beam parameter* and is a very useful quantity to determine the propagation of Gaussian beams along their paths through media like lenses with the help of the matrices known from the matrix formulation of geometrical optics [67, 68].

The brief summary on this matrix formulation method given in Winterfeldt [70] shall be repeated here since it will be used later to determine the optimal focusing conditions for the probe beam in the high-harmonic cross-correlation experiments (Sec. 5.3). The matrix formulation of geometrical optics, within the paraxial-ray approximation, is a very convenient and powerful tool to describe the propagation of light rays through an optical system including lenses and curved mirrors. It allows to calculate the influence of an arbitrary number of optical elements, including free space, on an input light ray by just multiplying the characteristic matrices describing the optical elements so that a single total matrix is obtained.

A ray vector r_1 at a given input plane $z = z_1$ of an optical element can be characterized by two parameters, namely, its radial displacement $r(z_1)$ from the z axis and its angular displacement θ_1 [67]. The output ray r_2 can be described accordingly. Within the paraxial-ray approximation angular displacements θ are assumed to be small enough to allow the following approximation: $\sin\theta \approx \tan\theta \approx \theta$. Input and output variables are then related by a linear transformation. Setting $\theta_i \approx (dr_i/dz)_{z_i} = r_i'$, we can write [67]

$$
\begin{aligned}
r_2 &= Ar_1 + Br_1', \\
r_2' &= Cr_1 + Dr_1',
\end{aligned}
$$
(2.25a)
(2.25b)

where A, B, C, and D are characteristic constants of the given optical element. Eqs. (2.25) can be recast in a matrix formulation as:

$$\begin{bmatrix} r_2 \\ r_2' \end{bmatrix} = \begin{bmatrix} A & B \\ C & D \end{bmatrix} \begin{bmatrix} r_1 \\ r_1' \end{bmatrix} \tag{2.26}$$

where the $ABCD$ matrix completely characterizes the given optical element within the paraxial-ray approximation.

The matrices that we will need later are the representations of a thin lens with focal length f,

$$\begin{bmatrix} A & B \\ C & D \end{bmatrix} = \begin{bmatrix} 1 & 0 \\ -1/f & 1 \end{bmatrix}, \tag{2.27}$$

and the matrix for propagation of the beam through a medium of length L with an index of refraction n,

$$\begin{bmatrix} A & B \\ C & D \end{bmatrix} = \begin{bmatrix} 1 & L/n \\ 0 & 1 \end{bmatrix}. \tag{2.28}$$

A derivation of these matrices can be found in Svelto [67] and Siegman [68]. Eq. (2.27) of course also holds for a concave mirror of curvature R. The value for f in Eq. (2.27) simply has to be replaced by the well-known relation $f = R/2$. When several optical components are passed all matrices have to be multiplied according to the rules of matrix multiplication.

The power of this matrix formulation lies in the fact that it is not only valid for geometrical optics but can also be used to describe the propagation of Gaussian laser beams. By solving the wave equation for the Gaussian beam and by comparing the solution to the transformation of the radius of curvature by an $ABCD$ optical system, we find that the Gaussian beam parameter q in Eq. (2.24) transforms according to [67, 71]

$$q_{\text{out}} = \frac{q_{\text{in}} A + B}{q_{\text{in}} C + D} \tag{2.29}$$

where the parameters A, B, C, and D are just the entries of the corresponding $ABCD$ matrix in ray optics. Eq. (2.29) is referred to as the *ABCD law of Gaussian beam optics*. With it, the propagation of a Gaussian beam through a general medium can be described completely. Using Eq. (2.24), the input Gaussian beam parameter q_{in} is constructed from the experimental values $w_{\text{in}}(z)$ and $R_{\text{in}}(z)$ and is propagated with the help of Eq. (2.29). The output parameter q_{out} can then be decomposed into the radius of curvature $R(z)$ and the spot size $w(z)$ using the real and imaginary part of q.

2.4 Mathematical description of ultrashort laser pulses

In order to understand the behavior of ultrashort light pulses in the temporal and spectral domain, it is necessary to formulate the relation between the two domains mathematically. They are linked through a Fourier transform, and so the modification of a laser pulse in one of the two domains either by propagation due to dispersion or actively by pulse shaping implies a modification of its properties in the conjugate domain as well. It is important to introduce the concept of the amplitude and the phase of the electric field because the generation, measurement, and shaping of ultrashort laser pulses is based on measuring and influencing these properties.

This mathematical description of ultrashort laser pulses largely follows the treatment presented in Winterfeldt [73]. The time behavior of a laser pulse at a fixed point in space including the envelope, the oscillations and the phase can be fully described by the real electric field $E(t)$. The electric field in the time-domain is invariably connected with its counterpart $E(\omega)$ in the frequency-domain via a Fourier transform:

$$E(\omega) = \frac{1}{\sqrt{2\pi}} \int\limits_{-\infty}^{+\infty} E(t) \, e^{-i\omega t} \, dt. \tag{2.30}$$

The inverse Fourier transform yields the original electric field in the time-domain:

$$E(t) = \frac{1}{\sqrt{2\pi}} \int\limits_{-\infty}^{+\infty} E(\omega) \, e^{i\omega t} \, d\omega. \tag{2.31}$$

These two ways of describing a laser pulse are completely equivalent. Which description to use depends on the special problem to solve or the best accessible property in an experiment. Note: Changing a feature in one domain affects the other domain as well.

Since $E(t)$ is real, the following relation holds for the Fourier coefficients:

$$E(\omega) = E^*(-\omega). \tag{2.32}$$

The electric field is therefore fully determined by the contributions of the positive frequencies. We can decompose the complex quantity $E(\omega)$ into the spectral amplitude $|E(\omega)|$ and the spectral phase $\Phi(\omega)$:

$$E(\omega) = |E(\omega)| \, e^{-i\Phi(\omega)}. \tag{2.33}$$

In most cases the spectral amplitude is centered about a center frequency ω_0. We can expand the phase into a Taylor series about ω_0:

$$\Phi(\omega) = \sum_{j=0}^{\infty} \frac{b_j}{j!} (\omega - \omega_0)^j. \tag{2.34}$$

The coefficient

$$b_j = \left. \frac{d^j \Phi(\omega)}{d\omega^j} \right|_{\omega=\omega_0} \tag{2.35}$$

is denoted spectral phase coefficient of j-th order.

The zero-order coefficient $b_0 = \Phi_0$ determines the location of the carrier peaks with respect to the pulse envelope. It is therefore called *absolute phase* or *carrier-envelope phase* (CEP) [74, 75]. Usually it can be neglected for laser pulses that contain more than a few cycles since in this case the electric field amplitude does not vary much from one cycle to the next[1]. At 800 nm this corresponds to pulses longer than about 10 fs. The CEP, however, has far-reaching consequences for pulses approaching the single-cycle limit [77, 78]. In general, this phase is not constant from pulse to pulse because the group and phase velocities differ inside the laser cavity. The absolute phase can be stabilized using a $f - 2f$ interferometric setup [74, 75, 79],

---

[1]For high-harmonic generation, however, which is very sensitive to the actual value of the electric field, carrier-envelope-phase phenomena have been observed for the long quantum path even in the multi-optical-cycle regime [76].

which, however, does not allow to determine its actual value. The measurement of the CEP can be performed using photoelectron emission in gases [80] or from solid surfaces [81].

The first-order coefficient $b_1 = \Phi'$ describes a temporal shift of the laser pulse and therefore does not give physically relevant contributions. The so-called *chirp*, a true phase modulation, is obtained from the higher orders. For *spectrally unchirped* pulses we have $b_j = 0$ for all $j \geq 2$.

Similarly, $E(t)$ can be expressed in terms of amplitude or temporal envelope $A(t)$ and temporal phase $\Phi(t)$:

$$E(t) = A(t)\, e^{i\Phi(t)} \tag{2.36}$$

We can now make a Taylor series expansion of the phase around $t = 0$,

$$\Phi(t) = \sum_{j=0}^{\infty} \frac{a_j}{j!} t^j \tag{2.37}$$

where we have the following relations for the temporal phase coefficient:

$$a_j = \left. \frac{d^j \Phi(t)}{dt^j} \right|_{t=0} . \tag{2.38}$$

The coefficient of zeroth order, a_0, again describes the carrier-envelope phase (CEP) Φ_0. The first order coefficient, a_1, determines the center frequency ω_0. Changing this coefficient will shift the pulse in frequency. Therefore we can write the phase as the oscillatory part of the carrier or center frequency ω_0 plus the remaining modulation $\varphi(t)$:

$$\Phi(t) = \omega_0 t + \varphi(t). \tag{2.39}$$

Hence we introduce the *instantaneous frequency*, which is given by the derivative of the phase with respect to time:

$$\omega(t) = \frac{d\Phi(t)}{dt} = \omega_0 + \frac{d\varphi(t)}{dt}. \tag{2.40}$$

This is often expressed as

$$\omega(t) = \omega_0 + \delta\omega(t) \tag{2.41}$$

where

$$\delta\omega(t) = \frac{d}{dt}\varphi(t) \tag{2.42}$$

denotes the variation of the instantaneous frequency. The instantaneous frequency is a well-defined concept and is given by Eqs. (2.41) and (2.42) whenever the amplitude $A(t)$ varies slowly compared to an optical cycle. If $a_j = 0$ for all $j \geq 2$, one speaks of *temporally unchirped* pulses, in analogy to the frequency domain. In this case we have $\omega(t) = const$. The angular frequency of a laser pulse does not change during this pulse. For $d\omega(t)/dt = d^2\varphi(t)/dt^2 > 0$ the instantaneous frequency increases with time, which yields an *up-chirp* (positive chirp, red comes before blue) in contrast to the *down-chirp* (negative chirp, blue comes before red) where we have $d^2\varphi(t)/dt^2 < 0$. If the instantaneous frequency $\omega(t)$ changes linearly with time,

$$a_2 \neq 0 \quad \text{and} \quad a_j = 0 \quad \forall j > 2 \tag{2.43}$$

we obtain the important special case of a *linear chirp*.

In the Gaussian system of units, the intensity associated with an electric field of the form

$$E(t) = Ee^{-i\omega_0 t} + \text{c.c.} \tag{2.44}$$

is [60]

$$I(\omega) = \frac{nc}{2\pi}|E|^2 \tag{2.45}$$

where n is the refractive index of the medium and c is the speed of light. I and E are measured in the corresponding CGS units erg/cm^2 and statvolts/cm, respectively. In the MKS or SI system of units, Eq. (2.45) transforms to

$$I(\omega) = 2nc\epsilon_0|E|^2 \tag{2.46}$$

where ϵ_0 is permeability of free space, and n and c are defined as above. I and E are now measured in W/m^2 and V/m, respectively.

In analogy, the intensity of ultrashort laser pulses in the time domain is usually given as the cycle-averaged squared modulus of the electric field:

$$I(t) = \epsilon_0 cn \frac{1}{T} \int_{t-T/2}^{t+T/2} dt' \, |E(t')|^2, \tag{2.47}$$

where ϵ_0 is the permeability of free space, c is the speed of light in vacuum, n is the index of refraction of the material under consideration, and T is the period of the oscillation of the carrier wave. This definition is applicable as long as the temporal variation of the envelope of the electric field $A(t)$ is slow compared to the carrier frequency ω (slowly-varying-envelope approximation, SVEA). In this case, the temporal intensity is proportional to the squared modulus of the envelope. For laser pulses approaching the single-cycle limit, this approximation breaks down as the envelope changes practically as fast as the underlying oscillations themselves. In this regime, many processes such as laser-dressed photoionization by high-harmonic photons (Sec. 5.1.2.5) are governed by the actual value of the electric field instead of the (slow) evolution of the envelope.

With "simple" pulse shapes such as a Gaussian pulse or a hyperbolic secant it is reasonable to introduce the pulse duration τ_p as the full width at half-maximum (FWHM) of the temporal intensity $I(t)$. In the same way we define the bandwidth $\Delta\omega = 2\pi\Delta\nu$ as full width at half-maximum of the spectral intensity distribution $I(\omega)$. However, with pulse shapes being more complex, a unique description can only be given by the complete relations $E(t)$ or $E(\omega)$.

The bandwidth product is defined as $\tau_p\Delta\nu$. From the properties of the Fourier transform it follows that the minimum value of the bandwidth product is limited by

$$\tau_p\Delta\nu \geq c_B \tag{2.48}$$

with the constant c_B being of an order of magnitude of 1 and depending upon pulse shape and definition of pulse widths. The equality sign in Eq. (2.48) holds for bandwidth-limited pulses.

To illustrate this, we provide a brief example. Consider an optical pulse with a carrier frequency ω_0 and a complex Gaussian envelope in the form [68]

$$E(t) = e^{-at^2} e^{i(\omega_0 t + bt^2)} = e^{-\Gamma t^2} e^{i\omega_0 t}. \tag{2.49}$$

The pulsewidth τ_p of this pulse is

$$\tau_p = \sqrt{\frac{2\ln 2}{a}}. \tag{2.50}$$

Using the instantenous frequency in Eq. (2.40),

$$\omega(t) = \frac{d}{dt}(\omega_0 t + b t^2) = \omega_0 + 2bt, \tag{2.51}$$

we see that our pulse is linearly chirped, with the parameter b being a measure of the chirp. It corresponds to a_2 in Eqs. (2.38) and (2.43).

The spectrum $E(\omega)$ of the pulse (2.49) can be found using the Fourier transform (Eq. (2.30)). The bandwidth then is

$$\Delta\nu = \frac{\sqrt{2a\ln 2}}{\pi}\sqrt{1 + \left(\frac{b}{a}\right)^2}, \tag{2.52}$$

yielding a time-bandwidth product of

$$\tau_p \Delta\nu = \left(\frac{2\ln 2}{\pi}\right)\sqrt{1 + \left(\frac{b}{a}\right)^2} \approx 0.441 \times \sqrt{1 + \left(\frac{b}{a}\right)^2}. \tag{2.53}$$

Thus we see that in the case of an unchirped pulse with Gaussian pulse envelope, *e.g.* $b = 0$, the pulse is bandwidth-limited with $c_B \approx 0.441$. The presence of chirp increases this time-bandwidth product correspondingly.

Analogously, if we have a transform-limited pulse and send it through a medium to acquire some quadratic phase due to material dispersion, the coefficient b_2 will be different from zero (the pulse is now chirped), and the pulse duration in this linearly chirped case is extended by the factor

$$\sqrt{1 + (4\ln 2 \cdot b_2 / \tau_0^2)^2} \tag{2.54}$$

compared to the original pulsewidth τ_0 [68, 82]. Note: The pulse still displays the same spectral width as before.

The meaning of the other components b_j will be made clear in the following Section on dispersion.

2.5   Dispersion

The behavior of an ultrashort laser pulse when it propagates through a linear non-absorbing dispersive medium is determined by the influence of the frequency-dependent refractive index $n(\omega)$ on the spectral phase components b_j (Eq. (2.35)). The electric field given by Eq. (2.33), propagating along the z axis, acquires an additional phase term $\Phi_{\mathrm{disp}}(\omega)$ caused by dispersion:

$$E(\omega, z) = |E(\omega)| e^{-i[\Phi(\omega) + \Phi_{\mathrm{disp}}(\omega)]}, \tag{2.55}$$

where the dispersive phase term is determined through the dependence of the wave vector $k(\omega)$ on the refractive index [60]:

$$\Phi_{\mathrm{disp}}(\omega) = k_{\mathrm{disp}}(\omega) z = n(\omega)\frac{\omega}{c} z. \tag{2.56}$$

Note: c is the speed of light *in vacuum*. For a non-absorbing medium, the effective speed of light is given by the group velocity $v_{gr}(\omega_0)$ at the center frequency ω_0:

$$v_{gr}(\omega_0) = \left(\frac{d\omega(k)}{dk}\right)_{k=k(\omega_0)} = \left(\frac{dk(\omega)}{d\omega}\right)^{-1}_{\omega=\omega_0} = \frac{c}{\left[n(\omega) + \omega\frac{dn(\omega)}{d\omega}\right]_{\omega=\omega_0}} = \frac{c}{n_{gr}(\omega_0)}. \quad (2.57)$$

Here we have defined the sum of the refractive index plus the derivate term as the group index $n_{gr}(\omega_0)$.

It is often adequate to describe the dependence of the dispersive phase on frequency in terms of a truncated power series expansion. We calculate the expansion Eq. (2.35) for the acquired phase term $\Phi_{disp}(\omega)$ around ω_0:

$$b_0 = \Phi_{disp}(\omega_0) = n(\omega_0)\frac{\omega_0}{c}z, \quad (2.58a)$$

$$b_1 = \frac{d\Phi_{disp}(\omega)}{d\omega}\bigg|_{\omega=\omega_0} = \frac{z}{c}\left[n(\omega) + \omega\frac{dn(\omega)}{d\omega}\right]_{\omega=\omega_0} = \frac{z}{v_{gr}(\omega_0)} = \tau_{gr}(\omega_0), \quad (2.58b)$$

$$b_2 = \frac{d^2\Phi_{disp}(\omega)}{d\omega^2}\bigg|_{\omega=\omega_0} = \frac{z}{c}\left[2\frac{dn(\omega)}{d\omega} + \omega\frac{d^2n(\omega)}{d\omega^2}\right]_{\omega=\omega_0} =$$

$$= \left[-\frac{z}{v_{gr}}\frac{dv_{gr}}{d\omega}\right]_{\omega=\omega_0} = \left[\frac{d\tau_{gr}}{d\omega}\right]_{\omega=\omega_0}. \quad (2.58c)$$

The zero-order coefficient b_0 in the first equation (2.58a) does not contain any derivatives of the refractive index and therefore does not depend on the dispersion. It describes the additional phase acquired during the propagation through the medium, which changes the value of the absolute phase. The first-order coefficient b_1 is the reciprocal of the group velocity times the propagation distance z and can therefore be identified as travel time through the medium or *group delay* τ_{gr}. Since the envelope travels with the group velocity v_{gr} determined by b_1 whereas the phase velocity is determined by b_0, this effect can be used to shift the carrier-envelope phase of few-cycle laser pulses [80].

The second-order coefficient b_2 is a measure of the dispersion of the group delay τ_{gr} as a function of frequency and is usually referred to as *group-delay dispersion* (GDD). It is closely related to the *group-velocity dispersion* (GVD). Higher-order terms (omitted here) are normally kept only up to the fourth order and are called *third-order dispersion* (TOD) and *fourth-order dispersion* (FOD), respectively. Numerical values for the group delay, the cubic, quartic, and quintic dispersions for several common optical materials such as fused silica, BK7, sapphire, quartz, KD*P, or air (N$_2$) can be found in Fittinghoff et al. [83].

Now we see that by sending an ultrashort laser pulse through a piece of glass it will – as a first approximation – acquire a linear chirp determined by $b_2 = \Phi''$. For optical frequencies this material dispersion is usually positive so that red frequencies travel faster than blue ones, resulting in an up-chirp of the laser pulse. The behavior is not desired e.g. for beamsplitters where both the reflected and transmitted beam should remain unaffected. It is also necessary to zero or at least minimize each order for ultrafast CPA systems. It can, however, be exploited for our benefit, for instance, to generate long chirped pulses as required for the SPIDER measurement (see Sec. 5.1.1.5).

A comprehensive review on the role of dispersion in ultrafast optics has been compiled by Walmsley et al. [84].

Chapter 3

Nonlinear frequency conversion

Contents

3.1 Low-order processes

The following Section provides a short introduction into the field of nonlinear optics. Although parts of this have already been published in a previous work [70], the relevant sections shall briefly be presented here again to offer a somewhat self-contained theoretical background for nonlinear frequency conversion. Outlooks to high-harmonic generation have been added where relevant. Gaussian units [60] are used for this Section.

As we have seen in the previous Chapter, ultrashort laser pulses can create very high light intensities inside a medium. In this case, the usual assumption of a linear dependence of the polarization P on the electric field E, $P = \chi E$ with the linear electric susceptibility χ, is no longer valid. Instead we have to expand the polarization into higher orders of the electric field [60, 68, 85] to account for nonlinear effects:

$$P(E) = \chi^{(1)}E + \underbrace{\chi^{(2)}E^2 + \chi^{(3)}E^3 + \dots}_{P^{NL}}, \tag{3.1}$$

where P^{NL} is the nonlinear part of the polarization P. The coefficients $\chi^{(n)}$ of the powers in E are called the higher-order nonlinear susceptibilities and are in general tensors of appropriate rank. The linear susceptibility χ has been renamed $\chi^{(1)}$ for clarity and consistency. The polarization is no longer linear but increasingly nonlinear with higher electric fields. This expansion can be derived using perturbation theory. Therefore it is valid only as long as the electric field strength is small compared to the inner-atomic electric field. This is true for low-order processes as considered in this Section. However, in the case of high-order harmonic generation, this expression breaks down for higher orders (see Sec. 3.4).

To examine the influence of the nonlinear polarization P^{NL} on the resulting electric field inside a medium, we have to substitute it as the source term into the nonlinear wave equation. Based on Maxwell's equations (in Gaussian units) [60, 71, 86] for the displacement D, the magnetic induction B, the electric field E, and the magnetic field H,

$$\nabla \cdot D = 4\pi\rho, \qquad \text{[Coulomb's Law]} \tag{3.2a}$$

$$\nabla \cdot B = 0, \qquad \text{[Absence of free magnetic poles]} \tag{3.2b}$$

$$\nabla \times E = -\frac{1}{c}\frac{\partial B}{\partial t}, \qquad \text{[Faraday's Law]} \tag{3.2c}$$

$$\nabla \times H = \frac{4\pi}{c}j + \frac{1}{c}\frac{\partial D}{\partial t}, \qquad \text{[Ampère's Law]} \tag{3.2d}$$

the optical wave equation for a non-magnetic material ($B = H$) with no free charges ($\rho = 0$) and no free currents ($j = 0$) can be derived by applying the curl to Eq. (3.2c), interchanging the order of space and time derivatives on the right-hand side of the resulting equation, and using the above side conditions [70]. By substituting the displacement D by the usual relation

$$D = E + 4\pi P, \tag{3.3}$$

where the full nonlinear response is contained in P, we arrive at the optical wave equation only in terms of the electric field E and the polarization P:

$$\nabla \times \nabla \times E + \frac{1}{c^2}\frac{\partial^2 E}{\partial t^2} = \frac{-4\pi}{c^2}\frac{\partial^2 P}{\partial t^2}. \tag{3.4}$$

Decomposing both D and P in Eq. (3.3) into their linear and nonlinear parts and inserting them into Eq. (3.4) yields the nonlinear wave equation of nonlinear optics,

$$\nabla \times \nabla \times E + \frac{\epsilon^{(1)}(\omega)}{c^2}\frac{\partial^2 E}{\partial t^2} = \frac{-4\pi}{c^2}\frac{\partial^2 P^{NL}}{\partial t^2}. \tag{3.5}$$

where $\epsilon^{(1)}$ is the generally complex and frequency-dependent linear dielectic tensor and P^{NL} is the nonlinear polarization containing only higher orders of the electric field (see Eq. (3.1)).

The nonlinear polarization is thus the source term in the nonlinear wave equation and is therefore responsible for the generation of new frequencies through its dependence on the higher orders of the electric field.

Let us consider the simple but important case of a second-order susceptibility $\chi^{(2)}$ only. Assuming an electric field $E = E_0 e^{-i\omega t}$ we see that by substituting this expression into Eq. (3.1) we obtain contributions to the nonlinear polarization at twice the fundamental frequency ω:

$$P^{(2)}(E) = \chi^{(2)} E^2 = \chi^{(2)} \left(E_0 e^{-i\omega t} \right)^2 = \chi^{(2)} E_0^2 e^{-i(2\omega)t}. \tag{3.6}$$

This process is therefore called *second-harmonic generation* (SHG) and was demonstrated experimentally [27] shortly after the invention of the laser by Maiman [25]. Several important pieces of information can be retrieved from Eq. (3.6). First, it shows that by exploiting the nonlinear susceptibility of a nonlinear medium, we can indeed frequency-double the light of an intense laser. Second, since the intensity is the square of the electric field, the second-harmonic yield depends quadratically on the intensity of the pump beam to be frequency-doubled. Increasing the fundamental intensity by a factor of two results in an increase of the second-harmonic light by a factor of four. Finally, the second-harmonic yield of course depends on the value of the second-order susceptibility $\chi^{(2)}$. However, in centrosymmetric materials (i.e. crystals having an inversion center of isotropic gases), the second-order susceptibility $\chi^{(2)}$ vanishes: $\chi^{(2)} \equiv 0$. This can be easily seen by substituting $-E$ into Eq. (3.6) instead of E: This corresponds to a symmetry operation of inversion. Hence the nonlinear polarization $P^{(2)}(E)$ should also change sign. However, the right-hand side of Eq. (3.6) is still equal to $P^{(2)}(E)$ due to the power of two. Therefore it follows that the second-order polarization must be zero and therefore $\chi^{(2)} \equiv 0$. The same is true for all even higher-order susceptibilities. This is one way to understand why only odd harmonics are usually emitted during high-harmonic generation in gases.

For non-vanishing even-order susceptibilities the inversion symmetry must be broken, either by using appropriate nonlinear crystals displaying an optic axis (choice of the medium) or by breaking the symmetry between subsequent oscillations of the electric field by using few-cycle laser pulses. The second case will be considered later for the production of single attosecond pulses.

Materials that display second-order susceptibility include barium titanate ($BaTiO_3$), crystal quartz, potassium dihydrogen phosphate (KDP), lithium niobate ($LiNbO_3$), beta-barium borate (BBO) and lithium triborate (LBO) [85].

Essentially all optical materials (solids, liquids and gases), however, have a third-order susceptibility term:

$$\boldsymbol{P}^{(3)}(\boldsymbol{E}) = \chi^{(3)} \boldsymbol{E}^3. \tag{3.7}$$

The total displacement $\boldsymbol{D}$ can thus be written as

$$\begin{aligned} \boldsymbol{D} &= (1 + 4\pi\chi^{(1)})\boldsymbol{E} + 4\pi\chi^{(3)}\boldsymbol{E}^3 \\ &= (1 + 4\pi\chi^{(1)} + 4\pi\chi^{(3)}\boldsymbol{E}^2)\boldsymbol{E}. \end{aligned} \tag{3.8}$$

Hence the dielectric constant $\tilde{\epsilon}$ according to $\boldsymbol{D} = \tilde{\epsilon}\boldsymbol{E}$ is

$$\tilde{\epsilon} = \epsilon_1 + \epsilon_2 \boldsymbol{E}^2 \tag{3.9}$$

and the index of refraction $n = \sqrt{\tilde{\epsilon}}$ becomes intensity-dependent,

$$n(I(\mathbf{r},t)) = n_0 + n_2 I(\mathbf{r},t) \quad (n_2 > 0), \tag{3.10}$$

where we have expanded the square root in terms of the electric field and retained only the first non-constant term. n_0 is the linear refractive index for low intensities, n_2 is the expansion coefficient for the linear term with respect to the intensity I and is proportional to the third-order nonlinear susceptibility $\chi^{(3)}$ [60]. From the expansion it follows that n_2 is always greater than zero, thus increasing the refractive index with increasing electric field. The phenomenon is known as the *Optical Kerr Effect*. In the femtosecond regime it originates mainly from a distortion of the electron cloud and therefore has a time response of the order of an electronic orbital period ($\approx 10^{-16}$ s) [87]. As this is much shorter than the pulse duration, the Kerr effect can be regarded as instantaneous.

Since the intensity depends on both spatial and temporal coordinates, $I = I(\mathbf{r},t)$, a high-intensity laser pulse experiences a spatially and temporally modulated index of refraction. The dependence on the radial coordinate leads to a lensing effect and can be exploited for Kerr-lens mode locking in femtosecond oscillators. This has already been discussed in Sec. 2.2. The temporal modulation is responsible for self-phase modulation (see Sec. 3.3).

As stated above, in general, the susceptibilities introduced in Eq. (3.1) must be written as tensors where $\chi^{(1)}$ becomes a second-rank tensor, $\chi^{(2)}$ becomes a third-rank tensor, $\chi^{(3)}$ a fourth-rank tensor, etc. We assume that the electric field vector of the light wave can be written as the discrete sum of a number of frequency components:

$$\mathbf{E}(\mathbf{r},t) = \sum_n \mathbf{E}_n e^{-i\omega_n t} \tag{3.11}$$

where

$$\mathbf{E}_n = \mathbf{E}(\omega_n) \tag{3.12}$$

and the condition

$$\mathbf{E}(-\omega_n) = \mathbf{E}(\omega_n)^* \tag{3.13}$$

holds to ensure that the electric field $\mathbf{E}(\mathbf{r},t)$ in Eq. (3.11) will be real (see Eq. (2.32)). The summation in Eq. (3.11) is taken over both positive and negative frequencies.

Similarly, the nonlinear polarization can be written as

$$\mathbf{P}(\mathbf{r},t) = \sum_n \mathbf{P}(\omega_n) e^{-i\omega_n t}. \tag{3.14}$$

According to [60], we now define the components of the second-order susceptibility tensor $\chi_{ijk}^{(2)}(\omega_n + \omega_m, \omega_n, \omega_m)$ as the constants of proportionality relating the amplitudes of the nonlinear polarization to the product of field amplitudes according to

$$P_i^{(2)}(\omega_n + \omega_m) = \sum_{jk} \sum_{nm} \chi_{ijk}^{(2)}(\omega_n + \omega_m, \omega_n, \omega_m) E_j(\omega_n) E_k(\omega_m), \tag{3.15}$$

where the indices *ijk* denote the Cartesian components of the fields. The third-order susceptibility is defined in an analogous manner as

$$P_i^{(3)}(\omega_o + \omega_n + \omega_m) = \sum_{jkl} \sum_{mno} \chi_{ijkl}^{(3)}(\omega_o + \omega_n + \omega_m, \omega_n, \omega_m) E_j(\omega_o) E_k(\omega_n) E_l(\omega_m). \tag{3.16}$$

Since $P_i(\mathbf{r}, t)$ is a physically measurable quantity just as the electric field, we have a relationship similar to Eq. (3.13) for the positive- and negative-frequency components of the polarization vector:

$$P_i(-\omega_n - \omega_m) = P_i(\omega_n + \omega_m)^*. \tag{3.17}$$

The electric fields and the polarization are related through the second-order susceptibility (Eq. (3.15)) which requires that

$$\chi_{ijk}^{(2)}(-\omega_n - \omega_m, -\omega_n, -\omega_m) = \chi_{ijk}^{(2)}(\omega_n + \omega_m, \omega_n, \omega_m)^*. \tag{3.18}$$

For a detailed description of symmetry relations for the second-order nonlinear susceptibility tensor the reader shall be referred to the book by Boyd [60]. A brief summary can be found in Winterfeldt [70].

In practice the tensor d_{ijk} is used instead of tensor $\chi_{ijk}^{(2)}$, the two tensors being interrelated by the equation

$$d_{ijk} = \frac{1}{2}\chi_{ijk}^{(2)} \tag{3.19}$$

where the frequency arguments have been suppressed for simplicity. The nonlinear polarization is then given by

$$P_i^{(2)}(\omega_n + \omega_m) = \sum_{jk}\sum_{nm} 2d_{ijk}^{(2)} E_j(\omega_n) E_k(\omega_m). \tag{3.20}$$

Depending on the configuration of the incident light fields, several low-order nonlinear frequency conversion processes can be realized:

sum-frequency generation (SFG)	$\chi^{(2)}$	$\omega_s = \omega_1 + \omega_2$	Two frequencies ω_1 and ω_2 can be added to yield the signal at ω_s.
difference-frequency generation (DFG)	$\chi^{(2)}$	$\omega_s = \omega_1 - \omega_2$	The frequency ω_2 is subtracted from ω_1 to yield the signal at ω_s.
second-harmonic generation (SHG)	$\chi^{(2)}$	$\omega_s = 2\omega_1$	Frequency-doubling of ω_1 yields the signal at ω_s.
third-harmonic generation (THG)	$\chi^{(3)}$	$\omega_s = 3\omega_1$	Frequency-tripling of ω_1 yields the signal at ω_s.
third-harmonic generation through SHG + SFG	$\chi^{(2)}$	$\omega_s = 2\omega_1 + \omega_1$	Frequency-tripling of ω_1 realized by SHG of ω_1 plus SFG with ω_1.
optical parametric generation/amplification (OPG/OPA)	$\chi^{(2)}$	$\omega_s = \omega_p - \omega_i$	The signal field at ω_s is amplified from the pump photons at ω_p, leaving the idler at ω_i due to energy conservation.
self-phase modulation (SPM)	$\chi^{(3)}$	$\omega_s = \omega_1 \pm (\omega_2 - \omega_3)$	New frequencies are generated on either side of the spectrum as a combination of available frequencies within the original spectrum.

Since the first four processes are more or less straight forward, we will briefly discuss the last three items. For self-phase modulation (SPM) the reader shall directy be referred to Sec. 3.3.1.

In principle, the third-harmonic can be directly generated using a $\chi^{(3)}$ process. It is, however, more efficient to use two cascaded $\chi^{(2)}$ processes since usually the second-order susceptibilities are higher and the residual fundamental laser from the first SHG process that frequency-doubles the laser can be reused for the sum-frequency process to yield the third-harmonic signal.

Optical parametric generation (OPG) is, roughly speaking, just the opposite of sum-frequency generation. An intense pump wave at ω_p generates two new waves, the signal at ω_s and the idler at ω_i, with the following relationship:

$$\omega_p = \omega_s + \omega_i \qquad \text{or} \qquad \frac{1}{\lambda_p} = \frac{1}{\lambda_s} + \frac{1}{\lambda_i}. \tag{3.21}$$

The signal is initially generated from quantum fluctuations, which are also the trigger for spontaneous emission in a laser resonator. However, since the gain curve in a laser medium is limited to a finite bandwidth, only certain frequencies are accessible. For a lossless nonlinear medium, the second-order susceptibility $\chi^{(2)}$ is essentially independent of the frequency [60]. Therefore we can, in principle, work with frequencies all over the transparency range of the nonlinear medium. This is one of the reasons why optical parametric chirped-pulse amplification (OPCPA, Dubeitis et al. [88], Ross et al. [89]) is an appropriate method to amplify sub-10-fs laser pulses since they have a huge bandwidth. In addition OPCPA offers a large single-pass parametric gain, a reduced B integral, low thermal load (no energy storage), and phase and phase-front preservation. Therefore it can be used for the phase-stable amplification of ultrashort pulses from a carrier-envelope phase-stabilized mode-locked oscillator [90].

The signal photon created from quantum fluctuation is then amplified from the pump photons according to Eq. (3.21), which states nothing than energy conservation. Therefore an idler at the difference frequency arises. The amplification process continues, and the strong signal at ω_s can be extracted. Since all frequency pairs fullfilling Eq. (3.21) can be generated, the desired wavelength must be selected by phase matching (see Sec. 3.2). By adjusted the phase-matching conditions, the tuning can be controlled.

If a weak seed wave at ω_1 or ω_2 is present in addition to the strong pump at ω_3 the process is called *optical parametric amplification* (OPA) and can be described as

$$\omega_{p,\text{pump}} + \omega_{s,\text{weak seed}} \rightarrow \omega_{p,\text{residual pump}} + \omega_{s,\text{amplified signal}} + \omega_{i,\text{idler}}. \tag{3.22}$$

In this case, the need for quantum fluctuations is eliminiated, the conversion process becomes more stable. The seed wave is amplified, increasing the overall output of the OPA. Another advantage is the preservation of the spectral phase of the seed pulse, so that phase-stable amplification of few-cycle laser pulses is possible using OPCPA (see above).

The performance of an OPA and the conversion efficiency can be calculated by solving the coupled nonlinear wave equations for the signal field at ω_1. Starting from a weak seed wave at ω_1 with intensity $I_1(0)$, the intensity of the signal after the wave has traversed a distance z in the crystal is given by [91]:

$$I_1(z) = I_1(0) \cosh^2(g_{\text{eff}} z) \tag{3.23}$$

where g_{eff} is the effective parametric gain coefficient. In the presence of phase mismatch (see also Sec. 3.2)

$$\Delta k = k_3 - k_2 - k_1 \tag{3.24}$$

the effective gain coefficient is given by [66, 91]

$$g_{\text{eff}} = \left[g^2 - \left(\frac{1}{2} \Delta k \right)^2 \right]^{1/2} \tag{3.25}$$

where

$$g = 2\sqrt{2}\pi \, d_{\text{eff}} \sqrt{\frac{I_3(0)}{\lambda_1 \lambda_2 n_1 n_2 n_3 \epsilon_0 c}}. \tag{3.26}$$

Eq. (3.26) is expressed in SI/MKS units, with n_j being the refractive indices at the wavelengths λ_j, the permeability ϵ_0 and the speed of light c. I_3 is the intensity of the pump wave. The quantity d_{eff} describes the effective nonlinear coefficient [60, 85]. It is a scalar quantity and takes a simple form for the different types of interactions (*oee*, *eoe*, etc.). It comprises all the summation operations along the polarization directions of the interacting waves. More details can be found in the work on the optical parametric amplifier described in Winterfeldt [70]. A review on the recent progress in the development of ultrafast optical parametric amplifiers has been compiled by Cerullo and De Silvestri [92], including the basic design principles for different frequency ranges.

More details about the interactions between light waves in a nonlinear dielectric can in general be found in the homonymous seminal work by Armstrong, Bloembergen, Ducuing, and Pershan [93].

So far, only the immediate generation of frequency-converted light on a single-atom basis has been considered. For the macroscopic build-up along the interaction path in the nonlinear medium, however, we have to ensure that the fundamental and the generated light remain in phase. This will be the subject of the following section.

3.2 Phase matching

In the previous Sections we have considered the origin of the nonlinear polarization based on the nonlinear electric susceptibilities. This single-particle response represents the microscopic source for nonlinear light frequency conversion processes. The energies of the newly generated light were simply determined by the conservation of the photon energy. However, for a macroscopic build-up of the desired signal (conversion efficiency) and for the determination of the generated wavelength in optical parametric generation, the propagation along the nonlinear medium is important.

3.2.1 Birefringence and phase-matching angle

Let us start with a three-wave mixing process where a frequency ω_3 is generated as the sum of two frequencies ω_1 and ω_2. In order for this process to be effective, the so-called phase-matching condition has to be fulfilled:

$$\boldsymbol{k_3} = \boldsymbol{k_1} + \boldsymbol{k_2} \tag{3.27}$$

where the $\boldsymbol{k_i}$ are the wave vectors of the respective waves. The important case of scalar (collinear) phase matching

$$k_3 = k_1 + k_2, \quad \text{or} \quad \omega_3 n_3 = \omega_2 n_2 + \omega_1 n_1 \tag{3.28}$$

shows that in order to satisfy the phase-matching condition we have to find a medium with a suitable dispersion relation. The refractive indices are frequency-dependent: $n_i = n(\omega_i)$. As an example consider again sum-frequency generation where we have

$$\omega_3 = 2\omega_1 \quad \text{and} \quad \omega_3 n_3 = 2\omega_1 n_1 \tag{3.29}$$

where $n_3 = n(\omega_3)$ and $n_1 = n(\omega_1)$. Eq. (3.29) therefore implies that

$$n(\omega_3) = n(\omega_1). \tag{3.30}$$

This, however, cannot be fulfilled as for the case of normal dispersion we have $dn/d\omega > 0$ and therefore $n(\omega_3) > n(\omega_1)$. Anomalous dispersion on the other side is connected with too many losses.

This problem can be solved using birefringent crystals. Let us consider here only uniaxial crystals which display a special direction, the *optic axis* or Z axis. The plane containing the Z axis and the wave vector $\boldsymbol{k}$ is called *principal plane*. A beam whose polarization is normal to the principal plane is an *ordinary beam (o-beam)* whereas the polarization of an *extraordinary beam (e-beam)* lies in the principal plane. The index of refraction for an ordinary wave, n_o, is independent of the propagation direction. For an extraordinary wave it depends on the propagation direction and is given by [85]

$$n^e(\theta) = n_o \sqrt{\frac{1 + \tan^2 \theta}{1 + (n_o/n_e)^2 \tan^2 \theta}} \tag{3.31}$$

where θ is the polar angle between the propagation direction and the Z axis and n_o and $n_e = n^e(90°)$ are the principal values of the refractive indices for the ordinary and the extraordinary wave, respectively. They can be calculated using the Sellmeier equations [94–96]. If the wave propagates along the Z axis, n_o and n_e have the same value. If n_e is smaller than n_o for propagation directions other than the Z axis the crystal is called optically negative, otherwise positive. Fig. 3.1 shows the dependence of the refractive index on light propagation direction z and polarization in a negative uniaxial crystal (such as BBO). For material parameters of BBO see e.g. Winterfeldt [70, Appendix B]. Therefore, when ordering a nonlinear optical crystal, crystal orientation (or crystal cut) and size have to be known. The crystal cut is given by the cut angle which is the polar angle between the optical axis and the surface normal of the entrance surface.

When a plane light wave propagates in a uniaxial crystal, the direction of propagation of the wave phase (wave vector $\boldsymbol{k}$) generally does not coincide with that of the wave energy (Poynting vector $\boldsymbol{s}$, see [86]). The direction of $\boldsymbol{s}$ can be defined as the normal to the tangent drawn at the point of intersection of the wave vector $\boldsymbol{k}$ with the $n(\theta)$ curve in Fig. 3.1. For an ordinary wave the two vectors $\boldsymbol{k}$ and $\boldsymbol{s}$ are still parallel, but for an extraordinary wave the Poynting vector $\boldsymbol{s}$ is rotated from the direction of $\boldsymbol{k}$ by the "birefringence" or "walk-off angle" ρ [85, 91] since the extraordinary index is represented by an index ellipsoid [97]:

$$\rho(\theta) = \pm \arctan \left[\left(\frac{n_o}{n_e} \right)^2 \tan \theta \right] \mp \theta, \tag{3.32}$$

where the upper (lower) sign stands for a negative (positive) crystal.

Let us now return to our example of second-harmonic generation. If we use a negative crystal and let ω_3 be an extraordinary wave and ω_1 an ordinary wave, Eq. (3.30) can be fulfilled. Due
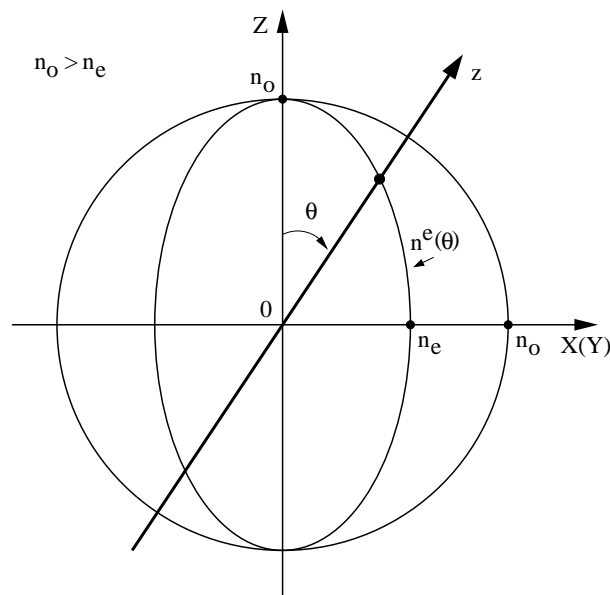
Figure 3.1 – Dependence of the refractive index on light propagation direction z and polarization in a negative uniaxial crystal.

to normal dispersion $n(\omega_3)$ is greater than $n(\omega_1)$ but our choice of extraordinary and ordinary wave in the negative crystal together with the appropriate phase-matching angle makes the two indices of refraction the same:

$$n^e(2\omega, \theta) = n_o(\omega). \tag{3.33}$$

One refers to type-I phase matching when the polarization directions of the two waves with lower frequencies ω_1 and ω_2 are equal and to type-II phase matching in the opposite case.

Therefore in an optical parametric amplifier the actual wavelength pair fulfilling Eq. (3.21) is determined by the phase-matching condition. The OPA can be tuned by turning the crystal which changes the extraordinary index of refraction according to Eq. (3.31). Usually a BBO nonlinear crystal is used which is angle-tuned. An example of such a tuning curve which shows the dependence of the signal and idler wavelengths upon the phase-matching angle is displayed in Fig. 3.2. For comparison, LBO (lithium tri-borate) is temperature-tuned due to the high temperature sensitivity of its birefringence [94]. When the pump wavelength is fixed at λ_p (see Eq. (3.21)), small changes of the refractive index due to the rotation of the crystal will change signal and idler wavelengths such that a new phase-matching condition is achieved. In addition to pure phase-velocity matching during frequency doubling, matching group velocities [98] by suitably predispersing the fundamental pulses prior to harmonic generation allows for the use of longer nonlinear crystal, thus increasing the overall yield.

For efficient amplification of the seed wave, the phase-matching condition Eq. (3.27) has to be fulfilled for all wavelengths present in the input spectrum. This is a demanding constraint for very-broadband ultrashort pulses. The situation of collinear phase matching Eq. (3.28) considered so far in principle allows only for phase matching of the central frequency (and a small set of neighboring frequencies). However, we see from Eq. (3.27) that the wave-vector mismatch is expressed by considering the full vectorial nature of the wave vectors. Broadband phase matching can therefore be achieved also in a non-collinear geometry, where pump and
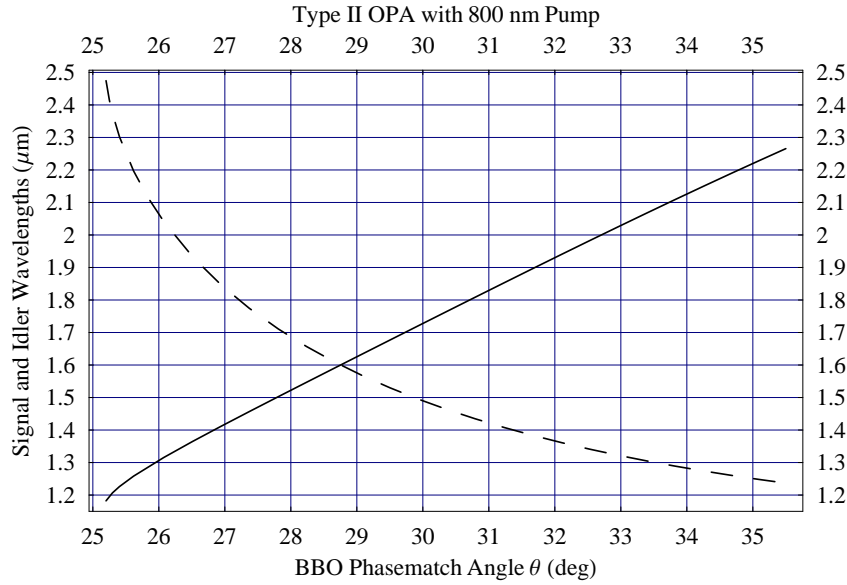
Figure 3.2 – Theoretical phase-matching curve for a BBO-based type-II OPA with a 800 nm pump. The wavelengths of the signal (solid line) and the idler (dashed line) vary as a function of the phase-matching angle θ, while for any angle the sum of the two corresponding photon energies is given by the pump photon energy (Figure taken from Winterfeldt [70]).

signal photons propagate along different directions at an angle Ψ. The angle Ψ introduces an additional degree of freedom for fulfilling the phase-matching condition. Choosing the correct angle effectively makes the projection of the group velocity of the idler the same as that of the signal, ensuring copropagating wave fronts along the conversion medium, thus allowing for broadband phase matching in a *noncollinear optical parametric amplifier* (NOPA). More information about the NOPA present in our laboratory can be found in the work by Sokollik [99].

The angular dispersion can also be exploited for broadband frequency doubling of few-cycle laser pulses. In general, it is very difficult to perform second-harmonic generation for the large bandwidths accompanied with few-cycle laser pulses. Kanai et al. [100] use the wavelength-dependent dispersion $d\beta/d\lambda$ of the angle of diffraction β when such an ultrashort laser pulse is diffracted by a grating. By matching the focusing conditions for this divergent ray bundle into the nonlinear crystal to the dispersion of the phase-matching angle $d\theta/d\lambda$, the phase-matching condition can be fulfilled simultaneously for a large range of wavelengths, thus enabling broadband frequency doubling.

3.2.2 Phase mismatch and coherence length

In general, the phase mismatch Δk is defined as the difference between the wave vectors of all input waves k_{in} and the wave vector of the signal wave k_{out}:

$$\Delta k = k_{\text{out}} - \sum k_{\text{in}}. \tag{3.34}$$

This can also be viewed as *momentum conservation*, in addition to *energy conservation* dictating the frequencies of the generated new photons. Whereas the nonlinear polarizability is
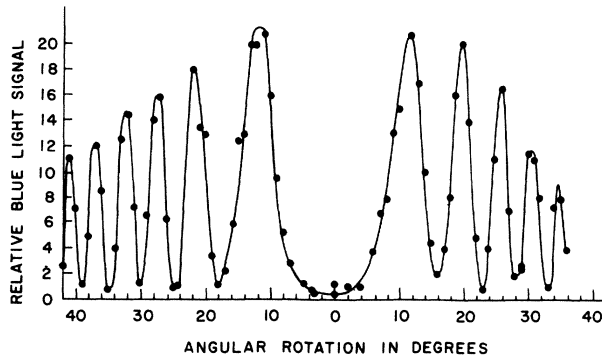
Figure 3.3 – Original plot of the intensity of second-harmonic blue light from a pulsed red ruby laser as function of the angle of a quartz plate [101]. The rotation changes the optical thickness and thus the term $\Delta k\,L$. The so-called Maker fringes are clearly visible.

only determined by the single atom response, phase matching is based on the propagation properties of the waves.

The physical process responsible for the mismatch is the following: The dispersion in the generating medium and of the generating geometry (refractive indices, dispersion of a hollow fiber, Gouy phase shift across a focus in a gas jet) causes the input light field and the generated signal radiation to propagate at different phase velocities. After a certain coherence length,

$$L_c = \frac{\pi}{\Delta k}, \tag{3.35}$$

the accumulated phase slip is π, leading to destructive interference between the two fields. This effect has already been observed in second-harmonic generation in crystals [101]: In this experiment a pulsed red ruby laser was focused into a single crystal of quartz and the intensity of the blue second-harmonic signal measured as the crystal was rotated, which corresponds to a change in the effective path length L. The signal amplitude can be seen to oscillate as a function of the quantity ΔkL which includes the phase mismatch Δk and the effective length L of the nonlinear medium (Fig. 3.3).

The effect of the so-called *Maker fringes* can be quantized by solving the coupled nonlinear wave equations for the electric field of the signal $E_s(L)$ after transversing the medium of length l which contains a term describing the contribution of the phase mismatch Δk [60]:

$$E_s(L) \propto \frac{e^{i\,\Delta k\,L} - 1}{i\,\Delta k}. \tag{3.36}$$

Since the intensity of the signal $I_s(L)$ is proportional to the squared modulus of the electric field, it can be written as

$$I_s(L) \propto |E_s(L)|^2 \propto \left| \frac{e^{i\,\Delta k\,L} - 1}{\Delta k} \right|^2 =$$

$$= L^2 \left(\frac{e^{i\,\Delta k\,L} - 1}{\Delta k} \right) \left(\frac{e^{-i\,\Delta k\,L} - 1}{\Delta k} \right) = L^2 \frac{\sin^2\left(\frac{\Delta k\,L}{2}\right)}{\frac{\Delta k\,L}{2}} \equiv L^2 \mathrm{sinc}^2\left(\frac{\Delta k\,L}{2}\right). \tag{3.37}$$

Note that the effect of wave vector mismatch is included entirely in this factor, accomodating propagation effects during the nonlinear interaction along the extended medium of length L. The single-particle response incorporating the nonlinear polarizability is contained in a pre-factor to Eq. (3.36). As the wave-vector mismatch Δk increases, the efficiency of the nonlinear conversion process drops quickly as determined by the sinc function in Eq. (3.37) and reaches zero at $\Delta kL/2 = \pi$. Coherent growth of the signal is thus only given as long as the argument

a) **No phase-matching:**   b) **Quasi phase-matching (periodically poled):**
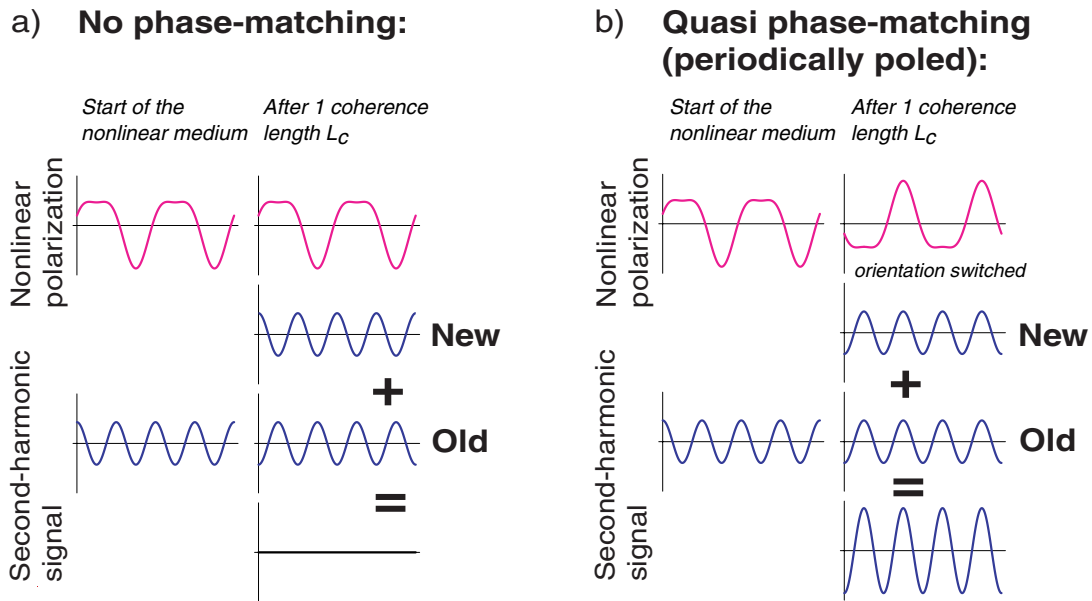
Figure 3.4 – Visualization of second-harmonic generation in a non-phase-matched (a) and in a quasi-phase matched (b) setup. The nonlinear polarization generates a second-harmonic signal which becomes out of phase by π after a coherence length L_c and therefore cancels with the newly generated signal. In periodically poled crystals, the crystal orientation is switched after one coherence length so that the nonlinear polarization changes sign and generates a new second-harmonic signal in phase with the old signal. The new and the old signal can now interfere constructively.

of the sinc function $\Delta k L/2$ is smaller than $\pi/2$ which yields the condition for the coherence length L_c as already defined in Eq. (3.35).

As shown above, this problem can be circumvented by using different polarization directions for the two beams in a birefringent crystal [60] such that pump and signal travel at the same speed through the ordinary and extraordinary index of refraction.

3.2.3 Quasi-phase matching

In cases where conventional phase matching is not possible, quasi-phase matching (QPM, [93]) has proven extremely useful. A technique very often used is second-harmonic generation in periodically poled nonlinear crystals. The QPM scheme is summarized in Fig. 3.4. The nonlinear polarization (top parts of Figs. 3.4a,b) causes the second-harmonic light field (bottom parts) to grow. After the coherence length, however, the second-harmonic field that is just being generated is out of phase by π with respect to the second-harmonic field generated first due to the phase velocity walk-off in the non-phase matched case (Fig. 3.4a). The idea of quasi-phase matching is to interrupt frequency conversion in these regions or to correct the phase relation by replacing the crystal by its inversion image [93]. In so-called periodically poled crystals (Fig. 3.4b) the crystal orientation is switched just after one coherence length so that the nonlinear susceptibility $\chi^{(2)}$ and therefore the nonlinear polarization change signs as well. The linear optical properties remain the same, and the new second-harmonic signal can now interfere constructively with the old signal, thereby contributing to the build-up instead of canceling the old field. A periodic repetition of this switching then leads to a steady
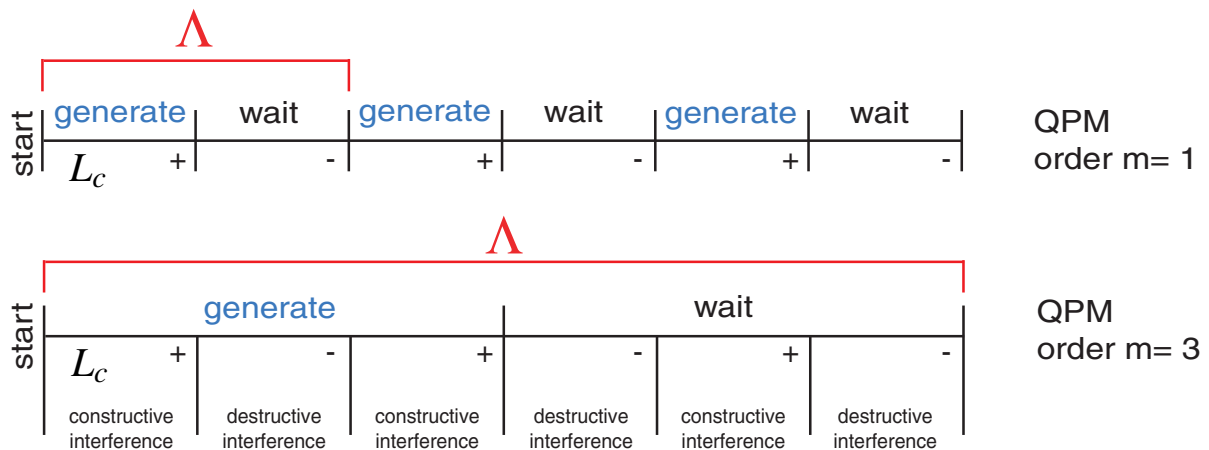
Figure 3.5 – Scheme for quasi-phase matching. The nonlinear process takes place in the regions labeled "generate" while there is no nonlinear interaction in the "wait" regions (or of course generation of a "'negative'" signal). Signal generation always takes place along one coherence length L_c, so by introducing the "wait" regions we avoid destructive interference between the "new" and the "old" signal (see text). The modulations periods for QPM with different orders (m) are denoted by Λ.

build-up of the signal.

In general, to obtain quasi-phase matching, we can introduce some modulation

$$\Lambda = \frac{2\pi\,m}{\Delta k} = 2m\,L_c \tag{3.38}$$

where m is the order of QPM as shown in Fig. 3.5. The signal is generated over the first coherence length. Instead of generating a signal of opposite sign in the second coherence length, we just wait, suspending signal generation. This process can be repeated periodically, leading to a stepwise build-up over the whole interaction region. If a modulation with a period of two coherence lengths is not possible, neither actively by periodically poling the material or passively by just waiting, a modulation with an elongated period of $\Lambda = 2m\,L_c$ (where m is an odd integer) is also possible (Eq. (3.38)). In this case, during the distance labeled "generate" in Fig. 3.5, the signal is generated twice and destroyed once, leaving a net gain. Applications of quasi-phase matching schemes in the spatial and in the temporal domain for high-harmonic generation will be discussed in Secs.4.3.4 and 4.4.

3.2.4 Phase matching in gases for harmonic generation

However, the solutions to achieve phase matching presented so far cannot be realized in gas media traditionally used for high-harmonic generation. Due to their isotropy, there is no distinction between ordinary and extraordinary waves; the index of refraction is a scalar quantity (as long as effects such as alignment are neglected). Conventional quasi-phase matching based on switching the orientation of the nonlinear medium is therefore not possible either.

The phase mismatch for harmonic generation in gases consists of several contributions which will be described at the appropriate place for high-harmonic generation in Sec. 3.4.4.

3.3   Kerr and plasma effects

3.3.1   Self-phase modulation (SPM)

Another process that relies on the intensity-dependent nonlinear index of refraction n_2 (Eq. (3.10)) and thereby on the third-order nonlinear susceptibility $\chi^{(3)}$ is *self-phase modulation*. It can be exploited to broaden the spectrum of an incoming laser pulse. Compression of this spectrum allows for the shortening of the original input pulses (see Sec. 4.2.2.2).

Self-phase modulation (SPM) arises from the temporal distribution of the nonlinear phase. Let a laser pulse with on-axis intensity distribution $I(z, \tau)$ propagate over a distance L through a nonlinear medium whose refractive index is determined by Eq. (3.10). The accumulated on-axis nonlinear phase distribution is then given by [60, 87]

$$\phi_{\mathrm{NL}}(t) = - \int_0^L n_2 I(z,t) \frac{\omega_0}{c} dz \qquad (3.39)$$

where c is the speed of light. The contribution by n_0 is constant for all intensities and is therefore omitted. Eq. (3.39) is referred to as the B integral in the description of self-focusing [102, 103]. Assuming that the nonlinear medium is sufficiently short so that no re-shaping of the optical pulse occurs within the medium, Eq. (3.39) reduces to

$$\phi_{\mathrm{NL}}(t) = -n_2 I(t) \frac{\omega_0}{c} L. \qquad (3.40)$$

If we consider an incoming laser pulse of the form

$$E(z,t) = A(z,t) e^{i(k_0 z - \omega_0 t)} + \text{c.c.}, \qquad (3.41)$$

we can calculate its temporal intensity so as to obtain the nonlinear phase that the laser pulse acquires during the propagation through the nonlinear medium. By adding the nonlinear phase term to the exponential in Eq. (3.41), we can determine the spectral content of the transmitted pulse by calculating its energy spectrum [60] through a Fourier transform,

$$S(\omega) = \left| \int_{-\infty}^{+\infty} A(t) e^{-i\omega_0 t - i\phi_{\mathrm{NL}}(t)} e^{i\omega t} dt \right|^2. \qquad (3.42)$$

Using the concept of the instantaneous frequency introduced in Section 2.4 with Eqs. (2.41) and (2.42), we can express the consequences of SPM in terms of the frequency shifts occurring at the leading and trailing edges of the pulse. These shifts range from the maximum Stokes extent at the leading edge

$$\Delta\omega_- = \left(\frac{d\phi_{\mathrm{NL}}(t)}{dt} \right)_{\min} \qquad (3.43)$$

to the maximum anti-Stokes extent at the trailing edge

$$\Delta\omega_+ = \left(\frac{d\phi_{\mathrm{NL}}(t)}{dt} \right)_{\max}. \qquad (3.44)$$

This shows that the front of the pulse is redshifted towards lower frequencies whereas the back is blueshifted towards higher frequencies. Thus the anti-Stokes components lag temporally
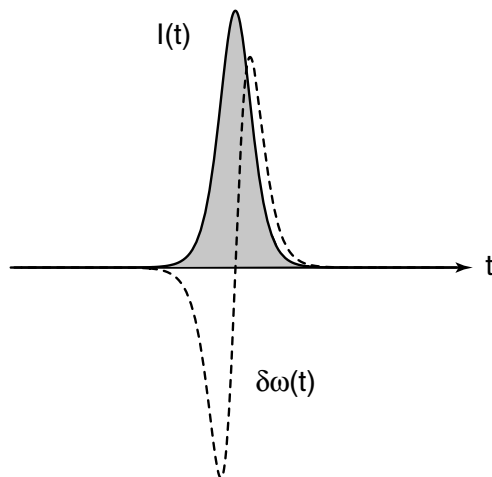
Figure 3.6 – Self-phase modulation. Time dependence of the intensity $I(t)$ of an incident pulse (solid line) and the variation in the instantaneous frequency $\delta\omega(t)$ of the transmitted pulse (dotted line) after the propagation through a nonlinear medium with a positive nonlinear index of refraction, n_2.

the Stokes components. For the commonly considered pulses shapes in the form of a Gaussian or a hyperbolic secant, Eqs. (3.43) and (3.44) yield a symmetric pulse reshaping to first order. When the amount of broadening is small compared to the laser frequency, any distortion of the intensity envelope in the time domain can be neglected [104].

Fig. 3.6 shows the time dependence of the incident pulse (hyperbolic secant) and the variation in the instantaneous frequency (Eq. (2.42)) of the transmitted pulse after the propagation through a nonlinear medium with a positive nonlinear index of refraction, n_2. The spectrum of such a self-phase-modulated laser pulse shows a pattern with periodic structures. For a simple intensity envelope the condition $\Delta\omega = d\phi_{\mathrm{NL}}(t)/dt$ for the instantaneous frequency shift is satisfied at two points t_1 and t_2 [104]. The two same frequencies generated at different times give rise to an interference pattern with a period that is determined by the difference between t_1 and t_2. Therefore the spectrum is no longer smooth but displays a modulated structure. A perfectly modulated spectrum arises only in the case of zero dispersion. If dispersion is present, the modulation is smoothened to a certain extent.
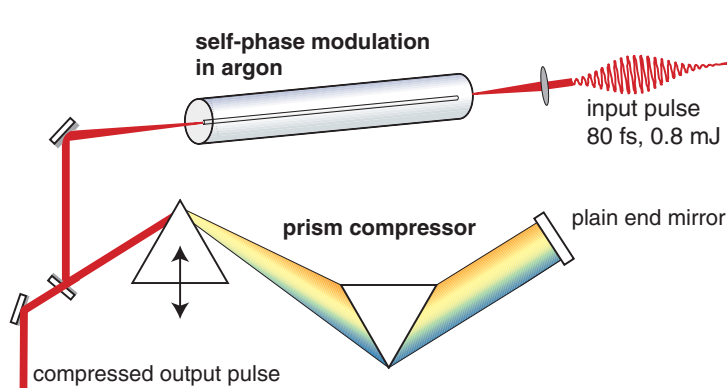
Figure 3.7 – Setup for self-phase modulation in a gas-filled hollow fiber. Ultrashort laser pulses from the amplifier are focused into the argon-filled hollow fiber. The guiding structure allows for maintaining a high intensity over a long interaction length. This maximizes the product IL appearing in the nonlinear phase term (Eq. (3.39)). The broadened spectrum can then be recompressed to shorter time durations in a prism compressor.

In our experiments, self-phase modulation is performed in a long gas-filled hollow fiber (length 60 cm, inner diameter 250 μm). The setup is displayed in Fig. 3.7 and has several advantages over SPM in solids or gas jets. The use of a gas as the nonlinear medium allows for higher intensities because there is virtually no damage threshold. The plasma that is created can be detrimental due to the plasma phase and defocusing but the gas medium is not destroyed. The guiding structure allows for maintaining a high intensity over a long interaction length. This maximizes the product IL appearing in the nonlinear phase term

(Eq. (3.39)). In a free focus there is a trade-off between the intensity I and the effective inter-action length determined by the confocal parameter b (Eq. (2.19)) because stronger focusing increases the divergence of the beam, thereby limiting the interaction length. In addition, the dispersion of the long gas column in the hollow fiber plays a decisive role for the compressibility of the broadened spectrum. The prism compressor usually can compensate only for a quadratic phase which corresponds to a linear chirp (the center part of $\delta\omega(t)$ in Fig. 3.6). The outer wings of $\delta\omega(t)$ cannot be compressed. However, if dispersion is present, the pulse is temporally stretched in time, thereby stretching the linear center part of $\delta\omega(t)$ while leaving the wings at approximately the same value. The prism compressor can now compensate for the linear chirp introduced during SPM over almost the whole duration of the pulse, thereby almost reaching the Fourier limit. The degree of insertion of the first prism into the beam path (movement perpendicular to the prism base) determines the quadratic phase compensation of the compressor.

The rigorous theory of strong SPM developed by Yang and Shen [105] shows an asymmetrical broadening that is stronger on the anti-Stokes side than on the Stokes side. Asymmetrical broadening towards the short-wavelength side also results from the spectral blueshifting [106–108]. However, if the group-velocity dispersion in the medium is negative, the spectrum can become narrower since the new frequencies interfere destructively in this case.
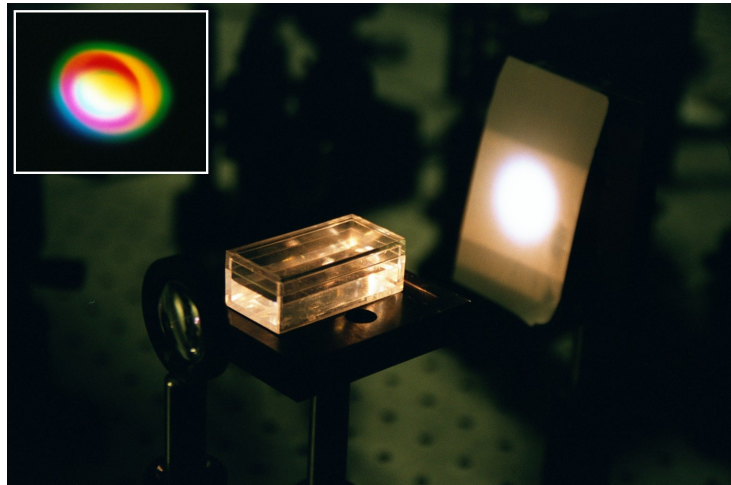
Figure 3.8 – White-light-continuum generation and conical emission. The white spectrum is generated in a cuveete of water by 800 nm, 750 μJ, 100 fs, 1 kHz repetition rate laser pulses. The inset demonstrates the conical emission accompanying white-light-continuum generation in sapphire (figures taken from Winterfeldt [70]).

The spectral broadening caused by self-phase modulation can be used for *white-light continuum generation* (WLC) from a laser, which in turn can be used to seed an optical parametric amplifier [70]. The first observation of supercontinuum generation in glass was made by Alfano and Shapiro [109]. As seen above, the spectral width of the white-light continuum depends on the medium in which it is generated and on the intensity of the incident laser pulse. Moreover, the polarization points into the same direction. The actual white-light continuum on axis is often surrounded by a distinct concentric rainbow-like pattern, which appears red to the eye in most cases. This phenomenon is called *conical emission* [110]. The emission wavelength decreases with increasing distance from the center, a trend opposite to that expected from normal beam diffraction. The appearance of the conical emission is attributed to contributions from several effects, ranging from a Cerenkov-based effect [111, 112] caused by moving focal spots [113] to the diffraction from the central plasma column [114, 115] due to the nonlinear ionization of the medium. Fig. 3.8 shows the white spectrum from white-light-continuum generation in a cuvette of water and the conical emission accompanying white-light-continuum generation in sapphire (inset) from an earlier work of the author [70]. Filamentation is exploited for super-
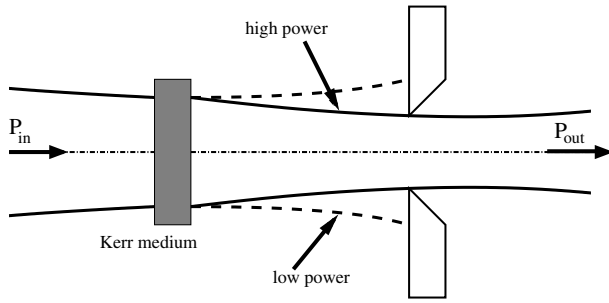
Figure 3.9 – Self-focussing of a Gaussian laser beam in a Kerr medium. A low-power beam experiences high losses from apertures present in the system. High-power beams (ultrashort pulses) are favored since they can pass apertures without attenuation and survive.

continuum generation for atmospheric applications [116–118] and as a replacement for pulse broadening and compression in hollow fibers [119–121].

3.3.2 Self-focusing

The dependence of the nonlinear refractive index on the radial coordinate (Eq. (3.10)) causes a lensing effect for a laser beam with a Gaussian radial intensity profile (Eq. (2.16)). This effect is therefore called *self-focusing*.

Let us consider Kerr-lens mode-locking, which is a passive mode-locking technique (see Sec. 2.2) to illustrate the self-focusing effect. An intense laser beam with a Gaussian transverse intensity profile (Eq. (2.16)) acquires a nonlinear phase shift upon propagating through the Kerr medium because the refractive index is no longer a constant according to Eq. (3.10):

$$\Delta\phi = k\Delta nL = kn_2 I_p L \exp[-2(r/w)^2].$$ (3.45)

This phase can be expanded into a power series

$$\Delta\phi \approx kn_2 I_p L[1 - 2(r/w)^2]$$ (3.46)

from which we see that the Kerr medium is equivalent to a spherical lens, induced by the laser beam itself, hence the term self-focussing. In the case of a Ti:Sapphire laser the sapphire, the host medium for the titanium dopant atoms, serves as the Kerr medium whereas the titanium represents the gain medium for the laser action.

Fig. 3.9 shows how this effect is exploited in practice in a Ti:Sapphire oscillator to achieve mode-locking. The laser beam is impinging from the left on the Kerr medium. For low intensities the phase shift acquired is constant over the width of the Kerr medium as the refractive index is a constant. A part of the beam therefore hits the edges of a following aperture (which includes hard apertures, mirrors, lenses etc.) and thus experiences losses. A high-intensity beam, however, is focussed and passes the aperture without any remarkable losses. The Kerr effect therefore favors high intensities and thus represents a suitable optical element with an intensity-dependent transmission as required for passive mode-locking (see Sec. 2.2).

Strong self-focusing can lead to the formation of leading to the formation of a filament (see Sec. 3.3.1). Self-focusing is usually balanced by diffraction and defocusing due to free electrons (plasma defocusing) created by avalanche ionization [122]. If self-focusing is not stopped, catastrophic self-focusing occurs at powers exceeding the critical power P_{crit}, leading to the collapse of the beam in a single point [87]:

$$P_{crit} = \frac{3.77\lambda_0^2}{8\pi n_0 n_2},$$ (3.47)

where λ_0 is the laser wavelength. For a wavelength of 800 nm and the material parameters for sapphire [123],

$$n_0 = 1.76, \tag{3.48a}$$

$$n_2 = 3.2 \times 10^{-16} \mathrm{cm}^2/\mathrm{W}, \tag{3.48b}$$

the critical power is $P_{\mathrm{crit}} = 1.7\,\mathrm{MW}$. The reason for the appearance of a critical power instead of a critical intensity is that the critical point is calculated as the ratio between the actual focusing force determined by $n_2 I$ and the counter-acting mechanism of diffraction determined by the beam cross-section. This way, the area cancels out, leaving a value for the critical power. In practice, since strong self-focusing leads to rapid ionization of the medium, which depends on intensity rather than on power, the actual intensity of the laser power still plays a role. Self-focusing is only mentioned for completeness and shall therefore not be covered further.

3.3.3   Blueshift

Due to the high laser intensity, the neutral gas along the propagation path becomes rapidly ionized. The rising density of free electrons causes the index of refraction to decrease [106, 108]:

$$n(z,t) = \sqrt{1 - \frac{n_e(z,t)}{n_c}}, \tag{3.49}$$

where $n_c = m\omega^2/4\pi e^2$ is the critical density at which the plasma frequency equals the laser frequency so that the plasma becomes completely absorbing for electromagnetic frequencies ω, and $n_e(z,t)$ is the momentary free-electron density. In SI units, the critical density is given by

$$n_c = \epsilon_0 \frac{m\omega^2}{e^2}. \tag{3.50}$$

According to the definition of the instantaneous frequency in Eq. (2.40), the rapidly ionized gas experiences a frequency blueshift caused by the creation of the free-electron plasma and the resulting decreasing index of refraction:

$$\Delta\omega = -\frac{\omega_0}{c} \int_0^L \frac{\partial n(z,t)}{\partial t} dz. \tag{3.51}$$

Since the plasma is generated on the timescale of the femtosecond laser pulse, the decreasing refractive index shifts the spectrum towards the blue. A rising index, caused by a decrease of the free-electron density, would conversely result in a redshift. However, plasma recombination occurs on much longer timescales when the ultrashort laser pulse has passed.

3.3.4   Plasma defocusing

The contribution of free electrons in a plasma to the refractive index according to Eq. (3.49) is also responsible fo plasma defocusing. For a Gaussian spatial shape of the fundamental laser pulse this means that the lowest refractive index can be found on axis where the laser intensity is highest, gradually increasing towards the wings in the radial profile. Such a progression of the refractive index directly corresponds to a defocusing lens.

3.4 High-harmonic generation

As opposed to low-order nonlinear frequency conversion processes such as second-harmonic generation where moderate laser intensities are sufficient, high-order harmonics result from the highly nonlinear interaction of high-intensity laser pulses with typically a gaseous medium. The laser radiation is converted into large integer multiples of the original laser frequency (~ 300 [124]), which reaches down to the XUV (extreme ultraviolet) and soft-x-ray range. In the following we will describe the high harmonics in detail, including their generation mechanism, their spectrum and phase, propagation properties, attosecond pulse generation and coherence.

3.4.1 Single-atom response (three-step model)

3.4.1.1 Overview

The basic generation mechanism for high-order harmonics can be explained very successfully using the semi-classical so-called *simple-man model* or *three-step model* by Corkum [125] and Kulander et al. [126] as summarized in Fig. 3.10. In the strong field of ultrashort high-intensity laser pulses, bound electrons from atoms or molecules are field-ionized close to the maximum of the laser field (tunnel ionization [127, 128]) and set free with zero initial velocity. They are then accelerated away from their parents ions by the same electric field and move on classical electron trajectories in a laser field. The potential of the nucleus is neglected in the strong-field approximation (SFA).

The average quiver energy of the electron in the laser field is called the ponderomotive energy U_p and is directly proportional to the intensity I of the driving laser and the square of the fundamental wavelength λ:

$$U_p = \frac{e^2 E_L^2}{4 m_e \omega_L^2} \propto I\lambda^2, \tag{3.52}$$

where e and m_e are the charge and the mass of the electron, E_L is the electric field strength of the laser with the angular frequency ω_L (or wavelength λ).

In the three-step model, as soon as the electric field reverses, the electrons are first decelerated and then accelerated back towards their parents ions, depending on the instant of birth into the continuum by ionization. Several processes can be realized when the electron returns to the core:

High-harmonic generation (HHG) The electron can recombine with its parent ion with a certain probability, leading to the emission of a broadband extreme-ultraviolet (XUV) photon. One photon per electron is emitted carrying the sum of the electron's kinetic energy plus the ionization potential I_p.

Above-threshold ionization (ATI) Above-threshold ionization (ATI) originates from the elastic scattering of the electron with the atom. The electron gains energy in excess of its initial energy in integer multiples of the fundamental laser frequency [129–131]. A typical photo-electron spectrum then shows a characteristic plateau of electron peaks, separated by one fundamental photon energy and rolling off at a cut-off of $10U_p$ [131–133]. The position of the ATI peaks can be shifted by the ponderomotive potential or even be suppressed, depending on the pulse duration of the driving laser [130].
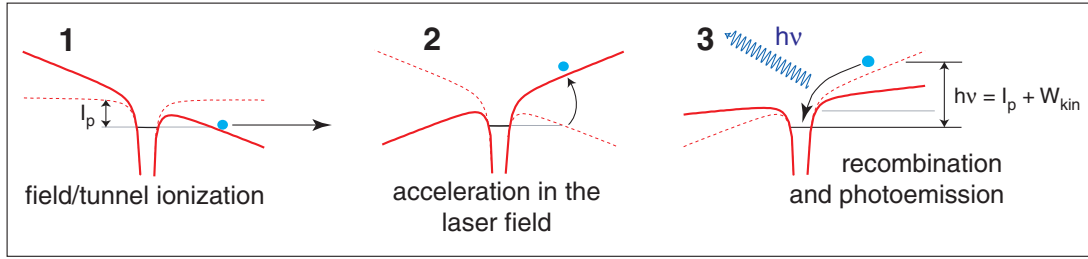
Figure 3.10 – Illustration of the three-step model for high-harmonic generation: 1. tunnel ionization of the electron, 2. acceleration in the laser electric field, 3. recombination and emission of a high-energy photon. The energy of the emitted photon depends on the ionization potential of the atom and on the kinetic energy of the electron upon its return to its parent ion.

Non-sequential double ionization (NSDI) When an inelastic collision of the electron with its parents ion occurs, another electron can be ionized so that in the end the atom is doubly ionized (non-sequential double ionization, NSDI [134, 135]). The intensity dependence of doubly ionized atoms follows the intensity dependence of single ionization, featuring a characteristic knee at the saturation intensity for single ionization.

Here we are only interested in high-harmonic generation and the control of their spectral and temporal properties. The energy of the photon that is emitted upon recollision of the accelerated electron with the ion core is determined by the sum of the ionization potential I_p and the momentary kinetic energy W_{kin} of the electron:

$$\hbar\omega = I_p + W_{\text{kin}}(\varphi). \tag{3.53}$$

The kinetic energy depends on the phase of the electric field at the moment of ionization. The maximum photon energy (cut-off energy) that can be achieved in this process can be calculated using classical [125] or quantum mechanics [136] and is given by

$$E_{\text{cut-off}} = \hbar\omega_{\text{max}} = I_p + 3.17\,U_p \tag{3.54}$$

where ω is the (angular) frequency of this photon and $\hbar$ is Planck's constant. The right-hand side of Eq. (3.54) is composed of the ionization potential I_p of the atom (the binding energy of the electron) and the maximum kinetic energy of the electron upon its return to the core: $3.17\,U_p$. This happens for a phase of $\varphi \approx 17°$ close to the maximum of the electric field where also the ionization rate is highest.

To visualize the laser intensities needed for a sizable ponderomotive potential U_p, Eq. (3.52) can be reformulated:

$$U_p[\text{eV}] = 0.93 \times 10^{-13} I[\text{Wcm}^{-2}]\, \lambda^2[\mu\text{m}^2]. \tag{3.55}$$

The corresponding laser intensities of $10^{14} - 10^{15}\text{Wcm}^{-2}$ are equivalent to an electric field amplitude of $E_L \approx 10^9\text{Vcm}^{-1}$, which is a typical value of the inner-atomic electric field.

Lower harmonic orders (long wavelenghts) can therefore still be described using perturbation theory, predicting a decrease of harmonic intensities towards higher orders following an I^q power law. The exponential of this power law is given by the number of the corresponding harmonic order q. For higher orders, perturbation theory breaks down since the electric field

of the laser approaches the inner-atomic electric field. The effective exponential p in the modified power law I^p is smaller than q [137]. Intermediate harmonic orders show a plateau in intensity [138] which ends at the cut-off energy for the highest harmonic orders (Fig. 3.10, upper panel).

According to Eq. (3.52), the cut-off can be extended to higher energies by using a longer-wavelength driving field [139]. On the other hand, the efficiency of high-harmonic generation is increased for shorter-wavelength pulses due to the reduced wave packet spreading of the electron during its excursion time [140]. Also, since the oscillation amplitude of the electron in the laser field scales as λ^2, the electron spends more time in the vicinity of the atom for the shorter-wavelength driver and, therefore, has a larger probability of emitting a harmonic photon per unit time [141].

An extension of the position of the cut-off is also possible by using a higher intensity of the driving laser pulse, provided that the plasma effects are properly controlled. The effect of plasma defocusing can be minimized and the plasma dispersion can be compensated for if a guiding geometry in a hollow-core fiber is used. Such a setup has been successfully demonstrated for high-harmonic generation [142].

However, at the same time an increased intensity poses some limits on high-harmonic generation even in the single-atom limit. In high-intensity laser fields the electrons may gain velocities of the order of the velocity of light. In this regime magnetic-field forces become comparable to electric-field forces. The electron follows a figure-of-eight trajectories due to the contribution of the $v \times B$ terms induced by the strong magnetic field components which leads to a significant motion of the electron in the propagation direction of the laser field. As a consequence, there is less interaction with the nucleus and very few harmonics can be found in the radiation spectrum [143]. Also, relativistic mass effects have to be taken into account, preventing the acceleration of the electron to even higher energies necessary for the extension of the cut-off.

3.4.1.2 Ionization

When an atom is subject to a high-intensity laser field, it can be ionized even if the energy of the photons is smaller than the ionization potential. Multi-photon ionization (MPI) can occur where more than one photon is used to bridge the energy gap of the ionization potential and to free the electron. If no resonances take part in this step, the intensity dependence of the multi-photon ionization process follows a power law where the exponential is given by the number of photons needed.

However, when the electric field of the laser becomes comparable to the inner-atomic electric field, the atomic Coulomb potential $V_C(\boldsymbol{r}, t) = -e^2/4\pi\epsilon_0 r$ is heavily deformed (Fig. 3.10, step 1) by the potential of the strong laser field, $V_L(\boldsymbol{r}, t) = eE(t)\boldsymbol{r}$, and a finite barrier is established by the combined field through which the electron can tunnel. This is called *tunnel ionization* or *optical field ionization*. Keldysh [127] introduced the parameter γ,

$$\gamma = \sqrt{\frac{I_p}{2U_p}}, \tag{3.56}$$

which divides two regimes for ionization depending on the ionization potential I_p and the ponderomotive potential U_p defined in Eq. (3.52): For $\gamma \gg 1$, multi-photon ionization prevails

whereas for $\gamma \ll 1$ tunnel ionization is the dominant process. This important parameter γ is now called *Keldysh parameter*. It can also be expressed in terms of the tunneling time τ_{tunnel} in relation to the optical laser frequency ω_L or laser period $T_L = 2\pi/\omega_L$ [144]:

$$\gamma = 2\tau_{tunnel}\omega_L = 4\pi \frac{\tau_{tunnel}}{T_L}. \tag{3.57}$$

The tunneling time τ_{tunnel} is the time taken for the electron to pass through the barrier and must be short compared to the cycle T_L, so that the oscillating field is effectively a static field while tunneling occurs [145]. For very high frequencies (photon energies), if ω_L is larger than the atomic-orbital frequency ω_{at}, there is no tunneling regime since γ does not decrease below unity until the electric field exceeds the critical electric field for above-barrier ionization [146]. The barrier established by the combined Coulomb potential and the laser potential changes its direction so fast that the electron does not have enough time for tunneling through this barrier within one optical cycle. The so-called *quasi-static limit* for low frequencies breaks down. The parameter γ becomes greater than unity, and tunnel ionization is suppressed. If we increase the intensity, γ will decrease until the ionization rate reaches a maximum at $\gamma \approx 1$, and as the intensity increases further, the rate falls toward zero, provided that there are no strong intermediate resonances.

In his work, Keldysh calculated an expression for the ionization rate w of a hydrogen atom in an intense laser field of strength E which is valid in the quasi-static limit [127, Eq. (20)]:

$$w_{Keldysh} = \frac{\sqrt{6\pi}}{4} \frac{I_p}{\hbar} \left(\frac{eE\hbar}{m^{\frac{1}{2}}I_p^{\frac{3}{2}}} \right)^{\frac{1}{2}} \exp\left[-\frac{4}{3} \frac{\sqrt{2m}I_p^{\frac{3}{2}}}{eE\hbar} \left(1 - \frac{m\omega^2 I_p}{5e^2E^2} \right) \right], \tag{3.58}$$

where I_p is again the ionization potential, E and ω are the strength and the frequency of the electric field, e and m are the electronic charge and mass.

A generalized extended formula (called ADK ionization rate) which is valid for arbitrary atoms in arbitrary initial electronic configuration was later found by Ammosov, Delone, and Krainov [128] and is given (in atomic units) by

$$w_{ADK}(t) = C_{n^*l^*}^2 f_{lm} \left(\frac{3E}{\pi(2I_p)^{\frac{3}{2}}} \right)^{\frac{1}{2}} I_p \left(\frac{2(2I_p)^{\frac{3}{2}}}{E} \right)^{2n^*-|m|-1} \exp\left[-\frac{2(2I_p)^{\frac{3}{2}}}{3E} \right] \tag{3.59}$$

with the ionization potential I_p, the electric field $E(t)$, the quantum number of angular momentum l, and the magnetic quantum number m. The effective principal quantum number $n^* = Z(2I_p)^{-1/2}$ and the effective orbital quantum number l^* include the degree of ionization Z. The parameters $C_{n^*l^*}$ (on the order of two) and f_{lm} take into account the atomic species and the initial electronic configuration via the mentioned quantum numbers:

$$C_{n^*l^*} = \frac{2^{2n^*}}{n^*\Gamma(n^*+l^*+1)\Gamma(n^*-l^*)}, \tag{3.60}$$

$$f_{lm} = \frac{(2l+1)(l+|m|)!}{2^{|m|}(|m|)!(l-|m|)!}. \tag{3.61}$$

Using Eq. (3.59) the density of free electrons $n_e(t)$ can be calculated as a function of time t for an initial gas density n_0:

$$n_e(t) = n_0 \left(1 - \exp\left[-\int_{-\infty}^{t} dt' w(E(t')) \right] \right). \tag{3.62}$$

A rising density of free electrons is responsible for effects such as spectral blueshifting as already discussed in Sec. 3.3.

When the electric field strength is increased more and more, the height of the tunnel barrier decreases until it disappears. A transition occurs from the tunnel-ionization regime to barrier-suppressed ionization (BSI, Augst et al. [147]). The electron can escape from the nucleus. This work by Augst et al. [147] also discusses the validity of the ADK model in more detail for a range of intensities.

3.4.1.3 Propagation

Let us now consider the evolution of an electron wave packet after it has been created by ionization of an atom in more detail, using classical mechanics as has first been analyzed by Corkum [125] and Kulander et al. [126]. Only the electric field of the laser is considered, neglecting the potential of the ion core. Based on an early study on above-threshold ionization by Corkum et al. [148] we can assume the initial position and velocity of the electron to be zero at the time of ionization. The quasi-free electron is accelerated in the electric field $E(t)$ of the laser,

$$m\boldsymbol{a}(t) = e\boldsymbol{E}(t) = E_0 \cos(\omega t + \varphi)\boldsymbol{e}_x + \alpha E_0 \sin(\omega t + \varphi)\boldsymbol{e}_y, \tag{3.63}$$

where m and e are the mass and the charge of the electron, a is the acceleration, E_0 is the amplitude of the electric field, ω its (angular) frequency, and φ the phase of the oscillation. The prefactor α allows for arbitrary polarization. The electron motion is then given by

$$
\begin{aligned}
v_x(t) &= \int_0^t \frac{eE_x(\tau)}{m}d\tau = \frac{eE_0}{m\omega}[\sin(\omega t + \varphi) - \sin\varphi] = \\
&= \frac{eE_0}{m\omega}\sin(\omega t + \varphi) + v_{d,x}, \tag{3.64a}
\end{aligned}
$$

$$
x(t) = \int_0^t v_x(\tau)d\tau = -\frac{eE_0}{m\omega^2}\cos(\omega t + \varphi) + v_{d,x}t + x_0, \tag{3.64b}
$$

and

$$
v_y(t) = -\alpha\frac{eE_0}{m\omega}\cos(\omega t + \varphi) + v_{d,y}, \tag{3.65a}
$$

$$
y(t) = \alpha\frac{eE_0}{m\omega^2}\sin(\omega t + \varphi) + v_{d,y}t + y_0. \tag{3.65b}
$$

The constant velocity v_d is the drift velocity of the electron, depending on the phase of the electric field at the instant of ionization. The electron oscillates about the position determined by the drift velocity. The average quiver energy of this oscillation is given by the ponderomotive potential U_p (Eq. 3.52). Depending on the initial phase $\omega t_b + \varphi$ (where t_b is the instant of birth), the electron periodically reencounters its parent ion at the origin, where it can recombine and emit high-harmonic radiation. For circularly polarized light, however, the electron trajectory never returns to the vicinity of the ion. For linearly polarized light, several trajectories are possible. However, only the first two contribute significantly to harmonic radiation since the dipole moment responsible for harmonic emission also depends on the transverse spread of the wave function. According to Corkum [125], for a constant rate of increase of this spread, the strength of the single atom response varies quadratically with the inverse of the laser period. Therefore most efficient high-harmonic generation is possible with the shortest pulses and the shortest wavelengths.
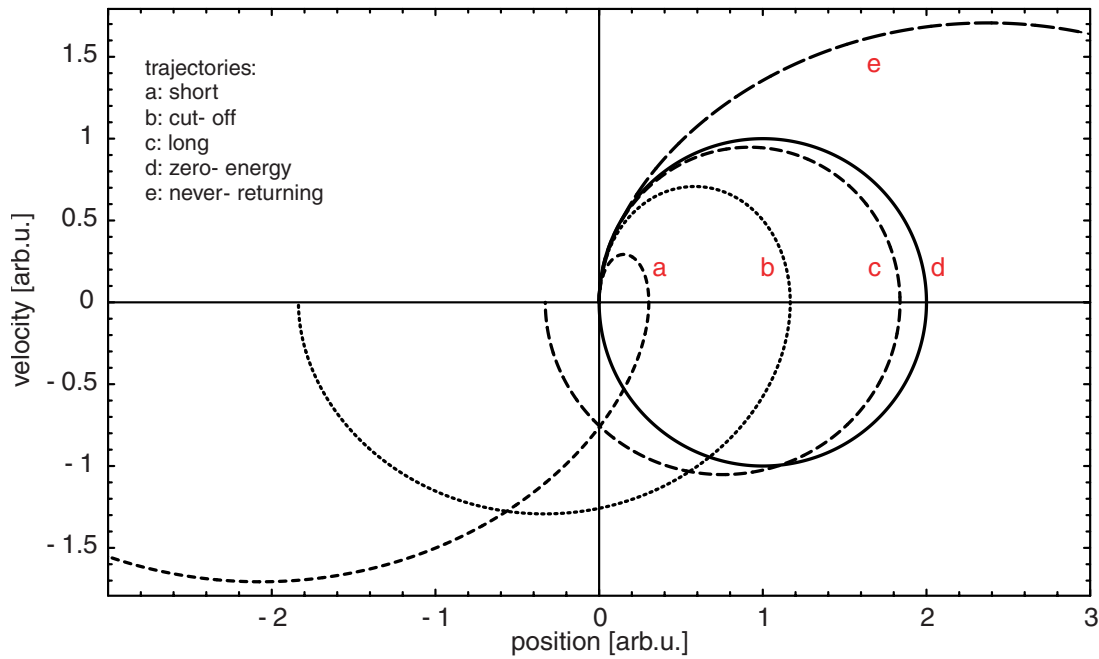
Figure 3.11 – Different classes of electron trajectories during the propagation phase of high-harmonic generation, plotted in the position-velocity plane: The trajectories start at the atom located at $(0,0)$. Depending on the phase Φ of the electric field at the instant of ionization, they can return to the core at position 0 with different kinetic energies, visualized by the intersection with the velocity axis. The traces $a(\Phi = 45°)$ and $c(\Phi = 3°)$ correspond to the short and long trajectory, respectively, leading to the same final energy. Class $b(\Phi = 17°)$ is a cut-off trajectory with the highest kinetic energy ($3.17U_p$), $d(\Phi = 0°)$ starts at the peak of the electric field where most electrons are produced but returns to the core with zero kinetic energy. Trajectory $e(\Phi = -45°)$ never returns to its parent atom.

Fig. 3.11 shows a plot of different classes of electron trajectories during the propagation in the electric field of the driving laser. The electrons start from the nucleus located at $(0,0)$. Depending on the phase Φ of the electric field at the instant of ionization, they can return to the core at position 0. The intersection with the velocity axis determines their final kinetic energies at the moment of recombination. The electron along the cut-off trajectory b was ionized at a phase of $\Phi = 17°$ and has the highest kinetic energy of $3.17U_p$ upon its return to the core. Electrons are most likely produced at the peak of the electric field ($\Phi = 0°$) but they return to the core with zero kinetic energy (d). Most electrons, however, are produced at unfavorable phases of the electric field and never return to the core (e). In the plateau region of high-harmonic spectra, there are typically two electron trajectories that give dominant contributions to high-harmonic emission, which interfere with each other [149]. The first short trajectory corresponds to a short return time (a), the second long trajectory (c) has a return time close to one period, which causes a strong intensity dependence of the phase. This can result in strong spectral broadening, leading to an overlap of neighboring peaks [40].

3.4.1.4 Recombination

Upon its return to the ion core, the accelerated electron can recombine to the ground state. In the process of high-harmonic generation, the corresponding energy is released as a high-energy photon. If the electron was at rest, this energy would just be the ionization potential I_p. However, an additional contribution comes from the kinetic energy $W_{\mathrm{kin}}(\varphi)$ that the electron gained in the laser field which depends on the phase φ of the driving electric field at the moment of the ionization of the electron (Eq. (3.53)). The kinetic energy of the returning electron can be calculated as a function of the phase by solving Eq. (3.64b) for $x(t) = 0$. The maximum kinetic energy is obtained for a phase of $\approx 17°$. This phase value is very close to the peak of the electric field where tunnel ionization is most efficient. This means that most electrons are indeed born into the continuum at that time of ionization that permits the highest photon energies. Tunnel ionization is locked to the phase of the laser pulse through its dependence on the momentary value of the electric field (Eq. (3.59)) whereas multi-photon ionization depends only on the cycle-average laser intensity. The kinetic energy at that phase takes the known value of $3.17 U_p$ so that the harmonic cut-off is located at

$$E_{\mathrm{cut-off}} = \hbar\omega_{\mathrm{max}} = I_p + 3.17\, U_p \qquad (3.66)$$

and therefore describes the highest harmonic photon energies that can be obtained (Fig. 3.12). This value had already been found in a numerical approximation by Krause and Kenneth J. Schafer [150].

The semi-classical approach presented so far mixes classical and quantum arguments: first quantum tunneling, then classical motion in the laser field, then quantum recombination. Many important quantum effects such as quantum diffusion of wave packets or quantum interferences are not taken into account. Refraining from solving the time-dependent Schrödinger equation we will present in the following an intermediate approximate solution to the problem of harmonic generation as published by Lewenstein et al. [136]. This model allows, for instance, to find the harmonic phase.

3.4.2 Intra-atomic phase

The phase of the harmonic emission can be determined using a quantum-mechanical formulation, the so-called *Lewenstein model* [136, 149]. This theory rephrases the classical models by Corkum [125] and Kulander et al. [126] in a fully quantum theory. It is valid in the single-active-electron approximation (SAE) in a low-frequency, high-intensity limit ($U_p \geq I_p$), and for high harmonics with energies greater than the ionization potential.

In atomic units, the Schrödinger equation takes the form

$$i\frac{\partial}{\partial t}|\Psi(x,t)\rangle = \left[-\frac{1}{2}\nabla^2 + V(x) - E(t)\cdot x\right]|\Psi(x,t)\rangle. \qquad (3.67)$$

The first step is the ionization from the ground state $|0\rangle$ to continuum states, labeled by the kinetic momentum of the outgoing electron, $|v\rangle$. The expression

$$d(v) = \langle v|x|0\rangle \qquad (3.68)$$

denotes the corresponding atomic dipole matrix element for this bound–free transition. The recombination step as the inverse process is given as the complex conjugate to describe the

transition from the continuum to the ground state:

$$d^*(v) = \langle 0|x|v \rangle. \tag{3.69}$$

For the following treatment, some assumptions can be made: Bound states (except the ground state) and intermediate resonances are unimportant and can be neglected as well as the depletion of the ground state. In the continuum, the electron can be treated as a free particle moving in the electric field with no effect of the atomic potential (strong-field approximation, SFA). Generally these asssumption are valid for a Keldysh parameter $\gamma = \sqrt{I_p/2U_p}$ of less than one, that is in the tunneling regime.

The time-dependent wave function can then be expanded as

$$|\Psi(t)\rangle = e^{iI_p t}\left(a(t)|0\rangle + \int d^3v\, b(v,t)|v\rangle\right), \tag{3.70}$$

where $a(t) \cong 1$ describes the ground-state amplitude, and $b(v,t)$ the amplitudes of the continuum states. After solving the Schrödinger equation (Eq. 3.67) for the amplitudes $b(v,t)$, we can calculate the time-dependent dipole moment $\mu(t)$:

$$\mu(t) = \langle\Psi(t)|x|\Psi(t)\rangle. \tag{3.71}$$

Neglecting the contributions from continuum-continuum transitions and neglecting the depletion of the ground state by setting $a(t) = 1$, we get the final expression for the dipole moment along an arbitrary direction n,

$$\mu_n(t) = i\int_0^t dt'\int d^3p \times \tag{3.72}$$
$$\times \underbrace{[n\cdot d^*(p - A(t))]}_{\text{recombination}} \times \underbrace{[E(t')\cdot d(p - A(t'))]}_{\text{ionization}} \times \underbrace{\exp[-iS(p,t,t')]}_{\text{propagation}} + \text{c.c.},$$

where the quantity S denotes the quasi-classical action that the electron experiences during its excursion:

$$S(p,t,t') = \int_{t'}^t dt''\left(\frac{1}{2}[p - A(t'')]^2 + I_p\right). \tag{3.73}$$

In the above equations we have introduced the canonical momentum

$$p = v + A(t), \tag{3.74}$$

where $A(t)$ is the vector potential of the electric field:

$$E(t) = -\frac{\partial A}{\partial t}. \tag{3.75}$$

Thus the electronic wave function acquires a phase factor equal to $\exp[-iS(p,t,t')]$ during propagation. This is a very important and far-reaching result of the Lewenstein model not gained from the classical model. However, the three steps of the classical model can be clearly seen in Eq. (3.72): ionization of the electron from the ground state at time t', propagation in the continuum during the time intervall $t - t'$, and transition from the continuum to the ground state (recombination) at time t.

Since the quasi-classical action (Eq. (3.73)) varies much faster than the other factors in Eq. (3.72), it is not necessary to solve the four-dimensional integral for the dipole moment but we can limit the evaluation of the integral over p to the stationary points of the classical action,

$$\nabla_p S(p, t, t') = 0. \tag{3.76}$$

Applying the same technique to evaluate the temporal integrals, we arrive at the following saddle-point equations:

$$\nabla_p S(p, t, t') = x(t) - x(t') = 0, \tag{3.77a}$$

$$\frac{\partial S(p, t, t')}{\partial t'} = \frac{1}{2}[p - A(t')]^2 + I_p = 0, \tag{3.77b}$$

$$\frac{\partial S(p, t, t')}{\partial t} = \underbrace{\frac{1}{2}[p - A(t)]^2}_{E_{\text{kin}}} - \underbrace{\frac{1}{2}[p - A(t')]^2}_{I_p} = 2q + 1, \tag{3.77c}$$

where all energies are expressed in terms of the photon energy, and the right-hand side of Eq. (3.77c) denotes the energy of the $(2q + 1)$-th harmonic. Eq. (3.77a) indicates that the only relevant electron trajectories are those where the electron leaves the atom at time t' and returns at time t. Eq. (3.77b) describes energy conservation in the process of tunneling, where the electron must have a negative kinetic energy at t', leading to a complex value of t'. Its imaginary part can then be assigned the tunneling time. Eq. (3.77c) finally is the energy conservation law at the moment of recombination.

The solution of these equations yields the cut-off energy of the harmonic spectra at

$$\hbar\omega_{\text{cut-off}} = 3.17 U_p + I_p \cdot f\left(\frac{I_p}{U_p}\right). \tag{3.78}$$

The factor $f\left(\frac{I_p}{U_p}\right)$ accounts for the fact that the electron cannot appear at the origin at tunneling and gains an additional kinetic energy on its way towards the origin. However, the electron diffusion limits this additional effect. The value of $f(x)$ is 1.32 for small x and decreases slowly for larger x.

Referring to Feynman's path integral formalism, Salières et al. [151] expressed the probability amplitude for high-harmonic generation as coherent superposition of contributions of all possible spatio-temporal paths that connect the initial and the final state of the system, the so-called quantum orbits. The weight of each path is a complex number whose phase is equal to the classical action S along this path. In general, only the first two quantum orbits with travel times of less than one ore two periods of the laser field contribute noticably. For harmonics in the cut-off region, there is only one relevant trajectory whereas for plateau harmonics two trajectories are needed for an accurate description. The implications of the spatio-temporal separation of high harmonic radiation into two quantum path components will be discussed in Sec. 3.4.6 on the coherence properties of high harmonics. A more detailed analysis of the frequency chirp of harmonic (femtosecond) pulses and attosecond pulses will be presented in Chap. 5.

Coherent control of harmonic generation is thus possible by the laser control over classical electron trajectories.
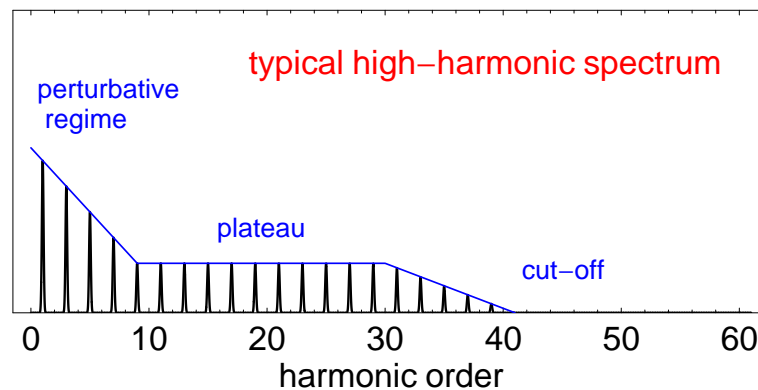
Figure 3.12 – Typical high-harmonic spectrum. The temporal periodicity of high-harmonic emission with half the laser oscillation period leads to a harmonic spacing of twice the fundamental frequency. The spectrum can be divided into three parts: the perturbative regime at low orders, the plateau for intermediate orders, and the cut-off at the highest orders.
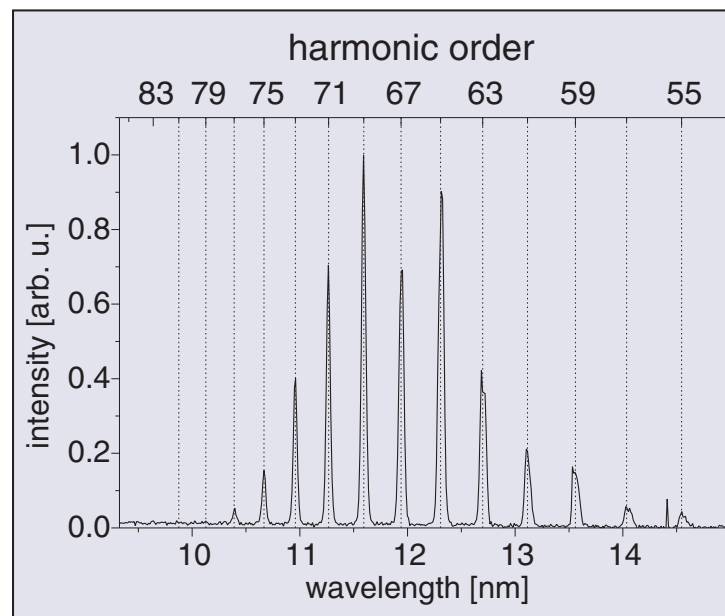
Figure 3.13 – Experimental high-harmonic spectrum obtained in a neon gas jet with a 80-fs laser pulse. Notice the existence of odd harmonics only and the decay of the intensity towards the cut-off at short wavelength. The decrease at longer wavelenghts is due to the zirconium filter used to block the fundamental radiation as well as low harmonics.

3.4.3   Harmonic spectrum

Since the generation of high-harmonic radiation is repeated every half-cycle of the electric field of the laser pulse, their spectrum consists of the odd harmonics of the fundamental laser frequency (Fig. 3.12 (schematical view) and Fig. 3.13 (experiment)). Each half-cycle of the driving laser pulse gives rise to a short burst of XUV radiation, leading to the emission of a sub-femtosecond XUV pulse (see Sec. 5). Therefore a driving pulse consisting of multiple

cycles produces a train of sub-femtosecond (attosecond) pulses, separated in time by half the oscillation period of the driving laser (attosecond pulse train, APT [28, 31, 152]). This periodicity of $T/2$ (where T is the laser period) is responsible for the observation of the harmonic spacing of 2ω. This behavior can simply be understood from the reciprocity of the Fourier transform, through which the electric field in the time domain and the spectral amplitudes are linked. Also, since consecutive bursts result from consecutive collisions from alternating directions, the corresponding spectral components have the same spectral amplitude but differ in sign. This results in destructive spectral interference for even-order harmonics ($\omega = 2m\omega_L$), while constructive interference occurs for odd harmonics ($\omega = (2m + 1)\omega_L$).

However, if the symmetry is broken, even-order harmonics can be generated. The symmetry can be broken both on the level of the laser pulses and on the level of the medium properties. For laser pulse durations approaching the single-cycle regime [51], even-order harmonics can be generated near the cut-off until the high-energy part of the harmonic spectrum merges into a continuum [124, 153]. This results from a loss of the strict periodicity of the electric field oscillations within a laser pulse for pulse durations of less than 10 fs. In this case, the pulses consist of only a few optical cycles, breaking the symmetry between consecutive oscillations.

The inversion symmetry between the upper and lower half-cycle, which yields the spectrum of odd harmonics only, can also be broken by adding the second harmonic of the driving laser pulse [41]. In this case, the shape and strength of the electric field in consecutive half-cycles differ beyond the simple sign change that occurs in a one color field, allowing for the production of attosecond pulse trains with only one pulse per infrared cycle with stable carrier-envelope phase. For a one-color driver, there is a π phase flip from pulse to pulse in the harmonic attosecond pulse train. The addition of a weak second-harmonic field can also be exploited to generate single attosecond pulse in the multicycle-driver regime where usually multiple attosecond pulses are produced [154].

The same effect of creating a difference between consecutive half-cycles can be realized by using oriented asymmetric molecules [155, 156]. The anisotropy of such a medium makes the contributions from the upper and the lower half-cycle of the laser oscillations different (even for multi-cycle laser pulses), thus allowing the generation of even-order harmonics. Alignment [157] alone is not sufficient because the symmetry is not broken.

A major step towards the realization of time-resolved soft-x-ray spectroscopy of biological samples was the extension of the harmonic cut-off into the so-called *water window* ($4.4 - 2.3$ nm) where water absorbs less than carbon [124, 158–160]. This breakthrough was only possible by the use of these ultrashort driver pulses.

Due to the dependence of the harmonic phases on intensity, a blue shift of the harmonic peaks can occur. Since this effect is more pronounced for the longer trajectories because they spend more time in the electric field the different amounts of blue shift between the different electron trajectories can even lead to a harmonic line splitting [161].

3.4.4   Propagation and phase matching

The three-step model describes high-harmonic generation in the single-atom response by calculating atomic dipole moments from the electron dynamics, leading to the emission of a high-energy photon. It does not completely describe the harmonic-generation process in a medium. The discrete nature of the spectrum as presented in Sec. 3.4.3 is a result of the peri-

odicity of the laser electric field. The final height and shape of the spectrum, however, are also determined by phase matching. General phase-matching considerations and phase-matching for low-order processes such as second-harmonic generation in solids can be found in Sec. 3.2.

Let us now consider the various contributions to the phase mismatch in gases where conventional phase-matching techniques do not apply or are very hard to implement. The wave vector k for a light wave transversing a gaseous medium can be written as follows [142]

$$k = \underset{\substack{\uparrow \\ \text{vacuum term}}}{\frac{2\pi}{\lambda}} + \underset{\substack{\uparrow \\ \text{neutral gas}}}{\frac{2\pi N_a\, n(\lambda)}{\lambda}} \underset{\substack{\uparrow \\ \text{plasma dispersion}}}{-N_e r_e \lambda,} \qquad (3.79)$$

where N_a is the density of neutral atoms in the medium (taking into account ionization losses), $n(\lambda)$ is the linear refractive index per unit neutral atom density (minus unity) at the wavelength λ, N_e is the density of free electrons, and r_e is the classical electron radius. The terms on the right-hand side in Eq. (3.79) represent the dispersion of the vacuum, the material, and the plasma. Note that the contribution from the free electrons in the plasma is negative.

As we will see later, it is very advantageous to generate high-order harmonics in a gas-filled hollow fiber. Inside a hollow capillary, a superposition of fiber modes [162] is excited, making the pressure dependence of high-harmonic generation and the spatial beam profile of the generated radiation more complex. In general, the phase-mismatch Δk between the generating laser field and the field of the high harmonics includes a dependence of the phase-mismatch $\Delta k = \Delta k(P, u_{nm})$ on the pressure P of the medium (the gas density) and the excited fiber modes u_{nm}.

In hollow fibers, we have another negative contribution given by the waveguide geometry, and the total wave vector can be written as

$$k = \frac{2\pi}{\lambda} + \frac{2\pi N_a\, n(\lambda)}{\lambda} - N_e r_e \lambda \underbrace{-\frac{u_{nm}^2 \lambda}{4\pi a^2}}_{\text{fiber dispersion}}, \qquad (3.80)$$

where (in addition to the quantities defined above) u_{nm} is the mth root of the Bessel function $J_{n-1}(z)$ for the waveguide (for the lowest order, $u_{11} = 2.405$), and a is the inner radius of the hollow fiber.

In a phase-matched high-harmonic-generation process where the phase velocities of fundamental and harmonic beam are equal the phase mismatch for the qth harmonic order

$$\Delta k_q = q k_{\text{laser}} - k_{\text{xray}} \overset{!}{=} 0 \qquad (3.81)$$

has to be equal to zero.

Substituting Eq. (3.80) in Eq. (3.81) and using $\lambda_{\text{xray}} = \lambda/q$ (where λ is the laser wavelength) we have

$$\Delta k_q = \frac{2\pi q}{\lambda} (1 - \eta)\, P\, \Delta n - P\, \eta\, N_{\text{atm}}\, r_e\, \lambda \left[\frac{q^2 - 1}{q} \right] - \frac{u_{nm}^2 \lambda}{4\pi a^2} \left[\frac{q^2 - 1}{q} \right], \qquad (3.82)$$

where we have introduced the pressure P (in atm), the ionization fraction η, the atomic number density at atmospheric pressure, N_{atm}, and the difference between the refractive indices of the neutral gas at atmospheric pressure, $\Delta n = n_{\text{laser}}^{\text{atm}} - n_{\text{xray}}^{\text{atm}}$. Since the highest harmonic conversion efficiency is obstand for $\Delta k = 0$ (phase matching), it is directly evident from Eq. (3.82) that there are several 'control knobs' available:
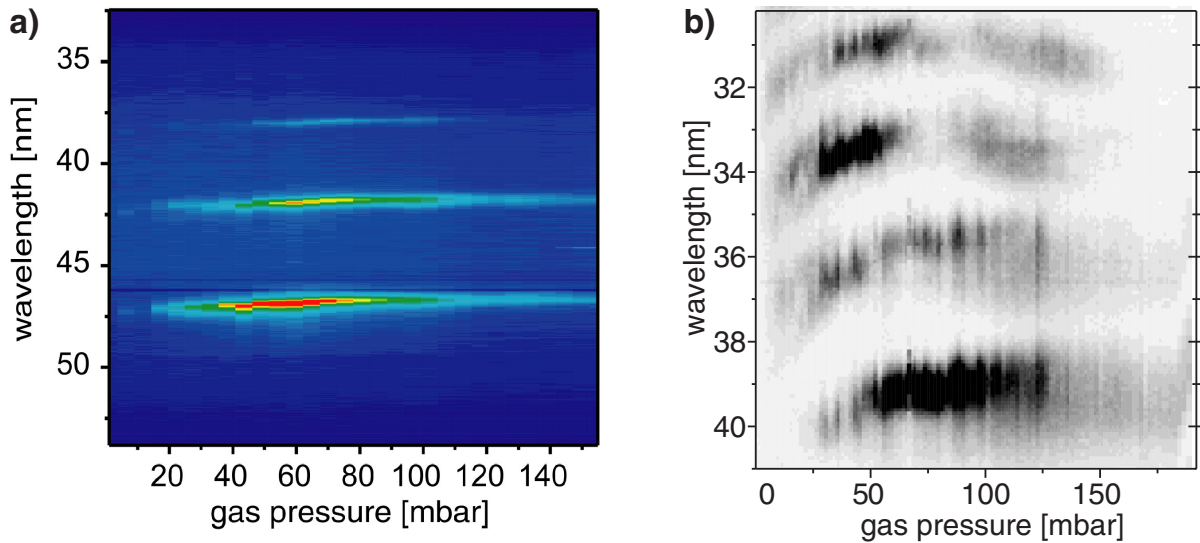
Figure 3.14 – Pressure and mode dependence of high-harmonic generation in hollow fibers. a) The excitation of one fiber mode shows the shift in maximum harmonic emission towards higher energies for increasing pressure. b) If two fiber modes are excited, two distinct local maxima can be seen, corresponding to phase-matching of the EH_{11} and EH_{12} fiber mode, respectively.

1. If we consider the case where only one fiber mode contributes to high-harmonic generation, there is still the possibility to adjust the remaining parameters to achieve phase-matching. It has been shown [142, 163] that the high-harmonic yield displays a maximum at a certain gas pressure P (neutral atom density), which corresponds to the phase-matched case $\Delta k = 0$ based on the pressure dependence of Δk. If we plot our experimental harmonic spectra versus the gas pressure in the capillary (Fig. 3.14a), we clearly see a shift of maximum harmonic emission towards higher frequencies for increasing pressure. Thus for a suitably chosen pressure, a certain range of harmonics is preferred.

2. Since the highest harmonic conversion efficiency is obtained for $\Delta k = 0$ (phase-matching), it is directly evident from Eq. (3.82) that there are several solutions of $\Delta k = 0$, one for each of the different fiber modes, i. e. different values of u_{nm}. Phase-matching can therefore be achieved by exciting a suitable fiber mode which determines the value of u_{nm}. Experimentally, if more than one fiber mode is excited, we should see several local maxima in the pressure dependence of phase-matching since the fiber-mode parameter u_{nm} assumes discrete values for different fiber modes. Fig. 3.14b was recorded in a regime in which two fiber modes were excited by the fundamental laser pulses. In this Figure one can clearly distinguish two separate local maxima of the harmonic yield as a function of the pressure. This experimental result matches very well with a theoretical calculation [43] based on Eq. (3.85).

Sometimes it is convenient to express Eq. (3.82) in terms of frequencies, the fundamental laser

frequency ω and the plasma frequency ω_p, defined as

$$\omega_p = \sqrt{\frac{N_e e^2}{m \epsilon_0}}, \tag{3.83}$$

where N_e is again the electron density, e and m are the electron charge and mass, respectively, and ϵ_0 is the permeability of free space. The classical electron radius is given as

$$r_e = \frac{1}{4\pi\epsilon_0} \frac{e^2}{mc^2}, \tag{3.84}$$

so that we arrive at

$$\Delta k = \underbrace{N_a[n(\omega) - n(q\omega)]\frac{\omega}{c}}_{\text{material dispersion}} + \underbrace{\frac{\omega_p^2}{2c\omega}\left[\frac{1-q^2}{q}\right]}_{\text{plasma dispersion}} + \underbrace{\frac{u_{nm}^2 c}{2a^2\omega}\left[\frac{1-q^2}{q}\right]}_{\text{waveguide dispersion}}, \tag{3.85}$$

where N_a is the density of neutral atoms in the medium, $n(\omega)$ and $n(q\omega)$ are the refractive indices per unit neutral atom density at the (angular) fundamental frequency ω and at the harmonic frequency $q\omega$, respectively, q is the harmonic order, c is the vacuum speed of light, ω_p is the plasma frequency, u_{nl} is the lth root of the Bessel function $J_{n-1}(z)$, and a is the inner radius of the hollow fiber. Real and imaginary parts of the refractive index in the (soft-)x-ray region are compiled in Henke et al. [164].

Another (yet technically sophisticated) 'knob' for dispersion control in a hollow-core fiber was proposed by Christov et al. [165]. By introducing thin glass plates with holes for the x-ray beam to pass into the waveguide, a periodic phase delay can be established for the fundamental, resulting in better phase matching.

If not a fiber is used for high-harmonic generation, but instead the driving laser is focused into the conversion medium, the Gouy phase $\eta(z)$ as defined by Eq. (2.23) has to be taken into account. The geometric contribution to the wavevector by the hollow fiber has to be replaced by the contribution caused by the Gouy phase which depends on the Rayleigh range z_R (or equally on the confocal parameter b):

$$k_{\text{Gouy}} = \frac{d\eta(z)}{dz} = \frac{d}{dz}\arctan\left(\frac{z}{z_R}\right) \approx \frac{1}{z_R} \quad \left(= \frac{2}{b}\right), \tag{3.86}$$

where the last approximation is valid close to the focus ($z \ll z_R$). The additional phase mismatch originating from the Gouy phase shift undergone by a Gaussian beam across the focus is thus given as [22]

$$\Delta k_{\text{Gouy}} = (q-1)\frac{2}{b}. \tag{3.87}$$

For very low gas densities, this term is actually the prevailing contribution to the total phase mismatch Δk [166]. However, in the presence of strong ionization, the phase relationship is strongly perturbed [167].

The contribution from the Gouy phase can be controlled by placing the focus at different positions with respect to the gas jet. This change in the phase-matching conditions allows the selection of the short or long electron quantum path in high-harmonic generation, influencing the spectral features of the emitted harmonic radiation [168]. The axial variation of the

laser intensity leads to different phase-matching conditions for the contributions from different quantum paths. Depending on the geometry, ionization, and pressure conditions, phase matching can enhance one class of the contributing trajectories at the expense of the others: When the laser is focused before the generating medium, phase matching on the optical axis is efficient and the spatial and spectral harmonics are regular. For a focus at the center of the nonlinear medium, the harmonic yield is low due to poor phase matching. When the laser focus is positioned after the medium, efficient phase matching is only ensured for off-axis emission, leading to a high conversion efficiency but to distorted spatial and temporal profiles.

3.4.5 Attosecond pulse generation

One of the most promising aspects of high-harmonic generation is the ability to produce single pulses or pulse trains on the attosecond time scale. An early consideration by Farkas and Tóth [69] shows that, similar to mode-locking in a femtosecond oscillator [54, 68], high harmonics can be superimposed to yield attosecond pulses (Fig. 2.6), provided a proper selection and phase relationship of the harmonics. The regular spacing of the harmonics in the spectral domain leads to the formation of attosecond pulse trains [28]. Phase-locking between five consecutive harmonics generated in argon was demonstrated by Paul et al. [31]. Isolated attosecond pulses with durations of 650 as could be generated by spectrally filtering the continuous cut-off region of few-cycle laser pulses [32].

Consecutive experimental results have examined the existence of high-harmonic-based attosecond pulses and pulse trains in more detail [33, 152, 169] and have described successful first experiments where the unique properties of this new radiation can be exploited to follow electronic dynamics in real time [36–38]. Recent review on attosecond physics have been compiled by Agostini and DiMauro [34] and Scrinzi et al. [39].

The time-structure of single attosecond pulses and attosecond pulse trains depends on the so-called *femto chirp* and *atto chirp* and will be discussed in more detail in Sec. 5.2.

3.4.6 Coherence

The first direct measurements of the temporal coherence of high-order harmonics were reported by Bellini et al. [170] and complemented by Lyngå et al. [171]. In the reported work, the authors measured the fringe visibility of the interference pattern in the far field of two spatially separated sources of harmonic radiation that were delayed in time with respect to each other. Whereas in general the coherence times are comparable to the expected pulse durations, the interference pattern exhibits two well separated spatial regions (concentric rings) with significantly different coherence times for some of the harmonics: the intense inner part has a long coherence time while the outer region displays a much shorter coherence time. From the semiclassical interpretation of high-harmonic generation (Section 3.4.1) there are actually two main trajectories that the electron can follow during the excursion time between ionization and recombination. The first (short) trajectory has a phase that does not vary much with laser intensity [149]. Consequently, the emitted radiation has a long coherence time and is very collimated. The dipole phase of the second (long) trajectory, however, varies rapidly with laser intensity [172], leading to a strong curvature of the phase front (due to the dependence of the intensity on the radial coordinate) and therefore to a strongly divergent angular

emission [168]. This radiation has a very short coherence time and a broad bandwidth since the harmonic pulse is strongly chirped because of the time-dependence of the intensity [173]. Due to the spatially differing behavior of the radiation originating from the two trajectories, it is possible to select only the short quantum path by placing an appropriate aperture in the harmonic beam, resulting in spatially and temporally highly coherent radiation.

The spatial coherence of the high-harmonic light can be measured through the double-pinhole (or double-slit) interference technique. The depth of modulation of the interference fringes after passing a beam through a pinhole pair is a direct measure for the degree of coherence across the spatial wavefront phase profile. If the phase difference between the two sampled points is constant, the fringe visibility will be unity whereas it is less than one if random phase variations exist. Bartels et al. [174] used such a two-pinhole setup to verify full spatial coherence of high-harmonic radiation generated in a phase-matched hollow-fiber geometry [142]. From a classical viewpoint, high-harmonic generation driven by coherent light is an inherently coherent process. However, the degree of coherence is degraded by mechanisms such as plasma refraction and the time-varying index of refraction. Also, as mentioned above, at least two trajectories with different phase behavior contribute to high-harmonic generation. However, the quasi-plane wave interaction in a hollow fiber and the long propagation distance select a single trajectory, which improves both the temporal and the spatial coherence including the beam mode quality.

Measurements by Lee et al. [175] confirmed the excellent spatial coherence of high-order harmonics from a gas-filled hollow fiber and used point-diffraction interferometry to show that the wave-front phase of a harmonic beam can be considered as a spherical wave within a phase error of less than $\lambda/15$.

The first measurement of the spatial coherence of high-order harmonic radiation in the soft-x-ray region was performed by Ditmire et al. [176]. They executed a series of Young's two-slit experiments to find that the harmonics (generated in a gas plume) exhibit good fringe visibility and high spatial coherence. At high intensities the coherence is degraded due to the rapid production of free electrons, which imparts a rapidly varying phase on the harmonic, lowering the degree of coherence.

Based on the experiments by Bellini et al. [170], Gaarde et al. [172] presented a spatio-temporal analysis of high harmonic radiation, demonstrating the separation into two quantum path components. Based on the numerical integration of the time-dependent Schrödinger equation, they determined the dipole moment $\mu_q(I)$ of the qth harmonic as a function of the intensity I of the laser field:

$$\mu_q(I) = A(I) \exp[i\Phi(I)]. \tag{3.88}$$

The dipole moment consists of several contributions with phases of the form

$$\Phi_k(r,z,t) = -\alpha_k I(r,z,t), \tag{3.89}$$

representing the different quantum paths, labeled by the index k. $I(r,z,t)$ is the space- and time-dependent intensity of the driving laser field, and α_k is the corresponding proportionality constant or slope of the phase function. By performing the equivalent of a time-frequency analysis using a window function for a range of intensities, the authors determined the "spectrum" of α_k. The result showed that the separation into different quantum path components is indeed justified. As representative values, they found the following numbers for the α_k for

the 15th harmonic in argon:

$$\alpha_1 \approx 1 \, \frac{\text{cm}^2}{\text{W}}, \qquad \alpha_2 \approx 27 \, \frac{\text{cm}^2}{\text{W}}. \tag{3.90}$$

The value for the long trajectory is much larger than for the short trajectory. Similar values are found in a study by Balcou et al. [177]. Gaarde [178] calculated time-frequency representations of high-order harmonics for a more detailed analysis of the different chirps present.

The variation in time of the intensity, $I(t)$, causes a frequency chirp $\Delta\omega_k(t) = -\partial\Phi_k(t)/\partial t$, leading to spectral broadening. In the same way, the radial variation of the intensity, $I(r)$, introduces a curvature of the phase front, causing the beam to diverge, depending on the values of α and I. We can estimate the influence on both the curvature of the phase front and the chirp for both components. Using the values for α_k from Eq. (3.90) we find the ratios of the spectral widths $\Delta\omega_k$ and of the divergence angles θ_k (in a geometrical-optics approximation) as

$$\frac{\Delta\omega_2}{\Delta\omega_1} \approx \frac{\theta_2}{\theta_1} \approx 27. \tag{3.91}$$

Since the spectrum of the long trajectory is dominated by the dipole chirp whereas the spectral width of the short trajectory is determined by its Fourier-transform-limited broadening, this ratio reduces to values between 10 and 20 but is still very large for the two quantum paths. As stated above, macroscopic separation of the two fields with a suitable aperture or introducing proper phase-matching conditions allows for the selection of one or the other contribution.

As we will see in Chapter 5, the atomic dipole phase (Eq. (3.89)) also depends on the harmonic order q. The α coefficients are closely related to the time the electrons spend in the continuum before recombination (return time or emission time, see Fig. 5.11). Differently from the determination of the atomic dipole phase based on the analysis of the harmonic frequency chirp (which is discussed in detail in Ch. 5), Corsi et al. [179] very recently employed the first direct interferometric measurement and observed the shift of the xuv interference fringes as a function of the intensity difference between two time-delayed fundamental pulses driving the harmonic generation process. By recording the phase shift between the fringes from the short and the long quantum path (spatially distinct emission zones), they were able to recover the different phase behavior of these two quantum paths as a function of harmonic order.

3.4.7   Challenges and goals

The goal of femtosecond or attosecond time-resolved XUV or soft-x-ray spectroscopy poses several challenges as summarized in Fig. 3.15: For instance, in order to be able to investigate the time-dependent shifts of absorption edges [180] the harmonic cut-off, which determines the highest energies possible, must be extended to shorter wavelengths [181–184]; for any kind of nonlinear optics in the XUV range [32, 152, 185–189] a large number of harmonic photons is desirable, therefore the efficiency of HHG should still be increased [190] to make the whole range of methods of pump-probe technology available to the XUV domain; moreover, for both spectroscopic applications and the optimization of attosecond pulse durations [33, 191] the selection of single harmonics or ranges of consecutive harmonics is necessary.

In order to increase the count rates in photoelectron spectroscopy with high-harmonic radiation, a higher repetition rate of the harmonics is desirable. While it is very hard to increase the repetition rate of the driving laser due to limitations in the pump energies of the pump lasers
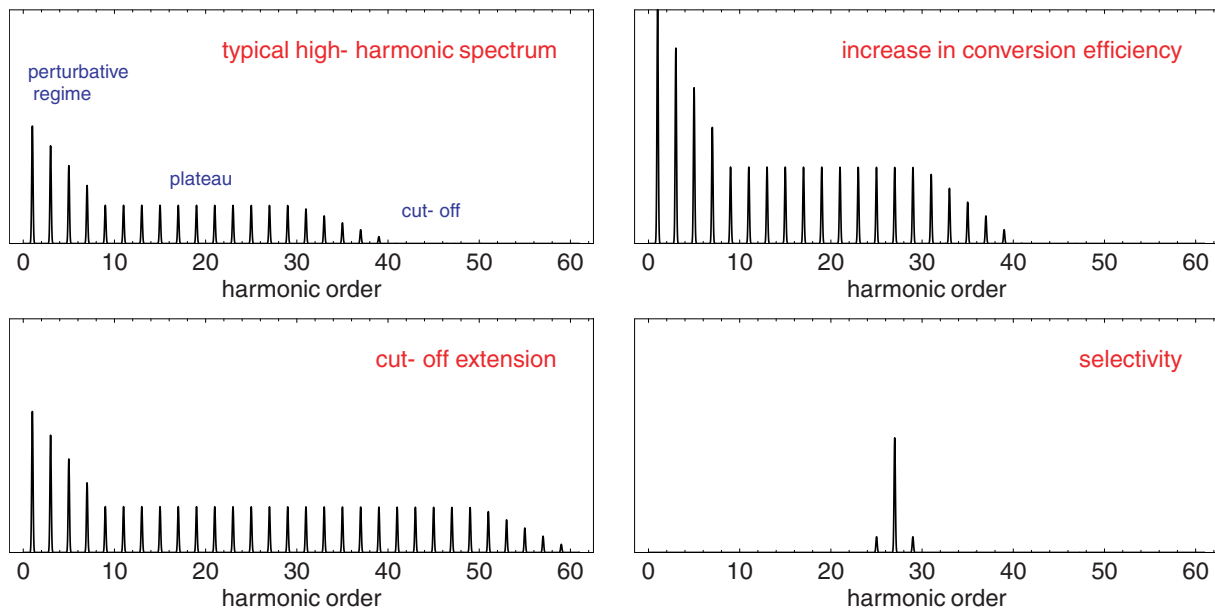
Figure 3.15 – Designed high-harmonic spectra with the challenges for further HHG experiments: extension of the cut-off energy, increase in the efficiency of the high-harmonic conversion process, and selection of single harmonics or range of harmonics.

in amplification stages, two groups [192, 193] have recently demonstrated high-harmonic generation directly from the oscillator. They succeeded in converting the frequency comb generated in a femtosecond oscillator cavity into the Extreme Ultraviolet (XUV) with intracavity high-harmonic generation at the full oscillator repetition rate by using an external build-up cavity with a xenon gas jet included in this cavity.

In this work we concentrate on the generation of engineered coherent soft-x-ray spectra where harmonics can be selected or suppressed, based on adaptive temporal and spatial shaping of the driving fundamental laser pulses. We first discuss several recent experiments treated in the literature on this topic. Examples from our own research are then used to illustrate progress and possibilities in this field.

Chapter 4

Controlling high-harmonic generation

Contents

4.1 Adaptive control

In order to shape high harmonics according to user-defined targets, it is very convenient and effective to employ adaptive control schemes. This provides a powerful method to steer quantum-mechanical processes by applying an optimal light field [194]. Numerous implementations in different areas have been reported in recent years, among others the control of chemical reactions [5, 6], molecular population transfer [4, 7–9], atomic multiphoton absorption [195], and high-harmonic generation [48]. The main experimental tool for achieving these goals is spectral phase shaping of femtosecond laser pulses [11], in combination with evolutionary-algorithm-based experimental feedback loops [3, 12, 13].

Likewise, we expect soft-x-ray pulse shaping to be a very efficient tool in our efforts towards the control of electronic motion. However, a direct transfer of pulse-shaping techniques developed in the optical wavelength range to the soft-x-ray regime is not feasible. Existing devices

require either spectral dispersion (e.g. liquid-crystal [10] or acousto-optical [196] spatial light modulators or deformable mirrors [197]) or extensive passage through material (the acousto-optical programmable dispersive filter "Dazzler" [198]), which precludes their applicability in the soft-x-ray spectral range due to small diffraction efficiencies for spectral dispersion and high absorption coefficients. It appears more desirable to directly generate a shaped soft-x-ray pulse, for instance by shaping the fundamental laser pulse prior to the conversion process than after its production. By shaping the ultra-short driving laser pulse it is possible to control the high-harmonic spectrum in a comprehensive way, far beyond earlier results on the control of particular spectral properties such as conversion efficiency and line width [48, 49] or the blueshift of harmonics [45].

Due to the temporally coherent nature of the soft-x-ray light generated by high-harmonic generation, spectral shaping and engineering on the other hand means the ability to shape the emerging trains of attosecond pulses or single attosecond pulses. These results open the road towards adaptive control in the soft-x-ray spectral range.

4.1.1 Working principle of adaptive control

Based on the complete Hamiltonian, the energy landscape and the dynamics of a quantum system can be calculated theoretically. In principle, the control of this quantum system is possible by applying the correct electric field (e. g. of a laser). The great difficulty is to determine the exact electric field that is needed to steer a quantum-mechanical reaction towards the desired output. Derived from simple resonance problems, researchers tried to selectively break a chemical bond by tuning the incident light field to the vibrational frequency of the selected bond. However, other than was expected, in most cases the weakest bond broke due to intramolecular vibrational redistribution (IVR). The vibrational energy coupled into the system by the light field quickly redistributes over the whole system through the coupling of the single oscillators given by the chemical bonds. A more complex electric field is therefore required to exactly cleave a desired chemical bond.

The problem of finding this electric field can be solved by applying different pulse shapes in a closed-loop optimization setup as proposed by Judson and Rabitz [3], which we also used for the adaptive control of high-harmonic generation in this work. Laser pulses are automatically tailored in a temporal or spatial pulse shaper according to user-defined optimization goals.

The basic working principle is depicted in Fig. 4.1. It relies on an evolutionary algorithm [12] that selects the optimal electric field. In brief, the incoming laser pulses are shaped in some sort of pulse shaper. The modulated laser pulses (in Fig. 4.1 a temporally shaped laser pulse is shown) are then used to perform the experiment in the quantum system. The experimental signal is analyzed and a fitness is assigned to the corresponding laser pulse. Utilizing this ranking, the evolutionary algorithm can automatically find the optimum laser pulse. The first experimental implementations by Yelin et al. [13] and Baumert et al. [12] automatically compressed chirped femtosecond laser pulses, without first characterizing the pulses.

In our setups to shape the high-harmonic spectra, the closed-loop optimization iteratively shapes the laser pulse either temporally with a deformable mirror (Section 4.2) or spatially using a two-dimensional liquid-crystal-display-based spatial light modulator (Section 4.3). The obtained spectrum is measured with a CCD camera. The applied algorithm is based on the evolutionary principle of 'survival of the fittest' as described elsewhere [12]. A fitness measure for each shaped laser pulse is derived from the high-harmonic spectrum. This mea-
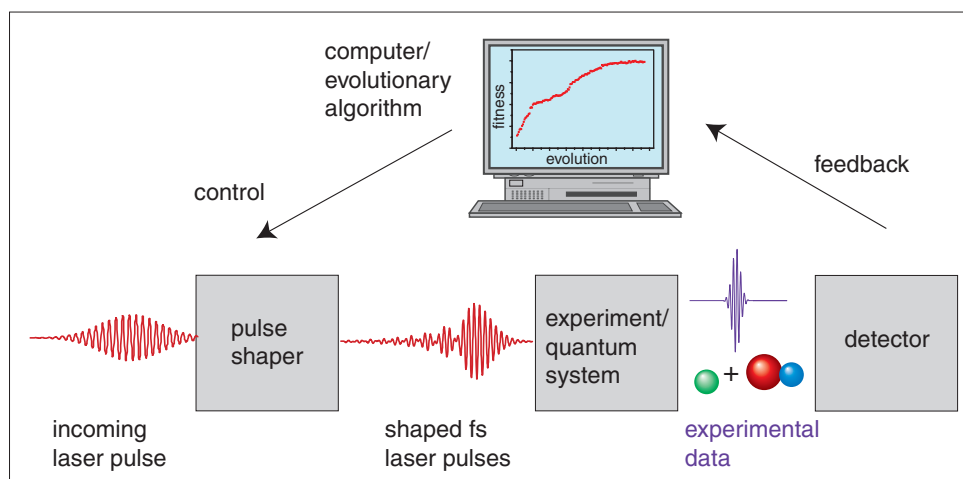
Figure 4.1 – Working principle of adaptive control. The incoming laser pulse is first shaped in a laser pulse shaper and is then used to perform the experiment in the quantum system. The experimental signal is analyzed and a fitness is assigned to the corresponding laser pulse. Utilizing this ranking, the evolutionary algorithm can automatically and iteratively find the optimum laser pulse shape.

sure, also termed fitness function, maps the shape of the complete high-harmonic spectrum onto a single number. In this way it is easily possible to rank the performance of different laser pulse shapes. Each pulse shape termed an individual is characterized by a number of genes, e.g. the nineteen high-voltage levels applied to the deformable mirror electrodes. These voltage parameters defining the pulse shape can therefore be regarded as the genetic elements of an individual laser pulse. Fifty different individuals represent a generation. The first generation consists of individuals each possessing randomly chosen genes (voltages) with values throughout the suitable voltage range. After applying those pulses in the harmonic generation experiment, their fitness is determined and the selection of the fittest is carried out. These best-performing individuals are kept for the next generation. Other members of the next generation are produced by cross-over (two individuals of the old generation each pass on a part of their genetic elements to their 'offspring') or mutation (some genetic elements are randomly changed) until a population size of fifty is reached again. This procedure is repeated for a number of generations, until the fitness of the fittest individual has converged. To obtain the desired result, the definition of an appropriate fitness function is crucial.

The application of evolutionary algorithms is not limited to the adaptive control of ultra-short large-bandwidth laser pulses. We successfully implemented this idea in a time-of-flight electron spectrometer [199]. Photoelectrons generated in the interaction region of the laser or high-harmonic pulses with a medium fly through a drift tube onto a multi-channel-plate-based detector. In order to increase the resolution and the throughput of the spectrometer, six electrostatic lens plates are built in before the drift tube. The voltages applied to the lens plate for focusing can be adjusted manually or fully automatically using an evolutionary algorithm that uses the total number of electron in a region of interest as feedback signal.

4.1.2   Control schemes

Laser pulses optimized by adaptive control are usually difficult to interpret since contributions may appear that turn out to be useless but which complicate the pulse shape. If analysis is possible, it turns out that the control achieved is related to one of the following basic ideas or mechanisms of single-parameter control:

pump–dump control This idea was developed by Tannor, Kosloff, and Rice [200] based on a first proposal by Tannor and Rice [201] and considers the temporal evolution of molecular wave packets. This wave packet is formed on an excited-state potential energy surface by a multiphoton process from the ground-state potential energy surface $|0\rangle$. The wave packet born at time t_0 will start to evolve on the excited-state potential energy surface. If a second ultrashort laser pulse is applied after the time t_1 so that the wave packet can be dumped through the Franck–Condon window onto the desired target state surface, the reaction can be steered into target state $|1\rangle$. For a different time t_2, target state $|2\rangle$ will be reached. Controlling the delay

$$\Delta t = t_{1,2} - t_0 \tag{4.1}$$

between two ultrashort laser pulses thus allows to selectively generate different chemical products. Since the wave-packet evolution on potential-energy surfaces is controlled, at least two dimensions are needed as provided by tri-atomic molecules.

ω–3ω scheme This technique proposed by Brumer and Shapiro [202] directly exploits the concept of wave packet interference. A resonant laser at the frequency ω resonantly couples some initial state $|0\rangle$ to a final state $|1\rangle$ in a one-photon transition. If a second phase-locked laser is incident at 3ω, the wave packets in the final state created by the two lasers can interfere constructively or destructively, depending on the relative phase

$$\Delta\Phi = \Phi_\omega - \Phi_{3\omega} \tag{4.2}$$

between the two light fields. Selective population transfer can thus be achieved by using the coherence properties of lasers.

These single-parameter control schemes form the basis for the understanding of the possibility of quantum control, although in many cases a more complex shape of the electric field is required.

Since a two-photon process is the minimum for interfering pathways and since the control of the appropriate time delay effectively corresponds to choosing the right relative phase between the different pathways, each of the above schemes can be reformulated in the other domain since they are essentially equivalent [203].

In some cases open-loop control based on analytical calculations is still possible, wonderfully demonstrated by the group of Silberberg [195].

Another control scheme is based on the stimulated rapid adiabatic passage (STIRAP) and was pioneered by the group of Bergmann [204, 205]. It relies on the coupling of energy levels in a so-called Λ scheme to completely transfer population from the lowest level to the second-lowest level without population the third (higher) level.

Although the effective control mechanisms for high-harmonic spectral engineering remain unclear, it can be derived from the laser-phase controlled electron quantum paths in Fig. 3.11 and the research on the coherence properties of high harmonics summarized in Sec. 3.4.6 that it must be possible to influence high-harmonic generation by using coherent-control setups. Therefore the following Section focuses on the control of high-harmonic generation by modifying the temporal properties of the driving laser pulses. As we will describe later in this work, temporal pulse shaping only is not sufficient for high-level harmonic spectral control but is a major ingredient.

4.2 Control of high-harmonic generation through temporal laser pulse shaping

Control of high-harmonic radiation should be possible in two fundamental ways, either by controlling the temporal evolution of the driving electric field or by controlling spatial properties in the broadest sense, including medium engineering and geometric effects. The temporal aspect will be described in this Section while spatial aspects can be found in Sec. 4.3.

The temporal evolution of the electric field $E(t)$ of an ultrashort laser pulse can be summarized as

$$E(t) = E_{\text{env}}(t)p(t)e^{i(\omega t + \varphi(t) + \varphi_0)} \tag{4.3}$$

where $E_{\text{env}}(t)$ is the envelope of the pulse effectively determining the pulse duration and pulse intensity, $p(t)$ is the polarization axis which can vary during the duration of the pulse, ω is the central frequency and can be modified e.g. in multicolor experiments, $\varphi(t)$ is the time-varying phase and determines the chirp of the laser pulse, and φ_0 is the carrier-envelope phase which we have written here explicitly since it plays an important role for few-cycle laser pulses and the generation of single attosecond pulses.

Here we describe a number of experiments that systematically adjusted one of these parameters manually in order to control high-harmonic radiation. This is also called open-loop control since no feedback from the experiment is used to close the optimization loop. As the number of possible configurations is extremely high, it is very convenient to use an evolutionary algorithm as presented in Sec. 4.1 to quickly find an optimum setting.

4.2.1 Open-loop control

Several attempts have been made to influence harmonic spectra and the corresponding harmonic light pulses. As explained in Section 3.4, the same intense laser field is responsible for the ionization of the medium *and* the subsequent acceleration of the electrons so that they can gain kinetic energy. In order to replace the initial effective multi-photon ionization by a linear single-photon step and to have control over the initial phase of the electron with respect to the accelerating laser field, it was first proposed and calculated by Schafer et al. [206] and experimentally verified by the group of Ursula Keller [207] to separate these two steps. First, a regularly spaced attosecond pulse train (APT) consisting of high-photon-energy harmonic pulses is generated in a hollow fiber filled with xenon gas. This attosecond pulse train is then directed into a helium gas jet, together with a strong fundamental laser pulse. The high-energy photon from the APT can now ionize the gas efficiently in a direct one-photon transition while the second fundamental laser field is responsible for the acceleration of the

electron. The timing between these two fields can be controlled, allowing for quantum-path selection on the single-atom level, decoupling the ionization step from the strong-field dynamics. The linear ionization removes the randomness and inefficiency of tunnel ionization. Also, the strong laser field now contributes wherever harmonic photons from the APT are present, thereby exploiting this volume effect for high-harmonic generation to increase the harmonic yield.

Another implication of the fact that usually the same laser field is employed for the ionization and acceleration of the electrons is the limit that is placed on the highest obtainable photon energy (cut-off energy). The actual laser intensity I in Eq. (3.52) has to be substituted by the saturation intensity I_s [158, 159], which the atoms can be exposed to before the ground state is depleted, i.e. the ensemble is fully ionized. For high-intensity pulses with longer pulse durations, the medium is depleted before the high peak intensity could be reached. This limit can be circumvented for the shortest driving pulses since the rise time of such pulses is so fast that ionization is effectively suppressed. The laser field can now exceed the barrier-suppression limit well before the ground state is depleted. Therefore electrons are born into a very strong electric field and can acquire higher kinetic energies than before, which extends the cut-off to shorter wavelengths. The cut-off energy no longer depends on the intensity of the laser pulse alone, but on the pulse duration as well [158, Eq. 2]. This dependence was used by Chang et al. [158, 26 fs pulses] and Schnürer et al. [159, sub-10-fs pulses] to extend high-harmonic generation into the water window.

Lee et al. [208] have shown that the high-harmonic generation process can be controlled coherently using chirped femtosecond laser pulses to produce sharp and strong harmonic spectra. For an efficient coherent control, a proper laser chirp condition must be chosen to suppress the harmonic chirp that broadens high harmonics and reduces their peak intensities. This chirp depends on the current laser intensity used. Chang et al. [209] have demonstrated theoretically and experimentally that for positively chirped pump pulses, the individual harmonic peaks are well defined and discrete, while for negatively chirped pump pulses, the harmonic output spectra merge into a continuum. Adjusting the laser chirp and/or energy also allows for continuous wavelength tuning of the high-order harmonics, covering the entire spectral region between two consecutive harmonics [210, 211].

A detailed analysis [212] including a cross correlation of the generated harmonics and a theoretical calculation [213] showed that a chirp on the pump pulse generating the harmonics is transferred to the qth harmonic as q times the fundamental chirp, verifying an earlier analysis by Chang et al. [209]. For bandwidth-limited pulses, the harmonics are negatively chirped due to the atomic dipole phase, so by adding a positive chirp on the pump pulse, the harmonic chirp can be compensated.

Brandi et al. [214] have reported the generation of tunable high-harmonic lines of very high spectral purity, using spectrally narrow, long laser pulses with durations of 300 ps.

Work done by a French-Swedish collaboration [215] demonstrates amplitude and phase control of attosecond light pulses by introducing a thin aluminum filter in the beam path of the harmonic pulses. High-harmonic pulses are intrinsically chirped due to the intensity dependence of the atomic phase (phase accumulated during excursion on the quantum paths [149, 151]). For the short quantum path which can be selected by placing a hard aperture in the fundamental laser beam prior to harmonic generation this chirp is positive. This results in temporally long harmonic pulses. This phase can be compensated by the negative material dispersion introduced by the aluminum filter in the XUV wavelength range. A train of

almost Fourier-transform-limited pulses with pulse durations of 170 attoseconds can be obtained, characterized with RABBITT [33, 216, 217] (see also Section 5.1). The same group [33] proposed to use a 'plasma compressor' for the synchronization of high harmonic since the free electrons in a plasma also induce the required negative group velocity dispersion. The use of material dispersion was suggested by the group of Nam [218] to obtain single sub-50-attosecond pulses. The use of extreme-ultraviolet chirped mirrors has also been proposed as a way to compres attosecond harmonic pulses [219].

Another way to control high-harmonic generation is offered by controlling the time-dependent polarization state of the electric field during the driving laser pulse duration. The process of high-harmonic generation is very sensitive to the ellipticity of the driving light field [220, 221]. Only for linear polarization can the electron come back to its parent ion to recombine and emit harmonic photons. A time-varying polarization can be realized by combining two short perpendicularly polarized pulses with slightly different center frequencies [222, 223], by polarization gating using two waveplates or other birefringent optics [224–226] or by direct polarization pulse shaping of the fundamental driving laser field [227] using a polarization pulse shaper. Polarization pulse shaping has recently been introduced by Brixner and Gerber [228] and has already been demonstrated e.g. for the two-photon ionization of potassium dimers [229]. Calculations [230] have shown that the chirp of a single attosecond pulse generated by polarization-gating is positive and its value is almost the same as that when a linearly polarized laser is used. Cross correlation measurements [231] have indicated that the duration of the xuv emission is indeed limited by the ellipticity gate, rather than by the harmonic generation process.

The wavelengths of harmonics generated in a gas-filled hollow capillary can be tuned by changing the average laser pulse intensity or by varying the quadratic spectral phase of the laser pulse [232]. This can be attributed to an ionization-induced blueshift inside the capillary.

4.2.2 Tailoring high-harmonic spectra by adaptive temporal pulse shaping (closed-loop control)

In addition to the open-loop results reported above, the implementation of a closed-loop scheme represents a very powerful method to comprehensively shape high-harmonic spectra, beyond the extent possible by simply modeling the high-harmonic generation process.

4.2.2.1 Adaptive optimizations in gas jets

There are two main geometries that can be employed to generate high harmonics in a gas target: generation in a gas jet or in a hollow gas-filled capillary (Fig. 4.2). A simple setup consists of the intense laser pulses being focused into a gas jet as shown in Fig. 4.2a. The XUV radiation produced in the gas jet by the highly nonlinear interaction of the laser pulses with the gas atoms is separated from the fundamental field by a suitable filter, e. g. by a thin 300 nm aluminum filter for harmonics in the energy range from 20-70 eV and is subsequently detected by a soft-x-ray spectrometer.

Earlier experiments performed in gas jets successfully tuned the harmonic wavelengths via blue-shift [45]. The 27th harmonic at 30 nm could be shifted to 31.16 nm (Fig. 4.3). The authors attribute this shift to ionization effects. They also attempted to enhance single harmonics relative to adjacent peaks. However, the selective control of single harmonics using such a
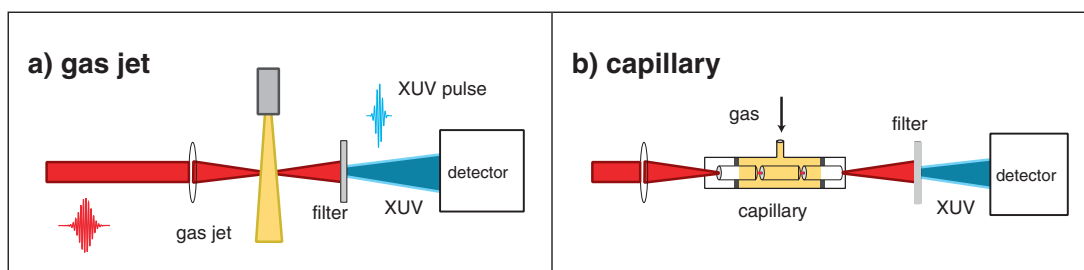
Figure 4.2 – Geometries for high-harmonic generation in atomic or molecular gaseous media. a) Generation in a free-focusing geometry (gas jet), selectivity of single harmonics is not possible. b) Generation inside a gas-filled hollow capillary, selectivity of different single harmonics can be achieved with a high contrast with respect to neighboring orders.

Figure 4.3 – Tuning of harmonic wavelenghts in a gas jet. The harmonic orders can be wavelength-shifted in an adaptive optimization. However, the selective control of single harmonics is not possible (figure taken from Reitze et al. [45]).
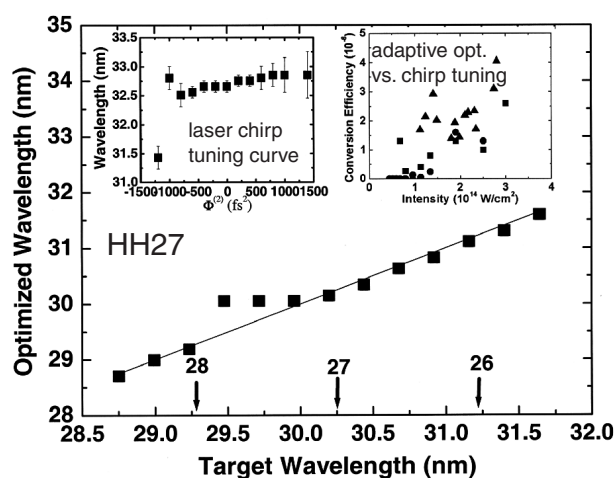
free-focusing geometry has not been achieved so far. Also our result in Fig. 4.4a shows the negative outcome of an optimization of a single harmonic in a gas jet (yield in region A compared to the yield in regions B).

On the other hand it is possible to extend the cut-off in a free-focusing geometry (Fig. 4.4b), using the deformable mirror as described in Sec. 4.2. The optimization of the cut-off position in HHG is due to the clean-up of higher-order phase distortions by the deformable mirror, thus increasing the laser peak intensity, leading to higher cut-off photon energies. An enhanced level of control including the selectivity of selected harmonic orders can only be achieved in a waveguide geometry such as a hollow fiber.

There has also been a theoretical study of the optimization of several features of high-harmonic generation in noble gases using a genetic algorithm [233]. Harmonic radiation could be tailored to different applications such as optimization of the pulse energy of one harmonic, minimization of the pulse duration, and the optimization of the temporal coherence of harmonics. This was done by adaptively adjusting the intensity of the laser, the gas pressure, the interaction length in the nonlinear medium, and the position of the focus relative to the gas jet.

Another theoretical investigation [234] used an efficient genetic algorithm to optimize short intense excitation laser pulses in order to generate high-order harmonics from which single attosecond pulses can be synthesized. Whereas the high-harmonic field generated by an un-
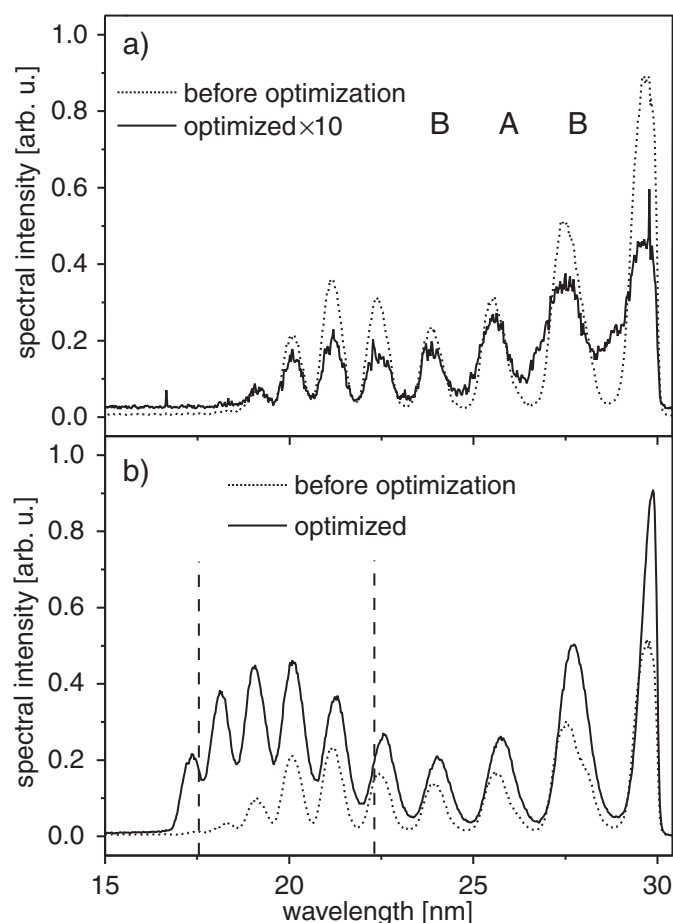
Figure 4.4 – Optimizations of harmonics performed in a free-focusing geometry. a) Negative outcome of a selective optimization of harmonics in region A compared to region B. No selectivity could be achieved. b) Cut-off extension in a free-focusing geometry. The optimization of the high-harmonic cut-off position is due to the clean-up of higher-order phase distortions by the deformable mirror, thus increasing the laser peak intensity, leading to higher cut-off photon energies.

optimized laser pulse exhibits the well-known train structure [28] with a number of satellites, single attosecond pulses appear after the optimization.

4.2.2.2 Enhanced control in hollow fibers

A capillary setup where the laser is focused into a hollow fiber filled with a noble gas (Fig. 4.2b) indeed allows for selective enhancement [42, 48, 49]. Earlier work [48] demonstrated the optimization of a single harmonic generated in an argon-filled hollow fiber. This was achieved using spectral-phase shaping with a micromachined deformable mirror. Additional work by the same group [49] showed the enhancement of different harmonic orders in different noble gases, although the contrast ratio between the selected harmonic and neighboring harmonics is lower.

Going far beyond these earlier results we demonstrate the complete control over the XUV
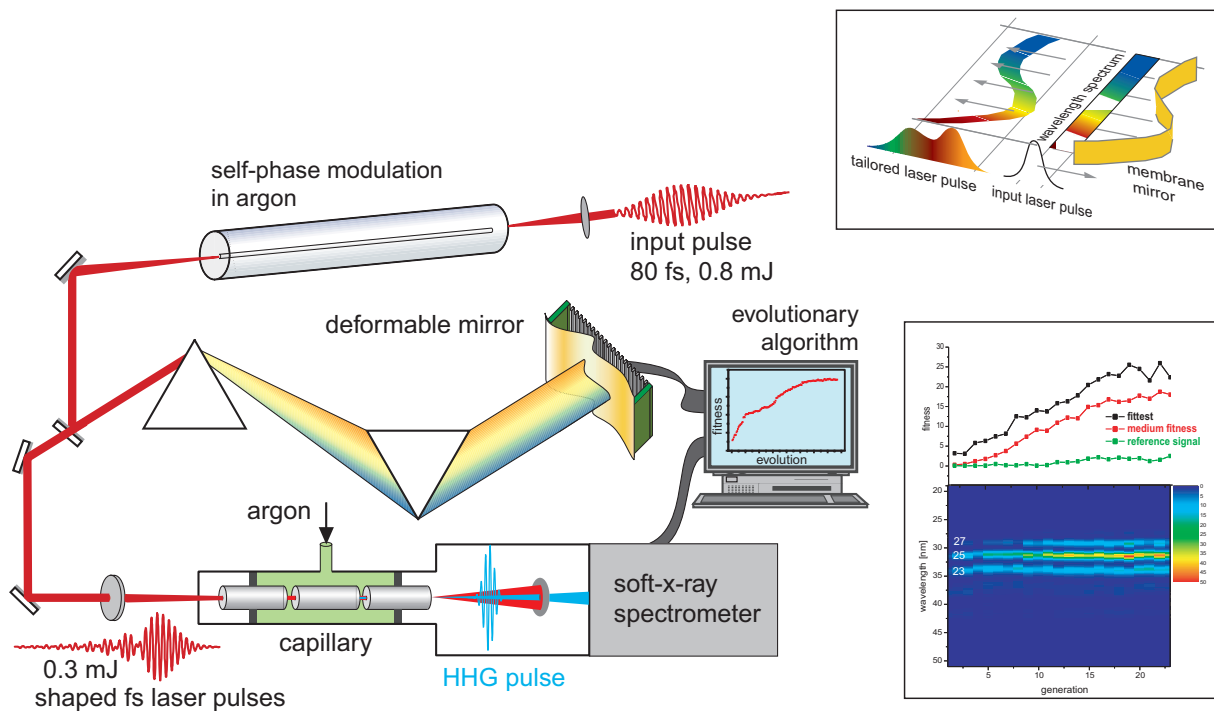
Figure 4.5 – Experimental setup for temporal pulse shaping. Ultrashort laser pulses from a regenerative amplifier undergo further spectral broadening and compression using self-phase modulation in an argon-filled hollow capillary and a prism compressor. A deformable mirror as the symmetry plane of the prism compressor allows temporal pulse shaping.

The shaped pulses generate high-harmonic radiation in a second argon-filled hollow fiber. The resulting spectrum is recorded by a CCD-camera equipped soft-x-ray spectrometer and analyzed by the computer which runs a closed-loop evolutionary algorithm to optimize the spectral shape. The upper inset depicts the modification of the optical paths of the different frequency components as introduced by the deformable mirror. The inset on the right shows a typical optimization run for the selection of a single harmonic. The fitness value increases as a function of the number of generations.

spectrum of high harmonics. We achieve both the enhancement and suppression of high-harmonic emission in a selected wavelength region as well as the enhancement of coherent soft-x-ray radiation over a selectable extended range of harmonics. In order to find the laser pulse shapes that are needed to exert this level of control we employ an evolutionary algorithm.

The experimental setup used for these experiments is displayed in Fig. 4.5: Ultrashort laser pulses from a regeneratively amplified Ti:sapphire laser system (80-fs pulse duration, 800-nm center wavelength, 0.8-mJ pulse energy, 1-kHz repetition rate) are spectrally broadened in an argon-filled hollow fiber (250-μm inner diameter, 0.6-m length, 0.6-bar pressure) by the process of self-phase modulation (SPM[1]) [235]. Using a prism compressor with a deformable mirror as symmetry mirror [236], we are able to obtain 20-fs pulses that can be phase-shaped by controlling the surface of the deformable mirror. The shaped pulses are focused into a second argon-filled fiber with an inner diameter of 140 μm and a length of 0.1 m. This fiber

---

[1]For more details on self-phase modulation in a gas-filled hollow fiber see Fig. 3.7 and the descriptive text in Sec. 3.3.1.
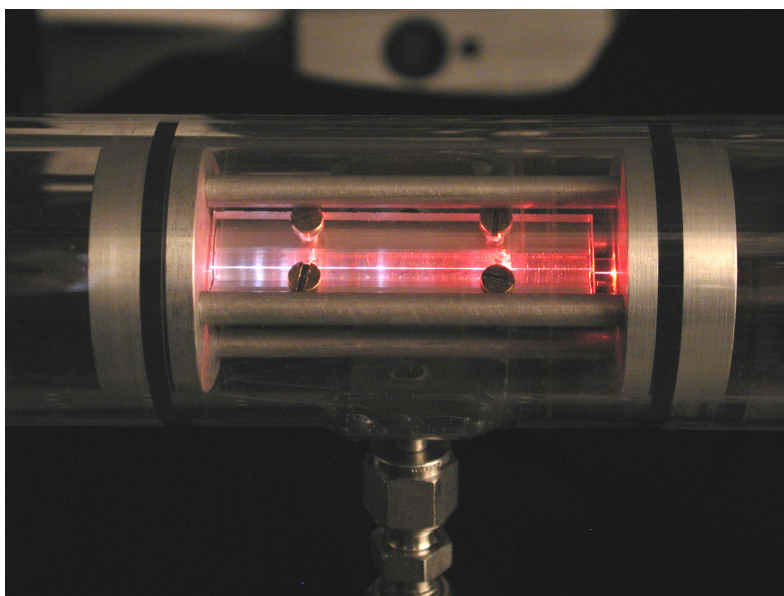
Figure 4.6 – Photographic image of the setup of the three-part hollow fiber in its cage. The outer segments serve as seals towards the vacuum while a constant pressure prevails in the center piece. The stray light comes from the scattering of the fundamental laser from the gas atoms and from the plasma in the hollow fiber core.

is split into three parts which are aligned on a v-groove mount with tiny gaps between them to ensure a constant pressure in the center segment where high-harmonic generation takes place. In the photographic image in Fig. 4.6, the stray light from the fiber can be seen. The outer segments serve as a seal towards the vacuum before and after the fiber. The laser intensity inside the capillary can be estimated as 2×10^{14} W/cm^2 from the cut-off scaling law. After a 0.3 μm-thick aluminum filter which blocks the fundamental and lower orders the harmonic radiation is detected with a soft-x-ray CCD camera mounted behind a grazing-incidence XUV spectrometer. Rundquist et al. [142] used a similar setup to demonstrate phase-matched generation of high harmonics in a hollow capillary for the first time. They were able to increase the harmonic output by two to three orders of magnitude compared to the non-phase-matched case. Similar values were reported by the group of Midorikawa [237]. Spatial effect inside a fiber such as phase-matching are discussed in more detail in Section 4.3.

Control over the high-harmonic spectrum is achieved by employing an evolutionary algorithm [12]. This algorithm drives the gold membrane of the deformable mirror (inset of Fig. 4.5) to shape the laser pulses by sending specific voltage values to electrodes behind the gold membrane. The gold membrane is deformed depending on the applied voltage and thus changes the optical path of the individual wavelength components of the laser pulse that are spatially dispersed in a prism compressor. The high-harmonic spectra generated by these shaped pulses are recorded by the CCD camera that evaluates them according to a given fitness function. The fitness function assigns a rank to each shaped laser pulse according to how well it produced the desired harmonic spectrum or spectral feature. The evolutionary algorithm itself is based on the principle of the 'survival of the fittest' and uses the ranking made by the fitness function to keep the best-performing laser pulses for the next generation. The rest is dismissed or transferred to the next generation by mutation or cross-over. The members of the
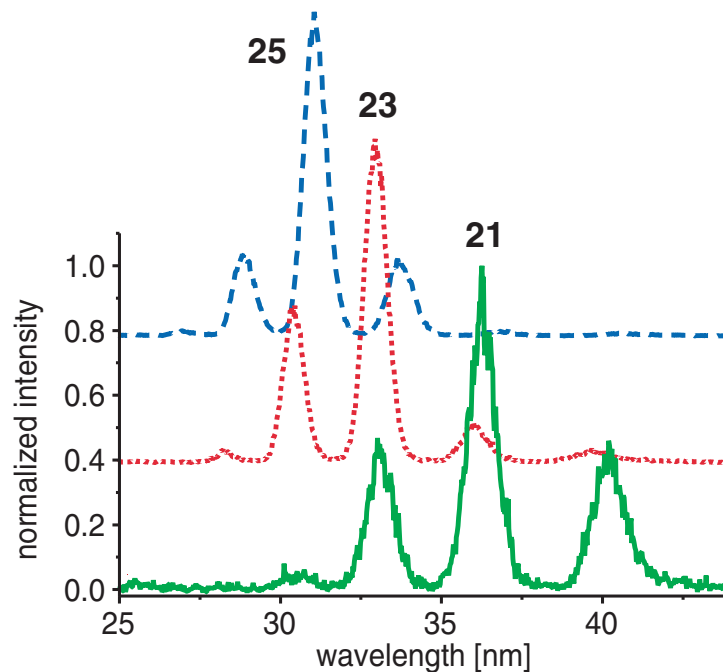
Figure 4.7 – Optimizations of different single harmonic orders in a hollow fiber. Harmonics can be selected with a high contrast ratio with respect to neighboring orders.

new generation are now tested for their performance in order to build the following generation, and the closed-loop optimization iteratively converges towards a maximum fitness value by gradually improving the laser pulse shapes from one generation to the next.

We can now follow our goals defined above and try to selectively generate single harmonics or a range of harmonics. We are able to enhance a particular harmonic order while simultaneously keeping neighboring orders at low intensity (Fig. 4.7). The fitness function in this case was defined as the spectrally integrated yield of the target harmonic divided by the integrated yield of the other harmonic orders. Compared to previous measurements [48, 49] our results show an unprecedented contrast ratio between the selected harmonic and the suppressed neighboring orders. Direct neighbors of the optimized harmonic order are relatively weak while there is a negligible contribution from all others. These tunable quasi-monochromatic high-harmonic spectra allow for time-resolved spectroscopy in the soft-x-ray region.

According to Milošević and Becker [238], the enhancement of particular harmonics is possible by a small variation of the laser-field intensity due to a resonance-like enhancement in the low-energy part of the plateau. This can be related to channel-closing effects. In a strong laser field, the ionization potential I_p is upshifted by the ponderomotive energy U_p, so that $n > (I_p + U_p)/\hbar\omega$ photons are needed for ionization. Channel closing (of the nth channel) occurs when with increasing field intensity and thus increasing U_p an n-photon ionization is no longer possible, and $n + 1$ photons are required. At the exact threshold laser intensity the electron is released into the continuum with zero drift momentum so that it can revisit its parent ion many times during the oscillations of the laser field. These long orbits have very long travel times, and their cut-off converges towards $I_p + 2U_p$. In this energy region the effects of the very long orbits are most pronounced. Resonance enhancement effects have also been reported by Toma et al. [239].
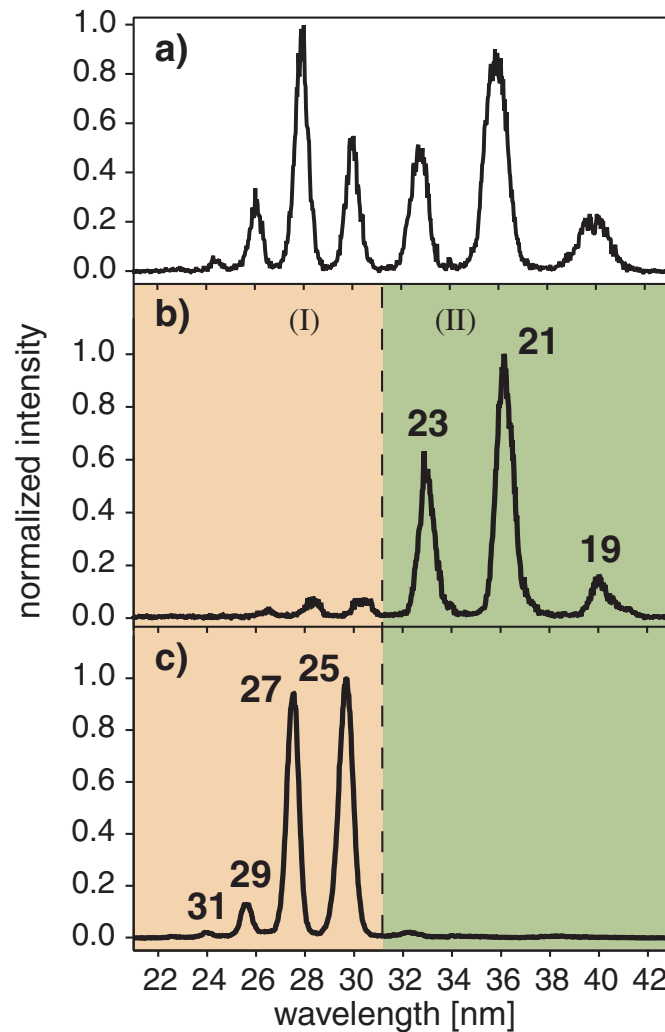
Figure 4.8 – Selection of extended frequency ranges of high-harmonic orders. a) Reference spectrum obtained with an unmodulated laser pulse. b) Optimization of the long-wavelength spectral part while simultaneously reducing the short-wavelength region and vice versa (c).

A comparison between the two experiments on the optimization of high harmonics in a gas jet and in a capillary (Fig. 4.4a and Fig. 4.7) reveals that an enhancement of single harmonics in a free-focusing geometry such as a gas jet is not possible. The results by Reitze et al. [45] confirm this finding. This contradicts the explanation given by Bartels *et al.* [48, 49, 240] which is based on the single-atom response only and does not include propagation effects. Instead, the comparison shows that a spatial contribution arising from the mode distribution in a hollow fiber is essential to the optimization. The results of our investigation of spatial effects in a capillary are summarized in Section 4.3.

We also succeeded at the selection of a certain range of consecutive harmonic orders. Fig. 4.8b shows the optimization of the long-wavelength spectral part while simultaneously reducing the short-wavelength region and vice versa (Fig. 4.8c). Considering the reduced peak intensity in a temporally shaped and thus chirped generating laser pulse, the selective generation of the lower-orders can be readily understood since the cut-off is shifted towards lower energies.
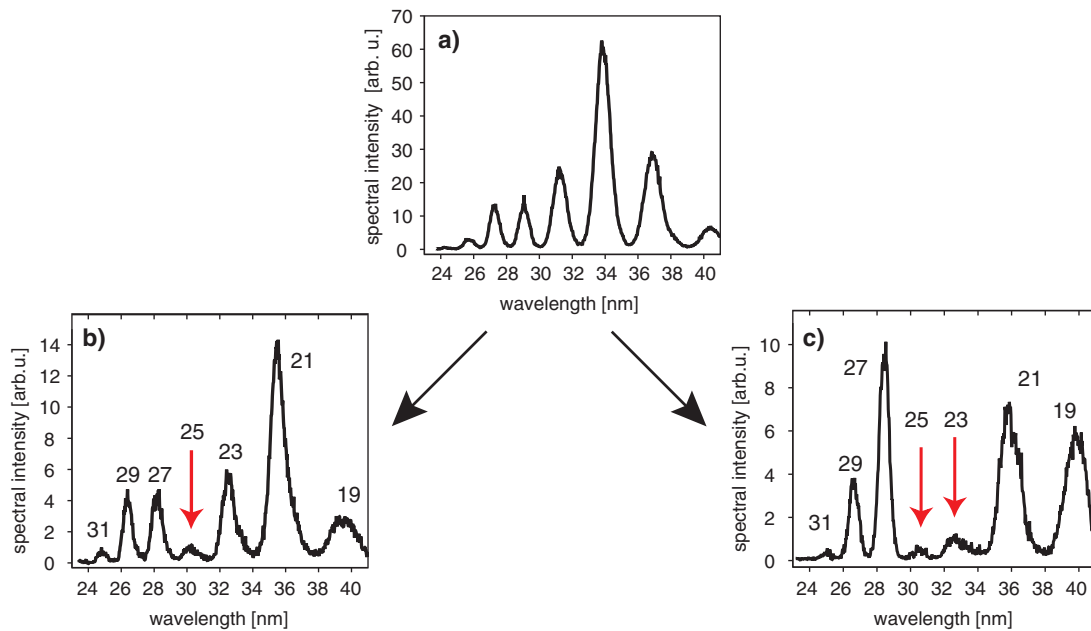
Figure 4.9 – Suppression of harmonics. Starting with a typical harmonic spectrum in the plateau region (a), we can suppress one (b) or two (c) harmonic orders. These modifications of the spectra imply major modulations of the harmonic time structure on an attosecond time scale.

However, it remains unclear what is responsible for the enhancement of higher orders while at the same time the lower orders are suppressed almost completely.

The controlled selection of range of harmonic orders is essential to the optimization of attosecond pulses. According to the work by Mairesse et al. [33], selecting a larger and larger region of harmonics does not necessarily lead to shorter (attosecond) pulses. More harmonics result in more spectral width, but since the harmonics are intrinsically chirped the harmonic pulse duration may effectively increase in spite of the broadened spectrum. The chirp results from the different excursion times of the electrons generating the different harmonic orders. In oder to produce the shortest attosecond pulse possible, the appropriate number of harmonics with suitable relative phases has to be chosen, which can now be done using our pulse shaping technique. This circumvents the problem to find a suitable filter that can select the desired range. Also, the conventional selection with a grating is accompanied with a loss of time resolution due to dispersion and with a substantial reduction in photon number and is thus not desirable. Besides providing a superior way of selecting specific high-harmonic frequencies our approach also allows for shifting the range of harmonics and consequently for tuning the wavelength of the resulting attosecond pulses or attosecond pulse trains.

Another example of our ability to control the generated harmonic spectra is displayed in Fig. 4.9. The upper part shows a typical harmonic spectrum in the plateau region while the lower part demonstrates the suppression of one and two harmonics, respectively. The shape of the unshaped spectrum reveals a maximum due to phase-matching inside the capillary. However, the harmonics are nearly equally intense, implying that the displayed range indeed lies in the plateau region. To our knowledge this is the first demonstration of the suppression of single plateau harmonics. Complete control over the shape of the soft-x-ray spectrum has a
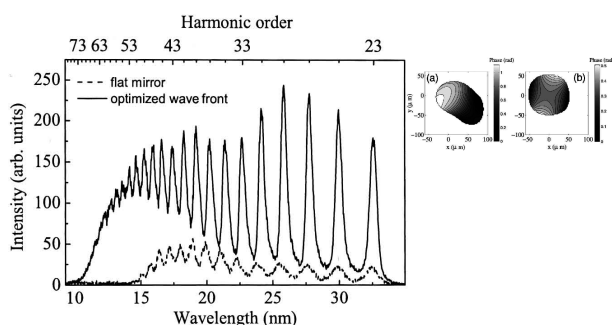
Figure 4.10 – Cut-off extension by spatial wavefront shaping. The phase front of the laser is controlled by a two-dimensional deformable mirror. The profiles before and after the optimization are shown in the inset on the right. The effect of the spatial shaping is the cleaning of higher-order spatial phase distortions (figure taken from Villoresi et al. [47]).

major impact on ultrafast energy-resolved spectroscopy and on the temporal structure of high harmonics. Section 5 discusses some of the implications on the attosecond time structure of the generated radiation. The following Section examines the spatial properties of high-harmonic generation in a hollow fiber and considers propagation effects such as phase-matching.

4.3 Control of high-harmonic generation through spatial engineering

Up to now only the temporal shaping of high-harmonic radiation in a hollow fiber has been considered. However, Figs. 4.4 and 4.7 imply that spatial effects determined by the waveguide geometry have to be taken into account in order to obtain the high level of control over the harmonics as demonstrated above. Control of the spatially coherent nature of the process has largely been ignored, for instance, by emphasizing the perfect phase-matching inside hollow fibers [142, 163].

4.3.1 Free-focusing geometry

Work done on controlling the spatial shape of the generating laser pulses by use of a two-dimensional deformable mirror has been able to enhance only the overall conversion efficiency in a jet geometry by cleaning up higher-order spatial phase distortions [46, 47]. Fig. 4.10 shows the original result by Villoresi et al. [47]. The graph closely resembles our own result in Fig. 4.4, which shows a similar effect. Note, however, that the cut-off extension in our experiments was mainly achieved by cleaning up the temporal profile of the laser pulse while higher-order spatial phase distortions are corrected in the work by Villoresi et al. [47].

Kazamias et al. [241] and Sutherland et al. [242] report marked enhancements in high-harmonic generation in a gas cell filled with noble gases when a partially closed aperture is placed in the path of the laser beam before the focusing lens (truncation). They attribute this effect to the effective f-number, the laser beam spatial quality, and the interplay between the laser phase and the intrinsic phase of the harmonics. Apparently, the aperture introduces phase variations on the laser wave front that minimize the phase mismatch. Here we demonstrate the importance of spatial effects in achieving *full* control over the process of high-harmonic generation.
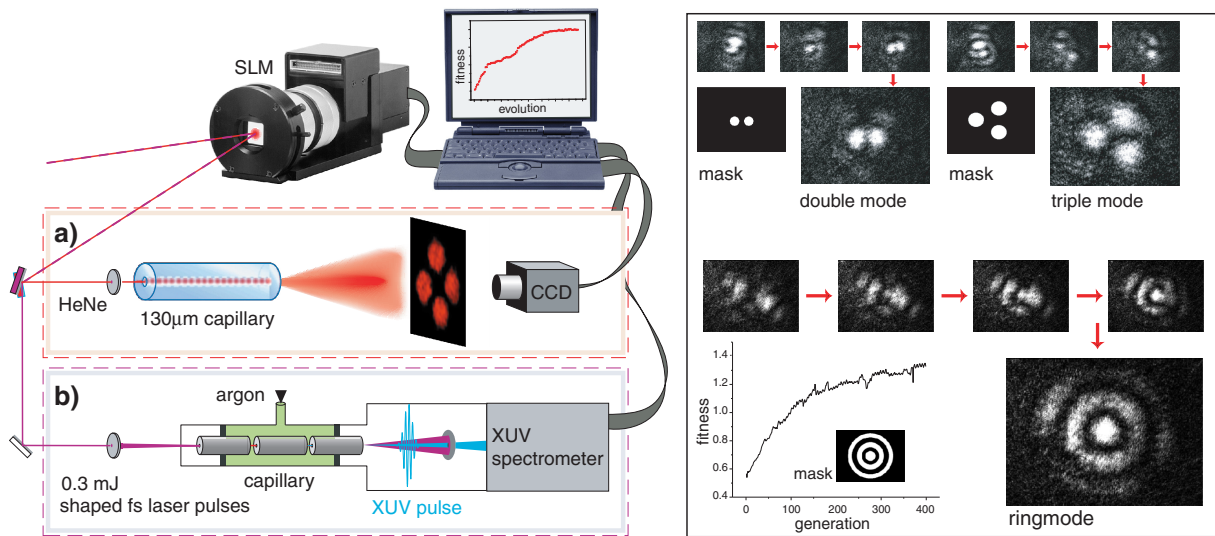
Figure 4.11 – Experimental setup (on the left) for spatial pulse shaping and selective excitation of different fiber modes. a) Setup for the optimization of fiber modes using a helium-neon laser. The pictures on the right show the controlled generation of different fiber modes using an evolutionary algorithm. b) Setup used to optimize high-harmonic generation in a hollow fiber using spatial pulse shaping.

4.3.2 Fiber-mode excitation

As we have seen in Sec. 3.4.4, several fiber modes can contribute to high-harmonic generation in a hollow fiber, opening different phase-matching windows (Fig. 3.14).

Which fiber modes are excited after the driving laser has been coupled into the fiber can be adjusted by modifying the spatial amplitude and phase profile of the driving laser pulse at the entrance of the fiber. However, the systematic selection of specific fiber modes is impossible due to mode-coupling effect. Near the critical power of self-focussing inside the fiber different fiber modes do no longer travel independently as linearly independent modes but start to mix [243, 244]. This effect is responsible for a changing mode distribution as a function of propagation along the fiber. Therefore we need an optimization algorithm that is able to manipulate the spatial properties of the driving laser pulse to fulfill the phase matching condition inside the fiber exactly at the harmonic generation point.

To examine the influence of the excitation of different fiber modes on the process of high-harmonic generation more thoroughly, a two-dimensional spatial pulse shaper for the fundamental laser pulses was set up in order to modify the spatial phase of the laser pulses before they are coupled into the fiber. By shaping the spatial phase of the laser pulse before focusing, we are able to control the amplitude and phase profile of the pulse in its Fourier plane located at the entrance of the capillary.

This pulse shaper is based on a computer-controlled electrically-addressable phase-only spatial light modulator by Hamamatsu Photonics (programmable phase modulator PPM X8267). An adjustable phase between 0 and 2π can be added to the local spatial phase of the laser pulse separately for each pixel [245, 246]. The shaped laser pulses excite different modes in the fiber used for high-harmonic generation. The harmonic spectra are recorded by a CCD camera, an evolutionary algorithm is used to run the closed-loop optimization of certain opti-
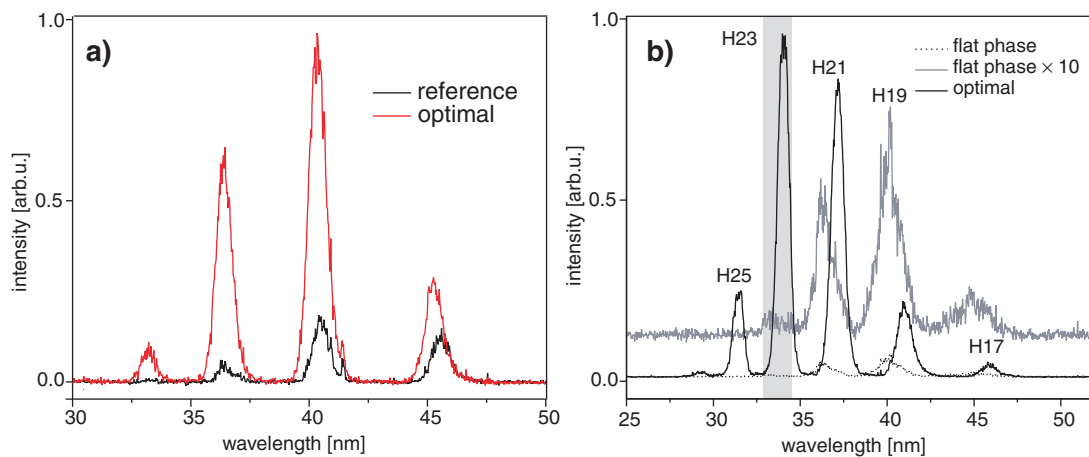
Figure 4.12 – Optimization of high-harmonic emission in a hollow fiber using spatial laser pulse shaping. a) Optimization of the total yield results in an increase by a factor of five. b) Selective enhancement of the 23rd harmonic (gray-shaded area) as optimization goal results in an increase by two orders of magnitude. However, no selectivity is achieved.

mization goals.

In order to test the abilities of this setup to excite arbitrary fiber modes as needed for the spatial optimization of high-harmonic generation we used a helium-neon laser focused into a similar fiber (length 10 cm, inner diameter 140 μm). The fiber output is recorded by a CCD camera to evaluate the excited fiber modes (Fig. 4.11a). The fitness function is defined as the integral overlap between the recorded picture and a predefined bitmap mask representing the desired fiber modes. The first target mask was the fundamental mode (not shown), followed by a double (Fig. 4.11, inset top-left) and a triple mode (Fig. 4.11, inset top-right). The pictures show the bitmap masks together with some snapsnots of the fiber modes during the run of the optimization. The bottom part of Fig. 4.11 (inset) depicts the optimization to a more complex ring mode. In addition to the target mask and the snapshots the evolution of the fitness during the optimization can be seen. It rises in the beginning until it saturates for later generations. We were thus able to selectively excite the fundamental mode, double and triple modes as well as ring modes or random patterns, demonstrating the capability of our setup for the adaptive spatial control of fiber modes and their excitation for high-harmonic generation [246].

4.3.3 Optimizations in a hollow-core fiber

The optimization of the high harmonics based on selective fiber mode excitation should now be possible, using the setup shown in Fig. 4.11b. Our first approach is to enhance the total harmonic yield beyond the value that can be achieved by manually optimizing the coupling of the laser into the fiber. After the adaptive optimization, the total yield increases by approximately a factor of five (Fig. 4.12a). We also tried to selectively enhance a single harmonic order as was done in the case of temporal pulse shaping (Section 4.2). The result is shown in Fig. 4.12b where the shaded area marks the wavelength range over which the yield of the selected harmonic is integrated, squared, and divided by the integrated yield of the neighboring orders to define the fitness function (gas pressure in the capillary: 170 mbars). As can be seen, the yield in the selected cut-off harmonic increases by more than two orders of magnitude.
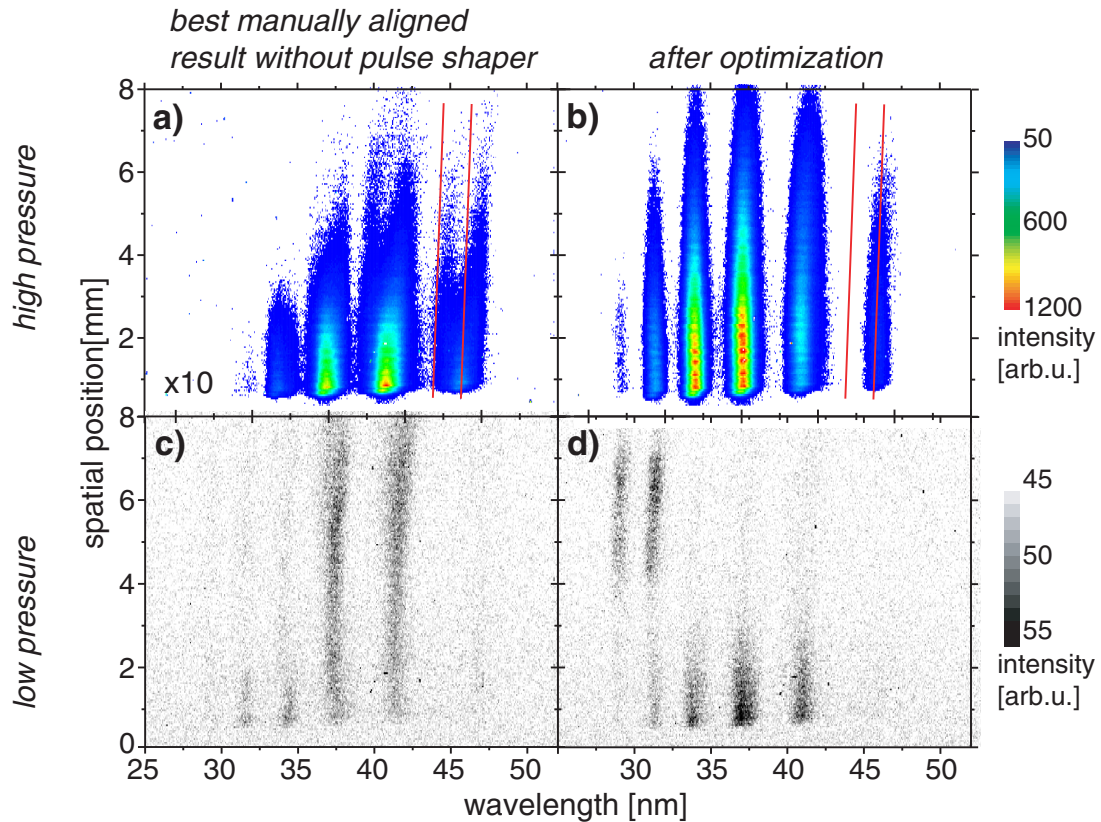
Figure 4.13 – Spatially resolved HHG spectra: a) and b) high pressure, c) and d) low pressure. Two fiber modes contribute to the signal in a) before the optimization while the optimized pulse (b) results in an overall increase in intensity of about ten. The excitation of a single mode is clearly visible. At low pressures the change in excited fiber modes from c) before the optimization to d) after the optimization becomes more evident.

Obviously spatial optimization of high-harmonic radiation is possible. However, the contrast ratio between the selected single harmonic and the neighboring orders is not nearly as high as in the case of temporal phase shaping (Fig. 4.7). This implies the necessity to use temporal *and* spatial pulse shaping in order to selectively enhance single harmonics.

The calculation of the expected harmonic mode profiles based on the initial spatial phase of the laser pulse is very difficult. Due to the high intensities that are present in the fiber, ionization of the conversion medium occurs and leads to significant distortions of the propagating laser pulse inside the fiber. The initially excited fiber mode distribution changes constantly due to this nonlinear mode coupling [247]. It is therefore important to excite a single fiber mode at the point inside the capillary where the harmonics are predominantly generated (center piece in our setup). Not only is it very difficult to calculate the initial spatial intensity and phase profile needed, but it is almost impossible to reproduce exactly the calculated profile experimentally. This again explains why a closed-loop optimization based on an evolutionary algorithm is of great value.

The excitation of different fiber modes can be made visible by spatially resolving the harmonic beam along the spectrometer slit (Figs. 4.13a and 4.13b). Before optimization (Fig. 4.13a), each harmonic is split up into two contributions at two distinct center wavelengths. The

two contributions originate from two fiber modes. Since the transverse intensity distribution within the fiber and thus the degree of ionization varies for different fiber modes, this results in different amounts of blueshift. After the optimization (Fig. 4.13b) with the goal to enhance the 23rd harmonic order the bimodal structure inherent to Fig. 4.13a disappears, leaving a clear single-mode harmonic spectrum.

The enhancement of the selected harmonic order could be due to better phase-matching based on the selection of suitable fiber mode that can fulfill Eq. (3.85). An increased intensity inside the fiber due to an improvement of the coupling into the fiber as a reason for the observed enhancement can be ruled out. In this case, the amount of blueshift should have increased whereas in our measurement there is less blueshift after the optimization. Furthermore, if the single-atom response was responsible for the enhancement, an increased intensity would have led to the production of higher harmonic orders, which is not the case. By decreasing the pressure in the fiber from 170 mbars to 20 mbars we are no longer in the phase-matching regime, thereby switching off the effective mode filter caused by phase matching. Nonlinear mode-coupling effects also become negligible with the consequence that spatial changes in the generating pulse directly carry over to the harmonic beam. Figs. 4.13c and 4.13d show substantial differences in the beam shape between neighboring harmonic orders for the unoptimized as well as for the optimized case. This clearly indicates the contribution from different fiber modes during the generation of high harmonics.

Future work on the control of high-harmonic generation and on the mechanisms of controllability will include a combination of temporal and spatial pulse shaping to investigate the physical background in more detail. To this end, the two-dimensional LCD-based pulse shaper can be modified for simultaneous spatial and temporal shaping by spatially dispersing frequency components along the horizontal direction and spatial (or wavevector) components in the vertical direction [248]. However, this only allows for a one-dimensional control of the wavefront of the laser beam. Two-dimensional wavefront shaping together with temporal shaping can be achieved either by combining two separate pulse shapers, a two-dimensional spatial and a one-dimensional temporal pulse shaper, or by dividing the area of our two-dimensional liquid-crystal display into two regions where the laser pulses are shaped consecutively first temporally (with a spectrally dispersed beam) and then spatially (with the direct laser beam) [249].

4.3.4 Optimizing the geometry: Quasi-phase-matched generation

Using a modulated hollow-core waveguide [250] instead of a hollow capillary with flat walls in order to periodically vary the intensity of the laser light driving the conversion, high harmonics can be generated at significantly higher photon energies, even in the presence of substantial ionization. Higher levels of ionization, caused by the higher intensity of the driving laser to extend the cut-off, normally cause the phase velocity of the pump beam to be too fast to be phase matched.

Fig. 4.14 shows a schematical and a microscopical view of two different modulated fibers used in the experiments performed in the group of Kapteyn and Murnane [182, 250]. In these works, the walls of the waveguide are sinusoidally modulated, alternatingly creating regions with high intensity (leading to HHG) and low intensity (no HHG due to the highly nonlinear dependence on intensity), which realizes the 'generate'–'wait' quasi-phase-matching scheme depicted in Fig. 3.5.

Figure 4.14 – Quasi-phase matching in a modulated waveguide (figures taken from Paul et al. [250] and Gibson et al. [182]). The intensity of the driving laser light is varied periodically, allowing for efficient EUV light generation even in the presence of substantial ionization due to the quasi-phase-matched configuration.
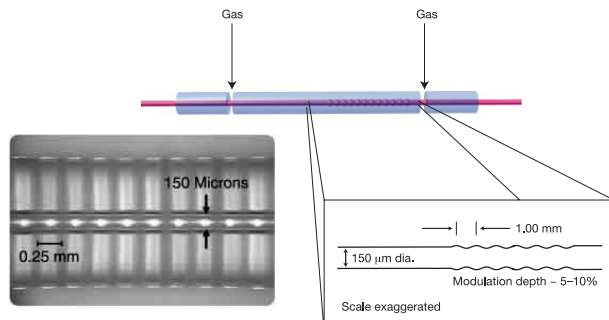
Quasi-phase matching (QPM), originally proposed by Armstrong et al. [93], introduces an additional term $K = 2\pi/\Lambda$ into the phase-matching expression Eq. (3.85), where Λ is the modulation period. A periodicity corresponding to twice the coherence length corrects the phase mismatch and allows for more efficient nonlinear frequency conversion. In the modulated waveguide the intensity of the laser is reduced in regions where the harmonic light is out of phase by $180°$ with the driving laser (after one coherence length) by expanding the diameter of the waveguide so that no new harmonics are generated. This pattern is repeated periodically for a full quasi-phase-matching scheme. Decreasing the modulation period of the walls of the waveguide [182], coherent light can even be generated in the water window using gas-filled hollow fibers.

Since these modulations must be introduced into the waveguide by sophisticated glassblowing techniques, we present the proposal for a new quasi-phase-matching scheme for the generation of high harmonics in an unmodulated waveguide in Sec. 4.4. This scheme works in the temporal domain and is therefore called *temporal quasi-phase matching* (TQPM).

A different method to achieve a periodically varying generation efficiency for nonlinear frequency upconversion can be realized by density modulations of the medium to modulate the nonlinear susceptibility [251].

4.3.5   Optimizing the medium

Since harmonic generation is a coherent process, the resulting harmonic electric field scales linearly with the particles density of the interacting medium, leading to a quadratic dependence of the intensity. However, for the cut-off harmonics, a maximum density is given by the ionization-induced defocusing of the laser pulse [252]. Instead of using gas targets, we made the transition from gaseous to liquid targets and investigated water micro-droplets as a source of high-harmonic radiation [253].

We studied the emission of XUV radiation from water microdroplets under excitation with either a single or a pair of intense femtosecond laser pulses (Ti:Sa, $80\,\mathrm{fs}$, $\sim 10^{14}\,\mathrm{W/cm^2}$, $800\,\mathrm{nm}$, $1\,\mathrm{kHz}$). Varying the delay between the two pulses we observed a transition from pure incoherent plasma emission to coherent high-harmonic generation. Under optimized conditions we obtained high-harmonic radiation up to the 27th order. For a more detailed description of the experimental results please refer to Appendix A.

High-harmonic generation in a dense medium such as water microdroplet also was the subject of a theoretical study by Strelkov et al. [254]. The three-dimensional Schrödinger equation was solved for a single-electron atom in the combined fields of the neighboring particles and the laser and the results were averaged using a Monte-Carlo method. Since the long and the

short trajectory are affected differently by the random variation of the harmonic phase in the presence of the medium, sharper harmonic lines and shorter attosecond pulses can appear due to the suppression of the long path. At very high densities, harmonic lines are compressed completely. Also, electrons can possibly be captured by neighboring ions. However, due to the random distribution of the particles in the medium no coherent emission occurs for these electrons. Hence there is no extension of the single-atom cut-off.

A different approach to overcome low particle densities is to increase the interaction length. This can be done by focusing the intense laser pulses into a gas-filled hollow capillary [162, 255] instead of a short gas jet. In combination with the negative dispersion of the hollow fiber the variation of the gas pressure inside the fiber provides an additional control parameter to compensate the phase mismatch between the fundamental wave and the generated harmonic. This results in a notable increase of the conversion efficiency [142, 163, 250]. The use of hollow fibers has already been discussed in the previous Sections of this work.

Proper phase-matching can also be ensured in a gas cell [256, 257] where the laser is loosely focused, provided the correct placement of the focus with respect to the entrance of the gas cell. Kazamias et al. [258, 259] used the analysis of the coherence length for constructive harmonic build-up based on Maker fringes [101] to optimize the conversion efficiency.

In addition to controlling the electric field that drives high-harmonic generation, the nonlinear medium itself can be engineered. Apart from atomic gases, high harmonics can be generated in simple [260] and complex molecules [261], clusters [262], or solid surfaces [263] (although the generation mechanism is different for the latter).

If a molecule is stretched out well beyond its equilibrium distance by preparing a highly excited vibrational state, harmonic peaks of much higher energies in units of the ponderomotive energy than those predicted for a single atom or ground-state molecule can be detected [264]. According to this numerical simulation, the large internuclear separation allows the electron to be detached from one of the cores, but recombine with the partner core. A similar behavior with kinetic energies reaching $8U_p$ has been found by Lein [265]. By using a two-color excitation in extended molecular systems, harmonics at energies of $6U_p$ to $10U_p$ can be generated [266]. A high-frequency prepulse ensures sufficient ionized electrons, while a second lower-frequency pulse accelerates them towards the other atom in the stretched molecule. Also, controlling the ground state wave function of the electron in a stretched molecule can increase the efficiency of high-harmonic generation [267]. Since the electronic wave function is more delocalized for a stretched molecule as compared to a ground-state molecule, it experiences less spreading during continuum propagation, increasing the probability of recombination of the returning electron with the parent ion.

4.4 Temporal quasi-phase matching

Based on the spatial quasi-phase matching in a modulated waveguide by the group of Kapteyn and Murnane as reported in Sec. 4.3.4, we propose a completely new quasi-phase-matching scheme for the generation of high harmonics in an unmodulated waveguide with uniform gas density. It relies neither on a modulated waveguide, which is hard to fabricate, nor on density modulations of the generating gas. Since the new scheme works in the time domain, it is called *temporal quasi-phase matching* (TQPM).

The basic idea is to transfer the spatial modulations of the waveguide into the time domain,
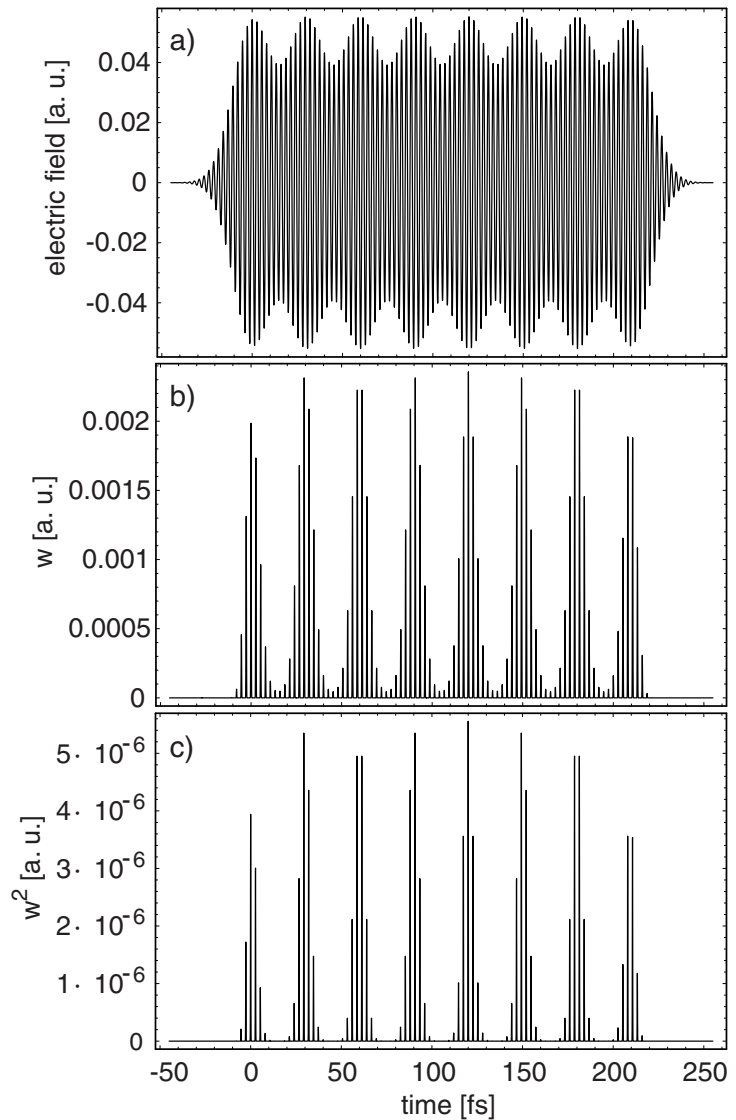
Figure 4.15 – Temporally modulated laser pulse and the corresponding ADK ionization rate and harmonic yield. The distance between the peaks (peak FWHM 15 fs) of the modulated laser pulse (a) is 30 fs. The corresponding ionization rate w (b) is based on the ADK model (see text). A peak intensity of $10^{14}\,\mathrm{W/cm^2}$ was used for the calculation. Since the harmonic production rate is proportional to the square of the ionization rate w^2 (shown in c), harmonics are only generated at the points determined by the modulation period of the fundamental laser pulse. This enables 'generate' and 'wait' regions for the temporal quasi-phase matching (TQPM) scheme. Although the modulation depth of the driving laser pulse is weak, the harmonic production rate in the wait regions in completely suppressed.

resulting in a periodically modulated envelope of an ultrashort laser pulse. Fig. 4.15a presents the realization of such a temporally modulated laser pulse (possibly created by pulse shaping), which bears marked similarities to the spatially modulated waveguide in Fig. 4.14. A weak modulation of the pulse envelope as present in Fig. 4.15a is sufficient to realize the 'generate'–'wait' quasi-phase matching scheme, which was introduced in Fig. 3.5. To understand this statement, we have to take a look at Fig. 4.15b which shows the ADK ionization rate w calculated using Eq. (3.59) for xenon as the gas medium and a laser peak intensity of $10^{14}\,\mathrm{W/cm^2}$. Due to the highly nonlinear dependence of the ionization rate w on the current value of the electric field, the modulation depth of the driving laser pulse is greatly enhanced for the ionization rate. This effect is even more pronounced in the square of the ionization rate w^2 (shown in Fig. 4.15c), which is a measure for the high-harmonic production rate since harmonic generation is a coherent process.

The pulse is virtually split into a kind of pulse train with a number of little pulselets with a certain spacing. The key mechanism is the difference in the phase and group velocities of these pulses due to dispersion. This difference causes a walk-off between the peak of the little

pulselets and the underlying phase. The peak structure given by the envelope then gradually slides over the phase of the electric field, creating regions with high and low intensity, respectively, alternating in time. The little pulses in this pulse train generate high harmonics. During propagation, when the harmonic and the fundamental phase fall out of phase, the group moves away from the original point of the phase. After a coherence length, when normally newly generated harmonics would interfere destructively with the previously generated harmonics, there is no intensity to produce new harmonics since the peak has moved away and the ionization rate is practically zero. Consequently, no destructive interference occurs, and harmonic generation is suspended, which corresponds to the "wait" region in Fig. 3.5. After another coherence length, by the time the harmonic phase and fundamental phase show no phase slip, the next group has moved into place and generates new harmonics, in phase with the already existing harmonics. Those two fields can now interfere constructively, adding positively to the harmonic intensity.

In order to deal with this problem more quantitatively, we considered the difference between phase and group velocity, v_{ph} and v_{gr}, of the fundamental laser at the frequency ω. With $k(\omega) = n(\omega) \cdot \omega / c$ we can write (cf. Sec. 2.5)

$$v_{\text{ph}} = \frac{\omega}{k} = \frac{c}{n(\omega)}, \tag{4.4}$$

$$v_{\text{gr}} = \frac{d\omega}{dk} = \left(\frac{dk}{d\omega} \right)^{-1} = \frac{c}{n_{\text{gr}}(\omega)}, \tag{4.5}$$

$$n_{\text{gr}}(\omega) = n(\omega) + \omega \frac{dn}{d\omega} = n + \omega n', \tag{4.6}$$

where n_{gr} is the group refractive index. The derivative of the (phase) refractive index n with respect to frequency (ω), causing dispersion, is responsible for the difference between group and phase velocity, which causes the walk-off between the peaks of the little pulselets and the underlying phase. Dispersion was also exploited to shift the carrier-envelope phase of few-cycle laser pulses by inserting variable amounts of fused silica into the beam [80].

A first approach yielded a solution for the derivative of the refractive index $n'(\omega)$ that was directly proportional to the phase mismatch Δk. This is a reasonable result since a higher phase mismatch (accompanied with a shorter coherence length) requires a stronger delay of the group with respect to the phase. In the phase-matched situation, $\Delta k = 0$, of course no difference between phase and group is needed. Refractive index data for the calculation of Δk can be found in Korff and Breit [268] and CXRO at Lawrence Berkeley National Laboratory [269]. In our case, we would need group velocities on the order of 97 % of the speed of light in vacuum.

Unfortunately, this first approach turned out to be wrong. A second approach is visualized in Fig. 4.16. The red pulse train depicts the modulated infrared pulse, or more specifically, the sharply modulated resultant ADK ionization rate (cf. Fig. 4.15c). Let us consider harmonic generation by the first pulselet at time $t_0 = 0$ and at position $z = 0$ (along the propagation direction z). Both the harmonic pulse and the infrared pulses propagate until they fall out of phase by π after the coherence length at $z = L_c$ at the time $t_1 = L_c / v_{\text{HHG}}$, where v_{HHG} is the group velocity of the high-harmonic pulse (which is practically identical to its phase velocity). New harmonic generation must be quelled at this point to avoid destructive interference. This can be achieved if the infrared pulselet in the modulated pulse has only traveled half the
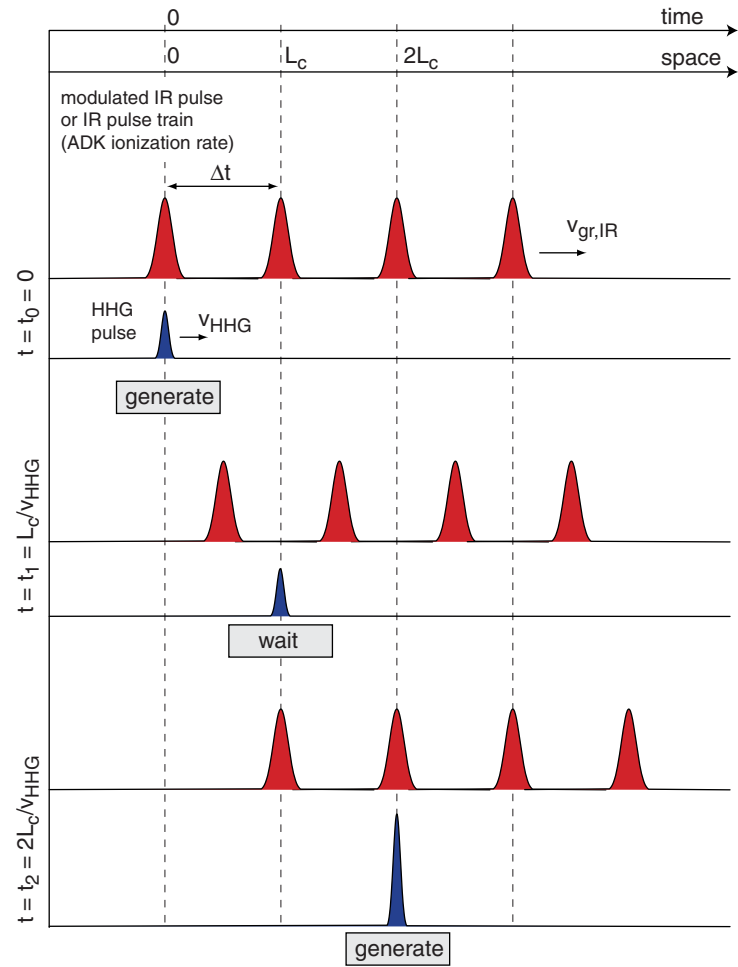
Figure 4.16 – Visualization of temporal quasi-phase matching. At time t_0 harmonic are generated at the position $z = 0$. Due to the difference in group velocities, harmonic generation is quelled at time t_1 at the position $z = L_c$ where new harmonics would interference destructively. At $z = 2L_c$ and $t = t_2$ harmonic generation is resumed by the second pulselet for coherent adding of the new harmonics to the old harmonics generated by the first pulselet. For a more detailed description see text.

distance, which requires

$$v_{\mathrm{gr,IR}} = \frac{v_{\mathrm{HHG}}}{2},\tag{4.7}$$

where $v_{\mathrm{gr,IR}}$ is the group velocity of the modulated infrared pulse. At the position $z = 2L_c$ harmonic pulse and infrared pulse are in phase again, allowing constructive interference for the new harmonics. If the modulation of the infrared pulse has a period of $\Delta t = L_c/v_{\mathrm{HHG}}$ harmonics are now generated constructively by the second pulselet at the position of the harmonics from the first pulselet. This mechanism is repeated until the end of modulated infrared pulse is reached.

As can be seen from Fig. 4.16, the period Δt can be chosen differently provided that the ionization rate is zero at the time t_1. Therefore an even number of additional pulses can be placed between the pulses already present in Fig. 4.16, which divides the period by $3, 5, \ldots$, which corresponds to higher-order phase matching (see Sec. 3.2.3).

However, the condition Eq. (4.7) cannot be fulfilled in common media, especially in gas media, where the group velocity of the infrared pulse almost equals the phase velocity due to the extremely small value of n'. In our case, the quantity $\omega n'$ in Eq. (4.6) must be equal to unity to satisfy Eq. (4.7).

To solve this discrepancy between the real n' and the required one we propose to exploit the technique of electromagnetically induced transparency (EIT, Harris et al. [270], Lukin [271])

in order to tailor the group index as needed. In EIT, we consider a so-called lambda system where the signal field couples the ground state and some excited state, whereas a control field is in resonance with some other state than the ground state and the same excited state as the signal field. Since both the signal and the control field couple to the excited state, there can be destructive interference between these two possible excitation pathways. As a consequence, the atoms are decoupled from the light field in ideal EIT: At resonance, the susceptibility vanishes and the refractive index becomes unity. The medium becomes transparent to the signal field, which would be absorbed at the resonance without the control field. Since this resonant absorption is accompanied by a steep variation of the refractive index with frequency, we still have a large n', even in the presence of the control field. The large group index (Eq. (4.6)) caused by the large value of n' is now responsible for a greatly reduced group velocity. Group velocities as slow as 17 m/s have been obtained in an ultracold atomic gas [272], demonstrating the power of EIT. Very low group velocities on the order of 90 m/s have also been reported in hot gases [273]. McCullough et al. [274] described coherent control of the real and imaginary parts of the refractive index both off resonance and near resonance. This might be another possibility to modify the group index in our system as desired.

In conclusion, by transferring the spatial modulation into the time domain, we describe theoretically the novel scheme of temporal quasi-phase matching for high-harmonic generation in an unmodulated waveguide through the use of a temporally periodically modulated laser pulse. This scheme allows for the use of higher laser intensities to extend the photon energy range of high-harmonic generation in a hollow fiber and for the use of higher densities of the generating medium beyond the pressure phase-matched range to increase the conversion efficiency of high-harmonic generation.

4.5   Applications of tailored harmonic radiation

Tailored harmonic spectra are of immediate interest and importance for the field of stationary or time-resolved spectroscopy in the XUV and soft-x-ray regions of the light spectrum [275]. A number of applications have already demonstrated the use of this laboratory-scale light source for probing matter properties both in the spectral and in the temporal domain, in an energy range and with a time resolution previously inaccessible. These applications include: EUV scanning microscopy and submicron XUV imaging at 13 nm [276, 277], high-harmonic wave packet interferometry [278], time-resolved photoemission spectroscopy of surface chemistry [279–282], ultrafast pump-probe studies on molecules in the gas phase [35], time-resolved measurements on the Auger decay and inner-shell lifetimes in gases [36, 38] and solids [283]. Also, during the recombination process of the three-step model of high-harmonic generation, quantum interference can take place in molecules [284, 285]. Kanai et al. [286] observed such characteristic modulation patterns of the harmonic signals measured as a function of the pump–probe delay.

The possibility to shape high harmonics greatly extends the field of applications and broadens the level of information retrieved from such measurements. For instance, a recent study [287] on absorptions edges of transitions metals using high-harmonic and syncrotron radiation in comparison revealed the competitiveness of this new light source with existing large-scale facilities. However, the authors stress the sampling of the measured spectra at the harmonic spacing of twice the fundamental frequency. Tuning and shaping of high-harmonic spectra can now close this last remaining gap.

Using tailored high-harmonic spectra, we have already been able to control the branching ratio of the photodissociaton reaction of sulfur hexafluoride (SF_6, Pfeifer [288], Pfeifer et al. [289]). An evolutionary algorithm is used to maximize and minimize the SF_5^+/SF_3^+ product ratio. The stability of our light source of shaped high harmonics is high enough to allow the algorithm to reach the optimization goal. Although the branching ratio can only be slightly changed, this experiment is a first demonstration of the applicability of high-harmonic spectral engineering to soft-x-ray optimal control.

Prospective applications of tailored high harmonics include, but are not limited to, time-resolved photoelectron spectroscopy in the solid phase, e. g. for the examination of surfaces and interfaces. One of the open question is, for instance, the mechanism of laser-induced damage in SiO_2 whether it occurs due to multi-photon ionization or avalance ionization. In such a typical pump–probe experiment a strong pulse pump is used to induce dynamics in the sample, which can then be investigated with a probe pulse. If an infrared probe pulse is employed, the high number of low-energy photoelectrons generated by the strong pump pulse easily obscures the real photoelectrons by the probe pulse. Due to the higher photon energies of high-harmonic radiation, these electrons can now be easily discriminated based on the kinetic energies. Moreover, while an infrared or visible can ionized valence electrons, high-harmonic photoelectron are element-specific through their excitation from deep-lying core levels. This is especially useful for the examination of interfaces to distinguish between photoeletrons from different constituents. Other possibilities include time-resolved measurements of the extended x-ray absorption fine structure (EXAFS) of Si [290].

The modifications of the high-harmonic spectrum have direct implications for the time structure of the harmonic radiation, including the possibility for temporal pulse shaping on an attosecond time scale. These issues will be discussed and elaborated in the following Chapter.

Chapter 5

High-harmonic time structure

Contents

5.1 Temporal characterization methods

5.1.1 Characterization of optical laser pulses

To evaluate experimental data, it is important to know the input parameters. In the case of (time-resolved) laser spectroscopy, this of course includes the complete characterization of the ultrashort laser pulses used for the experiment. As seen in Sec. 2.4, the knowledge of both the spectral amplitude *and* the phase is needed for a full reconstruction of the laser pulse in the time domain by Fourier transformation. Whereas a spectrum can be easily measured with a spectrometer, the phase is not accessible using conventional methods. In order to determine the temporal evolution of an ultrashort laser pulse, an event is needed that is equally short or even shorter. Electronic circuits as implemented in streak-camera setups have a lower limit of picoseconds, precluding their application in femtosecond measurement. Very recently, an optical streak camera incorporating high-harmonic-based attosecond pulses has been demonstrated [291] which indeed allows for the direct measurement of the oscillations of the electric field of the laser. However, this setup is very complex and not convenient to
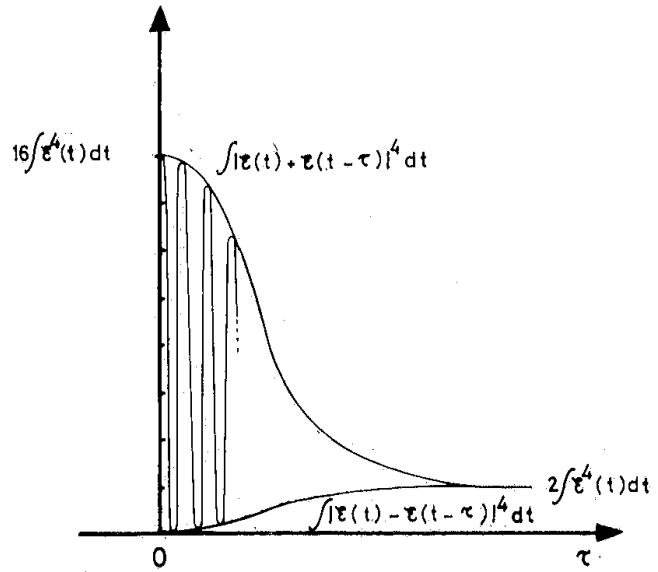
Figure 5.1 – Interferometric autocorrelation trace (figure taken from Diels et al. [292]). The peak-to-background ratio is 8 to 1 where the peak height is given by the coherent superposition of the two pulse replicas and the limit for long delays is simply the incoherent sum of the two fields.

use and has only been shown recently. Therefore in the past other methods were employed where the laser pulses themselves were used to retrieve the pulse duration or the phase of the laser pulse, and they will of course still be used in the future. In the following we will present the basic principles of the most common techniques because they also form the basis for the temporal characterization of high-order harmonics and high-harmonic-based attosecond pulses and pulse trains.

5.1.1.1 Autocorrelation

As stated above, usually an ultrashort laser pulse is the shortest available event for the characterization of ultrashort laser pulses. This laser pulse can either be the same as the one to be characterized; in this case the method is called *self-referencing* (it requires no other optical pulse except itself). Or the second pulse can be a different pulse, which is then described as a *cross-correlation*.

The simplest way is to take a replica of the pulse and to use it as a gate which is scanned temporally as a function of the delay τ across the pulse to be characterized. A signal is then recorded depending on the temporal overlap between the two replicas, allowing to obtain some information about the temporal properties of the unknown pulse.

Mathematically let us consider the superposition of two time-delayed copies of the laser pulse $E(t) = \mathcal{E}(t) \exp[i(\omega t) + \phi]$ where $\mathcal{E}(t)$ is its envelope (amplitude), ω is its center frequency, and ϕ is its phase. The resulting total electric field is then

$$E_{\text{tot}}(t, \tau) = E(t) + E(t - \tau), \tag{5.1}$$

where τ is the variable delay. If we measure the intensity of this signal with a time-integrating detector (virtually any detector is time integrating on the femtosecond time scale), we will obtain the typical trace of a Michelson interferometer (first-order autocorrelation), displaying fringes over a range of τ determined by the width of the spectrum of the laser pulses. However, this trace does not contain any information in addition to the spectrum.

In order to obtain a real gate as a function of τ, the total electric field measured must contain a product of $E(t)$ and $E(t - \tau)$ so that a signal is only detected when the gate pulse opens a window. By comparison with Eq. (3.1) we see that the easiest way to achieve this is a second-order nonlinear mixing process (higher-order processes can, of course, be used as well). In this case the second-order total electric field can be written as

$$E_{\text{tot}}^{(2)}(t, \tau) \propto [E(t) + E(t - \tau)]^2 = E(t)^2 + E(t - \tau)^2 + 2E(t)E(t - \tau). \tag{5.2}$$

The intensity recorded by the time-integrating detector is proportional to the temporal integral over the square of the electric field and is a function of the delay τ [292]:

$$I(\tau) \propto \int_{-\infty}^{+\infty} dt \, |E_{\text{tot}}^{(2)}(t, \tau)|^2 = \int_{-\infty}^{+\infty} dt \, \left| \left[\mathcal{E}(t)e^{i(\omega t + \phi)} + \mathcal{E}(t - \tau)e^{i[\omega(t-\tau)+\phi(t-\tau)]} \right]^2 \right|^2, \tag{5.3}$$

where $E(t) = \mathcal{E}(t)e^{i(\omega t + \phi)}$. This trace is called *interferometric autocorrelation*. A sketch from one of the original publications [292] is displayed in Fig. 5.1. At zero delay the signal, being a coherent superposition of the field $E(t)$ from each of the two replicas, is

$$I(\tau = 0) \propto \int dt \, [\mathcal{E}(t) + \mathcal{E}(t)]^4 = 2^4 \int dt \, \mathcal{E}(t)^4 \tag{5.4}$$

whereas for a long delay when the pulses are no longer overlapped temporally we have

$$I(\tau \to \infty) \propto \int dt \, \left[\mathcal{E}(t)^4 + \mathcal{E}(t)^4 \right] = 2 \int dt \, \mathcal{E}(t)^4. \tag{5.5}$$

The interferometric autocorrelation function therefore has a peak-to-background ratio of 8 to 1.

Starting again at zero time delay, we see that for a delay increment of one-half light period the two electric fields add with opposite phase resulting in a near-zero signal (Fig. 5.1). Therefore counting the fringes at half-maximum and multiplying by the light period quickly yields the duration of the pulse provided that there is no chirp.

[292] also describes the retrieval of information about the pulse chirp if some assumptions are made because various types of chirps have characteristic signatures. For a chirp caused by self-phase modulation (Sec. 3.3) the upper and lower envelopes are narrowed because the frequency chirp induced by SPM is largest in the center of the pulse where the intensity is highest. However, since the pulse tail and front remain coherent with each other, the fringe pattern of the interferometric autocorrelation will extend to delays as large as those for an unchirped pulse of the same duration. Therefore this narrowing can be used as a sensitive indicator of phase modulation in cases where the spectral broadening is small.

If the pulse possesses a linear chirp, the maxima of the lower envelope recede toward zero delay along a curve close to the collinear intensity autocorrelation as the chirp parameter is increased. The extraction of information about the chirp of the laser pulse requires knowledge about the type of chirp. In general, we do not have such knowledge but want to characterize completely unknown pulses. In principle, successive optical correlations of increasing order $(2, 3 \ldots n)$ would provide the answer [292]. However, low pulse energies and bandwidth requirements make it impractical to use higher-order processes.

Full phase information can be retrieved by extending the autocorrelation technique by additionally resolving the signal $I(\tau)$ spectrally which leads us to the FROG technique [293, 294]. Other methods such as spectral interferometry or SPIDER will also be described in the following Sections.

The experimental realization of an autocorrelation measurement consists of a beamsplitter
which splits the pulse to be characterized into two replicas. They are then recombined after
having passed through an adjustable optical delay to introduce the time delay τ. This can
be realized in a Michelson interferometer setup. The recombined beam then impinges onto a
second-order nonlinear crystal (such as BBO or KDP) which provides the nonlinear process
required for Eq. (5.2). The average power of the second harmonic is recorded with a time-
integrating detector as a function of the variable delay. If the measurement is performed with
interferometric accuracy, we obtain the interferometric autocorrelation trace. If the interference
fringes in the recombined beam are smeared out by averaging over the fringes or by sweeping
the delay τ sufficiently fast, it can be shown [292] that the recorded signal is proportional to

$$I(\tau) = 1 + \frac{2 \int dt\, I(t) I(t - \tau)}{\int dt\, I(t)^2}, \tag{5.6}$$

where I is the intensity of the light pulse. The fringes have disappeared, and the trace is
called *intensity autocorrelation*. The peak-to-background ratio of this function is 3 to 1 as can
be readily seen from Eq. (5.6). In order to get rid of this background, a modified experimental
setup is possible. Since the background arises from the second-harmonic signal of the two
pulses with themselves (first two terms on the right-hand side of Eq. (5.2)), we can recombine
the two pulses non-collinearly on the second-order crystal after the delay stage (Fig. 5.2).
In this case, due to phase-matching (Sec. 3.2), the second-harmonic signal of either of the
two pulses is generated into the propagation direction of the individual pulses. The sum-
frequency signal (last term on the right-hand side of Eq. (5.2)) goes into the direction of the
sum of the two wave vectors and is therefore emitted into the direction of the bisector between
the two incident waves. Proper spatial filtering selects only this contribution and allows for
the so-called *background-free intensity autocorrelation* given by

$$I_{\text{background−free autocorr}}(\tau) \propto \int dt\, I(t) I(t - \tau). \tag{5.7}$$

The intensity autocorrelation trace does not carry any phase information and therefore cannot
be used to determine the chirp of a laser pulse reliably. However, under the assumption of a
certain shape of the pulse envelope, a relatively accurate estimate of the pulse duration can
be made. For a gaussian-shaped and a sech^2-shaped laser pulse, the deconvolution factors
τ_{AC}/τ_p are given by

$$\left[\frac{\tau_{\text{AC}}}{\tau_p}\right]_{\text{gauss}} = \sqrt{2} = 1.414, \qquad \left[\frac{\tau_{\text{AC}}}{\tau_p}\right]_{\text{sech}^2} = 1.543, \tag{5.8}$$

where τ_{AC} is the FWHM of the intensity autocorrelation trace, and τ_p is the FWHM of the
corresponding laser pulse [295]. Since the values for the different pulse shapes are close to
each other, the exact knowledge of the pulse envelope is not required for an estimate.

In our laboratory we use a commercial autocorrelator (APE GmbH, Berlin) to control the pulse duration of the compressed self-phase-modulated laser pulses after the hollow fiber and the prism compressor (Fig. 4.5). A quick-and-dirty optimization of the laser pulse duration can also be performed by maximizing the brightness and loudness of the breakdown spark induced by the high-intensity laser pulses being focused in air by a high-speed lens. The air is ionized at the repetition rate of the laser pulses, resulting in an audible sound produced by the sound waves created by the electron leaving and returning to the core periodically and emitting a colorful spectrum through the recombination of the plasma.

5.1.1.2 Cross-correlation

Since the autocorrelation signal (Eq. (5.7)) involves the electric field to the fourth power (also see Eq. (5.4)), it is very difficult to detect very weak signals as e.g. present for high harmonics where in addition the nonlinear susceptibilities are extremely small. In the autocorrelation method Eq. (5.7) a copy of the unknown pulse is used as a gate that is scanned across the original pulse. Since the autocorrelation signal contains the product of these two pulses, we can replace the gate made up of the pulse to be characterized by a strong reference pulse. This is called *cross-correlation* with a trace given by

$$I_{\mathrm{cross-corr}}(\tau) \propto \int dt \, I(t) I_{\mathrm{ref}}(t - \tau), \qquad (5.9)$$

where I_{ref} is the intensity of the reference pulse. We can see that the correlation signal is virtually "amplified" by using a strong reference pulse. In addition no spectral overlap is needed between the test pulse and the fully characterized strong reference pulse. This enables us to measure the time duration of harmonics by using the high-intensity fundamental pulse as the reference pulse. More details about the characterization of high-order harmonics using cross-correlation will be given in Sec. 5.1.2.1. The drawback of cross-correlation is that the reference pulse must be characterized using another technique in order to be able to extract information about the unknown pulse from the cross-correlation trace. This technique is therefore not self-referencing any more.

Since a different pulse is used as a gate pulse for the cross-correlation, the basic mixing mechanism for the nonlinear signal is now sum-frequency generation instead of second-harmonic generation. Therefore it is also used e.g. to characterize blue 400 nm laser pulses with a 800 nm fundamental pulse since the second-harmonic of the blue pulse at 200 nm would be absorbed in all common nonlinear crystals. The sum-frequency signal at 266 nm, however, still lies in the transparency window. Other mixing processes such as difference-frequency mixing can also be used for cross-correlations. This is useful for the characterization of UV pulse at 266 nm (third harmonic) where the difference-frequency mixing with a fundamental photon at 800 nm yields a detectable signal at 400 nm.

5.1.1.3 Frequency-resolved optical gating (FROG)

FROG is an acronym for *frequency-resolved optical gating* and was developed by Kane and Trebino [293]. For a detailed review see Trebino et al. [294]. It is a member of the zoo of "animal diagnostics" (FROG, SPIDER, TADPOLE, CRAB) and can retrieve the full amplitude and phase information of an ultrashort laser pulse as opposed to a simple autocorrelation.

With FROG, it is possible to measure pulses over a wide range of wavelengths, pulse lengths, and complexities, and to do so in a manner that is general, robust, accurate, and rigorous. Complex apparatus is not necessary; FROG simply involves spectrally resolving the signal beam of an autocorrelation measurement. It therefore not only operates in the frequency domain *or* time domain but in the "time-frequency" domain. Measurements in the time-frequency domain involve both temporal and spectral resolution simultaneously and thus represent a two-dimensional description of the pulse. The so-called FROG trace contains all information without any approximations. Since the trace contains $N \times N$ data points, there is a significant overdetermination that can be used to get rid even of systematic errors.

Of the multitude of possible FROG configurations such as polarization-gate (PG) FROG, self-diffraction (SD) FROG or transient-grating (TG) FROG, second-harmonic-generation (SHG) FROG is most common since it is very sensitive and has a relatively simple setup. In SHG FROG, the two-dimensional FROG trace is given by the following mathematical form [294]:

$$I_{\text{FROG}}^{\text{SHG}}(\omega, \tau) = \left| \int_{-\infty}^{+\infty} E(t)E(t-\tau)e^{-i\omega t}dt \right|^2 \tag{5.10}$$

where $E(t)$ is the electric field of the pulse to be measured, and the same electric field (delayed by τ) $E(t-\tau)$ acts as a gate function in the spectrogram [294]. By adding the factor $e^{-i\omega t}$ to the expression in Eq. (5.10) as compared to the autocorrelation integral we obtain the spectrum of the second-harmonic signal as recorded by a spectrometer. This can easily be understood by reconsidering Eq. (2.30): The additional factor $e^{-i\omega t}$ changes the expression Eq. (5.10) to the Fourier transform from the time domain into the frequency domain. Therefore in FROG a number of spectra are recorded as a function of the delay τ, leading to the two-dimensional FROG trace. Note: The time integration in the case of the autocorrelation is caused by the slow detector whereas it is part of the Fourier transform for the FROG signal here. For the full FROG trace a number of measurements of the spectra as a function of the delay τ is needed.

Via one or more of several iterative and evolutionary phase retrieval algorithms, one can then reconstruct the full electric field and phase information from the measured FROG trace. The iterative procedure works by starting with an initial guess for an electric field, calculating its FROG trace and comparing it to the experimental data. Based on general projections corrections to the electric field are made. These steps are repeated until the error between the reconstructed and the original data is sufficiently small.

The setup of the SHG FROG involves an autocorrelator whose two output beams (at an angle) are focused into a nonlinear crystal with a cylindrical lens. The resulting background-free second-harmonic signal (the bisector between the two original beams) is then spectrally resolved using a regular spectrometer with an array detector.

When the second electric field in Eq. (5.10) is replaced by a different fully characterized electric field the configuration is called XFROG [296], which stands for cross-correlation frequency-resolved optical gating. The arguments for the use of XFROG such as the applicability of strong reference pulses and the relaxed constraint of spectral overlap are the same as given for ordinary cross-correlation in Sec. 5.1.1.2. XFROG as well as cross-correlation are non-interferometric. Applications of the XFROG method in the field of the characterization of high-harmonic pulses will be discussed in the corresponding Section.

A modification of the FROG setup that involves no moving parts, has no sensitive alignment parameters and a significantly greater sensitivity was demonstrated by [297] and is called

GRENOUILLE[1]. A Fresnel biprism [298] replaces the beam splitter, delay line, and beam-combining optics with a single fixed element. The biprism divides the incident beam into two parts which leave the biprism at an angle. The left portion of the wavefront is refracted to the right, and the right segment is refracted to the left. The two beams overlap in a thick SHG crystal. This way the relative beam delay is automatically mapped onto horizontal position at the crystal which is imaged onto a CCD camera. The crystal itself is a thick crystal as opposed to ordinary FROG. For FROG, a thin crystal must be used because the whole spectrum of the pulse must be phase matched. By choosing a thick crystal for GRENOUILLE, only one specific wavelength is phase matched for a specific angle of incidence, thereby acting as a spectrometer. A first cylindrical lens in GRENOUILLE must focus the beam into the thick crystal tightly enough to yield a range of crystal incidence (and hence exit) angles large enough to include the entire spectrum of the pulse. The wavelength is then mapped as a nearly linear function of vertical position onto the CCD camera. The resulting two-dimensional signal is then a SHG FROG trace which can be evaluated as usual. No moving parts are required, making the device very stable and easy to align. Moreover, since a thick crystal is used, it has a higher sensitivity because the conversion efficiency in the nonlinear crystal scales as the squares of the crystal length, so a higher signal is generated.

5.1.1.4 Spectral interferometry

If a fully characterized reference pulse (including both amplitude and phase) in the same frequency range as the unknown pulse is available, spectral interferometry (SI, Lepetit et al. [299]) can be applied. It relies on the linear superposition of these two pulses and allows for the retrieval of the phase of the unknown pulse by evaluating the resulting interferogramm.

Let us first consider two identical pulses $E(t)$ separated by a time delay τ. The superposition of these two pulses is the temporal analogon to the interference at a double slit. Time- and frequency domain are linked to each other by a Fourier transform similar to position and momentum space. As in the case of a Michelson interferometer, a certain delay leads to constructive interference for a certain wavelength. A change of the delay gradually results in destructive interference. For a fixed delay, a broad spectrum then shows maxima and minima at certain wavelengths, the so-called interference fringes. If the delay is increased, the fringe separation decreases and vice versa.

Mathematically speaking, the temporal intensity of two identical pulses $E(t)$ and delay τ is given by

$$I(t) \propto |E(t) + E(t + \tau)|^2. \tag{5.11}$$

The spectrum can be obtained via Fourier transform and yields

$$
\begin{aligned}
I_{\mathrm{SI}}(\omega) &= |E(\omega) + E(\omega)e^{-i\omega\tau}|^2 = \\
&= 2|E(\omega)|^2 + E^*(\omega)E(\omega)\left(e^{-i\omega\tau} + e^{i\omega\tau}\right) = \\
&= 2|E(\omega)|^2(1 + \cos(\omega\tau)) = \\
&= 2I(\omega)(1 + \cos(\omega\tau)), \tag{5.12}
\end{aligned}
$$

where $I(\omega) = |E(\omega)|^2$ is the spectral intensity (spectrum). This shows the regular modulation of the fringe spacing by $2\pi/\tau$.

---

[1] GRENOUILLE is the French word for FROG, but here it stands for grating-eliminated no-nonsense observation of ultrafast incident laser light e-fields [297].

For the combined field of the unknown pulse $E(t)$ ($E(\omega) = |E(\omega)|\exp(i\phi(\omega))$) and a known reference pulse $E_0(t)$ ($E_0(\omega) = |E_0(\omega)|\exp(i\phi_0(\omega))$), Eq. (5.11) must be modified:

$$I(t) \propto |E_0(t) + E(t + \tau)|^2. \tag{5.13}$$

The spectrum can then be written as

$$I_{\text{SI}}(\omega) = |E_0(\omega) + E(\omega)e^{-i\omega\tau}|^2 =$$
$$= I_0(\omega) + I(\omega) + 2\sqrt{I_0(\omega)I(\omega)}\cos(\phi(\omega) - \phi_0(\omega) - \omega\tau). \tag{5.14}$$

We still have a fringe spacing of $2\pi/\tau$ on average, with, however, slight variations depending on the phase difference $\Delta\phi(\omega) = \phi(\omega) - \phi_0(\omega)$ between the known and the unknown pulse. By measuring the spectral intensities $I_0(\omega)$ and $I(\omega)$ it is theoretically possible to retrieve the phase by inverting the cosine function. Experimentally, however, noise does not allow the full elimination of the spectral intensities from Eq. (5.14) so that values greater than unity would appear as the argument of the inverse cosine. A reliable phase retrieval can be obtained by a Fourier transform and filter technique. We first Fourier-transform Eq. (5.14) into the time domain. The transformed signal $S_{\text{SI}}(t)$ then consists of three contributions:

$$I_{\text{SI}}(t) = S_{\text{dc}}(t) + S_{\text{ac}}(t - \tau) + S_{\text{ac}}(t + \tau). \tag{5.15}$$

The signal $S_{\text{dc}}(t)$ at $t = 0$ represents the Fourier transforms of the spectral intensities $I_0(\omega)$ and $I(\omega)$ and is not important here. The contributions $S_{\text{ac}}(t - \tau)$ and $S_{\text{ac}}(t + \tau)$ at $t = \tau$ and $t = -\tau$ result from the cosine term and contain all of the phase information. The two ac terms and the dc term do not overlap if the time delay τ is sufficiently large so that two input pulses do not overlap in the time domain. The positive ac term at $t = \tau$ can now be selected using a suitable window function, e.g. a higher-order super Gaussian. The phase term can then be isolated by taking the argument of the inverse Fourier transform ($\mathcal{F}^{-1}$) back to the frequency domain since, by taking only the one ac term, the cosine term is converted into an exponential:

$$\phi(\omega) - \phi_0(\omega) - \omega\tau = \arg[\mathcal{F}^{-1}\{S_{\text{ac}}(t - \tau)\}] = \arg\left[\mathcal{F}^{-1}\left\{\sqrt{I_0(\omega)I(\omega)}e^{\phi(\omega) - \phi_0(\omega) - \omega\tau}\right\}\right]. \tag{5.16}$$

After subtracting the linear phase contribution $\omega\tau$ the phase of the unknown pulse can be determined by adding the retrieved phase difference to the phase $\phi_0(\omega)$ of the known pulse.

Constraints applying to the time delay τ and the spectrometer, respectively, will be discussed in the following Section.

If FROG is combined with spectral interferometry to accurately characterize the reference pulse, this technique is called TADPOLE (temporal analysis by dispersing a pair of light e fields, Fittinghoff et al. [300]).

5.1.1.5 Spectral phase interferometry for direct electric-field reconstruction (SPIDER)

The autocorrelation method presented above requires the assumption of a certain pulse shaper in order to deduce the approximate duration of the laser pulse. Statements about its phase are nearly impossible. Spectral interferometry allows for the determination of the phase of an unknown laser pulse. However, a known reference pulse in the same frequency range must

be available. A method that allows for the full retrieval of the phase and is self-referencing is called Spectral Phase Interferometry for Direct Electric Field Reconstruction (SPIDER, Iaconis and Walmsley [301, 302]). Two replica of the input pulse are sheared in frequency with respect to each other by a nonlinear mixing process. Their interferogramm then allows for the retrieval of the phase through the same series of windowed Fourier transforms as conventional spectral interferometry. Therefore, just as spetral interferometry itself, it does not require any iterations as opposed to FROG.

For SPIDER, all measurements are made exclusively in the frequency domain. A spectral interferogram is generated by the interference of two replicas of the pulse to be characterized. If the pulses were completely identical, the relative phase between them as retrieved by spectral interferometry would be zero, and no information on the actual phase of the input pulse could be gained. Therefore a shear Ω is imparted on the two replicas so that the frequency ω of one pulse can interfere with the frequency of the other originally located at $\omega + \Omega$.

The procedure is as follows: A pair of replicas of the pulse is separated in time by a *fixed* delay τ (*e.g.* by using a Michelson interferometer). SPIDER therefore requires no moving parts. The two replicas are mixed with a stretched pulse (highly chirped, *e.g.* in a grating compressor or by sending the original pulse through a highly dispersive glass rod) in a nonlinear medium. As the pulses in the test pair are delayed with respect to each other by τ, each is mixed with a different temporal, and hence spectral, slice of the stretched pulse. The result is a pair of replicas of the pulse to be characterized that have been frequency shifted and are spectrally sheared by some amount Ω (Fig. 5.3). The resulting interferogram can then be written similarly to Eq. (5.14):

$$I_{\mathrm{SPIDER}}(\omega) = |E(\omega) + E(\omega + \Omega)e^{-i\omega\tau}|^2 =$$
$$= I(\omega) + I(\omega + \Omega) + 2\sqrt{I(\omega)I(\omega + \Omega)}\cos(\phi(\omega) - \phi(\omega + \Omega) - \omega\tau). \quad (5.17)$$

The retrieval of the phase term through windowed Fourier transform then yields the phase difference between the spectral components at ω and $\omega + \Omega$ for the same input spectrum:

$$\Delta\phi_{\mathrm{SPIDER}}(\omega) = \phi(\omega) - \phi(\omega + \Omega) = \omega\tau + \arg[\mathcal{F}^{-1}\{S_{\mathrm{ac}}(t - \tau)\}] =$$
$$= \omega\tau + \arg\left[\mathcal{F}^{-1}\left\{\sqrt{I(\omega)I(\omega + \Omega)}e^{\phi(\omega) - \phi(\omega + \Omega) - \omega\tau}\right\}\right]. \quad (5.18)$$

The technique is therefore self-referencing because no reference phase in relation to which the phase difference is evaluated is needed. The last step of the SPIDER procedure is then to reconstruct the complete spectral phase $\phi(\omega)$. This can be done by concatenation of the spectral phase differences $\Delta\phi_{\mathrm{SPIDER}}(\omega)$ for a discrete set of frequencies separated by Ω or integration, using all data points.

Attention has to be paid to several constraints:

1. Since for the reconstruction of the spectral phase the phase differences $\Delta\phi_{\mathrm{SPIDER}}(\omega)$ are summed up (or integrated), a careful calibration of the linear phase term $\omega\tau$ is crucial to avoid large errors. The easiest and most precise way is to directly measure the time delay τ by spectral interferometry of the two identical pulses without imparting any shear.

2. Since SI and SPIDER rely on the analysis of the fringes in the interferogram, the oscillations in the spectrum must be clearly resolvable. The Nyquist limit requires at least two

sampling points per oscillations. Since the fringes are approximately spaced by $2\pi/\tau$, this requires a spectrometer resolution better than $\delta\omega = \pi/\tau$. However, τ must not be so small that the data inversion routine cannot separate the ac terms from the dc term. Usually τ can be taken on the order of ten times the original pulse duration.

3. According to the Whittaker-Shannon sampling theorem of information theory, any electric field pulse whose temporal support is included in the interval $[-\pi/\Omega, \pi/\Omega]$ can be accurately reconstructed [303]. This requires $\pi/\Omega \ll \tau$ or $\delta\omega \ll \Omega$. In practice, the ratio of these two quantities is of the order of ten [304]. However, the shear that is too small will likely lead to errors in the reconstruction in the presence of noise due to the concatenation of the phase at points sampled by Ω.

4. The chirp Φ'' introduced by the stretcher or by material dispersion must be sufficiently large to ensure that each pulse of the time-delayed pulses is upconverted with a quasi-cw slice of the stretched pulse. Ω is about 5 to 10 percent of the average width of the input spectrum. The chirped pulse would usually have a duration of several ps.

5. The offset frequency imparted to the time-delayed double pulses in the shearing process must be taken into account (see below).

Since SPIDER is quite insensitive to the crystal phase-matching bandwidth and to unknown detector spectral responsitivity, it is well suited to the measurements of ultrabroadband pulses.
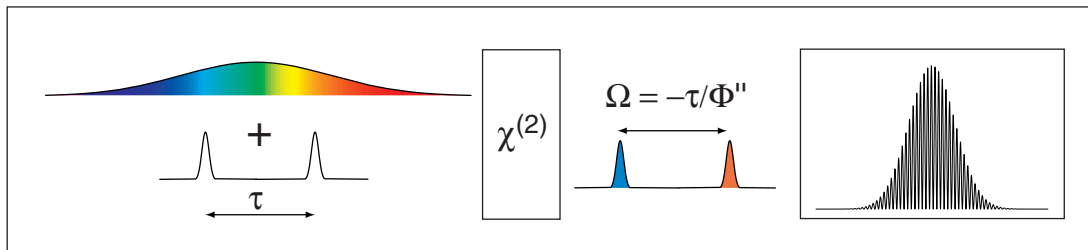
Figure 5.3 – Schematical SPIDER working principle: Two time-delayed replicas of the input pulse are sum-frequency mixed with a strongly chirped pulse in a nonlinear crystal. As a result, the two pulses are frequency-sheared with respect to each other, creating the SPIDER interferogram in the spectrometer.

The current principle setup of the SPIDER in our group is displayed in Fig. 5.4. An older setup was modified by Hofmann [305] and Mark [306]. The input pulse to be characterized is split into a weak and a strong pulse. The strong pulse is then sent through a highly dispersive glass rod to cause a strong chirp on this pulse. The pulse is considerably lengthened in time (tens of picoseconds). This chirp must be so large that the color content during the duration of the original input pulse is constant with time. The weak pulse is split into two replicas by using a Michelson interferometer. The interferometer replaced a thin glass plate that was originally installed in the SPIDER setup to generate the two replicas by using the back-reflection from the front and back surfaces of the glass plate. The transmitted pulse was used for the stretched pulse. In principle this works. The disadvantage, however, is that the time delay τ between the two weak pulses cannot be adjusted but is given by the thickness of the plate. Moreover, additional reflection at multiples of τ appear in the case of a glass plate. The shear Ω on the other side is directly related to the time delay τ through the relation $\Omega = -\tau/\Phi''$ where Φ''

is the quadratic phase of the stretched pulse. Therefore a variable time delay τ proves useful to control the shear. The interferometer has several other advantages over the glass plate: In addition to be able to adjust the time delay, the two replicas generated by the interferometer are completely identical, both in intensity and phase. Moreover, each arm of the interferometer can be blocked independently, making the determination of the spectral shear a lot easier.

The two weak time-delayed replicas and the long stretched pulse are then temporally and spatially overlapped in a second-order nonlinear crystal (BBO). The temporal overlap can be found using a fast photodiode for coarse alignment, and then by controlling the fringe spacing in spectral interferometry between one of the weak pulses and the long pulse. Through sum-frequency mixing the shear Ω between the two replicas is generated (Fig. 5.3). Since the two weak pulses are separated in time by τ, they mix with different frequency Ω_1 and Ω_2 within the long chirped pulse. The pulse pair overlaps temporally with a different section of the stretched pulse allowing differential frequency shifting. The shear Ω is simply determined by the frequency difference between these two portions: $\Omega = \Omega_1 - \Omega_2$. Note: Given a central frequency ω_0 of the input pulses and therefore also of the long chirped pulse, the mixing with Ω_1 and Ω_2 actually transfers the original pulse to approximately twice their original frequency. Therefore, in our case of red 800 nm laser pulses, the SPIDER signal can be found in the blue region at around 400 nm. This offset frequency must be taken into account when reconstructing the phase. In fact, $E(\omega)$ and $E(\omega + \Omega)$ in Eq. (5.17) and the subsequent equations must be replaced by $E(\omega + \Omega_1)$ and $E(\omega + \Omega_2)$, respectively. However, the precise knowledge of Ω_1 and Ω_2 is not required [302], only the shear $\Omega = \Omega_1 - \Omega_2$ must be determined precisely.
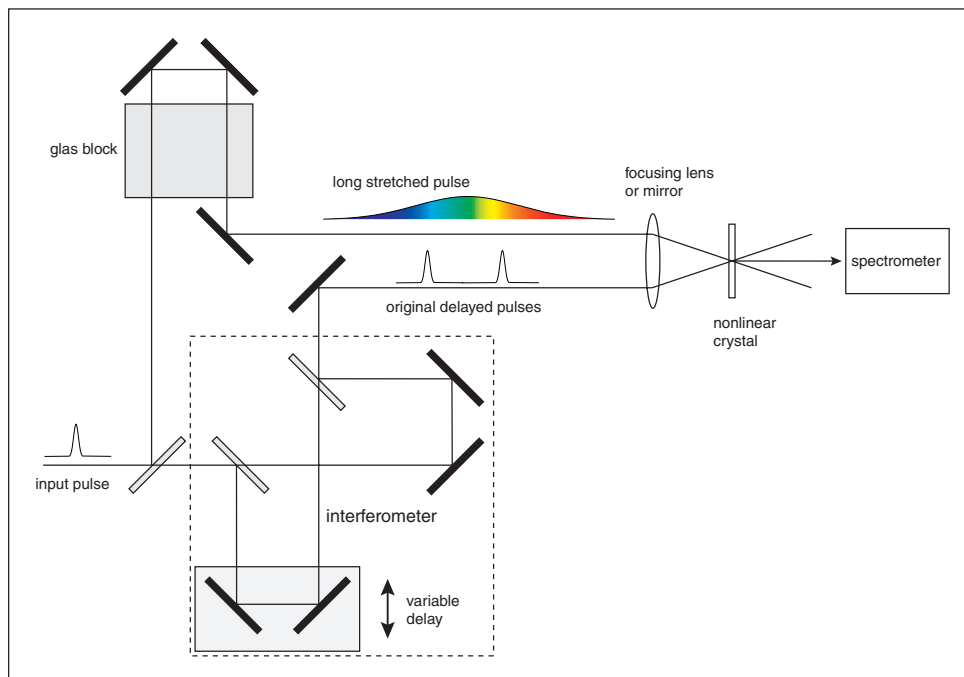
Figure 5.4 – Optical setup for a SPIDER measurement. The original input pulse to be characterized is split into a strong pulse that is temporally stretched in a glass block and into a weak pulse. The weak pulse is used to create two time-delayed replicas of the input pulse in an interferometer. By sum-frequency mixing in a nonlinear crystal, a spectral shear is imparted on the two time-delayed copies as required for SPIDER. The interferogram of these pulses is recorded in a spectrometer (Figure adapted from [305]).
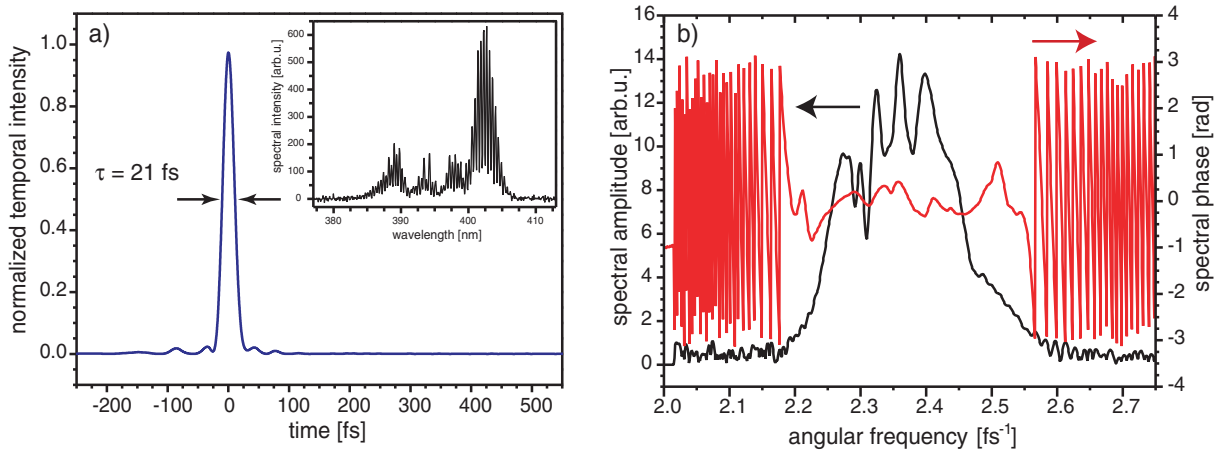
Figure 5.5 – SPIDER measurement for our self-phase-modulated laser pulses from the hollow fiber (see Fig. 4.5). a) Temporal intensity reconstructed from the SPIDER spectrum shown in the inset. The pulse duration is approximately 21 fs. b) Measured spectrum (left axis) and retrieved spectral phase (right axis).

Note that the nonlinear sum-frequency mixing is done in a non-collinear fashion in Fig. 5.4. This way, the second-harmonic signals of each of the pulse pair and the stretched pulse that propagate along their original paths can be blocked using a hard aperture. The sum-frequency signals at $\omega + \Omega_{1,2}$ are generated along the bisector $k + k_{1,2}$ due to momentum conservation and can thus be recorded background-free.

Fig. 5.5 shows a SPIDER measurement of the spectrally broadened and recompressed laser pulses from the self-phase-modulation fiber of our setup in Fig. 4.5. Fig. 5.5a displays the temporal intensity reconstructed from the experimentally recorded SPIDER spectrum shown in the inset. The pulse duration is approximately 21 fs, in accordance with an estimate from an autocorrelation measurement. The measured spectrum of the laser pulse and the spectral phase as retrieved by the SPIDER algorithm are depicted in Fig. 5.5b.

Other modifications of SPIDER demonstrated in the literature include zero-additional-phase SPIDER (ZAP SPIDER, Baum et al. [307]) or a SPIDER setup with a spatially encoded arrangement (SEA-SPIDER, Wyatt et al. [308]).

Since the SPIDER reconstruction algorithm does not allow for the determination of the absolute phase since concatenation is carried out from an arbitrary starting phase, the absolute phase of few-cycle laser pulses must be measured independently if needed. This can be done using the stereo-TOF setup by [80]. The few-cycle laser pulse generates photoelectrons in a gas which are subsequently detected with two time-of-flight electron spectrometers on either side of the gas jet in the plane of the laser polarization axis. By determining the number of electrons emitted to the left or to the right in this direction-sensitive setup, the carrier-envelope phase can be evaluated. A related idea based on the attosecond cross-correlation between an infrared femtosecond and an UV attosecond pulse was proposed by Bandrauk et al. [309].
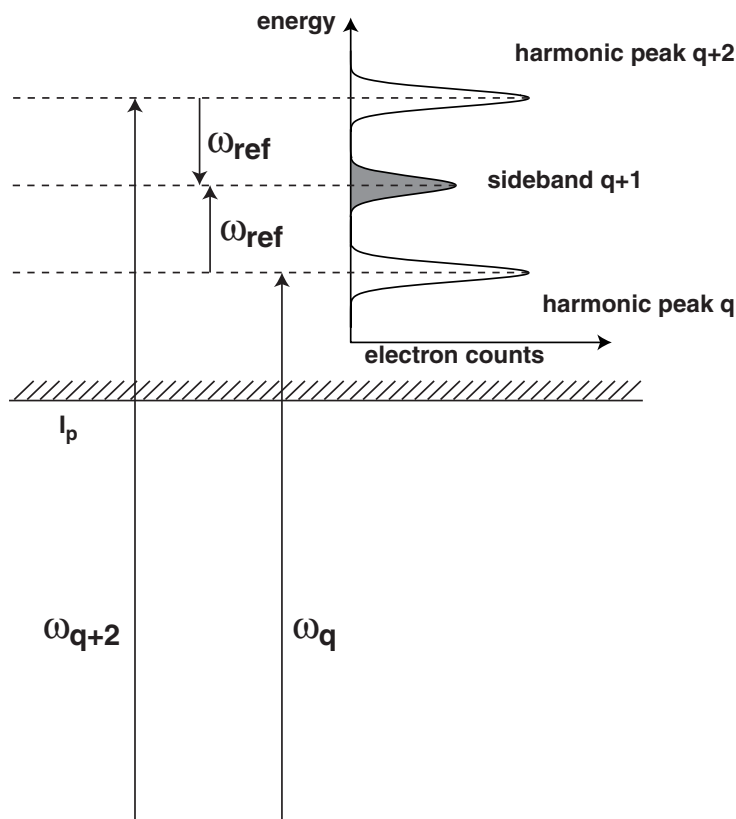
Figure 5.6 – Sideband at $(q+1)\omega$ originating from the two-photon two-color ionization of noble gases: absorption of one harmonic photon at $q\omega$ plus one fundamental photon, and the absorption of one harmonic photon at $(q+2)\omega$ minus the emission of one laser photon. This mechanism forms the physical basis for the determination of the high-harmonic time structure by XFROG or RABBITT.

5.1.2 Characterization of high-harmonic pulses

The results on temporal and spatial shaping presented in Ch. 4 demonstrate our capabilities to generate arbitrary high-harmonic spectra. However, the question of the time structure of our shaped harmonics as generated in a hollow capillary remains open.

Proper selection of harmonics generated in a gas jet enables pulse durations in the attosecond regime [31–33]. Isolated attosecond pulses [38], generated by phase-controlled few-cycle light pulses, can be generated when the high-energy continuum part of a harmonic spectrum is selected using suitable filters. These single attosecond pulses can be characterized using the attosecond-streak camera method [310] where the vector potential of the fundamental near-infrared laser pulse is used to deflect the photoelectrons ionized by the high-harmonic attosecond light pulse. In turn, single attosecond pulses allow for the direct measurement of light waves of the driving laser [291]. Single harmonics within the discrete harmonic comb, however, have pulse durations on the order of the fundamental laser pulses, that is in the femtosecond range [212].

Conventional techniques for the characterization of optical pulses such as FROG [293, 294] or SPIDER [301, 302] are very hard to implement in the soft-x-ray regime due to the small photon flux and the vanishing nonlinear susceptibilities. Although implementations such as XUV SPIDER exist [311–313], most measurements of the duration of harmonic pulses are based on the investigation of the sidebands [314–318] that arise from the cross-correlation between the harmonic pulse and a known fundamental infrared laser pulse.

The cross-correlation is based on the photoionization of a noble gas by harmonic photons. The generated photoelectrons are usually detected with a time-of-flight electron spectrometer. The

photoelectrons directly map the harmonic spectrum onto the photoelectron spectrum so that peaks separated by twice the photon energy of the fundamental laser pulse (the spacing of the harmonics) appear. When an intense fundamental laser pulse used as a probe is scanned (temporally) over the harmonic pulse, sidebands between the harmonic electron peaks appear in the photoelectron spectrum stemming from harmonic photoelectrons that absorb or emit another fundamental photon (Fig. 5.6). From the measured duration of these sidebands the harmonic duration can be deduced [212, 217].

In order to measure the phase difference between different harmonics for the reconstruction of the resulting attosecond pulses or attosecond pulse trains, techniques like RABBITT (reconstruction of attosecond harmonic beating by interference of two-photon transitions [33, 216, 217]) or FROG CRAB (frequency-resolved optical gating for complete reconstruction of attosecond bursts [319, 320]) are needed. Since RABBITT does not give access to the influence of the carrier-envelope phase (CEP) of the driving pulse on high-harmonic generation because it cancels out, additional schemes involving the beating between two consecutive spectrally broadened harmonics have been developed [321]. FROG CRAB can even retrieve the phase of non-identical attosecond pulses. All these schemes rely on two-color two-photon ionization since two different laser pulse wavelengths (harmonic and fundamental) are used. Other experiments have demonstrated the feasibility of performing an autocorrelation of the harmonic pulse, based either on the multi-photon ionization of a noble gas [152, 185] or on above-threshold ionization using two harmonic photons [188]. Another method relies on the sampling measurement of soft-x-ray-pulse shapes by femtosecond sequential ionization of Kr^+ in an intense laser field [322].

5.1.2.1   Cross-correlation techniques

Autocorrelation of high-order harmonics is an extremely daunting task. The cross section for a two-photon-induced transition from an inner-shell bound state to a free state scales approximately as λ^4 [190] and is therefore very small in the XUV region. Since the two-photon signal depends on the square of the electric field (Eq. (3.6)), this limitation could be overcome if a sufficiently strong harmonic field was used. However, harmonic photon numbers are still very limited.

Therefore, historically, cross-correlation schemes with a strong reference pulse (Sec. 5.1.1.2 and 5.1.2.1) were employed first to determine the time structure of high-order harmonics. In this two-color detection scheme noble gas atoms are first ionized by the radiation to be characterized. Direct photoelectron peaks map the photon spectrum onto the electron spectrum if secondary processes such as Auger decay are not considered. If another photon from the reference pulse is absorbed or emitted in the continuum state, sidebands appear on either side of the original photoelectron peak (Fig. 5.6). They are, in first approximation, proportional to the product of both beam intensities and therefore supply a cross-correlation signal from which the harmonic duration can be obtained. In a full quantum-mechanical treatment the absorption or emission of photons by an electron in the continuum can be described as stimulated inverse bremsstrahlung [323]. The sidebands are only present during the time period of temporal overlap between the two pulses. Temporally scanning the reference pulse across the unknown pulse allows for the retrieval of the approximate original pulse duration according to Eq. (5.9), provided that the fundamental signal is known.

For the cross-correlation, relatively moderate intensities are needed for the reference pulse
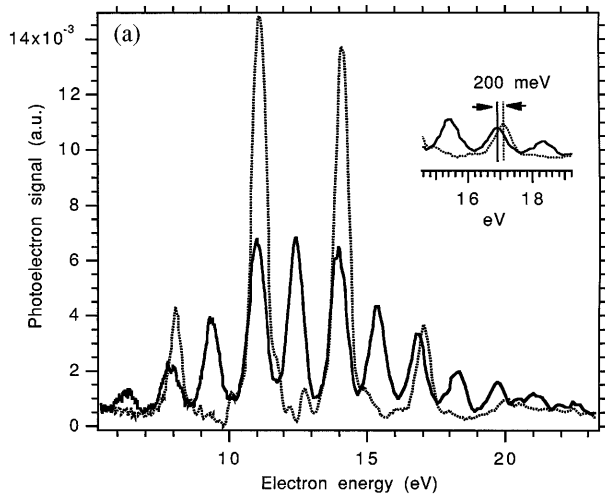
Figure 5.7 – Photoelectron spectra of helium in the presence (solid line) and absence (dashed line) of the dressing laser pulse. The appearance of sidebands and the ponderomotive shift (inset) is clearly visible (Figure from Glover et al. [315]).

as compared to above-threshold ionization (ATI). This can be understood from the classcial simple man's model: The average kinetic energy U of an electron with initial kinetic energy U_i introduced into the external optical field $E_0 \cos(\omega t)$ at the time t_0 is determined by [314]

$$U \approx U_i - \sqrt{8U_i U_p} \sin(\omega t_0) \cos\theta + U_p[1 + 2\sin^2(\omega t_0)], \tag{5.19}$$

where the intensity-dependent ponderomotive energy U_p is given by Eq. (3.52) and θ is the angle between the light polarization and the velocity vector of the electron. The last term in Eq. (5.19) can be neglected if $U_i \gg U_p$. Since according to the rule-of-thumb (Eq. (3.55)) the ponderomotive energy U_p is smaller than 1 eV even for intensities in the range of $10^{12} - 10^{13}\,\mathrm{W/cm^2}$, this condition is generally true for photoelectrons generated by high-order harmonics. Depending on the release time t_0 and the angle θ, the initial energy U_i can be shifted by a maximum amount of

$$\Delta U = \sqrt{8U_i U_p}. \tag{5.20}$$

For reference pulse durations above the few-cycle limit, this energy change will be quantized as a multiple of the photon energy $\hbar\omega$, resulting in the appearance of a number of sidebands on either side of the zero-field peak which can be calculated from

$$N = \frac{\Delta U}{\hbar\omega} = \frac{\sqrt{8U_i U_p}}{\hbar\omega}. \tag{5.21}$$

Eq. (5.21) clearly shows that even for very modest values of U_p sidebands can be observed since U_i is typically much larger than U_p. Schins et al. [314] used this dependency in the observation of laser-assisted Auger decay in argon to determine the time duration of x-ray pulses from a laser-generated gallium plasma. The laser intensity was always less than $1\,\mathrm{TW/cm^2}$ which is sufficient to observe sidebands but is smaller than what is needed for the generation of photoelectrons from argon by this dressing beam.

The first observation of laser-induced free-free transitions in the primary photoelectron spectra of gaseous helium ionized by ultrashort soft-x-ray pulses and the first direct measurements on the temporal duration of femtosecond high-order harmonics was reported by Glover et al. [315]. Fig. 5.7 shows the corresponding photoelectron spectra of helium obtained by the photoionization of helium by high-harmonic radiation in the presence (solid line) and absence

Figure 5.8 – Original sketch of the setup used to generate a doughnut-shaped (annular) laser beam. A central beam stop allows for the creation of an annular laser beam. Harmonics are mainly generated on axis and can easily be separated from the fundamental laser beam with suitable optics (Figure from Peatross et al. [328]).
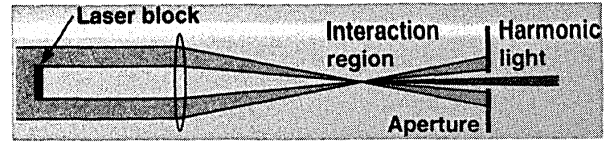
(dashed line) of the dressing near-infrared 800 nm laser pulse. Transient sidebands appear in integral units of the photon energy from which the pulse duration can be deduced. Furthermore, the peaks are shifted to lower energies compared to the field-free case. This shift is not due to space-charge effects but is caused by the ponderomotive shift [324–327]. It varies linearly with the intensity of the dressing pulse and can be used to calibrate their intensity. The ponderomotive potential effectively increases the binding energy of an atom in a high-intensity laser field. This can be understood either in terms of an ac Stark shift of continuum states or, equivalently, by the fact that the photoelectron must acquire sufficient energy at the moment of ionization in order to exist as a positive energy electron oscillating in the laser field [130, 315]. This energy is subtracted from the initial energy U_i of the photoelectron ionized by the soft-x-ray pulses. The energy of the electrons exposed to both frequencies can correspondingly be written as

$$E_{q,n} = \omega_{\text{XUV}} \pm n\omega_{\text{IR}} - I_p - U_p, \tag{5.22}$$

where $\omega_{\text{XUV}} = q\omega_{\text{IR}}$ (harmonic order q) and ω_{IR} are the photon energies, n is an integer number specifying the number of absorbed or emitted IR photons, I_p is the field-free ionization potential, and U_p is the ponderomotive potential [317].

Schins et al. [316] simultaneously performed similar experiments for the 21st harmonic of a 800 nm laser. The advantage of using free-free transitions in this mixed-color two-photon process in the perturbative regime is that no lifetime effects due to bound states are involved. If only one photon is absorbed or emitted by the XUV photoelectron, the sideband is linear in both field intensities and can be written as

$$I_{(q+1)\omega}(\tau) = \int dt \, I_{q\omega}(t - \tau)I_\omega(t), \tag{5.23}$$

which is the same as Eq. (5.9) with the appropriate fields inserted. If more than one harmonic is present in the radiation spectrum, a sideband may result from two possibly interfering contributions, which are, however, still linear in intensity. Higher-order processes such as a $1 + 3$ photon two-color ATI process would destroy this linearity. This scenario can be avoided if the intensity of the dressing laser is kept sufficiently low. In each of the two experiments, the harmonics were focused using a MoSi (molybdenum-silicon) multilayer mirror.

The lower limit of the measurable pulse width is imposed by the pulse width of the reference pulse for a usual cross-correlation measurement, while it is limited by the optical period for FROG or SPIDER [187].

At this point it is useful to introduce the concept of employing annular laser beams for harmonic generation. Since the harmonics created in a laser focus are emitted in the same direction as the propagating laser, they must be separated from the driving laser before they can be utilized. This can be done with a grating or a suitable filter. However, care must be taken with regard to the damage threshold of these two optics, and in addition both methods

are accompanied by a substantial reduction in photon number. Peatross et al. [328] demonstrated an alternative approach for eliminating the laser light from the path of the harmonic light. An annular profile is impressed onto the laser beam that generates harmonics simply by placing a central block into the beam of an axially peaked laser (Fig. 5.8). In the focus this laser beam will be axially peaked provided that its phase profile before focusing is uniphase. A non-uniphase annular beam such as a TM_{01} mode does not have an axially peaked focus. Since harmonic generation is a highly nonlinear process and since the harmonic wavelength is considerably shorter than the fundamental wavelength, the divergence of the harmonic beam is very small. Harmonics are mainly emitted close to the beam axis so that by placing a suitable beam stop after the focus the laser light can be blocked while the harmonics propagate unperturbed. The fundamental laser can be refocused using an appropriate optical element and be used as a probe pulse for high-harmonic cross-correlation measurements.

A more detailed study of the chirp of high-order harmonics on femtosecond and attosecond time scales as obtained from two-photon cross-correlation experiments will be presented in Sec. 5.2.

5.1.2.2 High-harmonic autocorrelation and frequency-resolved gating

Due to the extremely small susceptibilities in the XUV region and the low photon flux of high harmonics, autocorrelation techniques for the temporal characterization of this radiation pose a daunting task since the signal involves a nonlinear process of at least second order. Another problem is given by the lack of suitable beam splitters in the XUV region which makes it difficult to produce two replicas of the unknown pulse[2]. However, several groups have managed to overcome these obstacles and to record autocorrelation traces of high harmonics, which will be briefly summarized in the following.

Autocorrelation measurements in the XUV region were demonstrated for the first time by Kobayashi et al. [332]. A pulse duration of 27 fs was obtained by two-photon ionization of helium for the ninth harmonic generated by a Ti:sapphire laser in xenon. Two time-delayed replicas of the fundamental pulses were produced prior to high-harmonic generation. This experiment showed the feasibility of performing nonlinear optics at XUV wavelengths. Kobayashi et al. [185] also exploited the three-photon ionization of helium for the determination of the pulse width of the seventh harmonic by autocorrelation.

The first direct determination of the temporal characteristics of harmonic pulses in the subfemtosecond regime by measuring the second-order autocorrelation trace of a train of attosecond pulses was demonstrated by Tzallas et al. [152]. The group recorded the nonlinear volume autocorrelation trace (spatial redistribution of energy as a function of delay due to the shift of the foci in the gas plume) of the harmonics 7 to 15 from a xenon gas jet, which showed evidence for attosecond light bunching. Wavefront splitting by a spherical mirror cut into two halves was used to replace the beamsplitter unavailable in this wavelength region. The two parts were then brought to a common focus in a helium gas jet where the two-photon nonresonant ionization process served as an appropriate nonlinear detector with a sufficiently flat response [186, 333]. The choice of the filter material and the nonlinear medium allowed only two-photon ionization, either by two photon of the same energy or by any combination of the transmitted harmonics. The average duration of one pulse within the pulse train was found

---

[2]Transmission gratings were demonstrated as high-harmonic beamsplitters in Michelson interferometers [329–331].

to be 780 as. However, no information regarding individual pulse durations or spacings can be inferred. A more detailed analysis of these results is given in Nikolopoulos et al. [334].

In the experiments on autocorrelation mentioned so far, two-photon ionization was exploited as the required nonlinear process. However, this method is limited to relatively low-order harmonics because higher orders can already induce one-photon ionization. Miyamoto et al. [187] reported the first experimental observation of single-color two-photon above-threshold ionization in argon, xenon, and helium in the XUV range at 25 eV photon energy in spite of the small cross-sections for this process. Sekikawa et al. [188] then used the technology of single-color two-photon ATI to demonstrate for the first time an autocorrelation measurement of XUV pulses with photon energies larger than the ionization energy of helium. They generated the ninth harmonic of blue 400 nm laser at 27.9 eV with an extremely large bandwidth [100] that supported the production of isolated sub-femtosecond laser pulses from a single harmonic. Two optically delayed replicas of the driving pulse were again used to avoid the XUV beamsplitter. An 8-fs driving pulse yielded harmonic pulse durations of 950 as.

A mode-resolved autocorrelation technique also relying on the analysis of two-photon above-threshold ionization spectra of electrons allowed the first determination of the chirp in the attosecond pulse train with an autocorrelation technique [335], labeled PANTHER (photoelectron analysis with nonresonant two-photon-ionization for harmonic electric-field reconstruction) by the authors.

Very recently, the interferometric autocorrelation of an attosecond pulse train was demonstrated for the first time by Okino et al. [336]. The detected signal of N^+ ions with two-photon absorption of the harmonic fields exhibits interferometric fringes on the correlation trace of the envelope. The contributions of the 9th, 11th, and 13th harmonic field are clearly visible in the Fourier transform of the autocorrelation trace, in perfect agreement with a calculated trace.

The first extension of high-harmonic autocorrelation towards high-harmonic FROG was accomplished by Sekikawa et al. [337] who characterized the temporal profile and phase of the fifth harmonic of a Ti:sapphire laser. The FROG setup was based on two-photon ionization and can be analyzed in the same way as SHG FROG. The first XFROG measurements in the XUV region utilizing laser-assisted two-photon ionization were demonstrated by Norin et al. [338] and Sekikawa et al. [318].

As an extension of their previous experiment [188, see above], Kosuge et al. [339] very recently performed the first frequency-resolved optical gating measurement of an isolated attosecond harmonic pulse. From the FROG trace based on two-photon ATI, the shape and phase of the 860 as pulse could be determined simultaneously. This is the first full characterization of isolated attosecond pulses in the XUV region.

5.1.2.3 XUV-SPIDER

For the characterization of ultrashort pulses at XUV wavelenghts, the technique of spectral phase interferometry for direct electric field reconstruction (SPIDER, see Sec. 5.1.1.5) can be adapted to this wavelength region. The difficulty is to generate two time-delayed replicas of the XUV pulse and to impart a spectral shear on them.

SPIDER cannot be directly applied to attosecond soft-x-ray pulses because no optical nonlinear process is available in this spectral range to induce the required frequency shift. Apart from

the all-optical setup by Mairesse et al. [313] where the shear is imparted on the driving laser pulses prior to harmonic generation, several works [311, 312] therefore proposed to apply SPIDER to photoelectron wave packets produced by the ionization of atoms by high-harmonic photons. The two key questions to be solved for the application to SPIDER are whether such electron wave packets interfere so that the interference pattern can be evaluated for spectral-interferometry-type measurements and whether it is possible to impart the required shear between these wave packets.

It has been shown by Wollenhaupt et al. [340] that a pair of two ultrashort laser pulses can be used to generate free electron wave packets in the ionization continuum. These electron wave packets can interfere in an electron spectrometer, creating an interferogram. Interference of electron wave packets has also been demonstrated by Remetter et al. [278], Weinacht et al. [341] for the characterization of (Rydberg) wave packets. This technique can in principle be used to perform spectral interferometry of XUV harmonic pulses. However, pulse characterization by spectral interferometry requires knowledge of the amplitude and phase of the reference pulse (see Sec. 5.1.1.4).

As for the required shear, Mauritsson et al. [311] proposed to have a strong IR pulse interacting with the gas at the same time as the second replica of the XUV pulse. The ponderomotive potential of the strong laser shifts the ionization potential of the gas and hence the energies of the photoelectrons produced by the second pulse, thereby introducing the required shear. In order for the ponderomotive shift to be well defined, the IR pulse must be long enough to shift the photoelectron spectrum without changing its shape (the ponderomotive potential must be approximately constant) but short enough to only influence the second pulse. Moreover, the duration of the XUV pulse must be longer than the period of the electric field. This proposal therefore applies to longer pulses, e. g. to characterize single harmonics.

A method incorporating attosecond spectral shearing interferometry that allows to fully characterize pulses shorter than ~ 400 as was proposed by Quéré et al. [312]. Two time-delayed replicas of the XUV pulse produce wave packets through photoionization of atoms in the presence of a strong laser field, which provides the required energy shift. This is accomplished by the so-called *streaking* method (see Sec. 5.1.2.5). The laser field induces a change of the electron energy through a change of the velocity vector (see Eq. (5.24)), depending on the laser electric field strength, on the time of ionization t_0, and on the observation angle θ, measured from the laser polarization direction. At $\theta = \pi/2$, the energy shift is independent of the original energies of the photoelectrons, allowing an exact mapping of the XUV SPIDER onto optical SPIDER. The x-ray pulse can then be reconstructed with the algorithm developed for optical pulses.

The first complete temporal characterization of high-harmonic XUV pulses by spectral phase interferometry with an all-optical setup was demonstrated by Mairesse et al. [313]. In this work, the authors used a Dazzler [342], which works on the principle of diffraction of the incident optical wave from an acoustic wave, to produce time-delayed replicas of the driving laser pulses prior to harmonic generation. The Dazzler can be programmed to automatically introduce a shear $\delta\omega$ during the generation of two time-delayed pulses. The high-harmonic pulses generated by such a pair of driving laser pulses will consequently be automatically frequency-shifted by $\Omega = q\,\delta\omega$ and time-delayed, allowing to record a SPIDER interferogram with a micro-channel-plate-coupled CCD camera, without the intermediate steps of photo-electron wave packets created by high harmonics. A dazzler was also used by Kornelis et al. [343] who produced frequency-sheared time-delayed extreme-ultraviolet pulses by a strongly

chirped (third order) driving laser pulse.

5.1.2.4 Spectral interferometry between consecutive harmonics

A different method to retrieve the phase differences between consecutive harmonics was experimentally demonstrated by Sansone et al. [321]. It relies on the spectral interferometry pattern that arises from the interference between overlapping spectral regions of two consecutive harmonics. In general two harmonics do not overlap. However, a spectral overlap is necessary to apply spectral interferometry (Sec. 5.1.1.4). Therefore the first step is the use of a physical mechanism that leads to sepctral broadening of the harmonic peaks. As shown in Sec. 3.4.6 the temporal variation of the harmonic phase as a function of the intensity of the driving laser pulse leads to a variation of the instantaneous frequency, broadening the spectrum of each individual harmonic. This phase dependence is much larger for the long quantum path, which can be selected by positioning the gas jet at the laser focus. When the intensity is increased high enough, the harmonic peaks eventually overlap in the spectral region between consecutive odd harmonics, where distinct spectral peaks are formed, provided that the carrier-envelope phase (CEP) is stabilized. This beat pattern resulting from the spectral superposition of the temporally delayed components can be experimentally measured and evaluated using the algorithm of Fourier-transform spectral interferometry.

5.1.2.5 Attosecond streaking

The idea of the attosecond streak camera [310] is that an electron generated by x-ray photoionization can be deflected by a strong laser field, whose phase at ionization determines the energy and angle distribution of the electron. The ionization of atoms by x-rays in the presence of laser fields also forms the basis for the cross-correlation measurement presented above. However, in those cases, the duration of the XUV pulses was longer than the optical period of the laser field. Here we consider XUV pulses with durations shorter than the optical cycle of the dressing field (subcycle pulses). The sidebands broaden and merge (causing interference), and the ponderomotive shift is no longer observable [310]. By appropriately choosing the laser phase, the interferences can either lead to spectral distortions that are subsequently used in the attosecond streak camera or can shift the whole photoelectron spectrum without distortion, making attosecond SPIDER as presented above possible.

In the limit where the ponderomotive potential U_p is much larger than the laser frequency ω and the x-ray photon energy is much larger than the ionization potential, the time-dependent velocity $v(t)$ of the electrons in the laser electric field with the vector potential $A(t)$ is expressed as [310]

$$v(t) = -\underbrace{\frac{e}{m}A(t)}_{\text{quiver motion}} + \underbrace{v(t_0) + \frac{e}{m}A(t_0)}_{\text{final drift velocity}}, \qquad (5.24)$$

where t_0 is the moment of ionization. In Eq. (5.24), the term describing the quiver motion of the electron vanishes as the laser pulse ends. The term labeled "final drift velocity" is the drift velocity of the electron after the laser pulse is over. The additional contribution of $A(t_0)$ to the final drift velocity represents gain or loss of energy from the laser field due to energy conservation [324] and can be interpreted as the absorption, emission, and scattering of laser photons by the photoelectron. Therefore the velocity distribution is translated by an
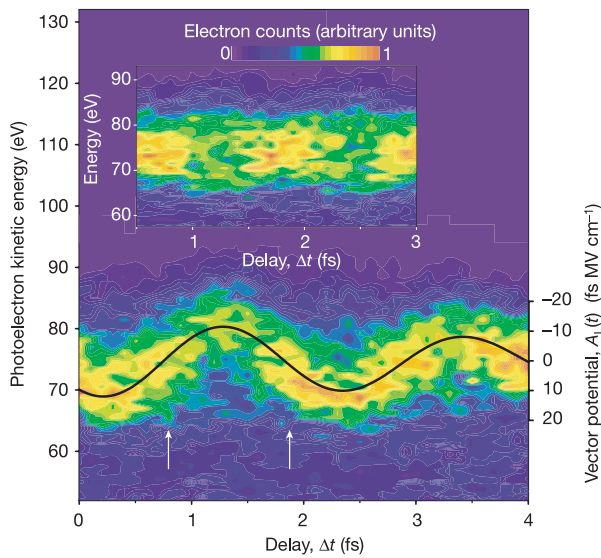
Figure 5.9 – Photoelectron spectra from the atomic transient recorder [38]. The photoelectrons generated by a single attosecond pulse in the presence of a phase-stabilized few-cycle laser field allow for a direct probing of the vector potential of this laser pulse. The light field oscillations are clearly visible. The inset shows the doubled periodicity when the carrier-envelope phase is left unstabilized (Figure from Kienberger et al. [38]).

amount $\delta v = \frac{e}{m} A(t_0)$ in the presence of the laser field. The direction of δv depends on the laser field polarization. The final velocity (and thus the energy distribution) of the electrons will also depend on the time of ionization t_0. This allows a mapping of the momenta of the electrons on the phase of the laser field, which can then be used to characterize the initial XUV pulses. The resulting photoelectron spectra (kinetic energies of the electrons) depend on the ponderomotive potential $U_p(t_0)$ at the time of ionization (through the vector potential $A(t_0)$), the observation angle θ, and the laser polarization. Depending on the chosen configuration, the photoelectron spectra are broadened in energy or angle. Itatani et al. [310] also present a quantum-mechanical calculation with expressions for the amplitude of populating a state $|v\rangle$ with kinetic momentum v, which of course also depends on the vector potential $A(t)$. Since this is not important for understanding the principle of streaking measurements, the reader shall be referred to this publication for more details.

The phase dependence of the shifts and broadening of the electron spectra was used to characterize single harmonic pulses on the sub-femtosecond time scale. Hentschel et al. [32] demonstrated the first experimental verification of the existence of isolated attosecond pulse in an extension of a previous experiment [30]. Harmonic radiation near the cut-off around 90 eV was selected and the momentum transfer from the infrared laser field to the harmonic photo-electrons exploited to observe a shift and a broadening of the spectra. A modulation of this signal at twice the fundamental frequency could be seen although the carrier-envelope phase of the laser was not stabilized. In this case, we would expect the momentum shift caused by the laser to be smeared out due to the fluctuations of the absolute phase. The fact that the modulation is still visible is attributed to the inherent phase stabilization in the cut-off region. The highest harmonic orders can only be generated for a $\pm\cos$ laser pulse, which is also required for the apparition of single attosecond pulses. This way, the photoelectron signal is only visible for a cos-like laser pulse, even without active phase stabililization. The ambiguity of the sign of the cosine function is responsible for the observed doubled modulation frequency. A fit to a theoretical model of two-color x-ray photoionization allowed the extraction of a pulse duration of 650 ± 150 as for the harmonic pulse.

Fig. 5.9 shows the original image from the work of Kienberger et al. [38] in an enhanced version of the experiment with a phase-stabilized few-cycle laser pulse. The photoelectrons

generated by a single attosecond pulse in the presence of a phase-stabilized few-cycle laser field allow for a direct probing of the vector potential of this laser pulse. The light field oscillations are clearly visible. The inset shows the doubled periodicity when the carrier-envelope phase is left unstabilized. The retrieved XUV pulse duration is 250 as. The direct measurement of light waves is now possible using the new tool of attosecond high-harmonic pulses [291].

In the attosecond streaking measurements presented above, the time-dependent vector potential of the dressing infrared pulse (and thus the electric field) was used to modify the electron energies. Ponderomotive streaking, where the change of the ponderomotive potential U_p (determined by the envelope of the electric field) at the rising edge of a dressing laser pulse [344] was to used transiently shift the ionization potential I_p [345], was performed by Toma et al. [327].

5.2 Frequency chirp of harmonic (femtosecond) pulses and attosecond pulses

As it was shown in Sec. 2.4, the temporal structure of ultrashort light pulses is not simply determined by the spectral content of the radiation. A broad spectrum is a necessary condition for the generation of femtosecond and attosecond pulses, but it is not sufficient. A suitable relationship must exist between the different spectral components. In most cases a flat phase is desirable for the generation of bandwidth-limited pulses.

In order to determine the time structure of high-order harmonics and to use their potential to generate attosecond pulse trains and even isolated attosecond pulses, knowledge of the phase is crucial. Let us therefore rewrite Eqs. (3.88) and (3.89) in more detail to include the various contributions to the harmonic phase. The dipole moment μ_q of the qth harmonic can be written as a sum over all contributing quantum paths [346]:

$$\mu_q = \sum_j A_j^q \exp\left[i\Phi_j^q([r_j(t_i, t_r, \boldsymbol{p})])\right], \tag{5.25}$$

where each path $r_j(t_i, t_r, \boldsymbol{p})$ with the amplitude A_j^q is labeled by the index j. The important term in Eq. (5.25) is the phase term:

$$\Phi_j^q([r_j(t_i, t_r, \boldsymbol{p})]) = q\omega t_r - \int_{t_i}^{t_r} \left(\frac{1}{2}[\boldsymbol{p} - A(t)]^2 + I_p\right) dt. \tag{5.26}$$

The quantities determining the value of the phase are the frequency ω and the vector potential A of the driving laser, and the electron ionization and recombination times, t_i and t_r. I_p is again the ionization potential, and $\boldsymbol{p}$ is the drift momentum of the electron. The parameter α_j^q already mentioned in Eq. (3.89) describes the intensity dependence of the phase [346]:

$$\alpha_j^q = -\frac{\partial \Phi_j^q}{\partial I}. \tag{5.27}$$

The corresponding values for the first (short) and second (long) trajectory can be found using a modified time-frequency analysis (see Eq. (3.90)). The dependence of the short quantum orbit on the intensity of the generating laser pulse is much weaker, but the fast variation

of this intensity during the driving laser pulse nonetheless induces a frequency chirp on the harmonic pulse by the temporal modulation of the harmonic phase Φ_j^q. According to Eq. (2.40), the instantaneous frequency can be calculated with the first derivative of the phase, so that the frequency chirp b_j^q is given by the second time derivative [346]:

$$b_j^q = -\frac{\partial^2 \Phi_j^q}{\partial t^2} = -\frac{\partial \Phi_j^q}{\partial I}\frac{\partial^2 I}{\partial t^2} - \frac{\partial^2 \Phi_j^q}{\partial I^2}\left(\frac{\partial I}{\partial t}\right)^2 \approx 8\ln 2 \frac{I_0}{\tau_0^2}\frac{\partial \Phi_j^q}{\partial I},\tag{5.28}$$

where the last approximation is valid for a Gaussian fundamental laser pulse of duration τ_0. The harmonic chirp is negative: "blue" frequencies are located at the leading edge of the harmonic pulse and are therefore ahead of the "red" frequencies which travel at the falling edge of the pulse. The magnitude of the chirp depends on the the laser peak intensity I_0 and on the derivate $\partial \Phi_j^q / \partial I$. It is therefore inversely proportional to the square of the fundamental pulse duration and depends on the order q. This shows that electrons with different return energies travel along different trajectories.

If the fundamental pulse possesses a chirp of the form $\Phi_{\text{fund}} = -\omega t - b_{\text{fund}}t^2/2$, this phase is added as q times the fundamental chirp to the chirp of the emitted harmonics:

$$b_j^q = -\frac{\partial^2 \Phi_j^q}{\partial t^2} + q b_{\text{fund}}.\tag{5.29}$$

XFROG measurements based on the two-color two-photon ionization of rare gas atoms [347] allows us to determine the frequency chirp rate b_j^q in addition to the pulse duration of the harmonics. The sideband spectrum caused by the ionization of electrons by the harmonic photons and subsequent absorption or emission of a fundamental photon can be written as:

$$S(\omega, \tau) = \left| \int_{-\infty}^{+\infty} dt\, e^{i\omega t} E_{\text{XUV}}(t) E_{\text{IR}}(t - \tau) \right|^2.\tag{5.30}$$

The duration of the XUV pulses τ_{XUV} can be obtained from the duration of the sideband τ_{SB} according to [212]

$$\tau_{\text{XUV}} = \sqrt{\tau_{\text{SB}}^2 - \tau_{\text{IR}}^2 - \tau_{\text{geo}}^2}\tag{5.31}$$

if the duration τ_{IR} of the infrared probe pulse is known (e.g. from a SPIDER measurement). The geometrical factor τ_{geo} accounts for the slightly noncollinear geometry of the experiment. The chirp rate b_{XUV} is proportional to the sideband chirp rate b_{SB}:

$$b_{\text{XUV}} = b_{\text{SB}}\left[1 + \frac{\tau_{\text{IR}}^2 + \tau_{\text{geo}}^2}{\tau_{\text{XUV}}^2}\right].\tag{5.32}$$

Mauritsson et al. [212] examined the influence of transform-limited and both positively and negatively chirped fundamental pulses on the frequency chirp of the harmonics. Fig. 5.10 (upper panel) shows the corresponding photoelectron spectra obtained from sideband 18 as a function of time. The lower panel presents the solution of the time-dependent Schrödinger equation in slowly varying envelope, paraxial, and single-active-electron approximations. The chirp of a given sideband q is the average chirp of harmonics $q - 1$ and $q + 1$. However, since the slope of the sidebands does not vary rapidly with order, this is sufficient to extract the desired information. Harmonics were generated with a 35-fs transform-limited 815 nm laser
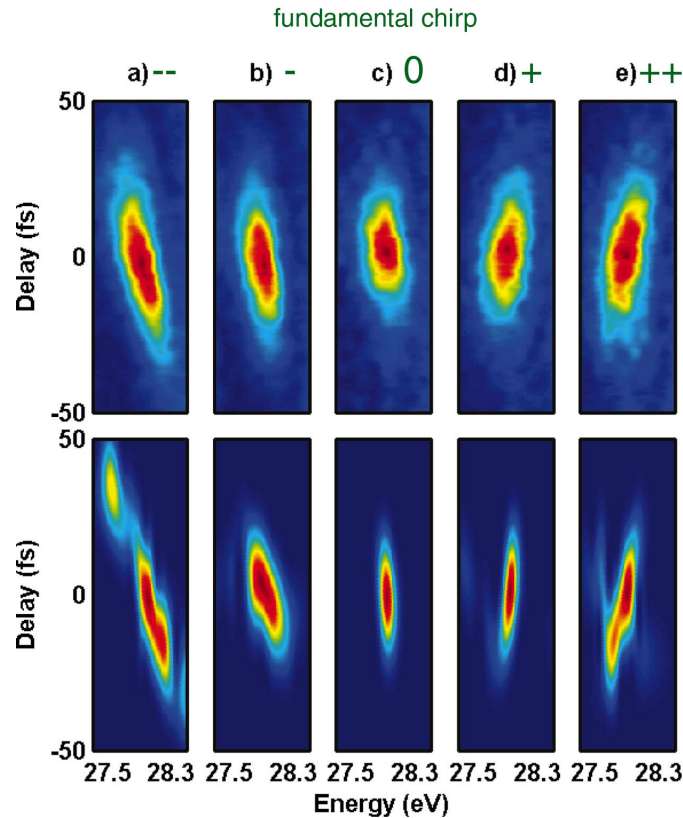
Figure 5.10 – Measured (top panel) and simulated (bottom panel) photoelectron spectra corresponding to sideband 18 as a function of time. For (c) the fundamental pulse is transform limited while the fundamental chirp increases towards higher negative values to the left (b,a) and towards higher positive values (d,e) to the right. The harmonics are negatively chirped in the case of a transform-limited fundamental pulse (Figure adapted from Mauritsson et al. [212]).

pulse, a 12-fs transform-limited probe pulse was used to generate the sidebands. The chirp of the pump pulse could be adjusted by introducing glass plates in either beam and adjusting the compressor to always obtain transform-limited probe pulses. For a flat phase on the pump beam, harmonics are clearly negatively chirped (Fig. 5.10c). The harmonic negative chirp increases if also the pump pulses are negatively chirped (Fig. 5.10b,a). A positive chirp on the fundamental pulses (Fig. 5.10d,e) can compensate for the negative harmonic chirp. Note that in addition to the single-atom response given by Eq. (5.26) macroscopic time-dependent effects such as ionization must be taken into account. These can be neglected if the ionization is low.

Since the chirp considered so far determines the temporal structure of single harmonics on the femtosecond time scale, it is called *femto chirp*. The harmonic chirp is a direct consequence of the temporal variation of the driving laser intensity and vanishes for a constant laser intensity. Effectively, the harmonic chirp is always present because laser pulses are used for high-harmonic generation. Since the driving laser intensity changes from cycle to cycle, the contributing electron trajectories are also changed in time to keep the same return kinetic energy for the generation of the same harmonics, thereby temporally modulating the harmonic
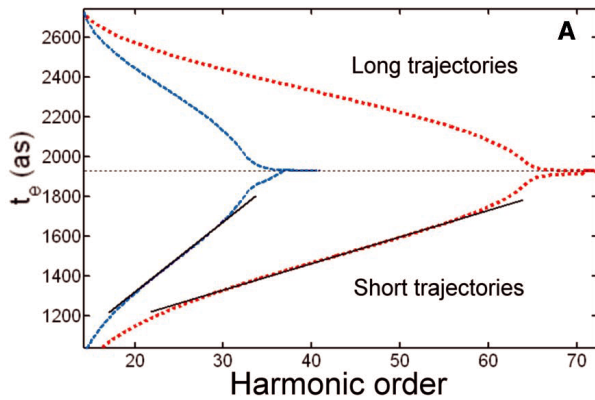
Figure 5.11 – Emission times $t_{e,j}^q$ of the short and long trajectories calculated as a function of harmonic order for two different intensities. The emission times vary approximately linearly with order, increasing for the short trajectory and decreasing for the long trajectory, until they coincide for harmonics in the cut-off region (Figure adapted from Mairesse et al. [33]).

phase. Therefore the time scale of the harmonic chirp or femto chirp is determined by the laser pulse envelope.

As opposed to the femto chirp, the time scale of the so-called *atto chirp* is the laser cycle. Different harmonic orders originate from different return kinetic energies and thus from different electron trajectories, leading to different emission times within an optical cycle. The atto chirp is always present, even at fixed laser intensity. It describes the phase relationship from one (monochromatic) harmonic peak to the next and is therefore important for the generation of attosecond light pulses. The complete phase of high-order harmonic is composed of a slow variation of the central phase of the single harmonic peaks (atto chirp) and an additional variation around each harmonic frequency (femto chirp).

Although the harmonic chirp lives on a femtosecond time scale governed by the laser pulse envelope, it controls the spacing of the attosecond pulses within an attosecond pulse train due to its order dependence [212, 346]. For the short trajectory, the spacing between the attosecond light bursts increases throughout the train. Since the harmonic chirp is negative, the variable spacing can be compensated with a positively chirped driving laser pulse.

Mathematically, let us consider the electric field of the coherent sum of harmonic orders from q_i to q_f at a fixed laser intensity. A fixed laser intensity essentially means a monochromatic laser field, and the harmonics are now discrete spikes. The atto chirp is the phase difference between those spikes. The complete electric field can be written as [346]

$$E(t) = \sum_{q=q_i}^{q_f} \mu_q e^{-iq\omega t} = \sum_j \sum_{q=q_i}^{q_f} A_j^q e^{-i(q\omega t - \Phi_j^q)}. \tag{5.33}$$

The derivatives of the spectral phase Φ_j^q with respect to harmonic frequency (or equivalently, harmonic order) are responsible for the temporal characteristics of this attosecond pulse train. The first derivative is the group delay (cf. Eq. (2.58b)) and can be identified as the real part of the recombination time t_r of the trajectory leading to the emission of the considered harmonic. It is also called emission time [33, 346]:

$$t_{e,j}^q = \frac{1}{\omega} \frac{\partial \Phi_j^q}{\partial q}. \tag{5.34}$$

The emission times vary approximately linearly with order for harmonics in the plateau region, increasing for the short trajectory and decreasing for the long trajectory, until they coincide for harmonics in the cut-off region (Fig. 5.11) where the harmonics are perfectly

Figure 5.12 – Photoelectron spectrum from the two-photon two-color ionization of argon by harmonic and fundamental photons (RABBITT measurement). The oscillations of the sidebands due to the interference term are clearly visible. The shift of the emission time for different harmonic orders can be seen from the tilt of the thick white line along the location of the sideband maxima. The thin white line is vertical (Figure adapted from Mairesse et al. [33]).
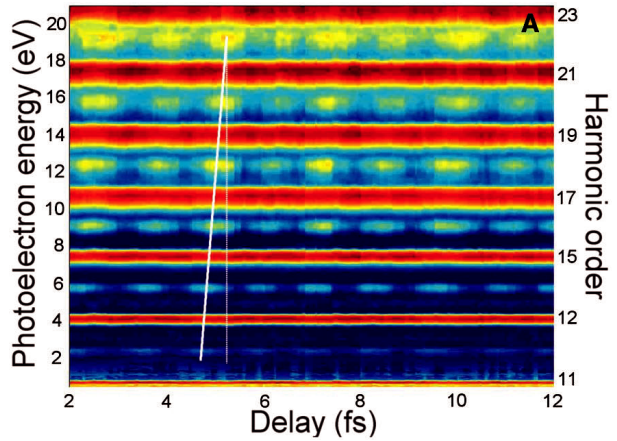
phase-locked [191]. The linear increase (decrease) leads to an approximately constant positive (negative) group delay dispersion given by the second-order spectral phase $\partial^2\Phi_j^q/\partial q^2$, which becomes zero in the cut-off region. If both the short and the long trajectories contribute to the harmonic radiation, the temporal profile will be severely distorted due to the considerable variations of the phase over the available bandwidth. The selection of one class of quantum paths (preferably the short one) through phase matching or spatial filtering (see Sec. 3.4.6) is therefore desirable to obtain clean attosecond pulses.

The measurement of the relative phase between harmonics was first demonstrated by Paul et al. [31] with a technique called RABBITT (Reconstruction of Attosecond Beating By Interference of Two-photon Transitions) as proposed by Muller [216]. By the evaluation of all phase changes experienced by the harmonics and the probe during the propagation from the generation to the ionization points (due to dispersion, geometrical effects, or other processes), an extended version [348] of the first RABBITT experiment [31] yielded the absolute timing of the high-harmonic attosecond pulse train with respect to the generating IR pump cycle at the generation point.

RABBITT is essentially based on the two-photon two-color ionization of rare gases such as the XFROG measurement of high harmonics presented above. Three main differences exist, though: first, the two beams must necessarily propagate collinearly (this can be realized with an annular laser beam, see above), a nonlinear setup is not possible; second, the IR probe pulse duration need not be ultrashort as required by XFROG; third, the relative delay between the two pulses must be stable and be controlled on the time scale of one laser cycle. If these conditions are met, we can see oscillations of the sideband spectrum as a function of delay (Fig. 5.12) due to the interference of the two multi-photon processes that lead to the same final continuum state at $q+1$ in the sideband: absorption of one harmonic photon at q plus one fundamental photon, and the absorption of one harmonic photon at $q+2$ minus the emission of one laser photon (Fig. 5.6).

The corresponding two-photon sideband spectrum can be written similarly to Eq. (5.30) as [217]

$$S(\omega, \tau) = \left| \int_{-\infty}^{+\infty} dt\, e^{i\omega t} |E_{\text{XUV}}(t)| |E_{\text{IR}}(t-\tau)| \left[e^{-i\Phi_j^q} e^{i\omega_{\text{IR}}\tau} + e^{-i\Phi_j^{q+2}} e^{-i\omega_{\text{IR}}\tau} \right] \right|^2. \qquad (5.35)$$

where we have explicitly shown all contributing phase terms. $|E_{\text{XUV}}(t)|$ and $|E_{\text{IR}}(t-\tau)|$ are the envelopes of the XUV and IR electric fields, while Φ_j^q and Φ_j^{q+2} are the harmonic absolute
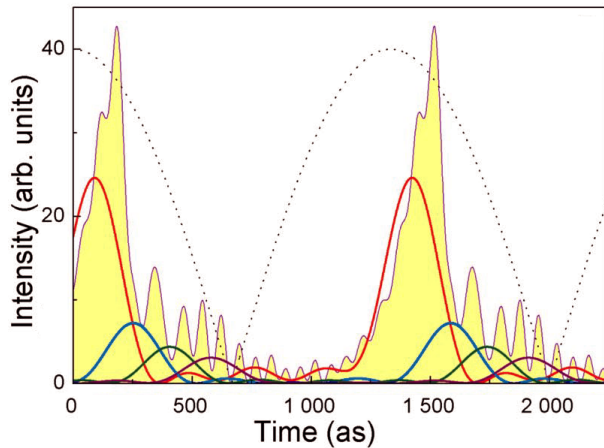
Figure 5.13 – Time structure of harmonic emission in neon. The yellow filled curve corresponds to the full bandwidth from H25 to H69 and shows the strong distortion and broadening of the pulse. The selection of five consecutive harmonics in different spectral range (red: H25–H33, green: H35–H43, blue: H45–H53, purple: H55–H63) allows for shorter pulses and shows the shift of the emission times with respect to the laser field envelope (dotted line). Low orders are emitted close to the peak while the highest orders are emitted at the zero-crossing of the laser field (Figure adapted from Mairesse et al. [33]).

phases of the harmonics q and $q+2$, respectively, that contribute to the sideband at $q+1$. Factorization of the phase term leads to an oscillatory term in the sideband spectrum proportional to

$$\cos(2\omega_{IR}\tau + \Delta\Phi^{q+1}) \qquad (\Delta\Phi^{q+1} = \Phi_j^{q+2} - \Phi_j^{q}), \tag{5.36}$$

where $\Delta\Phi^{q+1}$ is the relative phase difference between consecutive harmonics at $q\omega_{IR}$ and $(q+2)\omega_{IR}$ from which the emission time $2\omega_{IR}t_{e,j}^{q+1} \approx \Delta\Phi^{q+1}$ at the frequency $(q+1)\omega_{IR}$ can be calculated [33].

For the case of the characterization of single attosecond pulses or very short trains of such pulses where the photoelectrons produced by single- and two-color multiphoton ionization have overlapping energy distributions, Aseyev et al. [349] proposed to exploit their angular distribution to distinguish single-photon and two-photon events.

Fig. 5.12 [33] shows a RABBITT measurement of harmonics 13 through 23 in argon. In the photoelectron spectrum from the two-photon two-color ionization of argon the oscillations of the sidebands resulting from the interference of the two contributions according to Eq. (5.36) are clearly visible. The shift of the emission time for different harmonic orders (Eq. (5.34)) can be seen from the tilt of the thick white line along the location of the sideband maxima. The thin white line is vertical. The dephasing of the sideband oscillations as a function of order is a direct indication of the lack of synchronization, leading to order-dependent emission times.

The reconstruction of the temporal profile of harmonic emission in neon from the measured data is shown in Fig. 5.13 (from Mairesse et al. [33]). The yellow filled curve corresponds to the full bandwidth from H25 to H69 and shows the strong distortion and broadening of the pulse. The selection of five consecutive harmonics in different spectral ranges (red: H25–H33, green: H35–H43, blue: H45–H53, purple: H55–H63) allows for shorter pulses and shows the shift of the emission times with respect to the laser field envelope (dotted line). Low orders are emitted close to the peak while the highest orders are emitted at the zero-crossing of the laser field (Figure adapted from Mairesse et al. [33]). This temporal drift in the emission process for different orders directly mirrors the dynamics of the electrons responsible for high-harmonic generation and sets a limit on the minimum pulse duration that can be achieved by increasing the bandwidth without external phase control.

Experimentally, it is difficult to achieve a selection of a range of harmonics. For conventional filtering, a material with the specific transmission and absorption characteristics must be avail-

able. Even if there is one for a certain range, tuning of this range is not possible due to the lack of "neighboring" filter materials. The use of gratings is excluded since either the time resolution is lost in the case of one grating or too many photons are lost in a compensated two-grating configuration. The selection of ranges of harmonics by adaptive pulse shaping as demonstrated in Sec. 4.2.2.2 provides a superior way to solve this problem and even includes the possibility for easy wavelength tuning of the emerging attosecond pulses.

For the full reconstruction of attosecond pulse trains, the narrowband data for the chirp of single harmonics obtained from XFROG measurements and the broadband data for the phase variation between consecutive harmonics as retrieved from RABBITT measurements must be combined to yield the complete phase information [217]. To this end, both measurements must be performed on harmonics generated under the exact same conditions. Varjú et al. [350] proposed a new method to reconstruct the electric field of attosecond pulse trains. Their proposal is based on the Taylor expansion of the harmonic phase around the maximum of the laser pulse envelope in the time domain and around the central harmonic in the frequency domain, thereby giving access the (mixed) partial derivatives of the phase with respect to intensity and harmonic order.

A new method called FROG CRAB (frequency-resolved optical gating for complete reconstruction of attosecond bursts, also called CRAB) was proposed by Mairesse and Quéré [319]. An electron wave packet is generated in the continuum through the photoionization by the unknown attosecond XUV pulse, and a low-frequency dressing laser pulse acts as a pure phase gate similar to conventional FROG. The advantage of CRAB is that it is valid for arbitrarily shaped XUV fields and therefore allows even for the reconstruction of non-identical attopulses in an attosecond pulse train. In the limit of single XUV pulses that extend over many laser cycles, the CRAB trace displays sidebands as in the cross-correlation or FROG measurements presented above. In the other limit of attosecond pulses that are significantly shorter than the period of the dressing optical field, it is equivalent to streaking-type or attosecond-spectral-shearing-interferometry-type measurements. CRAB also covers the intermediate regime of XUV pulse durations and imposes no assumptions on the XUV fields to be characterized. A number of examples for the different limiting cases are illustrated in a more detailed publication on CRAB [320]. The full temporal reconstruction of an attosecond pulse train using CRAB for the first time has been recently demonstrated Kim et al. [351].

In a method related to RABBITT and based on the ω–3ω control scheme presented in Sec. 4.1.2, Papalazarou et al. [352] were able to reconstruct the full temporal intensity distribution of the third harmonic from its spectral phase and amplitude distributions.

To summarize, different phase modulation regimes exist depending on the duration of the XUV pulse with respect to the optical period of the dressing probe laser beam: For an XUV pulse much shorter than the optical period, the photoelectron spectrum produced by the XUV pulse alone is shifted depending on the intensity and phase of the optical field; for an XUV pulse comparable to the optical period, the photoelectron energy spectrum experiences a time-dependent phase modulation, and for an XUV pulse much longer than one optical cycle (such as single harmonics) the photoelectron spectrum displays sidebands between the harmonic peaks [353].

5.3   Experimental progress towards the temporal characterization of shaped harmonics

As shown in the previous Sections, several characterization techniques allow for the determination of the temporal and spectral properties of high-harmonic radiation. Single harmonics or groups of harmonics within the harmonic comb have beeen characterized as well as single attosecond pulses generated in the harmonic continuum. In general, harmonics within the harmonic comb generated in a gas jet have pulse durations on the order of the driving laser pulse, which can be readily understood from the three-step model.

However, these results cannot be transferred to shaped harmonic spectra. We demonstrated the ability to tailor harmonic spectra in a hollow fiber according to various user-defined optimization goals, achieved by spectral-phase shaping of the fundamental laser pulses. The pulse modifies the spectral phase of the driving laser pulses, thus influencing also the harmonic phase. Several groups have found that the chirp of the driver is transferred to the harmonic as q times the fundamental chirp, where q is the harmonic order [212]. But: As we have already discussed for the case of fiber-mode excitation in Sec. 4.3.2, the fundamental laser pulse undergoes substantial reshaping during the propagation through the hollow fiber. It is therefore not possible to make predictions for the influence of the fundamental chirp on the generated harmonics.

That means that knowledge about the temporal structure of our shaped harmonics from the hollow fiber can only be gained by performing a measurement. The easiest way to get a rough estimate is to use a cross-correlation technique (Sec. 5.1.2.1) since the use of a strong infrared probe pulse allows the characterization of weak harmonic fields. In brief, photoelectrons are generated by the harmonic radiation through a one-photon ionization step. The resulting photoelectron spectrum directly maps the optical harmonic spectrum, provided a flat spectral response of the transition dipole matrix elements. Peaks in the photoelectron spectrum appear, separated by twice the fundamental frequency as in the photon spectrum. Through the absorption or emission of probe photons, sidebands between the harmonic peaks appear when the two pulses are temporally and spatially overlapped. Scanning the relative delay allows the determination of the duration of the harmonic pulses.

5.3.1   Experimental setup

We have realized several setups that provide different probe pulse szenarios:

NOPA probe Using the same fundamental laser as pump and probe, the sideband photoelectron energy is the same for the qth harmonic plus a fundamental photon (absorption) and for the harmonic at $(q + 2)$ minus a fundamental photon (emission) (see Fig. 5.6). The harmonic duration retrieved from the sideband therefore constitutes an average value for the two neighboring harmonics. Since the phase between successive harmonic orders is not expected to vary much, this is in general not a concern. However, since we have a noncollinear optical parametric amplifier (NOPA) at our disposal (which is driven by the same laser system and thus synchronized to it), we are able to choose a different wavelength for the probe pulse. In this case, sidebands from neighboring harmonic orders no longer overlap, allowing for the unambigious retrieval of the pulse duration of a specific harmonic [217]. We used the NOPA set in the green range around

Figure 5.14 – Experimental setup for the determination of the duration of single harmonics selected by adaptive shaping of the driving laser pulse. Spectrally shaped ultrashort laser pulses (see Fig. 4.5) from a deformable-mirror-based pulse shaper generate high harmonics of user-defined shape in a hollow gas-filled capillary. The high-harmonic photons produce photoelectrons in a gas jet that can be detected with a time-of-flight electron spectrometer. A fraction of the pump laser is split off to be used as a probe pulse in a cross-correlation two-photon two-color ionization experiment. The absorption or emission of probe photons by the high-harmonic photoelectron should lead to the appearance of sidebands between harmonic photoelectron peaks, from which the duration of single harmonics can be deduced.

532 nm for a cross-correlation experiment. No sidebands were visible which we attribute to the low pulse energies ($< 10\,\mu$J) available from the NOPA.

Laser probe In order to obtain higher pulse energies for the probe, the fraction of the laser beam from the amplifier system that was split off before the self-phase-modulation fiber to pump the NOPA was used directly as a probe. This, of course, limits us to the fundamental wavelength again, but a higher pulse energy of 120 μJ is available. However, these pulses are relatively long ($\approx$ 80 fs as opposed to $\approx$ 20fs for the self-phase-modulated pump pulses), thereby precluding a high temporal resolution in the deconvolution according to Eq. (5.31).

SPM-pulse probe A higher temporal resolution can be gained if the compressed self-phase-modulated pulse after the prism compressor is used (Fig. 5.14). This allows for probe pulses with shorter time durations and, provided the same pulse energies, higher intensities. An 84/16 beamsplitter was used to divide the pump and the probe pulses after the prism compressor, so in reality the energies of the probe pulse are smaller than before ($\approx$ 30 − 40 μJ). However, since the pulse duration is only a fourth of the previous value, the final probe intensity is roughly maintained.

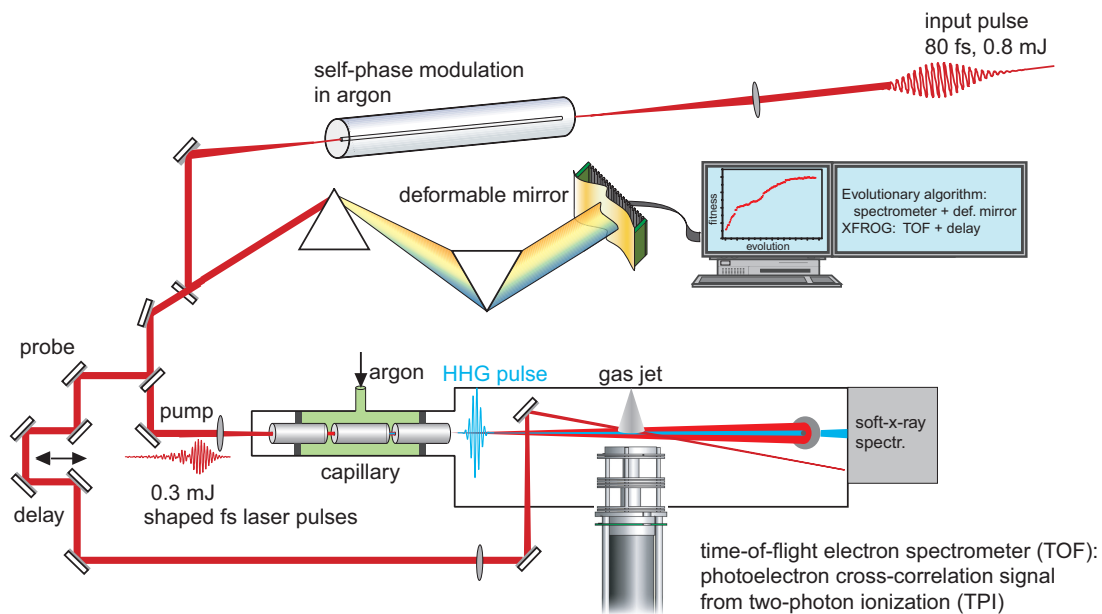Fig. 5.14 shows the complete current experimental setup for the determination of the duration of single harmonics selected by adaptive shaping of the driving laser pulse. Spectrally shaped

ultrashort laser pulses (see Fig. 4.5) from a deformable-mirror-based pulse shaper generate high harmonics of user-defined shape in a hollow gas-filled capillary. The high-harmonic photons produce photoelectrons in a gas jet that can be detected with a time-of-flight electron spectrometer [199]. A fraction of the pump laser is split off to be used as a probe pulse in a cross-correlation two-photon two-color ionization experiment (see Sec. 5.1.2.1). The absorption or emission of probe photons by the high-harmonic photoelectron should lead to the appearance of sidebands between harmonic photoelectron peaks, from which the duration of single harmonics can be deduced.

5.3.2   Time-of-flight electron spectrometer

A new time-of-flight electron spectrometer was developed [199, 354] for the detection of the harmonic photoelectrons. The kinetic energy of electrons is determined by measuring the time it takes for the electrons to drift from the interaction region at their time of generation to a detector at the end of a drift tube. Usually there is an electrostatic lens system at the entrance to the time-of-flight spectrometer for focussing and collimation of the electrons. The detector counts the electrons as a function of their flight time. To obtain the energy spectrum, the flight time must be converted to energy by using the simple formula for the kinetic energy $E = 1/2 m_e v^2 = 1/2 m_e (l/t)^2$ where m_e is the electron mass and v is their velocity given by the length of the drift tube l and the flight time t. However, attention must be paid to include the Jacobi transform $|\partial E/\partial t|$ when converting the count rate on the ordinate axis. The inclusion of this nonlinear factor is necessary due to the changed and nonlinear bin widths on the abscissa as a result of the nonlinear relation between kinetic energy and flight time.

The low number of electron requires an electrostatic lens design with a very high transmission over a broad energy range. The spectrometer should be able to measure photoelectrons within a range up to $100\,\mathrm{eV}$ with a resolution of better than $0.5\,\mathrm{eV}$. The transmission window should be flat and cover a range of $10\,\mathrm{eV}$ in order to detect several harmonics simultaneously.

The newly designed spectrometer of the time-of-flight (TOF) type consists of two electrostatic lenses, a straight drift tube, and a microchannel plate as detector. The major advantage of a TOF analyzer as compared to hemispherical analyzers is that wide range of electron energies can be measured at the same time without scanning.

The optimal lens configuration was found by starting with a numerical modeling of the spectrometer. For the simulation of the electron trajectories through the electrostatic lens system and the drift tube we employed the commercial software SIMION [355], leading to an asymmetric electrostatic lens design (Fig. 5.15). Six plates of stainless steel with varying hole diameters define the electrostatic field to collimate and focus the electron beam while the electrons are decelerated. In both Einzel lenses the central plate is substantially longer than the two outer ones. Such an asymmetric configuration reduces the chromatic aberration of the lens system as compared to plates with equal thickness and diameter. Admittedly the smaller chromatic aberration results in a smaller focusing ability for one specific photoelectron energy but places us in a position to observe a wide energy window at once.

We tested the spectrometer with laser-generated ATI photoelectrons (Fig. 5.15). The ATI electron spectrum was measured without (Fig. 5.15a) and with (Fig. 5.15b) retardation voltage. Applying a retardation voltage to the drift tube without adjusting the lens voltages at the same time resulted in a total loss of the signal. Therefore the lens voltages were controlled manually to follow the shift of the electron spectrum (Fig. 5.15c) as the retardation voltage was
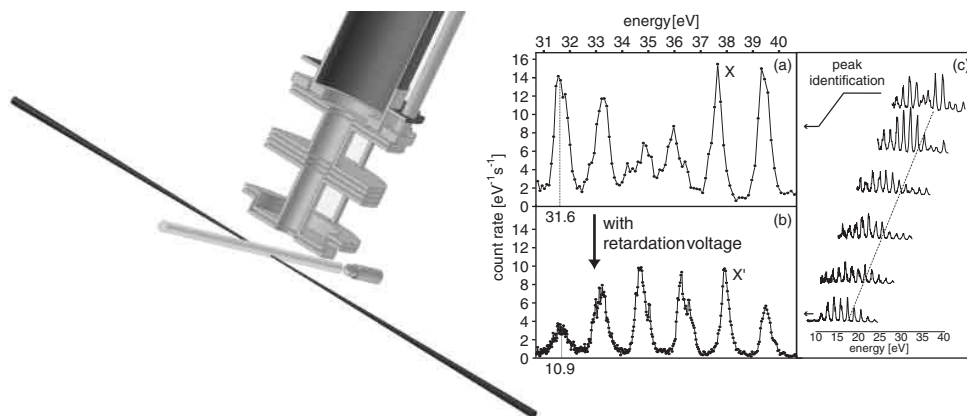
Figure 5.15 – Asymmetric electrostatic lens design of the new time-of-flight electron spectrometer. Six plates of stainless steel with varying hole diameters define the electrostatic field to collimate and focus the electron beam while the electrons are decelerated. In both Einzel lenses the central plate is substantially longer than the two outer ones. On the right: ATI electron spectrum of xenon measured (a) without and (b) with retardation voltage. (a) This curve was measured without any voltages applied to the lenses and the drift tube. (b) This spectrum was obtained with a retardation voltage of 20 V and the optimum voltages applied to the lenses. Using either simulated or experimental data we were able to reliably assign the shifted peaks to the original ones. The peak marked with an X in the original spectrum shifted to the position X′ with activated lens system. (c) These graphics were created from experimental data and show some of the steps used to reassign the decelerated peaks to the original peaks (figure adapted from Paulus et al. [199]).

increased in small steps. The peaks in the final spectrum are narrower than in the original spectrum. Moreover, the increased point density and an improved signal-to-noise ratio allow to discern spectral features more easily. Fig. 5.15c also demonstrates that the calculated bandpass characteristic of the lens system is well reproduced. The transmission in the center has a maximum and is constant as it can be clearly seen by the equal peak heights. Only electrons having initial energies in the range of 30-40 eV are detected.

However, adjusting the potential of the lens plates to maximize the throughput is very sophisticated. One possibility to solve this problem and to speed up this process considerably is employ a closed-loop optimization with an evolutionary algorithm as described in the first chapters of this work. The algorithm varies the voltages applied to the six lens plates adaptively (Fig. 5.16a). The results for the deceleration and the focusing of electrons in a small energy region as found by the evolutionary algorithm are summarized in Fig. 5.16b.

The count rates of the decelerated electrons were even higher than the one for the unaffected electrons. The number of counts increased by a factor of 3 in the observed energy region. Also, the signal-to-noise ratio got better by 25% in average during the optimization process. The higher signal together with an increased point density and an improved signal-to-noise ratio result in an improvement of the effective resolution. Applying a retardation voltage alone would allow for a better resolution of the electron kinetic energies due to the nonlinear relation between flight time and energy but the evolutionary algorithm provides a practical and qualified technique to maintain acceptable count rates.

More experimental and technical details on this electron spectrometer can be found in Paulus
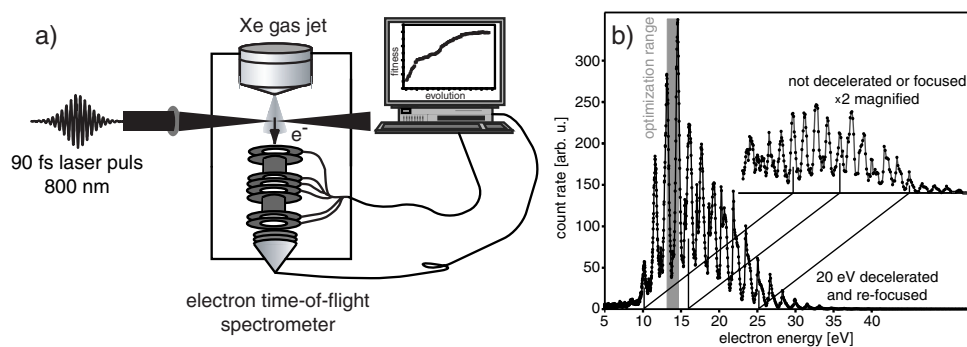
Figure 5.16 – The closed-loop optimization of the electron time-of-flight spectrometer was accomplished with ATI electrons from xenon. The spectrally integrated count rate is measured and represents the fitness. (a) Experimental setup. The voltages applied to the six lens plates are adaptively adjusted by the evolutionary algorithm. (b) ATI spectrum without retardation voltage (upper spectrum) and with retarded electrons and the adaptively optimized lens system. A higher effective resolution is obtained from an increased point density and an improved signal-to-noise ratio (figure adapted from Paulus et al. [199]).

[354] and Paulus et al. [199].

5.3.3 Temporal and spatial overlap

Before the relative delay between the harmonic pulse and the dressing probe pulse can be scanned, temporal and spatial overlap of the two beams in the interaction region must be ensured. To this end, we first searched for the overlap of the two red (harmonic-generating pump and fundamental probe) beams since both beams are visible. The determination of the correct setting of the delay for the probe pulse proceeded in several steps:

1. Measurement of the different propagation paths for pump and probe using a ruler: Since as a rule of thumb light travels at a speed of $1\,\text{ft/ns}$, a determination of the optical path length with a precision of $1\,\text{cm}$ allows for a setting of the delay within $\approx 30\,\text{ps}$.

2. The range setting of the delay stage can then be verified using a fast photodiode. Observing the peaks of the two pulses delivered by the photodiode alternately on an oscilloscope triggered on the laser synchronization output makes it possible to determine the delay with a precision of tens of picoseconds (several millimeters). However, since the housing of the photodiode is too big to be placed at the exact position of the interaction region for the cross-correlation experiment, supplementary and more reliable methods are necessary.

3. A more precise determination of the pulse separation is possible using spectral interferometry (SI, see Chap. 5.1.1.4). However, a mirror setup must be used for this purpose. A fiber-coupled spectrometer cannot be used unless it is a single-mode fiber. Also, both pulses must overlap in some spectral region in order for spectral interferometry to work.

4. If there is no spectral overlap between the two pulses (e. g. for fundamental pulses and pulses from our NOPA), a measurement method based on the transient diffraction from a laser-produced plasma can be used. The strong $800\,\text{nm}$ laser pulse is focused in air

using a high-speed lens so that a plasma spark is created. The co-propagating green NOPA pulse at 532 nm is also focused to this spot, and the beam is observed at some distance after the focus. If the strong plasma-generating red pulse comes after the green pulse, nothing happens. However, if it comes before, the green beam will be diffracted from the free electrons in the plasma, making the observed image downstream look unstable and blotchy. The onset of this behavior can be used as a measure of temporal overlap.

5. Based on background-free optical cross-correlation, we placed a lithium triborate (LBO) crystal at the interaction point. Since the pump and probe beams propagate non-collinearly in the vacuum chamber, the blue second-harmonic signal from each of the two red beams can be seen separated in space on a white card behind the crystal. When the two pulses overlap temporally and spatially inside the crystal, a blue sum-frequency signal can be seen along the bisector. This method is quite accurate for the temporal overlap but since a big crystal ($2 \times 2 \times 2\,\mathrm{mm}^3$) was used, the condition of spatial overlap cannot be verified precisely.

6. When the delay has been determined using the above methods with an accuracy such that the point of temporal overlap is guaranteed to fall within the scan range of the delay stage, we used a thin gold wire that was mounted exactly at the interaction point to find the exact temporal and spatial overlap. This will be described in the following in more detail. On a daily basis, only the last step using the gold wire is needed. This is another advantage of this last method since it can be performed in vacuum and the vacuum chamber need not be opened.

When either of the two red 800 nm beams of pump or probe hits the gold wire, it can generate electrons through a multiphoton ionization step which can be detected using our time-of-flight electron spectrometer. If this is indeed a nonlinear step requiring the absorption of more than one photon, we can use the cross-correlation signal of both beams to find the temporal overlap. The spatial overlap is then given automatically due to the dimensions of the gold wire and the probe beam.

As a first step we verified the nonlinearity of this process as we expected it since the work function of gold falls into the $4-5$ eV range. Using fundamental photons at 800 nm with photon energies of 1.55 eV, this requires ≈ 3 photons. The exact value of the work function of gold can be modified due to surface adsorbates but is not important as long as we can use it as a nonlinear process, i.e. the work function must be larger than the photon energy. Therefore as a first step we did an intensity scan to verify the nonlinearity. The total number of electrons is recorded as a function of the intensity of the probe pulse. The result of a quick check is shown in the inset of Fig. 5.17. The slope of the curve in this log-log plot is well above unity and therefore displays the nonlinearity required to find the temporal overlap (the *zero*) between the two red beams in a cross-correlation-type experiment.

Fig. 5.17 shows a representative of a typical delay scan to find the temporal overlap between the pump and probe pulses. Both the fundamental red (800 nm) harmonic-driving laser beam as well as the red probe beam at the same wavelength were directed onto a thin gold wire ($\varnothing = 0.125\,\mathrm{mm}$). The total photoelectron signal was recorded as a function of delay time. The nonlinear enhancement at the position of temporal overlap is clearly visible. This procedure can easily be carried out on a daily basis to ensure the correct setting of the delay.
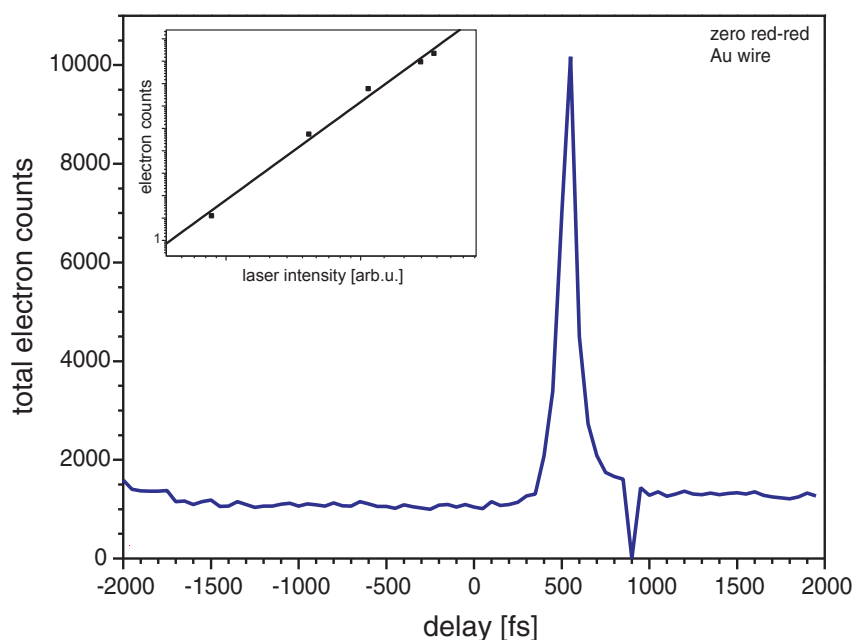
Figure 5.17 – Scan of the temporal delay between the harmonic-generating strong pump pulse and the red probe pulse. The total photoelectron signal from a thin gold wire clearly shows the nonlinear enhancement at the position of the temporal overlap. Inset: Intensity scan for the number of photoelectrons from a gold wire. The number of electrons is recorded as a function of the intensity of the probe pulse. The slope is larger than unity and therefore displays the required nonlinearity.

If the temporal overlap has been found using the gold wire, the spatial overlap between the two pulses is automatically guaranteed due to the small dimensions of the gold wire. However, this procedure was done for the two red (800 nm) beams[3]. Although the harmonics are expected to propagate collinearly with the driving laser from the hollow fiber, it is safer to directly determine the spatial overlap between the harmonic beam and the probe beam. To this end, we use a pinhole ($\varnothing = 0.1$ mm) that can be mounted at the interaction point in the harmonic beam path. The lateral position of the pinhole is adjusted by observing the harmonic beam on our two-dimensional soft-x-ray CCD camera after the pinhole. The probe beam can then be steered through the same pinhole and checked with an infrared viewer on a card. This procedure ensures the spatial overlap between the harmonic beam itself and the probe beam.

5.3.4   Harmonic photoelectron spectra

The next step is to verify whether we can record a photoelectron spectrum, generated by the one-photon ionization of noble gases by high-harmonic photons. The harmonic radiation emerges from the hollow fiber in which it was generated with a divergence of 1–2 mrad. This translates into a spot size of ≈ 0.5 mm at the interaction region (Fig. 5.14). A continuous-flow gas nozzle effuses the selected noble gas close to the entrance hole in the front cap of

---

[3]In addition, the diverging pump beam from the fiber has already increased considerably when it reaches the gold wire.

Figure 5.18 – Experimental photoelectron spectrum of high harmonics in xenon, showing a double-peak structure spaced by the typical harmonic spacing of twice the fundamental frequency ω. In addition, the spin-orbit splitting between the $^2P_{1/2}$ ($I_p = 13.44\,\text{eV}$) and $^2P_{3/2}$ ($I_p = 12.13\,\text{eV}$) orbitals of 1.3 eV is clearly visible.

the time-of-flight electron spectrometer. The pressure in the vacuum chamber was kept at about $1 \times 10^{-3}\,\text{mbar}$. The photoelectrons can be analyzed using a multiscaler card (National Instruments) with 4 GHz sample rate. Their kinetic energies should reflect the typical high-harmonic spectral structure.

A photoelectron spectrum of the high harmonics from the fiber recorded in a xenon gas jet is displayed in Fig. 5.18. The line doublet spaced by the typical harmonic spacing of twice the fundamental frequency ω is caused by the spin-orbit splitting of 1.3 eV between the $5\,^2P_{1/2}$ and $5\,^2P_{3/2}$ valence orbitals in xenon [187, 338]. From the $^2P_{3/2}$ level, the ionization potential is 12.13 eV whereas it amounts to 13.44 eV for the $^2P_{1/2}$ level. Nugent-Glandorf et al. [356] reported the observation of additional line doublets (e. g. $4\,d_{3/2}$ and $4\,d_{5/2}$) for higher-order harmonics with higher photon energies. The ionization potentials for the valence electrons of different noble gases used in our experiments are compiled in Table 5.1. Attention has to be paid to the photoionization cross sections which decay drastically with higher photon energies. For instance, the total photoionization cross section of xenon near threshold for 13 eV-photon is 66 Mb, while it is 22 Mb for 23 eV photons and only 3.8 Mb for 34 eV [357]. Therefore for high-order harmonics, lighter noble gases with higher ionization potentials should be considered, so that ionization occurs closer to the ionization threshold. On the other hand, heavier noble gases in general exhibit higher polarizabilities and therefore higher transition dipole matrix elements, allowing for a higher ionization probability.

For krypton, the spin-orbit splitting in the $4p$ level is 0.67 eV [358, 359] ($I_p[\text{Kr I}\,^2P_{3/2}] =$
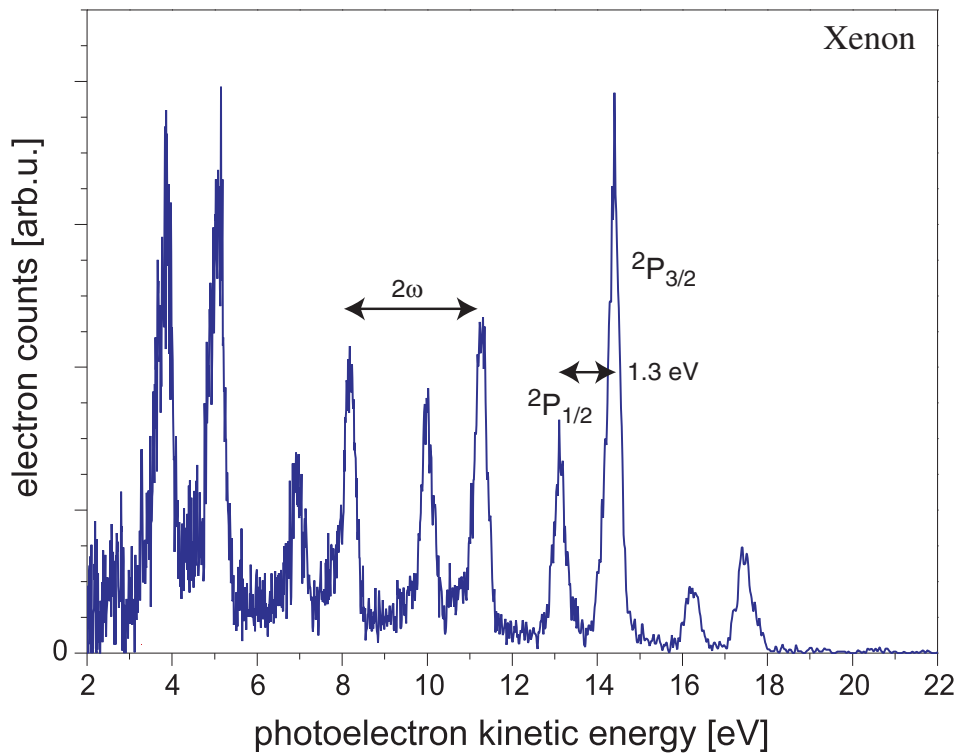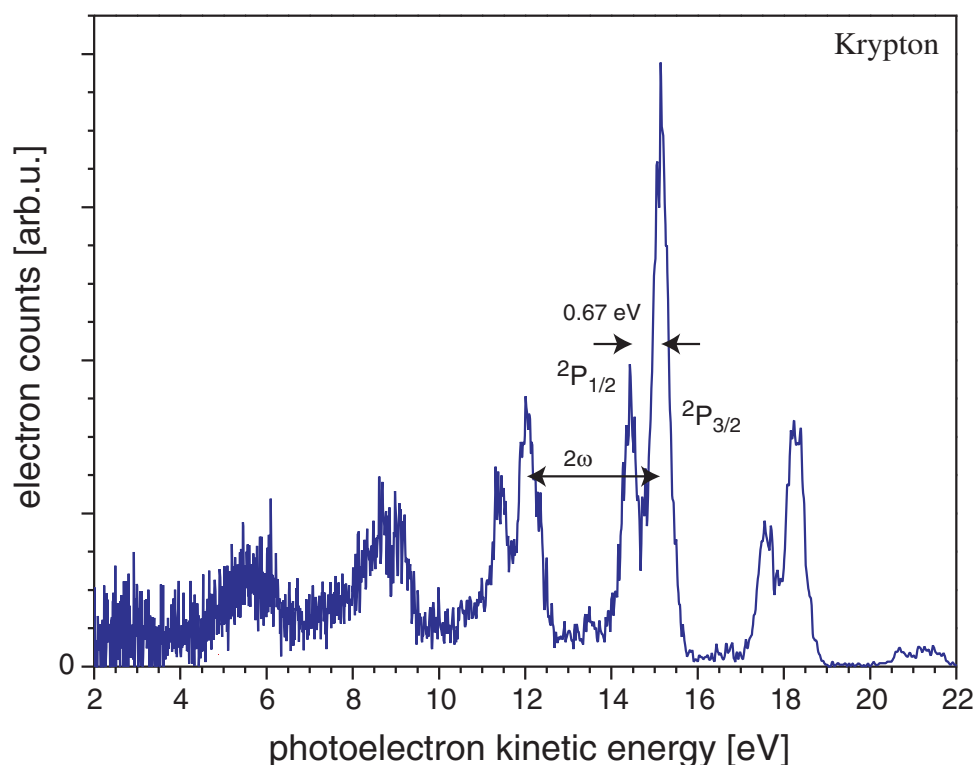
Figure 5.19 – Experimental photoelectron spectrum of high harmonics in krypton, showing a double-peak structure spaced by the typical harmonic spacing of twice the fundamental frequency ω. In addition, the spin-orbit splitting between the $^2P_{1/2}$ ($I_p = 14.67$, eV) and $^2P_{3/2}$ ($I_p = 14.00$ eV) orbitals of 0.67 eV is clearly visible.

14.00 eV, $I_p[\text{Kr I }^2P_{1/2}] = 14.67$ eV). This is clearly reproduced in the photoelectron spectra displayed in Fig. 5.19.

The peak splitting for argon is still smaller as can be seen from Table 5.1. Therefore we do not observe a double-peak structure for photoelectrons in argon (Fig. 5.20). In this spectrum a large number of harmonics spaced by 3.1 eV can be seen, reaching out to a well-resolved 25th order. Sporadic photoelectrons emerge for harmonic orders 27 and 29. Very weak sidebands might indeed be visible but they are not reliably reproducible. The inset in Fig. 5.20 displays the corresponding high-harmonic photon spectrum, recorded with an x-ray CCD camera equipped grazing-incidence spectrometer.

5.3.5   The quest for sidebands

We are now able to generate photoelectrons from the ionization of a noble gas by the harmonic photons and simultaneously focus the probe beam into the interaction region of the harmonics and the gas jet. A typical scan for krypton is shown in Fig. 5.21. The kinetic energies of the photoelectrons resulting from the ionization by one harmonic photon are recorded as a function of the delay. These electrons are always present, independent of the delay. Sidebands due to the absorption or emission of a fundamental photon from the probe pulse (see Fig. 5.6) should appear and disappear as a function of delay and in between the harmonic bands.
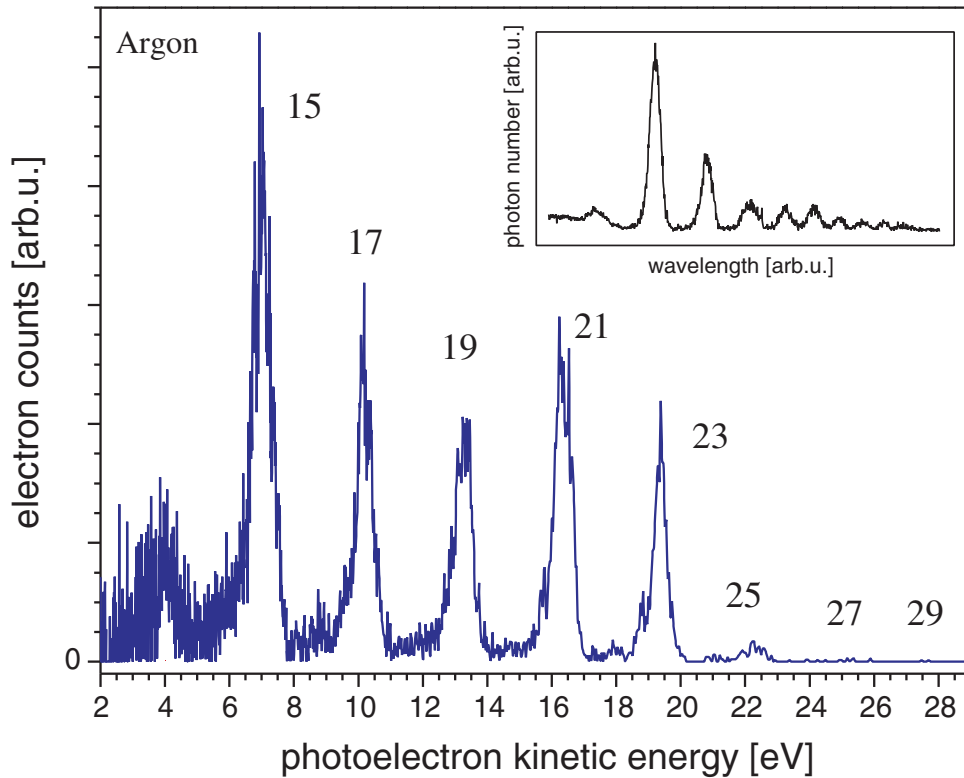
Figure 5.20 – Experimental photoelectron spectrum of high harmonics in argon. Distinct photoelectron peaks of high harmonics up to the 25th order are observable. Sporadic electron counts emerge near 25 eV and 28 eV, corresponding to harmonics 27 and 29, respectively. Very weak sidebands might indeed be visible but they are not reliably reproducible. The inset shows the associated high-harmonic photon spectrum, recorded with an x-ray CCD camera equipped grazing-incidence spectrometer.

element	reaction	first ionization potential/eV		
		$^2P_{3/2}$	$^2P_{1/2}$	$^2S_{1/2}$
He	$\mathrm{He}\,1s^2 + h\nu \rightarrow \mathrm{He}^+\,1s^1 + e^-$			24.59
Ne	$\mathrm{Ne}\,2s^22p^6 + h\nu \rightarrow \mathrm{Ne}^+\,2s^22p^5 + e^-$	21.56	21.70	
Ar	$\mathrm{Ar}\,3s^23p^6 + h\nu \rightarrow \mathrm{Ar}^+\,3s^23p^5 + e^-$	15.76	15.94	
Kr	$\mathrm{Kr}\,4s^24p^6 + h\nu \rightarrow \mathrm{Kr}^+\,4s^24p^5 + e^-$	14.00	14.67	
Xe	$\mathrm{Xe}\,5s^25p^6 + h\nu \rightarrow \mathrm{Xe}^+\,5s^25p^5 + e^-$	12.13	13.44	

Table 5.1 – Ionization potentials for different noble gases (data compiled from Miyamoto et al. [187], Norin et al. [338], Sugar and Musgrove [358], NIST [359], Derevianko et al. [360]).

Unfortunately, no sidebands could be detected so far.

Several critical points were investigated that could possibly be responsible for the absence of sidebands. Although the integration time for each time step in Fig. 5.21 is only 30 s, the spin-orbit splitting for krypton (cf. Fig. 5.19) can be resolved in the two-dimensional contour plot, and enough free space is present between the harmonic peaks. The resolution of the electron spectrometer is therefore not the limiting factor. Further points will be discussed in
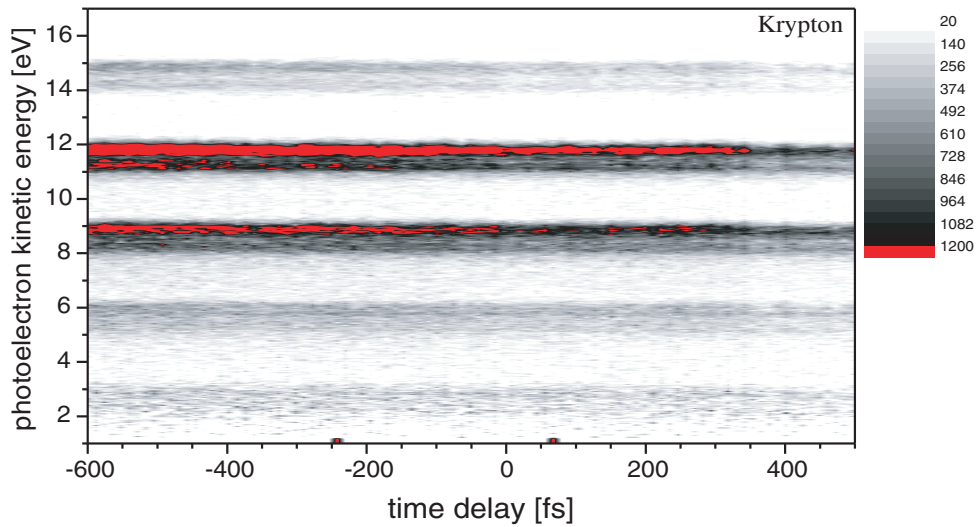
Figure 5.21 – Photoelectron spectrum of krypton versus pump–probe delay. The photoelectrons resulting from the ionization by one harmonic photon are independent of the delay. Sidebands due to the absorption or emission of a fundamental photon from the probe pulse should appear and disappear as a function of delay and in between the harmonic bands. Unfortunately, no sidebands could be detected.

the following.

Historically, we started the search for the sidebands by using green NOPA pulses at 532 nm as probe pulses as mentioned above. Due to the different wavelengths of harmonic-pump and probe pulses, this approach prevents overlapping sidebands from neighboring harmonic orders. The appropriate focusing conditions for the probe pulse can be determined by first calculating the required spot size w_{probe} for a certain intensity I from the input parameters such as power P, repetition rate of the laser f, and pulse duration τ:

$$w_{\text{probe}} = \sqrt{\frac{P}{I\pi\tau f}}. \tag{5.37}$$

The required focusing lens can then be evaluated using the plain-wave approximation [68]

$$w = f^{\#}\lambda, \tag{5.38}$$

where the f-number or 'speed' $f^{\#}$ of the lens is given by $f^{\#} = f/D$ with the focal length f and the beam diameter D, and λ is the wavelength of the radiation used. Since the finite radius of curvature of the laser beam and diffraction are not included in this formula, it is only valid for moderately focused laser beams which are collimated prior to focusing. For a more rigorous calculation, the Gaussian ABCD matrix methods have to be employed (see Sec. 2.3).

Note that the harmonics emerge from the hollow fiber unfocused, resulting at a spot size of ≈ 0.5 mm at the interaction region. This issue will be addressed later in this work.

In determining the appropriate focusing conditions for the probe beam, we have to deal with a trade-off between the probe intensity and a volume effect. A higher intensity of the probe pulse provides a higher 'density' of photons, thereby increasing the probability of absorption by a harmonic photoelectron. This can also be stated from Eq. (5.19) which shows that a

higher kinetic energy is transferred to the harmonic photoelectron for a higher ponderomotive potential U_p of the probe pulse. However, the high intensity or density is limited to the small region determined by the size of the focal spot. Since in our case the harmonic beam is relatively large at the interaction region, photoelectrons are generated over an extended volume which are then recorded by the electron spectrometer. If now only in a tiny fraction of this region sideband electrons are produced by the small probe focus, their small number is obscured by the majority of primary photoelectrons. This disproportion can be mitigated if a larger focal spot size is used for the probe pulse. This way, the volumes covered by both beams in the interaction regions can be matched, at the cost of probe intensity. Another way is to reduce the volume covered by the harmonic beam. To this end, apertures of different sizes can be moved into the harmonic beam to crop the angular divergence. A different possibility is to focus the harmonic beam, which will be addressed below.

Proceeding with the measurement, we first have to find the temporal overlap between pump and probe. The overlap must first be found between the 800 nm fundamental pulse and the NOPA also set to 800 nm. The utilization of sum-frequency mixing in a nonlinear crystal between the red fundamental pulse and the green NOPA would yield a signal in the UV range invisible to the eye. The use of a two-photon photodiode is also precluded at these wavelengths since the bandgap of our two-photon photodiode allows a one-photon transition for the green NOPA. However, using 800 nm for both beams, both methods can be employed. After finding the red–red overlap inside the vacuum chamber, the zero between the green NOPA and the red fundamental can be found on the optical table using the plasma method described above. This ensures the temporal overlap between the two colors also in the vacuum chamber. However, no sidebands could be found using the NOPA set at 532 nm. Therefore we adjusted the NOPA for output at 800 nm (degeneracy point) to be used as probe. Since these pulses turned out to be much too long ($> 300\,\mathrm{fs}$), we decided to set up a new delay line in which the 800 nm fraction that pumped the NOPA could be used directly as a probe ($\approx 35 - 40\,\mathrm{mW}$ as opposed to $< 10\,\mathrm{mW}$).

The starting experiments were done in argon for two reasons: first, the photoelectrons from argons show a simple structureless spectrum (see Fig. 5.20) without additional peaks such as caused by the spin–orbit splitting, and second, since high-harmonic generation is done in argon, gas leaking from the fiber does not disturb the measurement. Since we tried looking for sidebands to no avail, we switched to the heavier noble gases, krypton and xenon. The higher polarizabilities of these gases infer higher transition dipole matrix elements, providing us with more electrons. In spite of the increased number of photoelectron counts, no sidebands could be seen.

The highly nonlinear process inherently present in high-harmonic generation poses further difficulties: Since a very high intensity is required, it can easily damage the entrance of the fibers for self-phase modulation and high-harmonic generation. These fibers have to be cleaved, rotated, or even be replaced from time to time. Moreover, the laser must always be adjusted for maximum power output since even a slight power reduction is accompanied with a slump of harmonic yield and photoelectron counts. Also, the laser has to be temporally and spatially stable, with no beam-pointing variations (fiber entrances must be hit) and power fluctutations. A changing intensity is always associated with a changing blueshift (see Sec. 3.3), shifting the photoelectron spectra accordingly. For good focusing, the beam profile should be smooth and Gaussian, and should not display any spatial chirp. The favorable conditions have to be maintained for hours to record a two-dimensional XFROG trace. The total recording time for Fig. 5.21 was about one hour and shows an excellent stability of the posi-
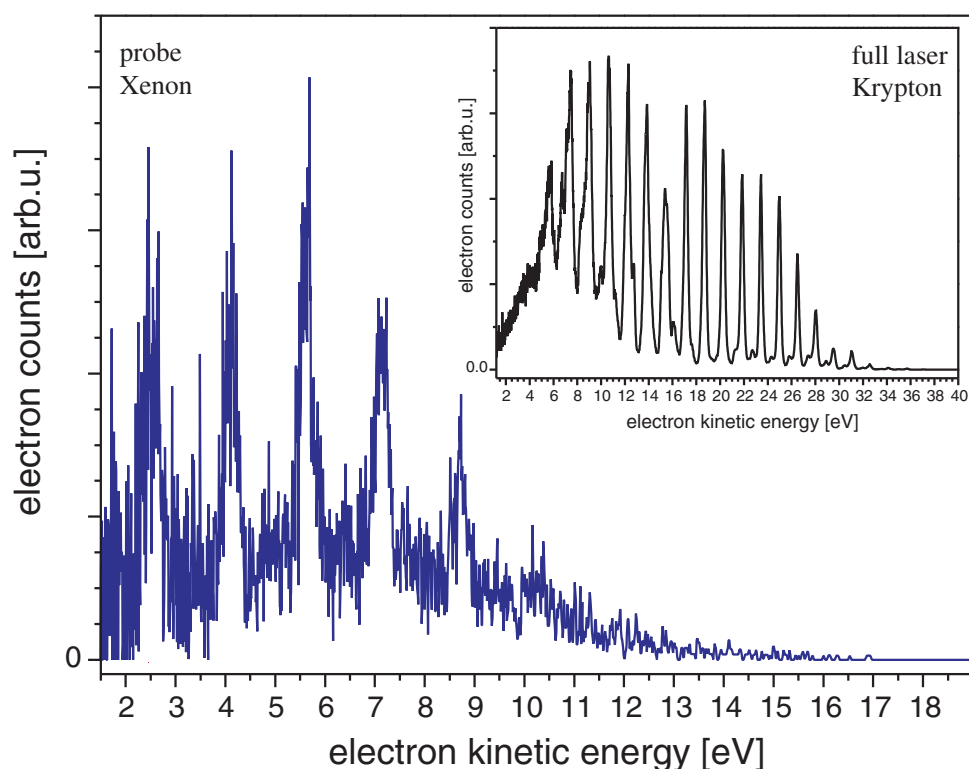
Figure 5.22 – Electron spectra resulting from the above-threshold ionization (ATI) of noble gases. The large spectrum results from the probe laser after it has been split off from the main laser after the SPM fiber and prism compressor. From the approximate position of the cut-off, a probe intensity of 1–$2 \times 10^{13}\,\mathrm{W/cm^2}$ can be estimated. The inset shows an ATI spectrum of krypton by using the full laser. For the continuous background that is present in both spectra see text.

tions of the harmonic photoelectron peaks. Often, longer measurement times were needed to increase the integration time per time step for an improved signal-to-noise ratio, which could extend recording times up to 5–8 hours.

Sometimes we were indeed able to observe sidebands in the photoelectron spectrum. However, these sidebands were independent of the pump–probe delay and did not disappear as a function of delay or when the probe beam was blocked. It turned out that these 'permanent sidebands' were caused by the residual red fundamental beam that emerges from the hollow fiber together with the harmonic radiation. Based on the geometry of our experiment, we estimate the remaining pump beam intensity at the gas jet for photoelectron generation to be in the range of 10^9–$10^{10}\,\mathrm{W/cm^2}$ which is sufficient to produce sidebands. Another proof was given by the fact that these permanent sidebands could be made to disappear by placing a thin aluminum filter behind the fiber exit and before the interaction region. This way, the fundamental beam responsible for the sidebands is blocked while the harmonics are transmitted (though attenuated) through the thin metal foil. The emergence of the permanent sidebands complicated the search for the proper sidebands because peaks at the expected positions of the sidebands are always present. It is not advisable to use the aluminum filter for the cross-correlation run due to the substantial reduction of available harmonic photons.

Another increase in probe intensity can be gained if the probe beam is split off from the main

beam *after* the SPM fiber and prism compressor (a 84/16 beamsplitter is used). The full laser is sent through the pulse-compression setup. The power of the probe pulses is approximately the same as before. However, since the pulses are much shorter (20–30 fs as opposed to 80–90 fs from the laser), a higher intensity is possible. The probe intensity can be estimated from the position of the cut-off at $10\,U_p$ in above-threshold-ionization (ATI) spectra (Fig. 5.22). In the cross-correlation experiment no sidebands were visible, although the probe intensity in the range of 1–$2 \times 10^{13}\,\text{W/cm}^2$ should be sufficient to observe the two-color ionization process according to Eq. (5.21) since it is even high enough to generate ATI electrons. For comparison, an ATI spectrum generated by the full laser in krypton is shown in the inset of Fig. 5.22. Apart from the discrete ATI peaks, a continuous part is visible in those spectra. These contributions have been observed by other groups as well as and can probably be attributed to a background of electrons freed by multi-photon ionization (MPI) which do not recollide with their parent ions and therefore do not take part in the ATI process [361]. Classically, the maximum kinetic energy for such electrons is $2U_p$ with an exponential decrease [148]. This distribution must be convolved with the transmission curve of the electron spectrometer, which has a low value for slow electrons.

A new way to match the volumina covered by harmonic and probe pulses is to focus the harmonics in order to keep the probe focus small. The main problem here arises from the poor reflectivities of materials in the soft-x-ray region. Multilayer mirrors can provide reflectivities of more than 30% in the spectral region from 10 to 60 nm. However, their bandwidth is limited to typically 2-3 nm, which allows for the selection of single harmonics only. Broadening the bandwidth by a factor of two is usually accompanied with a loss of reflectivity by a factor of two. However, a very recent publication [362] employed a three-material multilayer approach to achieve reflectivities of about 20% and to be able to control dispersion over a bandwidth between 35 and 50 eV. Standard multilayer mirrors in this wavelength region consist of periodic stacks of only two materials, such as Mo/Si or B_4C/Si. An alternative for broadband reflection is the use of metal-coated grazing-incidence mirrors. Mashiko et al. [363] examined the focusing properties of a platinum-coated ellipsoidal mirror, which is basically free from spherical aberrations and astigmatism.

For gold at normal incidence the reflectivity is less than 9% for 30 eV photons [269]. Approaching grazing incidence, reflectivities can reach values of close to unity. However, for angles different from normal incidence, astigmatism arises, creating two distinct foci [68, 295], the sagittal focus f_s and the tangential (meridional) focus f_t at

$$f_s = \frac{f}{\cos \Theta}, \tag{5.39a}$$
$$f_t = f \cos \Theta \tag{5.39b}$$

for a spherical mirror of focal length f (normal incidence) where Θ is the angle of incidence measured from the mirror normal (not the glazing angle). These formulae allow us to assess the usability of available spherical gold mirrors. The appropriate focal length was found using geometrical optics and Gaussian ABCD matrices for the divergent harmonic beam (see Sec. 2.3). The mirror with radius of curvature $R = 0.50\,\text{m}$ was installed into a mirror mount in a small vacuum chamber downstream behind the interaction region, creating a harmonic focus at an image distance of $b = 38\,\text{cm}$ in front of the electron spectrometer. The probe beam is focused to the same point with the same mirror. This requires the angle between the two incident rays to be the same as the divergence of each of the rays. Those three quantities have to be matched to ensure a common focus, which we could indeed solve in spite of geometrical
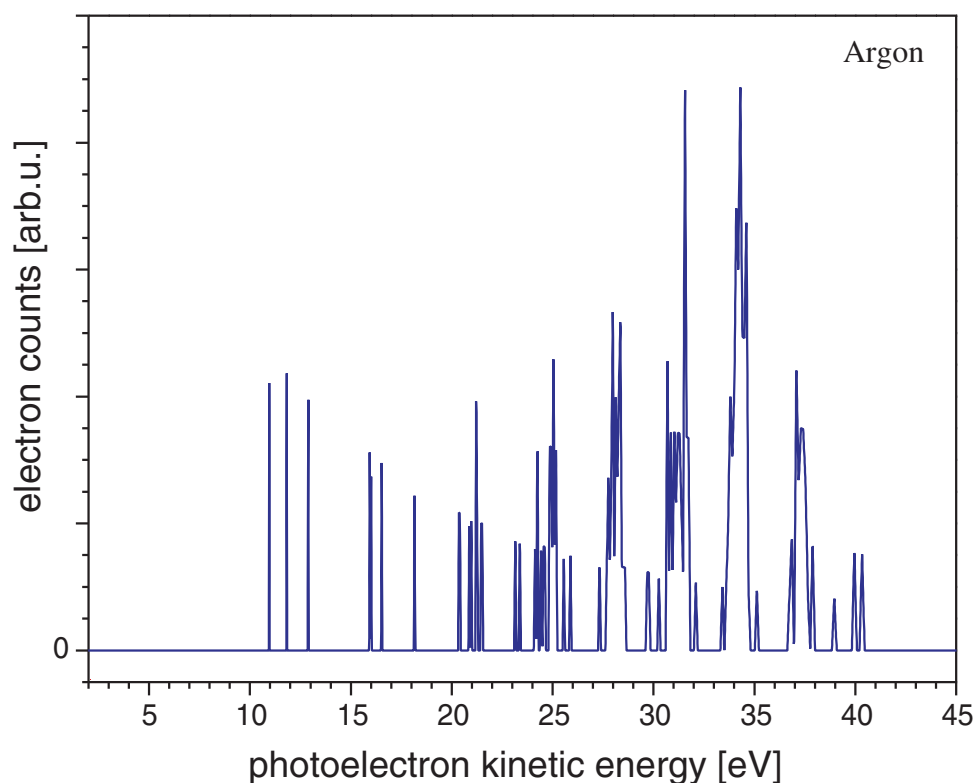
Figure 5.23 – Photoelectron spectrum of argon. The harmonic beam from the hollow fiber is focused into an argon gas jet with a curved gold mirror (see text). Very high kinetic energies can be observed for the photoelectrons from the ionization by harmonic photons. This infers the presence of very-high-order harmonics. The suppression of lower-order harmonics (as compared to Fig. 5.20) might be due to the higher divergence of the lower orders, resulting in higher losses on the path to the curved mirror and back. Another reason might be changed experimental conditions. The final explanation remains unclear.

constraints.

In consequence of experimental rebuildings and repairs, very high harmonic orders could now be observed at low pressures in the region around 25 mbar. A corresponding photoelectron spectrum in argon is shown in Fig. 5.23, which was recorded by focusing the harmonic from the fiber with the above-mentioned curved gold mirror. Another 'window' for harmonic generation (weaker signal and lower orders) was found around 130 mbar and around 450 mbar. At this highest pressure, however, strong plasma emission could be seen from the gas inside the hollow fiber. The appearance of different generation windows is due to phase matching in different pressure and fiber-mode regimes. Sidebands were still missing, so we measured the reflectivity of the gold mirror under 45° angle of incidence in a new setup directly from the harmonic photon flux on our x-ray CCD camera. Values of 1–5% were derived, which is too low for the desired cross-correlation measurement. In principle, this loss is balanced by the expected gain in intensity by about a factor of 100 due to the focusing. However, in this geometry the search for the spatial overlap equals that of a needle in a haystack.

In our quest for sidebands, several issues could still prevent us from seeing the two-photon-ionization electrons. First, space-charge effects can limit the energy resolution of the electron
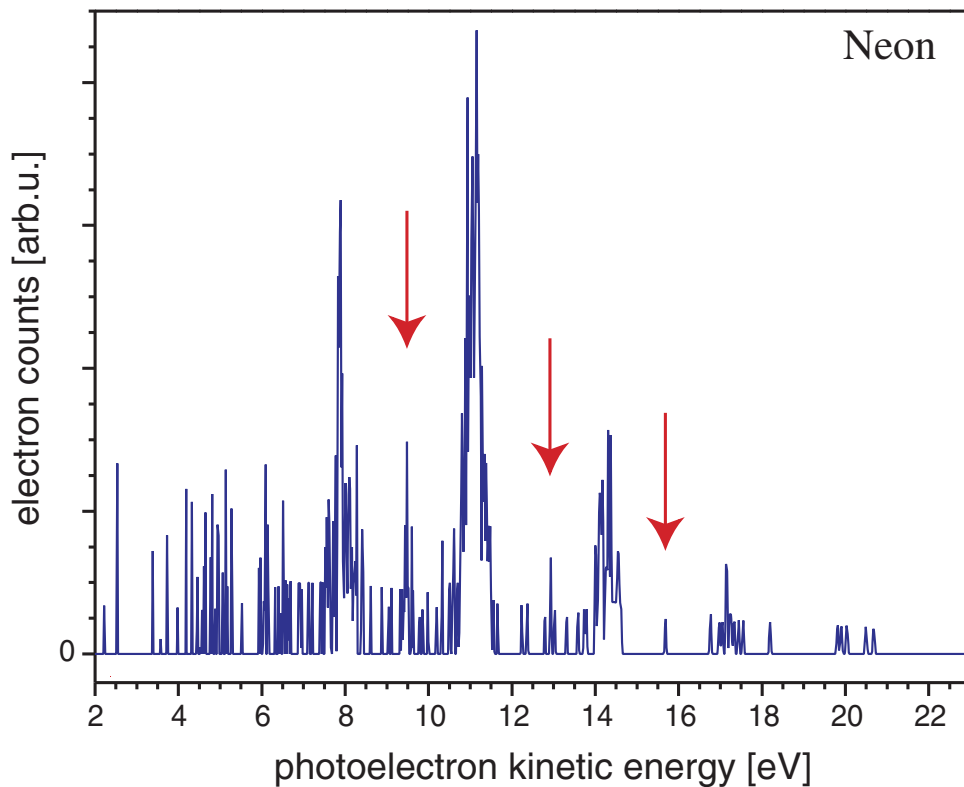
Figure 5.24 – High-harmonic photoelectron spectrum of neon. Some counts can be detected at the interpeak positions between the harmonic photoelectrons where the sidebands should appear. These peaks are very weak and unstable and cannot be reproduced reliably due to the low signal and bad signal-to-noise ratio. Neither longer integration times nor a delay scan across time zero could verify these counts to result from sideband electrons. As discussed in the text, it was not possible to observe sidebands.

spectrometer and the total number of counts by accelerating, decelerating, and deflecting the electrons. To eliminate this possibility, we used gases with higher ionization potentials such as neon or helium (Table 5.1) to reduce the number of electrons produced by ionization. For the lower-I_p gases (Ar, Kr, Xe) we observed the photoelectron spectrum while increasing the gas pressure in the interaction region. No shifts or other changes were visible, ruling out space-charge effects. Second, the volume effect mentioned above can keep us from seeing the sideband electron that might actually be produced. Therefore we exchanged the cap of our electron spectrometer for one with a smaller entrance hole ($\varnothing = 1\,\text{mm}$ instead of $3\,\text{mm}$) to confine the solid angle seen by the spectrometer. This should enhance the contribution from the sideband electrons to the overall electrons reaching the detector. The modification reduced the number of counts to about 10% (as expected from geometrical arguments), but did not produce sidebands. Third, to increase the throughput of the electron spectrometer, an evolutionary algorithm can be applied to the six-element electrostatic lens system of the spectrometer [199]. A region of interest in the photoelectron spectrum can be selected as optimization goal for the evolutionary algorithm to increase the overall count rate. A gain factor of approximately three could be achieved for a central harmonic order, however, neighboring harmonic fell off very quickly. This optimized energy window is therefore too small to reliably detect sideband electrons.

In summary the biggest problem that we face in determining the time structure of our shaped harmonics is the low energy available in the laser pulses from our laser system. Higher laser intensities would at the same time allow for a higher harmonic flux and for a more-intense probe pulse, making it possible to either use focusing optics for the harmonic beam or to expand the probe beam in the interaction region. On several occasions, photoelectrons were observed at the interpeak positions in the harmonic photoelectron spectrum. A very promising result in neon is shown in Fig. 5.24. However, the overall photoelectron signal is very weak, in spite of a long integration time of almost six minutes. Usually, the small number of photoelectrons at interpeak positions is still much lower, making the possible sidebands practically indiscernible. Moreover, for the presentation in Fig. 5.24, the spectrum has been smoothed by a binning method to reduce at least some of the noise. A scan of the delay is almost impossible. In addition, tentative sidebands were sometimes present, sometimes not. Scanning the delay sometimes showed sideband peaks for several disjunct positions of the delay, demonstrating the highly instable nature of such an experiment. High photoelectron yields would allow for short integration times, fast scans, and good signal-to-noise ratios. In an effort to reach this goal, the three-part split fiber for harmonic generation was replaced by an identical fiber with the exception that the fiber is not broken completely into three pieces, but two cuts are made at the respective positions that just touch the inner hollow capillary to allow the gas to flow in. This way, a smoother transition from one piece to the next could possibly ensure a higher laser intensity along the fiber and a higher harmonic yield. Such a cut fiber was used later in our experiments, but to no avail. No higher harmonic fluxes were obtained. Maybe a more comprehensive modification of the experimental setup will finally allow the observation of sidebands from shaped harmonics: an upgrade of the whole laser system to higher intensities, including the deployment of another amplification stage such as a bow-tie amplifier.

5.4 Attosecond pulse shaping

The experiments cited in Secs. 5.1 and 5.2 used bandwidth-limited laser pulses or laser pulses with a controlled linear chirp and high-harmonic generation was done in a gas jet. On the other hand, during our optimization of harmonic generation in a gas-filled hollow fiber, the spectral phase of the driving laser pulses is adapted continuously according to the fitness in order to reach the predefined optimization goal. This in turn modifies the harmonic phase. In addition, there are propagation effects inside the relatively long fiber compared to the focus in a gas jet or gas cell. Therefore the pulse duration of such a single adaptively selected harmonic order is completely unknown. The knowledge is crucial for spectroscopic applications since conventional filtering using gratings is accompanied with a loss in time resolution due to dispersion and a significant decrease in photon number. Therefore work is in progress (Sec. 5.3) to determine the time structure of our adaptively shaped harmonics using a cross-correlation setup. Nevertheless, some statements regarding the time structure of shaped harmonic spectra as demonstrated in this work can be made, showing the implications for attosecond pulse shaping.

Currently there is huge interest in the generation of attosecond pulses. In addition to characterization experiments cited above there are efforts to actively control the phase of high harmonics in order to get rid of its inherent wavelength dependence to produce bandwidth-limited attosecond pulses. This can be achieved using aluminum filters that have a negative
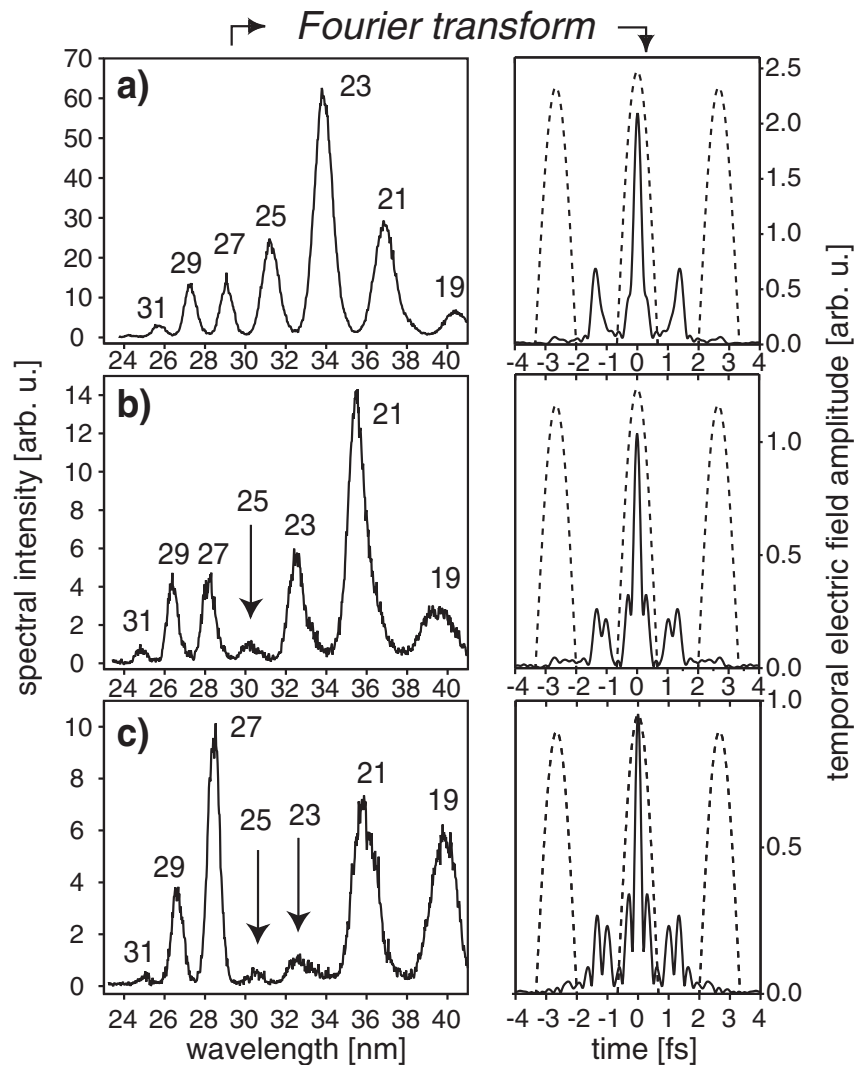
Figure 5.25 – High-harmonic spectra and their corresponding Fourier transform assuming a flat spectral phase. This assumption is reasonable since for a phase behavior that deviates too far from a well-behaved case, the duration of the generating laser pulses would increase significantly, quickly inhibiting high-harmonic generation due to the corresponding intensity decrease of the long driving laser pulses. a) The unshaped spectrum shows the periodicity of $T/2$ for the harmonic pulses in the time domain as expected. One (b) or two (c) suppressed harmonic result in an increased effective spacing of frequency components and thus in a sub-half-cycle modulation of the harmonic time structure.

dispersion in the desired energy range [215] or by designing XUV chirped mirrors [219].

A recent theoretical study [364] showed that by optimizing the chirp and initial phase of the driving laser pulses with the help of a genetic algorithm, the peak intensity of single attosecond pulses can be enhanced by one or two orders of magnitude. In addition the pulse duration is automatically greatly compressed and the optimal propagation distance determined.

Our ability to shape the spectrum of high-harmonic pulses as demonstrated in Sections 4.2 and 4.3 enables us to modify the time structure of high harmonics on an attosecond time scale.

Fig. 5.25 (left column) displays shaped harmonic spectra where one or two orders have been suppressed. The right column of Fig. 5.25 represents the corresponding Fourier transforms of these spectra, assuming a flat phase. Of course, the assumption is not valid since harmonics are known to have a remaining linear chirp. In addition, our shaped harmonics must have additional contributions from the chirp of the driving laser pulse since at least part of it is transferred to the harmonics in the fiber. However, the assumption of a flat phase as a first approximation is reasonable since for a phase behavior that deviates too far from the well-behaved case, the duration of the generating laser pulses would increase significantly, quickly inhibiting high-harmonic generation due to the corresponding intensity decrease of the long driving laser pulses.

The calculation shows interesting features caused by the suppression of one or two harmonics. Since in addition to the harmonic spacing of 2ω there is another spacing of more than 2ω between the harmonic contributions on the left and on the right of the suppressed orders, there must be a modulation in the time domain of less than half a laser period. The dotted line in Fig. 5.25 shows the envelope of the electric field with a period of T so that harmonics are generated with a period of $T/2$. This results in the harmonic spacing of $\frac{2\pi}{T/2} = 2\omega$. Since the spacing in the frequency domain is effectively larger in the presence of the suppressed orders, the period of the harmonics in the time domain is smaller than $T/2$, which means that there is a sub-half-cycle or attosecond modulation. Even though the assumption of a flat spectral phase is not true, these results are qualitatively valid and show the attosecond modifications of the harmonic pulses caused by adaptively shaping them using the pulse shaper. This consideration demonstrates the potential of our technique for extending pulse shaping into the attosecond regime.

Chapter 6

Summary

6.1 Summary (English version)

High-harmonic generation provides a powerful source of ultrashort coherent radiation in the XUV and soft-x-ray range, which also allows for the production of attosecond light pulses, a regime that had not been accessible before. Based on the unique properties of this new radiation it is now possible to perform time-resolved spectroscopy at high excitation energies (for example for the real-time investigation of the dynamics of inner-shell electrons), from which a wide field of seminal discoveries can be expected. Since the exploration and observation of the corresponding processes in turn are accompanied by the desire to control them, this work deals with new ways to manipulate and characterize the properties of these high-harmonic-based soft-x-ray pulses.

After introductory remarks on femtosecond laser science, nonlinear optics, and nonlinear frequency conversion including many aspects of the high-harmonic generation process and the properties of the high-harmonic radiation, this work first presents a comprehensive overview over recent developments and achievements on the field of the control of high-harmonic radiation in order to classify the experimental results obtained in this work.

The experimental progress achieved in this work includes the control of high-harmonic radiation both by temporally shaping and by manipulating the spatial properties of the fundamental laser pulses. In addition, the influence of the conversion medium and of the setup geometry (gas jet, gas-filled hollow fiber) was investigated.

Using adaptive temporal pulse shaping of the driving 800 nm laser pulse by a deformable mirror, this work demonstrates the complete control over the XUV spectrum of high harmonics. Based on a closed-loop optimization setup incorporating an evolutionary algorithm, it is possible to generate arbitrarily shaped spectra of coherent soft-x-ray radiation in a gas-filled hollow fiber. Both the enhancement and suppression of narrowband high-harmonic emission in a selected wavelength region as well as the enhancement of coherent soft-x-ray radiation over a selectable extended range of harmonics (multiple harmonics) can be achieved.

Since simulations that do not take into account spatial properties such as propagation effects that arise in a hollow-fiber-based setup cannot reproduce the experimentally observed high contrast ratios between adjacent harmonics, a feedback-controlled adaptive two-dimensional spatial pulse shaper was set up to examine selective fiber mode excitation and the optimization of high-harmonic radiation in such a geometry. It is demonstrated that different fiber modes

contribute to harmonic generation and make the high extent of control possible.

These results resolve the long-standing issue about the controllability of high-harmonic generation in free-focusing geometries such as gas jets as compared to geometries where the laser is guided. Temporal pulse shaping alone is not sufficient to exert the high level of control. It was possible to extend the cutoff position of harmonics generated in a gas jet, however, selectivity cannot be achieved. Therefore future work on the control of high-harmonic generation should include a combination of temporal and spatial pulse shaping in order to investigate the physical background in more detail.

As another way to increase the harmonic conversion efficiency, a novel phase-matching scheme called Temporal Quasi-Phase Matching (TQPM) was proposed in this work. The spatial modulation present in conventional quasi-phase matching schemes is transferred into the time domain by periodically modulating the envelope of an ultrashort laser pulse. The difference in phase and group velocities due to dispersion causes a walk-off between the modulated envelope and the underlying phase of the electric field. This creates temporally variable regions with high and low intensity, respectively, at the corresponding positions where normally only destructive interference would occur, resulting in phase-matched high-harmonic generation in an unmodulated waveguide.

The modifications of the high-harmonic spectrum demonstrated experimentally by temporal and spatial laser pulse shaping have direct implications for the time structure of the harmonic radiation, including the possibility for temporal pulse shaping on an attosecond time scale. To this end, known methods for the temporal characterization of optical pulses and high-harmonic pulses (determination of the harmonic chirp on femtosecond and attosecond time scales) were introduced. Some of these methods were subsequently employed. The experimental progress in this work comprises the demonstration of different setups that are in principle suitable to determine the time structure of shaped harmonic pulses based on two-photon two-color ionization cross-correlation techniques. Photoelectron spectra of different noble gases generated by photoionization with high-harmonic radiation reproduce the spin-orbit splitting of the valence electrons and prove the satisfactory resolution of our electron time-of-flight spectrometer for the temporal characterization of high harmonics. Unfortunately no positive results for this part could be achieved so far, which can probably be attributed mainly to the lack of the focusability of the high harmonics and to the low available power of our laser system.

However, we have shown that shaping the high-harmonic radiation in the spectral domain must result in modifications of the time structure on an attosecond time scale. Therefore this constitutes the first steps towards building an attosecond pulse shaper in the soft-x-ray domain.

With engineered harmonic radiation we now have a versatile tool at hand that can be adapted to experimental needs. Prospective applications of tailored high harmonics include, but are not limited to, time-resolved (pump–probe) photoelectron spectroscopy in the solid phase, e. g. for the examination of surfaces and interfaces. One of the open questions is, for instance, whether laser-induced damage in SiO_2 occurs due to multi-photon ionization or avalance ionization. Due to the high photon energies of high-harmonic radiation, photoelectrons generated by infrared and soft-x-ray photons, respectively, can be easily discriminated in such experiments. Moreover, high-harmonic photoelectrons from inner-shell levels are element-specific and are thus useful to distinguish between different elements at interfaces.

Together with the ultrashort time resolution, high harmonics open great possibilities in the

field of time-resolved soft-x-ray spectroscopy, for example of inner-shell transitions. Tailored high-harmonic spectra as generated in this work and shaped attosecond pulses will represent a multifunctional toolbox for this kind of research.

6.2 Zusammenfassung (deutsche Version)

Note: This Chapter constitutes the German translation of the summary presented in Sec. 6.1 as required by the examination regulations for dissertations in physics at the Bayerische Julius-Maximilians-Universität Würzburg.

Die Erzeugung von Hohen Harmonischen stellt eine leistungsfähige Quelle ultrakurzer und kohärenter Strahlung im extremen Ultraviolett- und weichen Röntgenbereich dar, die auch die Erzeugung von Attosekundenlichtimpulsen erlaubt, ein Bereich, der bisher nicht zugänglich war. Durch die einzigartigen Eigenschaften dieser neuen Strahlung ist es nun möglich, zeitaufgelöste Spektroskopie mit hohen Anregungsenergien (beispielsweise für die Echtzeit-Untersuchung der Dynamik von Innerschalen-Elektronen) durchzuführen, was eine Vielzahl bahnbrechender Entdeckungen erwarten lässt. Da die Erforschung und Beobachtung entsprechender Prozesse gekoppelt sind mit dem Wunsch, diese zu kontrollieren, beschäftigt sich die vorliegende Arbeit mit Wegen, die Eigenschaften dieser Röntgenpulse aus Hohen Harmonischen zu manipulieren und zu charakterisieren.

Nach einleitenden Bemerkungen über Femtosekunden-Lasertechnologie, Nichtlineare Optik und nichtlineare Frequenzkonversion, einschließlich vieler Aspekte des Prozesses der Erzeugung von Hohen Harmonischen und der Eigenschaften dieser Strahlung, gibt diese Arbeit zunächst einen umfassenden Überblick über neueste Entwicklungen und Ergebnisse auf dem Gebiet der Kontrolle von Hohen Harmonischen, um die in dieser Arbeit erreichten experimentellen Ergebnisse einordnen zu können.

Der experimentelle Fortschritt, der im Rahmen dieser Arbeit erzielt werden konnte, beinhaltet die Kontrolle der Strahlung von Hohen Harmonischen sowohl durch die zeitliche Formung als auch durch die Manipulation der räumlichen Eigenschaften der fundamentalen Laserpulse. Untersucht wurde auch der Einfluss des Konversionsmediums und der Geometrie des Aufbaus (Gasstrahl, gasgefüllte Hohlfaser).

Durch adaptive zeitliche Pulsformung der erzeugenden Laserpulse bei 800 nm mit Hilfe eines deformierbaren Spiegels zeigt die vorliegende Arbeit die komplette Kontrolle über das XUV-Spektrum von Hohen Harmonischen. Basierend auf einem Optimierungsexperiment mit einer Rückkopplungsschleife und einem evolutionären Algorithmus ist es möglich, willkürlich geformte Spektren von kohärenter Strahlung im weichen Röntgenbereich in einer gasgefüllten Hohlfaser zu erzeugen. Sowohl die Steigerung und Unterdrückung von schmalbandiger Hohen-Harmonischen-Strahlung über einen ausgewählten Wellenlängenbereich als auch die Verstärkung von kohärenter weicher Röntgenstrahlung über einen wählbaren ausgedehnten Bereich von Harmonischen können erreicht werden.

Da Simulationen ohne die Berücksichtigung von räumlichen Eigenschaften wie zum Beispiel Propagationseffekten, wie sie in einem Hohlfaser-basierten Aufbau auftreten, die experimentell beobachteten hohen Kontrastverhältnisse zwischen benachbarten Harmonischen nicht reproduzieren konnten, wurde ein rückkopplungsgesteuerter adaptiver zweidimensionaler räumlicher Pulsformer in Betrieb genommen, um die gezielte Anregung von Fasermoden und die Optimierung von Hohen Harmonischen in einer solchen Geometrie zu untersuchen.

Es wird gezeigt, dass verschiedene Fasermoden zur Erzeugung von Harmonischen beitragen und erst das hohe Maß an Kontrolle ermöglichen.

Diese Ergebnisse lösen eine lang bestehende Frage nach der Kontrollierbarkeit der Erzeugung von Hohen Harmonischen in Geometrien mit einem freien Fokus wie zum Beispiel in Gasstrahlen im Vergleich zu Geometrien, in denen der Laser geführt wird. Zeitliche Pulsformung allein reicht nicht aus, um das hohe Niveau an Kontrolle auszuüben. In einem Gasstrahl konnten zwar beispielsweise die höchsten erzeugten Harmonischen zu kürzeren Wellenlängen hin verschoben werden, eine Selektivität ist jedoch nicht möglich. Daher soll in zukünftigen Arbeiten zur Kontrolle der Erzeugung von Hohen Harmonischen auch eine Kombination von zeitlicher und räumlicher Pulsformung aufgebaut werden, um die physikalischen Hintergründe genauer zu untersuchen.

Als eine weitere Möglichkeit zur Steigerung der Konversionseffizienz von Harmonischen wurde ein neuartiges Phasenanpassungsschema mit dem Namen Zeitliche Quasi-Phasenanpassung (Temporal Quasi-Phase Matching, TQPM) in dieser Arbeit vorgeschlagen. Die räumliche Modulation von konventionellen Quasi-Phasenanpassungsschemata wird in den Zeitbereich übertragen, indem die Einhüllende eines ultrakurzen Laserpulses periodisch moduliert wird. Der Unterschied zwischen Phasen- und Gruppengeschwindigkeit aufgrund der Dispersion bewirkt ein Auseinanderlaufen der modulierten Einhüllenden und der darunterliegenden Phase des elektrischen Feldes. Dadurch werden zeitlich veränderliche Gebiete mit hoher bzw. niedriger Intensität an den Stellen erzeugt, an denen normalerweise nur destruktive Interferenz auftritt, so dass insgesamt eine phasenangepasste Erzeugung von Hohen Harmonischen in einem unmodulierten Wellenleiter möglich ist.

Die Modifizierungen des Spektrums von Hohen Harmonischen, die experimentell durch die zeitliche und räumliche Laserpulsformung gezeigt werden konnten, haben direkte Auswirkungen auf die Zeitstruktur der Harmonischen-Strahlung, einschließlich der Möglichkeit für zeitliche Pulsformung im Attosekundenbereich. Dazu wurden bekannte Methoden zur zeitlichen Charakterisierung von optischen Pulsen und Hohen-Harmonischen-Pulsen (Bestimmung des harmonischen Chirps auf Femtosekunden- und Attosekundenzeitskalen) vorgestellt, die dann teilweise angewendet werden konnten. Der experimentelle Fortschritt in dieser Arbeit beinhaltet die Demonstration von verschiedenen Aufbauten, die im Prinzip geeignet sind, die Zeitstruktur von geformten Harmonischen-Pulsen mit Kreuzkorrelationsmethoden durch Zwei-Photonen-zwei-Farben-Ionisation zu bestimmen. Photoelektronenspektren verschiedener Edelgase, die durch Photoionisation mit der Hohen-Harmonischen-Strahlung erzeugt wurden, können die Spin-Bahn-Aufspaltung der Valenzelektronen reproduzieren und belegen die ausreichende Auflösung unseres Elektronen-Flugzeit-Spektrometers zur zeitlichen Charakterisierung von Hohen Harmonischen. Leider konnten bislang keine positiven Ergebnisse zu diesem Teil erzielt werden, was sich wohl hauptsächlich auf die fehlende Fokussierbarkeit der Harmonischen und die zu niedrige zur Verfügung stehende Leistung unseres Lasersystems zurückführen lässt.

Allerdings haben wir gezeigt, dass die Formung der Hohen-Harmonischen-Strahlung im Spektralbereich Veränderungen der Zeitstruktur auf Attosekundenzeitskalen nach sich ziehen muss. Dies stellt daher erste Schritte in Richtung des Baus eines Attosekundenpulsformers im weichen Röntgenbereich dar.

Mit der formbaren Harmonischen-Strahlung haben wir nun ein vielseitiges Werkzeug zur Verfügung, das an experimentelle Bedürfnisse angepasst werden kann. Mögliche Anwendungen dieser maßgeschneiderten Hohen Harmonischen beinhalten unter anderem die zeitaufge-

löste (Anrege–Abfrage-)Photoelektronen-Spektroskopie von Festkörpern, beispielsweise zur Untersuchung von Oberflächen und Grenzflächen. Eine der offenen Fragen ist zum Beispiel, ob laserinduzierte Schäden in Siliziumdioxid durch Multiphotonenionisation oder Lawinenstoßionisation verursacht werden. Aufgrund der hohen Photonenenergien der Hohen-Harmonischen-Strahlung können in solchen Experimenten Photoelektronen, die durch infrarote Laserstrahlung bzw. durch weiche Röntgenstrahlung erzeugt wurden, leicht auseinandergehalten werden. Darüberhinaus sind die Photoelektronen von Hohen Harmonischen aus inneren Schalen elementspezifisch und sind dadurch nützlich, um zwischen den verschiedenen Elementen an Grenzflächen zu unterscheiden.

Zusammen mit der ultrakurzen Zeitauflösung eröffnen Hohe Harmonische daher viele Möglichkeiten auf dem Gebiet der zeitaufgelösten Spektroskopie im weichen Röntgenbereich, beispielsweise bei Innenschalen-Übergängen. Maßgeschneiderte Spektren von Hohen Harmonischen, wie sie in dieser Arbeit erzeugt werden konnten, und geformte Attosekundenpulse werden dabei vielseitige Werkzeuge darstellen.

Appendix A

High-harmonic generation and plasma radiation from water microdroplets

We studied the emission of XUV radiation from water microdroplets under excitation with either a single or a pair of intense femtosecond laser pulses (Ti:Sa, 80 fs, $\sim 10^{14}$ W/cm^2, 800 nm, 1 kHz). Varying the delay between the two pulses we observed a transition from pure incoherent plasma emission to coherent high-harmonic generation. Under optimized conditions we obtained high-harmonic radiation up to the 27th order.

The following presentation is directly based on our publication in Flettner et al. [253], with some additional remarks added.

A.1   Introduction

Generation of ultrashort pulses of extreme ultraviolet (XUV) light has proven able to spawn new areas of research, e. g. the rapidly growing field of ultrafast (femtosecond and attosecond time-resolved) x-ray optics [36, 37, 365] and microscopy [276]. Laser to XUV frequency conversion can also be employed for commercial applications such as nanoscale lithography and quality inspection purposes. Conversion efficiencies are on the order of one percent [366, 367].

Microdroplets turned out to be very efficient media to convert visible laser radiation into the XUV and soft x-ray spectral region [366, 367]. So far, however, they have only been used as sources of incoherent XUV light being emitted into a solid angle of 4π [366]. To collect a large amount of this radiation sophisticated optics have to be employed. A much more desirable light source for many applications would feature a fully coherent directional emission, which is provided by high-order harmonic generation (HHG). In this process, laser radiation is converted into integer multiples of its fundamental wavelength up to very high orders ($\sim$300 [124]). This phenomenon occurs when intense ultrashort (femtosecond) laser pulses interact with a dielectric medium. Classically speaking, initially bound electrons are field-ionized at particular phases of the laser electric field (close to its maximum) and are driven away from their parent ion. As soon as the electric field of the laser reverses, the electrons decelerate on their outward bound path, stop and accelerate back towards their parent ions. Some of the ionized electrons finally return to the ion core they left and recombine. At the time of recombination the electrons generally possess nonzero kinetic energy. One photon per electron

is emitted carrying the sum of the electron's kinetic energy plus the ionization potential I_p. Classical and quantum calculations show that the maximum photon energy to be emitted in this process scales as $\hbar\omega = I_p + 3.17 U_p$, where U_p represents the ponderomotive potential, i.e. the average quiver energy of the electron in the laser field [125, 136].

Harmonic generation has become a vivid field of research during the last decade and our understanding of the processes has indeed reached a considerable extent *for atomic systems*. HHG in molecular and cluster media has not been widely studied so far and even less do we really understand about the mechanisms in these more extended systems. From recent experiments we know that molecular HHG is sensitive to the alignment of the molecules [368, 369]. Experiments recently performed in our group show that molecular media are relatively more efficient than atoms in HHG when the driving field is elliptically polarized in a sense that the harmonic conversion efficiency in molecules drops more slowly for higher ellipticities [370]. An interpretation of this finding is based upon the larger spatial extent of the molecule [221]. A recent theoretical study sheds some light on the process of harmonic generation in extended systems [371]. There it is shown that already simple diatomic *molecular* systems can easily be manipulated to increase the harmonic yield by large amounts, exceeding the nonlinear single *atom* response by far. Other considerations based on symmetry properties of molecules show that in systems possessing discrete rotational symmetry only particular harmonic orders are produced [372], which is desirable for wavelength selection. HHG on solid state systems is under investigation [263, 373], however restricted to the surface of the solid material. Coherent frequency conversion in bulk solid-state systems could finally promise very high efficiency, due to the large nonlinear susceptibilities present in high-density media.

In this sense, HHG on water droplets can be regarded as a pioneering experiment in this direction. In contrast to liquid jets having infinite extent on the scale of the laser focus, water droplets provide mass-limited targets. Due to their spherical symmetry and their small dimensions, their expansion dynamics after plasma formation are readily tractable for models and can thus be understood more easily.

In this study we show that a strong interdependence of HHG and plasma radiation exists. Our observation points to the fact that both radiation processes cannot happen simultaneously.

The droplets start to expand after the interaction of a strong prepulse (from here on referred to as pump pulse). Thus, we can directly assess different density regimes ranging continuously from liquid down to gaseous by employing a second (driver) pulse which generates the high-harmonic radiation. Using this pump-drive scheme we gain insight up to which densities HHG is possible, which is an important issue for efficiency considerations.

Another interesting feature about microdroplets is their breaking up into nanometer-sized fragments upon irradiation by a strong pulse. Such clusters are extensively studied with respect to their unique frequency conversion properties [17, 262, 374]. In some of these studies it has been shown that clusters can be used to reach conversion efficiencies for incoherent plasma radiation comparable to those obtained in solid state systems. HHG in clustered media turned out to occur at smaller intensities, to have a higher photon energy cutoff and to saturate at higher laser intensities as compared to mono-atomic targets. The effects of a prepulse on the laser-induced EUV radiation conversion efficiency from water droplets based on direct line transitions (e. g. 13 nm corresponds to the strong $O^{5+}(4d) \rightarrow (2p)$ transition) has been investigated by Düsterer et al. [375]. Other studies of the EUV yield have been performed by Rajyaguru et al. [376]. Microdroplets plasmas are also exploited for the generation of energetic electrons and protons [377, 378].
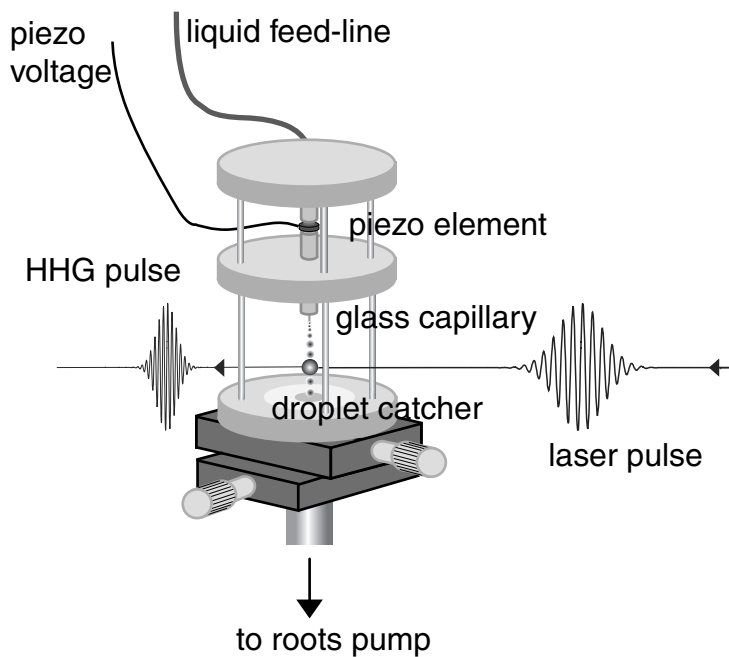
Figure A.1 – Schematic setup. The glass capillary is mounted inside a vacuum chamber. The water droplet jet is produced vertically downwards. A piezo element can be used to control the droplet repetition rate. Droplets not used in the experiment are removed by direct pumping with a roots pump. Laser pulses interact with the water droplet jet ~5 mm below the capillary exit to induce plasma luminescence or HHG.

Here we present experimental results on high-order harmonic generation from water-droplets, with harmonic orders up to the 27th. To our knowledge, this is the highest harmonic order ever observed from water. So far, harmonic generation from water only up to the seventh order has been reported [379].

A.2 Setup and Droplet Characterization

The water microdroplets are produced by a glass capillary of 10 μm inner diameter backed with liquid water (see Fig. A.1). With a controlled fluid pump the pressure can be kept constant in a range of 2 to 5 MPa. The capillary and the fluid pump are commercial products of 'Microjet Components' (Sweden). The capillary is mounted vertically such that the water leaves at the lowermost end. A continuous water jet streams out of the capillary. After a certain propagation distance droplets are formed due to the Rayleigh-Taylor instability. To ensure reproducible droplet sizes, the capillary is equipped with a piezo transducer to modulate the capillary diameter. Applying a high-frequency voltage of 15 V results in a fixed droplet repetition rate. The frequency has to be close to the 'natural' repetition rate given by the Rayleigh-Taylor instability. In our case, these frequencies are between 0.9 and 1.1 MHz. In Fig. A.2 we show photographs of the droplet jet taken with a microscope objective and a CCD camera. The jet was illuminated by laser pulses incident on a screen placed behind the jet. When the backing pressure is increased, larger droplet diameters are obtained. On the other hand, increasing the piezo-frequency results in smaller droplets.

For the XUV emission experiments, the capillary is mounted inside a vacuum chamber to avoid reabsorption of the generated radiation by air or the water vapor. With a 880 l/s turbo pump we achieved a background pressure of $\sim 2 \cdot 10^{-3}$ mbar. Differential pumping stages along the way to the spectrometer lowered the pressure further until it reached $\sim 10^{-5}$ mbar at the spectrometer. At a distance of ~ 5 mm below the exit of the capillary, the laser beam interacts with the droplet jet (see Fig. A.1). Further down, after ~ 40 mm, the jet enters
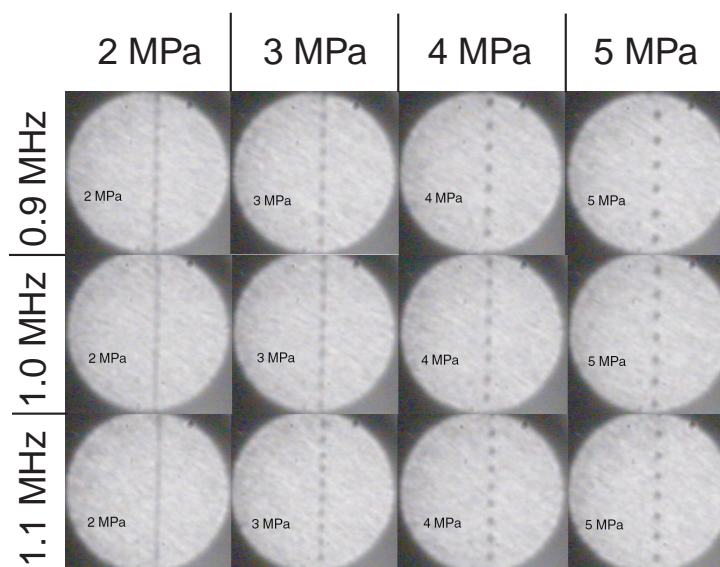
Figure A.2 – Droplet size characterization. Increasing the backing pressure results in larger droplets. An increase of the piezo AC frequency decreases the droplet diameter.

through a small diameter aperture (0.5 mm) into a separate "catcher" compartment, which is kept evacuated directly by a roots pump. In order not to damage the pumps, a liquid nitrogen cooled cold trap is installed between the chamber and the pump. As liquid water at room temperature brought into vacuum tends to freeze and grow stalagmites where it hits an obstacle, it is important to keep the catcher at an elevated temperature of about 350 K. If the temperature is too low, ice stalagmites will grow all the way up to the exit of the capillary, preventing stable operation of the jet.

The laser is a regeneratively amplified Ti:sapphire system from 'Spectra Physics' (Millennia-Tsunami, Merlin-Spitfire) delivering pulses of 80 fs pulse duration, 0.8 mJ energy per pulse, 800 nm central wavelength at a repetition rate of 1 kHz. Focusing with a 20 cm focal length lens provides laser intensities on the order of $5 \cdot 10^{14}$ W/cm^2.

We detect the emitted XUV radiation with different monochromators for two different photon energy ranges. The low energy radiation is characterized by a home-built Seya-Namioka monochromator (referred to as MC1) with a spherical concave grating. The full scanning range provides access to harmonic orders three (H3) to nineteen (H19). A scintillator (Na-salicylate) behind the exit slit is used to convert the XUV radiation into the visible. A photomultiplier is then used to acquire the spectrum as the grating rotates. The signal is DC-converted by a boxcar-averager which is read by a computer. The other monochromator (MC2) consists of a toroidal concave grating illuminated under grazing incidence. The accessible photon energy range extends from ~20 eV (H13) to around 80 eV corresponding to H51. The spectrum is acquired with a back-side illuminated thinned X-ray CCD camera ('Roper Scientific'). With plasma emission lines, we were able to estimate the resolution of the spectrometer to be better than 0.3 nm in a wavelength range of 17 to 25 nm. Fig. A.1 displays a schematic view of the droplet system. The system is aligned in such a way that the laser beam propagates directly into the spectrometer. For detecting harmonic orders greater than H17, we inserted two aluminum filters (thicknesses 0.3 and 0.8 μm) in order to block the fundamental light.

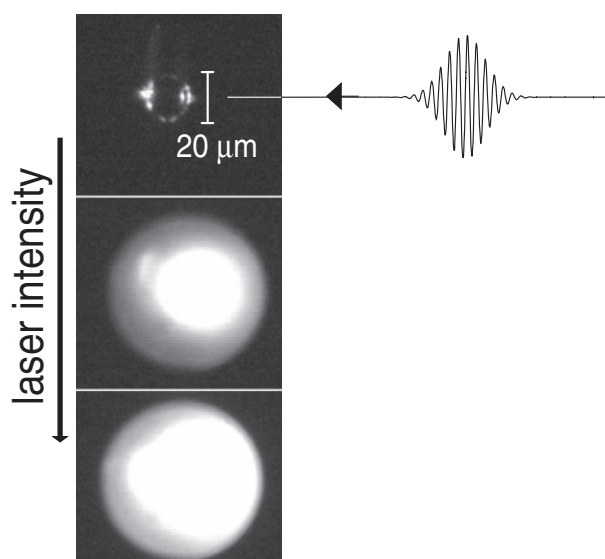**Figure A.3** – Photographic images of water droplets for irradiation with different laser intensities. Laser pulses arrive from the right hand side as indicated. Intensity increases from top to bottom. The top picture shows the unperturbed droplet. The center and bottom picture were taken through a BG40 filter to remove contributions of the fundamental laser radiation. An increasing amount of light is emitted from the laser input side of the droplet.

A.3   Experiments

For the experiments presented in this work, the droplet-generating system was operated at a backing pressure of 5 MPa. The piezo driver was not used, i.e. the jet was operated in the free-running Rayleigh-Taylor instability regime. Under this conditions water droplets with a diameters of about 20 μm were produced.

Fig. A.3 is a photographic picture of a water droplet illuminated by different laser intensities. For the medium (center picture) and high intensities (lower picture) a BG40 filter was used to suppress the fundamental laser light. For very low intensity, only the unperturbed spherical droplet is visible, while at increasingly higher intensities we observe bright light from the front face (towards the laser) of the droplet. Two possible explanations for this finding are: (1) Optical breakdown and plasma mirroring of the fundamental laser radiation close to the front face of the droplet or (2) plasma emission [380] from a backward directed emission plume of the droplet similar to the one reported by Eickmans et al. [381].

Regarding emission spectra, we first of all show results for single laser pulses interacting with the microdroplets. Employing the spectrometer MC2, we detect strong plasma recombination light emitted from the droplets. Comparison with literature values [382, 383] shows that the lines can be attributed to highly ionized oxygen (up to O^{5+}). We can observe the spectrum only for wavelengths longer than 17 nm, which is the L edge of Al.

No high-harmonic emission for orders H17 and higher could be observed using a single laser pulse. Switching to spectrometer MC1 without Al filters third harmonic emission can faintly be observed. We measure single photon events of the fifth harmonic on the photomultiplier about each 5000 laser shots. No harmonic signal for higher orders is detected. This situation changes dramatically when we distribute our pulse energy between two pulses. In a first approach, we used the Pockels cell of the regenerative amplifier to release two pulses spaced by the round-trip time of the laser cavity, which is 10 ns. The material dispersion corresponding to an additional round-trip of the second pulse results in an increase of its pulse duration to $\sim$300 fs and a frequency upchirp. However, by switching from single pulse to this double pulse operation mode a large increase (by about three orders of magnitude) in harmonic generation efficiency could be observed for the third and the fifth harmonic. In Fig. A.5 we show
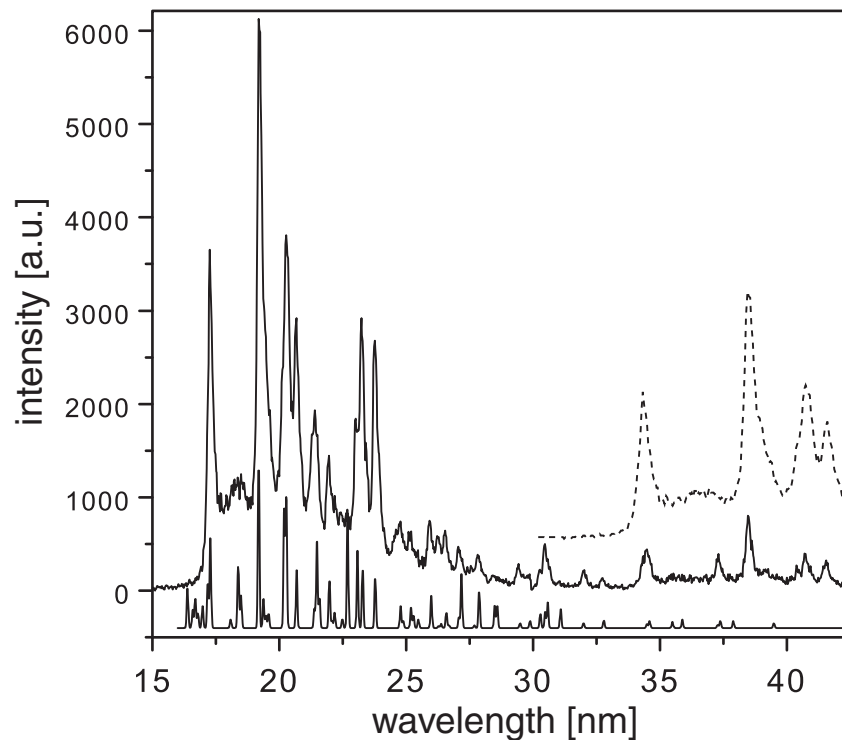
Figure A.4 – Typical plasma emission spectrum observed in our experiments for short pump-drive pulse delays. Literature values for emission lines of highly ionized oxygen (O^{4+}, O^{5+}) are plotted underneath. The cutoff for frequencies below 17 nm is due to the absorption edge of the aluminum filter. Signal at longer wavelengths is partly caused by the second diffraction order of the spectrometer grating. For better visibility, the detected first order signal has been manually converted to second order (dotted line).

harmonic emission spectra for lower orders (H3-H11) acquired using MC1.

In order to obtain a deeper insight into the droplet dynamics, we set up a delay stage to control the time delay between pump and driver pulse. For these pump-drive experiments, we use a noncollinear excitation geometry. The pump laser pulse does not enter the spectrometer directly, while the driver one does. XUV emission characteristics from the water droplets change qualitatively at a certain delay time (~650 ps), which is shown in Fig. A.6. At early times, only plasma emission can be observed (in second diffraction order) while at later times HHG is present almost exclusively. At a time delay of ~650 ps, a rapid transition occurs leading to inhibition of plasma emission and promotion of HHG. This observed behavior can be explained as follows: I) The first pulse ionizes the water molecules creating a hot and dense plasma [384, 385] with nearly solid state density. Dense plasmas are well known as efficient emitters of line radiation. If the delay between the two pulses is small both pulses contribute evenly to the heating of the plasma. II) The hot and dense plasma starts to expand immediately. The second pulse interacts with a less dense plasma resulting in a reduced conversion efficiency. Similar behavior has also been observed using Ar and Kr microdroplets. McNaught et al. [367] have measured a decay time of the plasma emission of a few hundreds of ps, which is in agreement with our observations. III) After 600 ps we have estimated a density where the average distance between atoms is greater than the classically calculated excursion length of the electron during HHG. This gives the electrons the chance to return to
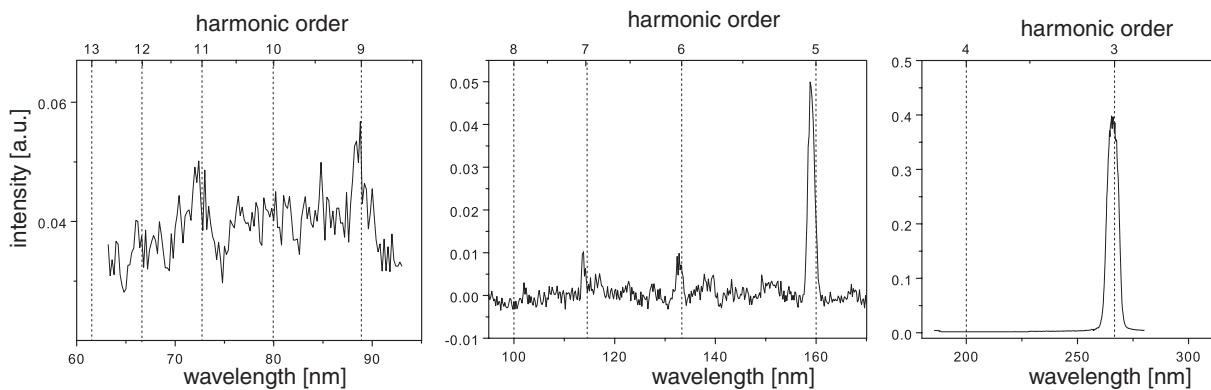
Figure A.5 – Lower-order harmonic emission spectra detected for droplets interacting with a double pulse (see text). Harmonics from order H3 up to H11 can be detected with decreasing emission strengths. The signal close to the sixth harmonic can be attributed to a strong plasma line.
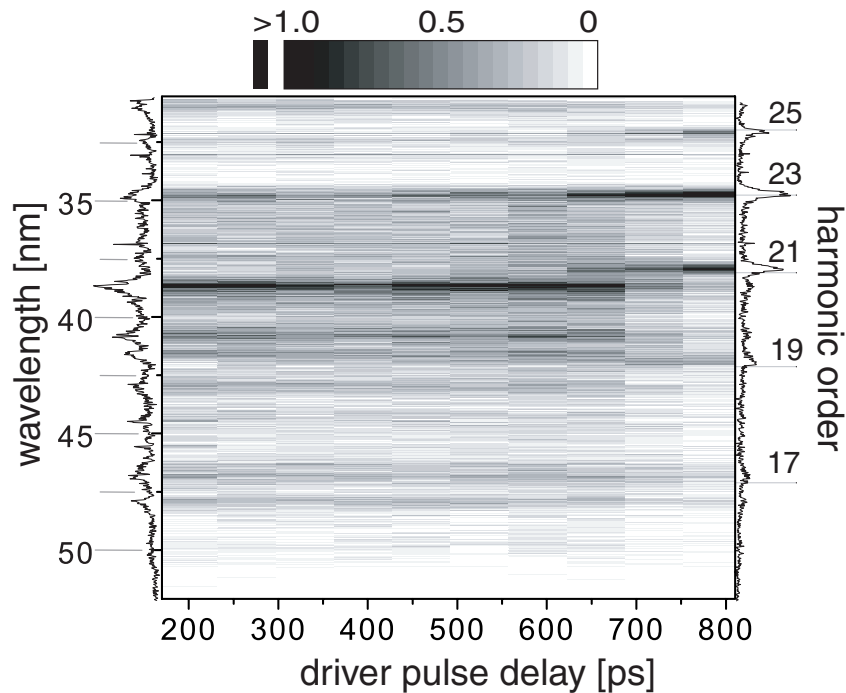
Figure A.6 – Transient XUV-emission spectrum for the pump-drive setup. A transition occurs at ~650 ps from a regime where only plasma luminescence is detected (in second diffraction order) into a different one with high-harmonic generation being the dominant contribution to the spectrum.

their parent ion without colliding with other molecules which would impair the generation of spatially and temporally coherent high-harmonic radiation. Besides the single particle response propagation effects play a major role in HHG. Therefore we have to consider a significant spatial and temporal distortion by the existing and newly generated plasma. After ~1 ns the plasma generated by the combined action of the two pulses is subcritical. This
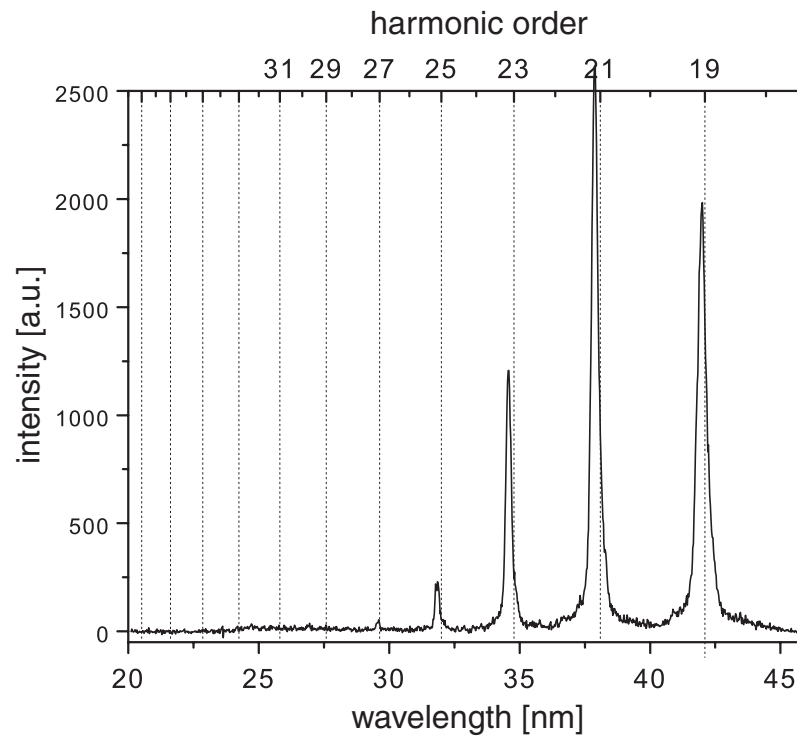
Figure A.7 – High harmonics in the cutoff region of the spectrum acquired at a time delay of ∼1 ns.

explains why the increase in high-harmonic signal at a particular time delay coincides with the decline of plasma line emission, since effective plasma heating by the second pulse rules out its undisturbed propagation through the medium. Additionally, as long as the electron density is too high, phase-matching between the high-harmonic radiation and the fundamental is not possible over significant length scales.

We show the highest harmonic orders observed to date in our experiments in Fig. A.7. They were recorded for a time delay of ∼1 ns with the MC2 spectrometer using the Al filters mentioned above. Within the three-step model of HHG introduced by Corkum [125] and Kulander et al. [126] applying our driving pulse intensities of $\sim 2 \cdot 10^{14} \mathrm{W/cm^2}$ yields a harmonic cutoff frequency ($I_p(H_2O)$=12.6 eV) around the 33rd harmonic. This can be regarded to be in accordance with the experimental position of the cutoff (∼27th harmonic), in particular since the laser intensity corresponds to the value obtained when focusing into vacuum. In our experiment however, we expect defocusing of the incoming laser due to plasma build-up.

A.4   Conclusion

We report the observation of HHG up to the 27th order in water microdroplets for the first time to our knowledge. This can be achieved only for slightly expanded droplets, whereas it is absent for laser interaction with unperturbed droplet targets. In the latter case, only

plasma luminescence from highly charged states of oxygen (up to O^{5+}) can be observed. Depending on the delay of the driver pulse (generating harmonics) with respect to a pump pulse (expanding the droplet) we can observe a sharp transition from a regime (for short time delays) where only plasma recombination light is emitted into another region (at longer time delays) where HHG takes place with negligible contribution from plasma emission.

By means of our pump-drive setup, using water droplets as providers of high density material, it becomes possible to study HHG in media of particle densities spanning the entire range from liquid state down to gaseous density. In order to push HHG conversion efficiency to the maximum, we must acquire knowledge about which are the maximum tolerable particle densities. On the other hand, once limitations to maximum density are encountered, our experimental environment will serve as a versatile tool and testbed in finding ways to overcome these problems. These studies will be the subject of future work in our group.

This work is carried out in an effort to spur further research on the subject of HHG in extended systems i.e. other than monoatomic ones which are the ones currently routinely used. The latter can be regarded as very well understood and almost optimally exploited. On the other hand, large improvements in coherent XUV generation efficiency are to be expected by switching to molecular [371] or even more complex media.

Appendix B

TOF computer program

In order to facilitate the evaluation of the time-of-flight data recorded by the multiscaler card for the multichannel-plate detector in the time-of-flight spectrometer, a LabView programm called

    p7887_eTOF-master.llb\p7887_eTOF-master.vi

was written and constantly extended according to our needs. This program can read the electron time-of-flight from the multiscaler card and transform the spectra into the energy domain to make it easy to evaluate the peak positions. A screenshot of the program in offline-mode is displayed in Fig. B.1. In this offline-mode, the program allows to view saved spectra sequentially and randomly. All experimental parameters such as the actual delay position or the integration time are saved in addition to the raw bins from the multiscaler card. Recording the raw bins allows to recalibrate the electron spectra at any later time. By selecting the online mode in the 'mode of operation' box the program directly reads the electron spectra from the multiscaler card and allows to make an automatic delay scan for pump–probe measurements by controlling the delay stage. Several other features such as the use of a shutter or sending a trigger signal for the acquisition of a harmonic photon spectrum with the soft-x-ray CCD camera are also implemented.

For the analysis of the two-dimensional data as recorded for the delay scans (spectrum vs. time), a complementary LabView program

    p7887_eTOF-viewer2.llb\p7887_eTOF-view-calibrated-2D.vi

was developed. In addition to displaying a full two-dimensional XFROG trace (cf. Fig. 5.21) on-the-fly by simply selecting the appropriate data folder in an automatically generated list of saved measurements, it also allows to view single spectra where regions of interest (e. g. the expected positions of the sidebands) can be selected with cursors and be energy-integrated in order to spot the appearance of sidebands for easily. This viewer program can be used during a running measurement because it watches the data folder for new measurements and add the most recent photoelectron spectra automatically to the two-dimensional view.
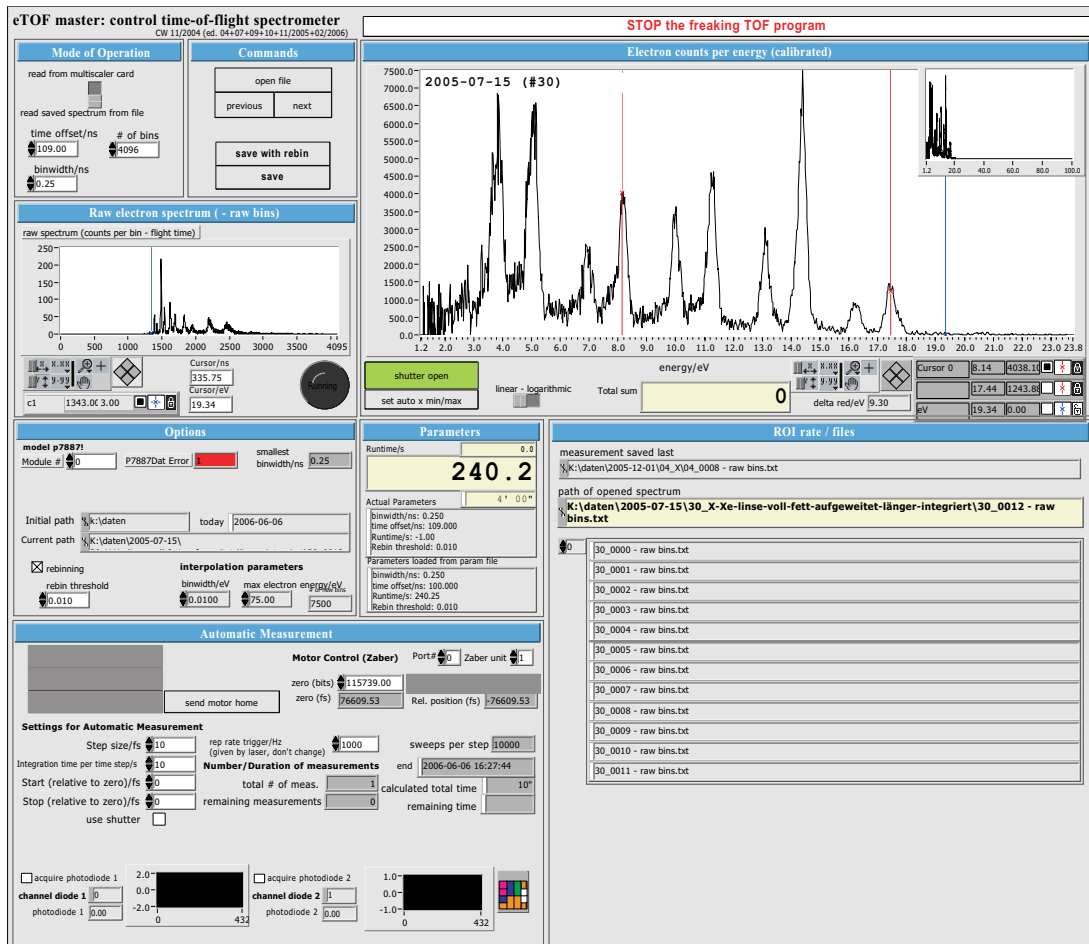
Figure B.1 – Screenshot of the eTOF master program written with LabView (offline mode). This program can read the electron time-of-flight from the multiscaler card and transform the spectra into the energy domain. It also allows to view saved spectra sequentially and randomly, and to make an automatic delay scan for pump–probe measurements. Several other features such as the use of a shutter are also implemented.

Appendix C

Useful formulae and rules-of-thumb

The following paragraphs present a compilation of useful general formulae and rules-of-thumb for the daily lab use and quick estimates. These are not formulae such as the harmonic cut-off law (Eq. (3.54)) but mostly equations for the conversion of several different units. The quantities used should be self-explanatory.

Wavelength–to–energy conversion:

$$E[\text{eV}] = \frac{1240}{\lambda[\text{nm}]}, \tag{C.1a}$$

$$\lambda[\text{nm}] = \frac{1240}{E[\text{eV}]}. \tag{C.1b}$$

Ponderomotive potential:

$$U_p[\text{eV}] = 0.93 \times 10^{-13} I[\text{Wcm}^{-2}]\,\lambda^2[\mu\text{m}^2]. \tag{C.2}$$

Time–bandwidth product for bandwidth-limited ultrashort laser pulses:

$$\Delta\tau[\text{fs}]\,\Delta\lambda[\text{nm}] \approx 1000. \tag{C.3}$$

Optical cycle T and angular frequency ω at 800 nm:

$$T \quad \approx 2.67\,\text{fs}, \tag{C.4a}$$

$$\omega \quad \approx 2.36\,\text{fs}^{-1}. \tag{C.4b}$$

Electric field E, intensity I:

$$E[\text{V/cm}] = 27.4\sqrt{I[\text{W/cm}^2]}. \tag{C.5}$$

Acknowledgments

This work would not have been possible without the continuing support from a number of people. It is a pleasure for me to thank them at this point.

I am especially indebted to my supervisor Professor Dr. Gustav Gerber who gave me the opportunity to work in his group on a great project combining laser physics and laser engineering, high-intensity laser–matter interaction, time-resolved XUV spectroscopy, the generation, shaping, and application of coherent soft x-rays, and attosecond physics. He had recommended to me to work with Professor Mike Downer during my stay in Austin, Texas, who made me delve into the field of nonlinear optics. Professor Gerber also sent me to a number of conferences where I could present my work and learn about recent results in my research field.

I am grateful to Professor Dr. Christian Spielmann for a lot of fruitful discussions during weekly meetings and support on the experiments in the lab. I acknowledge his readiness to give advice on various topics.

It is a pleasure to acknowledge the cooperation with and the assistance of Dr. Thomas Pfeifer and Dominik Walter during the first part of this work on the temporal and spatial control of high harmonics, and of Alexander Paulus during the second part on photoelectron spectroscopy and characterization of shaped harmonic spectra, for long hours of alignment, setup, tweaking, and data taking involving several highly nonlinear processes. They all resolved with me difficult and strange problems during the daily work in a high-intensity femtosecond laboratory. I also thank my other collegues and diploma students in the high-harmonic-generation group over the years, Robert Spitzenpfeil, Thomas Sokollik, Frank Dimler, Ron Kemmer, Jan Lohbreier, Marisa Mäder, Stefan Eyring, Sebastian Jung, and Nico Franke. I acknowledge that I have benefitted from physical and technical advice from them in the lab.

I acknowledge the work done on various topics in our lab by the advanced lab students Daniel Kurfeß, Philipp Mertsch, Dimitri Ebel, Stefan and Melanie Eyring, Alexander Heinz, Daniel Höhne, Andreas Wörle, Matthias Ossadnik, and Stefan Scharf.

I could also draw upon the diverse expertise of my collegues from the other labs in the group, among them Patrick Nürnberger, Gerhard Vogt, Gerhard Krampert, Christian Tutsch, Florian Langhojer, Sandra Dantscher, Dr. Tobias Brixner, and Prof. Dr. Walter Pfeiffer.

I would also like to thank the readers of earlier versions of this work, Alexander Paulus, Sebastian Jung, and Beate Winterfeldt.

I am thankful for the handling of lab-related work to the computer administrators Robert Spitzenpfeil, Dominik Walter, and Christian Dietl, to our technical and administrative staff Helga Schwark, Monika Seifer, and Diep Phan, and especially to the machine shop with the most helpful assistance of Rainer Brauner and his collegues.

I acknowledge the continued financial support from the Studienstiftung des deutschen Volkes (German National Adademic Foundation) through their support program for doctoral students, and some other organizations for travel grants to various conferences.

I am especially indebted to my wife Beate who supported me with a lot of understanding and love.

Bibliography

[1] T. Baumert, M. Grosser, R. Thalweiser, and G. Gerber, *Femtosecond time-resolved molecular multiphoton ionization: The Na$_2$ system*, Phys. Rev. Lett. **67**, 3753 (1991).

[2] A. H. Zewail, *Femtochemistry: Atomic-scale dynamics of the chemical bond*, J. Phys. Chem. A **104**, 5660 (2000).

[3] R. S. Judson and H. Rabitz, *Teaching lasers to control molecules*, Phys. Rev. Lett. **68**, 1500 (1992).

[4] C. J. Bardeen, V. V. Yakovlev, K. R. Wilson, S. D. Carpenter, P. M. Weber, and W. S. Warren, *Feedback quantum control of molecular electronic population transfer*, Chem. Phys. Lett. **280**, 151 (1997).

[5] A. Assion, T. Baumert, M. Bergt, T. Brixner, B. Kiefer, V. Seyfried, M. Strehle, and G. Gerber, *Control of chemical reactions by feedback-optimized phase-shaped femtosecond laser pulses*, Science **282**, 919 (1998).

[6] R. J. Levis, G. Menkir, and H. Rabitz, *Selective bond dissociation and rearrangement with optimally tailored, strong-field laser pulses*, Science **292**, 709 (2001).

[7] T. C. Weinacht, J. L.White, and P. H. Bucksbaum, *Toward strong field mode-selective chemistry*, J. Phys. Chem. A **103**, 10166 (1999).

[8] T. Brixner, N. H. Damrauer, P. Niklaus, and G. Gerber, *Photoselective adaptive femtosecond quantum control in the liquid phase*, Nature **414**, 57 (2001).

[9] J. L. Herek, W. Wohlleben, R. J. Cogdell, D. Zeidler, and M. Motzkus, *Quantum control of energy flow in light harvesting*, Nature **417**, 533 (2002).

[10] A. M. Weiner, D. E. Leaird, J. S. Patel, and J. R. Wullert, *Programmable femtosecond pulse shaping by use of a multielement liquid-crystal phase modulator*, Opt. Lett. **15**, 326 (1990).

[11] A. M. Weiner, *Femtosecond pulse shaping using spatial light modulators*, Rev. Sci. Instrum. **71**, 1929 (2000).

[12] T. Baumert, T. Brixner, V. Seyfried, M. Strehle, and G. Gerber, *Femtosecond pulse shaping by an evolutionary algorithm with feedback*, Appl. Phys. B **65**, 779 (1997).

[13] D. Yelin, D. Meshulach, and Y. Silberberg, *Adaptive femtosecond pulse compression*, Opt. Lett. **22**, 1793 (1997).

[14] K. Yamane, Z. Zhang, K. Oka, R. Morita, M. Yamashita, and A. Suguro, *Optical pulse compression to 3.4fs in the monocycle region by feedback phase compensation*, Opt. Lett. **28**, 2258 (2003).

[15] M. M. Murnane, H. C. Kapteyn, M. D. Rosen, and R. W. Falcone, *Ultrafast x-ray pulses from laser-produced plasmas*, Science **251**, 531 (1991).

[16] A. Rousse, P. Audebert, J. P. Geindre, F. Falliès, J. C. Gauthier, A. Mysyrowicz, G. Grillon, and A. Antonetti, *Efficient kα x-ray source from femtosecond laser-produced plasmas*, Phys. Rev. E **50**, 2200 (1994).

[17] T. Ditmire, T. Donnelly, R. W. Falcone, and M. D. Perry, *Strong x-ray emission from high-temperature plasmas produced by intense irradiation of clusters*, Phys. Rev. Lett. **75**, 3122 (1995).

[18] J. Andruszkow et al., *First observation of self-amplified spontaneous emission in a free-electron laser at 109 nm wavelength*, Phys. Rev. Lett. **85**, 3825 (2000).

[19] H. Wabnitz, L. Bittner, A. R. B. de Castro, R. Döhrmann, P. Gürtler, T. Laarmann, W. Laasch, J. Schulz, A. Swiderski, K. von Haeften, et al., *Multiple ionization of atom clusters by intense soft x-rays from a free-electron laser*, Nature **420**, 482 (2002).

[20] V. Ayvazyan, N. Baboi, J. Bähr, V. Balandin, B. Beutner, A. Brandt, I. Bohnet, A. Bolzmann, R. Brinkmann, O. Brovko, et al., *First operation of a free-electron laser generating gw power radiation at 32 nm wavelength*, Eur. Phys. J. D **37**, 297 (2006).

[21] Y. Silberberg, *Physics at the attosecond frontier*, Nature **414**, 494 (2001).

[22] X. F. Li, A. L'Huillier, M. Ferray, L. A. Lompré, and G. Mainfray, *Multiple-harmonic generation in rare gases at high laser intensity*, Phys. Rev. A **39**, 5751 (1989).

[23] J. J. Macklin, J. D. Kmetec, and C. L. Gordon, III, *High-order harmonic generation using intense femtosecond pulses*, Phys. Rev. Lett. **70**, 766 (1993).

[24] A. L'Huillier and P. Balcou, *High-order harmonic generation in rare gases with a 1-ps 1053-nm laser*, Phys. Rev. Lett. **70**, 774 (1993).

[25] T. H. Maiman, *Stimulated optical radiation in ruby*, Nature **187**, 493 (1960).

[26] N. Bloembergen, *From nanosecond to femtosecond science*, Rev. Mod. Phys. **71**, S283 (1999).

[27] P. A. Franken, A. E. Hill, C. W. Peters, and G. Weinreich, *Generation of optical harmonics*, Phys. Rev. Lett. **7**, 118 (1961).

[28] P. Antoine, A. L'Huillier, and M. Lewenstein, *Attosecond pulse trains using high-order harmonics*, Phys. Rev. Lett. **77**, 1234 (1996).

[29] I. P. Christov, M. M. Murnane, and H. C. Kapteyn, *High-harmonic generation of attosecond pulses in the "single-cycle" regime*, Phys. Rev. Lett. **78**, 1251 (1997).

[30] M. Drescher, M. Hentschel, R. Kienberger, G. Tempea, C. Spielmann, G. A. Reider, P. B. Corkum, and F. Krausz, *X-ray pulses approaching the attosecond frontier*, Science **291**, 1923 (2001).

[31] P. M. Paul, E. S. Toma, P. Breger, G. Mullot, F. Augé, P. Balcou, H. G. Muller, and P. Agostini, *Observation of a train of attosecond pulses from high harmonic generation*, Science **292**, 1689 (2001).

[32] M. Hentschel, R. Kienberger, C. Spielmann, G. A. Reider, N. Milosevic, T. Brabec, P. Corkum, U. Heinzmann, M. Drescher, and F. Krausz, *Attosecond metrology*, Nature **414**, 509 (2001).

[33] Y. Mairesse, A. de Bohan, L. J. Frasinski, H. Merdji, L. C. Dinu, P. Monchicourt, P. Breger, M. Kovačev, R. Taïeb, B. Carré, et al., *Attosecond synchronization of high-harmonic soft x-rays*, Science **302**, 1540 (2003).

[34] P. Agostini and L. F. DiMauro, *The physics of attosecond light pulses*, Rep. Prog. Phys. **67**, 813 (2004).

[35] L. Nugent-Glandorf, M. Scheer, D. A. Samuels, A. M. Mulhisen, E. R. Grant, X. Yang, V. M. Bierbaum, and S. R. Leone, *Ultrafast time-resolved soft x-ray photoelectron spectroscopy of dissociating Br_2*, Phys. Rev. Lett. **87**, 193002 (2001).

[36] M. Drescher, M. Hentschel, R. Kienberger, M. Uiberacker, V. Yakovlev, A. Scrinzi, T. Westerwalbesloh, U. Kleineberg, U. Heinzmann, and F. Krausz, *Time-resolved atomic inner-shell spectroscopy*, Nature **419**, 803 (2002).

[37] R. Kienberger, M. Hentschel, M. Uiberacker, C. Spielmann, M. Kitzler, A. Scrinzi, M. Wieland, T. Westerwalbesloh, U. Kleineberg, U. Heinzmann, et al., *Steering attosecond electron wave packets with light*, Science **297**, 1144 (2002).

[38] R. Kienberger, E. Goulielmakis, M. Uiberacker, A. Baltuška, V. Yakovlev, F. Bammer, A. Scrinzi, T. Westerwalbesloh, U. Kleineberg, U. Heinzmann, et al., *Atomic transient recorder*, Nature **427**, 817 (2004).

[39] A. Scrinzi, M. Y. Ivanov, R. Kienberger, and D. M. Villeneuve, *Attosecond physics*, J. Phys. B: At. Mol. Opt. Phys. **39**, R1 (2006).

[40] P. Salières, P. Antoine, A. de Bohan, and M. Lewenstein, *Temporal and spectral tailoring of high-order harmonics*, Phys. Rev. Lett. **81**, 5544 (1998).

[41] J. Mauritsson, P. Johnsson, E. Gustafsson, A. L'Huillier, K. J. Schafer, and M. B. Gaarde, *Attosecond pulse trains generated using two color laser fields*, Phys. Rev. Lett. **97**, 013001 (2006).

[42] T. Pfeifer, D. Walter, C. Winterfeldt, C. Spielmann, and G. Gerber, *Controlling the spectral shape of coherent soft x-rays*, Appl. Phys. B **80**, 277 (2005).

[43] T. Pfeifer, R. Kemmer, R. Spitzenpfeil, D. Walter, C. Winterfeldt, G. Gerber, and C. Spielmann, *Spatial control of high-harmonic generation in hollow fibers*, Opt. Lett. **30**, 1497 (2005).

[44] C. Winterfeldt, T. Pfeifer, D. Walter, R. Kemmer, A. Paulus, R. Spitzenpfeil, G. Gerber, and C. Spielmann, in *Photon Management II* (2006), vol. 6187 of *Proc. SPIE*, p. 61870F, ISBN 0-8194-6243-8.

[45] D. H. Reitze, S. Kazamias, F. Weihe, G. Mullot, D. Douillet, F. Augé, O. Albert, V. Ramanathan, J. P. Chambaret, D. Hulin, et al., *Enhancement of high-order harmonic generation at tuned wavelengths through adaptive control*, Opt. Lett. **29**, 86 (2004).

[46] D. Yoshitomi, J. Nees, N. Miyamoto, T. Sekikawa, T. Kanai, G. Mourou, and S. Watanabe, *Phase-matched enhancements of high-harmonic soft x-rays by adaptive wave-front control with a genetic algorithm*, Appl. Phys. B **78**, 275 (2003).

[47] P. Villoresi, S. Bonora, M. Pascolini, L. Poletto, G. Tondello, C. Vozzi, M. Nisoli, G. Sansone, S. Stagira, and S. D. Silvestri, *Optimization of high-order harmonic generation by adaptive control of a sub-10-fs pulse wave front*, Opt. Lett. **29**, 207 (2004).

[48] R. Bartels, S. Backus, E. Zeek, L. Misoguti, G. Vdovin, I. P. Christov, M. M. Murnane, and H. C. Kapteyn, *Shaped-pulse optimization of coherent emission of high-harmonic soft x-rays*, Nature **406**, 164 (2000).

[49] R. Bartels, S. Backus, I. Christov, H. Kapteyn, and M. Murnane, *Attosecond time-scale feedback control of coherent x-ray generation*, Chem. Phys. **267**, 277 (2001).

[50] C. Winterfeldt, C. Spielmann, and G. Gerber, *Adaptive temporal and spatial control of high-harmonic generation*, Reviews of Modern Physics p. in preparation (2006).

[51] T. Brabec and F. Krausz, *Intense few-cycle laser fields: Frontiers of nonlinear optics*, Rev. Mod. Phys. **72**, 545 (2000).

[52] C. Spielmann, P. F. Curley, T. Brabec, and F. Krausz, *Ultrabroadband femtosecond lasers*, IEEE J. Quantum Electron. **30**, 1100 (1994).

[53] D. Strickland and G. Mourou, *Compression of amplified chirped optical pulses*, Opt. Commun. **56**, 219 (1985).

[54] G. D. Reid and K. Wynne, *Ultrafast Laser Technology and Spectroscopy*, Encyclopedia of Analytical Chemistry (John Wiley & Sons Ltd, Chichester, 2000).

[55] E. B. Treacy, *Optical pulse compression with diffraction gratings*, IEEE J. Quantum Electron. **5**, 454 (1969).

[56] R. L. Fork, O. E. Martinez, and J. P. Gordon, *Negative dispersion using pairs of prisms*, Opt. Lett. **9**, 150 (1984).

[57] O. E. Martinez, J. P. Gordon, and R. L. Fork, *Negative group-velocity dispersion using refraction*, J. Opt. Soc. Am. A **1**, 1003 (1984).

[58] R. Szipöcs, K. Ferencz, C. Spielmann, and F. Krausz, *Chirped multilayer coatings for broadband dispersion control in femtosecond lasers*, Opt. Lett. **19**, 201 (1994).

[59] A. Stingl, C. Spielmann, F. Krausz, and R. Szipöcs, *Generation of 11-fs pulses from a ti:sapphire laser without the use of prisms*, Opt. Lett. **19**, 204 (1994).

[60] R. W. Boyd, *Nonlinear Optics* (Academic Press, San Diego, 1991).

[61] Spectra-Physics, *Spitfire - Multikilohertz Pulsed Ti:Sapphire Amplifier with Pulse Stretcher and Compressor, User's Manual*, Spectra-Physics Lasers (1998).

[62] W. H. Lowdermilk and J. E. Murray, *The multipass amplifier: Theory and numerical analysis*, J. Appl. Phys. **51**, 2436 (1980).

[63] M. W. B. Mason and U. Weichmann, *Documentation on the Würzburg 4-pass bow-tie Amplifier*, documentation, unpublished, Physikalisches Institut, Universität Würzburg (2001).

[64] Ulrich Weichmann, *Erzeugung hoher Harmonischer von Femtosekunden-Laserpulsen*, Dissertation, Universität Würzburg, Physikalisches Institut (2001).

[65] A. Fernandez, T. Fuji, A. Poppe, A. Fürbach, F. Krausz, and A. Apolonski, *Chirped-pulse oscillators: a route to high-power femtosecond pulses without external amplification*, Opt. Lett. **29**, 1366 (2004).

[66] W. Koechner, *Solid-State Laser Engineering* (Springer, Berlin, 1999), 5th ed.

[67] O. Svelto, *Principles of Lasers* (Plenum Press, New York and London, 1998), 4th ed.

[68] A. E. Siegman, *Lasers* (University Science Books, Sausalito and CA, 1986), 1st ed.

[69] G. Farkas and C. Tóth, *Proposal for attosecond light pulse generation using laser induced multiple-harmonic conversion processes in rare gases*, Phys. Lett. A **168**, 447 (1992).

[70] C. Winterfeldt, *Optical parametric amplifier for nonlinear optical spectroscopy*, Master's thesis, Department of Physics, The University of Texas at Austin (2002).

[71] A. Yariv, *Quantum Electronics* (John Wiley & Sons, New York, 1989), 3rd ed.

[72] F. Lindner, G. G. Paulus, H. Walther, A. Baltuška, E. Goulielmakis, M. Lezius, and F. Krausz, *Gouy phase shift for few-cycle laser pulses*, Phys. Rev. Lett. **92**, 113001 (2004).

[73] C. Winterfeldt, *Adaptive Pulsformung*, Vortrag/Handout, Physikalisches Institut, Universität Würzburg (2001).

[74] J. Reichert, R. Holzwarth, T. Udem, and T. W. Hänsch, *Measuring the frequency of light with mode-locked lasers*, Opt. Commun. **172**, 59 (1999).

[75] D. J. Jones, S. A. Diddams, J. K. Ranka, A. Stentz, R. S. Windeler, J. L. Hall, and S. T. Cundiff, *Carrier-envelope phase control of femtosecond mode-locked lasers and direct optical frequency synthesis*, Science **288**, 635 (2000).

[76] G. Sansone, C. Vozzi, S. Stagira, M. Pascolini, L. Poletto, P. Villoresi, G. Tondello, S. De Silvestri, and M. Nisoli, *Observation of carrier-envelope phase phenomena in the multi-optical-cycle regime*, Phys. Rev. Lett. **92**, 113904 (2004).

[77] S. T. Cundiff and J. Ye, *Colloquium: Femtosecond optical frequency combs*, Rev. Mod. Phys. **75**, 325 (2003).

[78] M. Nisoli, G. Sansone, S. Stagira, S. D. Silvestri, C. Vozzi, M. Pascolini, L. Poletto, P. Villoresi, and G. Tondello, *Effects of carrier-envelope phase differences of few-optical-cycle light pulses in single-shot high-order-harmonic spectra*, Phys. Rev. Lett. **91**, 213905 (2003).

[79] H. R. Telle, G. Steinmeyer, A. E. Dunlop, J. Stenger, D. H. Sutter, and U. Keller, *Carrier-envelope offset phase control: A novel concept for absolute optical frequency measurement and ultrashort pulse generation*, Appl. Phys. B **69**, 327 (1999).

[80] G. G. Paulus, F. Lindner, H. Walther, A. Baltuška, E. Goulielmakis, M. Lezius, and F. Krausz, *Measurement of the phase of few-cycle laser pulses*, Phys. Rev. Lett. **91**, 253004 (2003).

[81] C. Lemell, X.-M. Tong, F. Krausz, and J. Burgdörfer, *Electron emission from metal surfaces by ultrashort pulses: Determination of the carrier-envelope phase*, Phys. Rev. Lett. **90**, 076403 (2003).

[82] T. Brixner, *Kohärente Kontrolle von Photodissoziationsreaktionen mit optimal geformten ultrakurzen Laserpulsen*, Diplomarbeit, Physikalisches Institut, Universität Würzburg (1998).

[83] D. N. Fittinghoff, B. C. Walker, J. A. Squier, C. S. Tóth, C. Rose-Petruck, and C. P. J. Barty, *Dispersion considerations in ultrafast CPA systems*, IEEE J. Sel. Topics Quantum Electron. **4**, 430 (1998).

[84] I. Walmsley, L. Waxer, and C. Dorrer, *The role of dispersion in ultrafast optics*, Rev. Sci. Instrum. **72**, 1 (2001).

[85] V. G. Dmitriev, G. G. Gurzadyan, and D. N. Nikogosyan, *Handbook of Nonlinear Optical Crystals* (Springer, 1999), 3rd ed.

[86] J. D. Jackson, *Classical Electrodynamics* (John Wiley & Sons, 1998), 3rd ed.

[87] A. Brodeur and S. L. Chin, *Ultrafast white-light continuum generation and self-focusing in transparent condensed media*, J. Opt. Soc. Am. B **16**, 637 (1999).

[88] A. Dubeitis, G. Jonasauskas, and A. Piskarskas, *Powerful femtosecond pulse generation by chirped and stretched pulse parametric amplification in bbo crystal*, Opt. Commun. **88**, 437 (1992).

[89] I. N. Ross, P. Matousek, G. H. C. New, and K. Osvay, *Analysis and optimization of optical parametric chirped pulse amplification*, J. Opt. Soc. Am. B **19**, 2945 (2002).

[90] R. T. Zinkstok, S. Witte, W. Hogervorst, and K. S. E. Eikema, *High-power parametric amplification of 11.8-fs laser pulses with carrier-envelope phase control*, Opt. Lett. **30**, 78 (2005).

[91] V. Petrov, F. Rotermund, and F. Noack, *Generation of high-power femtosecond light pulses at 1 kHz in the mid-infrared spectral range between 3 and 12 μm by second-order nonlinear processes in optical crystals*, J. Opt. A **3**, R1 (2001).

[92] G. Cerullo and S. De Silvestri, *Ultrafast optical parametric amplifiers*, Rev. Sci. Instrum. **74**, 1 (2003).

[93] J. A. Armstrong, N. Bloembergen, J. Ducuing, and P. S. Pershan, *Interactions between light waves in a nonlinear dielectric*, Phys. Rev. **127**, 1918 (1962).

[94] G. Ghosh, *Temperature dispersion of refractive indices in β-BaB$_2$O$_4$ and LiB$_3$O$_5$ crystals for nonlinear optical devices*, J. Appl. Phys. **78**, 6752 (1995).

[95] K. Kato, *2nd-harmonic generation to 2048 Å in beta-BaB$_2$O$_4$*, IEEE J. Quant. Electron. **QE-22**, 1013 (1986).

[96] D. Zhang, et al., *Optical parametric properties of 532-nm-pumped beta-barium-borate near the infrared absorption edge*, Opt. Comm. **184**, 485 (2000).

[97] A. Yariv and P. Yeh, *Optical Waves in Crystals* (John Wiley & Sons, New York, 1984).

[98] T. R. Zhang, H. R. Choo, and M. C. Downer, *Phase and group velocity matching for second harmonic generation of femtosecond pulses*, Appl. Opt. **29**, 3927 (1990).

[99] T. Sokollik, *Erzeugung Hoher Harmonischer mit Hilfe ultrakurzer, bichromatischer Laserpulse*, Diplomarbeit, Universität Würzburg, Physikalisches Institut (2005).

[100] T. Kanai, X. Zhou, T. Sekikawa, S. Watanabe, and T. Togashi, *Generation of subterawatt sub-10-fs blue pulses at 1-5khz by broadband frequency doubling*, Opt. Lett. **28**, 1484 (2003).

[101] P. D. Maker, R. W. Terhune, M. Nisehoff, and C. M. Savage, *Effects of dispersion and focusing on the production of optical harmonics*, Phys. Rev. Lett. **8**, 21 (1962).

[102] M. D. Perry, T. Ditmire, and B. C. Stuart, *Self-phase modulation in chirped-pulse amplification*, Opt. Lett. **19**, 2149 (1994).

[103] M. K. Reed, M. K. Steiner-Shepard, M. S. Armas, and D. K. Negus, *Microjoule-energy ultrafast optical parametric amplifiers*, J. Opt. Soc. Am. B **12**, 2229 (1995).

[104] F. Shimizu, *Frequency broadening in liquids by a short light pulse*, Phys. Rev. Lett. **19**, 1097 (1967).

[105] G. Yang and Y. R. Shen, *Spectral broadening of ultrashort pulses in a nonlinear medium*, Opt. Lett. **9**, 510 (1984).

[106] E. Yablonovitch, *Self-phase modulation and short-pulse generation from laser-breakdown plasmas*, Phys. Rev. A **10**, 1888 (1974).

[107] S. C. Wilks, J. M. Dawson, and W. B. Mori, *Frequency up-conversion of electromagnetic radiation with use of an overdense plasma*, Phys. Rev. Lett. **61**, 337 (1988).

[108] W. M. Wood, C. W. Siders, and M. C. Downer, *Measurement of femtosecond ionization dynamics of atmospheric density gases by spectral blueshifting*, Phys. Rev. Lett. **67**, 3523 (1991).

[109] R. R. Alfano and S. L. Shapiro, *Emission in the region 4000 to 7000 Å via four-photon coupling in glass*, Phys. Rev. Lett. **24**, 584 (1970).

[110] E. T. J. Nibbering, P. F. Curley, G. Grillon, B. S. Prade, M. A. Franco, F. Salin, and A. Mysyrowicz, *Conical emission from self-guided femtosecond pulses in air*, Opt. Lett. **21**, 62 (1996).

[111] J. Watson, F. Salin, P. Georges, and A. Brun, *Conical emission accompanying spectral continuum generation: a Cerenkov-based effect*, SPIE **2041**, 120 (1994).

[112] I. Golub, *Optical characteristics of supercontinuum generation*, Opt. Lett. **15**, 305 (1990).

[113] M. M. T. Loy and Y. R. Shen, *Study of self-focusing and small-scale filaments of light in nonlinear media*, IEEE J. Quantum Electron. **QE-9**, 409 (1973).

[114] A. Brodeur, C. Y. Chien, F. A. Ilkov, S. L. Chin, O. G. Kosareva, and V. P. Kandidov, *Moving focus in the propagation of ultrashort laser pulses in air*, Opt. Lett. **22**, 304 (1997).

[115] W. Liu, S. A. Hosseini, Q. Luo, B. Ferland, S. L. Chin, O. G. Kosareva, N. A. Panov, and V. P. Kandidov, *Experimental observation and simulations of the self-action of white light laser pulse propagating in air*, New J. Phys. **6**, 6 (2004).

[116] H. Wille, M. Rodriguez, J. Kasparian, D. Mondelain, J. Yu, A. Mysyrowicz, Sauerbrey, J. Wolf, and L. Wöste, *Teramobile: A mobile femtosecond-terawatt laser and detection system*, Eur. Phys. J. AP **20**, 183 (2002).

[117] M. Rodriguez, R. Sauerbrey, H. Wille, L. Wöste, T. Fujii, Y.-B. André, A. Mysyrowicz, L. Klingbeil, K. Rethmeier, W. Kalkner, et al., *Triggering and guiding megavolt discharges by use of laser-induced ionized filaments*, Opt. Lett. **27**, 772 (2002).

[118] J. Kasparian, M. Rodriguez, G. Méjean, J. Yu, E. Salmon, H. Wille, R. Bourayou, S. Frey, Y.-B. André, A. Mysyrowicz, et al., *White-light filaments for atmospheric analysis*, Science **301**, 61 (2003).

[119] S. A. Trushin, S. Panja, K. Kosma, W. E. Schmid, and W. Fuß, *Supercontinuum extending from > 1000 to 250 nm, generated by focusing ten-fs laser pulses at 805 nm into Ar*, Appl. Phys. B **80**, 399 (2005).

[120] C. P. Hauri, W. Kornelis, F. W. Helbing, A. Heinrich, A. Couairon, A. Mysyrowicz, J. Biegert, and U. Keller, *Generation of intense, carrier-envelope phase-locked few-cycle laser pulses through filamentation*, Appl. Phys. B **79**, 673 (2004).

[121] M. Mäder, *Nonlinear Frequency Conversion of Ti:Sapphire Laser Pulses for Spectroscopy*, Diplomarbeit, Universität Würzburg, Physikalisches Institut (2006).

[122] N. Bloembergen, *The influence of electron plasma formation on superbroadening in light filaments*, Opt. Comm. **8**, 285 (1973).

[123] R. DeSalvo, A. A. Said, D. J. Hagan, E. W. Van Stryland, and M. Sheik-Bahae, *Infrared to ultraviolet measurements of two-photon absorption and n_2 in wide bandgap solids*, IEEE J. Quant. Electron. **32**, 1324 (1996).

[124] C. Spielmann, N. H. Burnett, S. Sartania, R. Koppitsch, M. Schnürer, C. Kan, M. Lenzner, P. Wobrauschek, and F. Krausz, *Generation of coherent x-rays in the water window using 5-femtosecond laser pulses*, Science **278**, 661 (1997).

[125] P. B. Corkum, *Plasma perspective on strong-field multiphoton ionization*, Phys. Rev. Lett. **71**, 1994 (1993).

[126] K. C. Kulander, K. J. Schafer, and J. L. Krause, in *Super-Intense Laser-Atom Physics*, edited by B. Piraux, A. L'Huillier, and K. Rzazewski (New York: Plenum, 1993), vol. 316 of *NATO Advanced Study Institutes, Series B: Physics*, p. 95.

[127] L. V. Keldysh, *Ionization in the field of a strong electromagnetic wave*, Soviet Physics JETP **20**, 1307 (1965).

[128] M. V. Ammosov, N. B. Delone, and V. P. Krainov, *Tunnel ionization of complex atoms and of atomic ions in an alternating electromagnetic field*, Sov. Phys. JETP **64**, 1191 (1986).

[129] P. Agostini, F. Fabre, G. Mainfray, G. Petite, and N. K. Rahman, *Free-free transitions following six-photon ionization of xenon atoms*, Phys. Rev. Lett. **42**, 1127 (1979).

[130] R. R. Freeman, P. H. Bucksbaum, H. Milchberg, S. Darack, D. Schumacher, and M. E. Geusic, *Above-threshold ionization with subpicosecond laser pulses*, Phys. Rev. Lett. **59**, 1092 (1987).

[131] G. G. Paulus, W. Nicklich, H. Xu, P. Lambropoulos, and H. Walther, *Plateau in above threshold ionization spectra*, Phys. Rev. Lett. **72**, 2851 (1994).

[132] G. G. Paulus, W. Becker, W. Nicklich, and H. Walther, *Rescattering effects in above-threshold ionization: a classical model*, J. Phys. B: At. Mol. Opt. Phys. **27**, L703 (1994).

[133] D. Milošević, G. Paulus, and W. Becker, *High-order above-threshold ionization with few-cycle pulse: a meter of the absolute phase*, Opt. Express **11**, 1418 (2003).

[134] D. N. Fittinghoff, P. R. Bolton, B. Chang, and K. C. Kulander, *Observation of nonsequential double ionization of helium with optical tunneling*, Phys. Rev. Lett. **69**, 2642 (1992).

[135] B. Walker, B. Sheehy, L. F. DiMauro, P. Agostini, K. J. Schafer, , and K. C. Kulander, *Precision measurement of strong field double ionization of helium*, Phys. Rev. Lett. **73**, 1227 (1994).

[136] M. Lewenstein, P. Balcou, M. Y. Ivanov, A. L'Huillier, and P. B. Corkum, *Theory of high-harmonic generation by low-frequency laser fields*, Phys. Rev. A **49**, 2117 (1994).

[137] L. A. Lompré, A. L'Huillier, M. Ferray, P. Monot, G. Mainfray, and C. Manus, *High-order harmonic generation in xenon: intensity and propagation effects*, J. Opt. Soc. Am. B **7**, 754 (1990).

[138] A. L'Huillier, K. J. Schafer, and K. C. Kulander, *High-order harmonic generation in xenon at 1064nm: The role of phase matching*, Phys. Rev. Lett. **66**, 2200 (1991).

[139] B. Shan and Z. Chang, *Dramatic extension of the high-order harmonic cutoff by using a long-wavelength driving field*, Phys. Rev. A **65**, 001804(R) (2001).

[140] G. Tempea and T. Brabec, *Optimization of high-harmonic generation*, Appl. Phys. B **70**, S197 (2000).

[141] T. Ditmire, J. K. Crane, H. Nguyen, L. B. DaSilva, and M. D. Perry, *Energy-yield and conversion-efficiency measurements of high-order harmonic radiation*, Phys. Rev. A **51**, R902 (1995).

[142] A. Rundquist, C. G. Durfee III, Z. Chang, C. Herne, S. Backus, M. M. Murnane, and H. C. Kapteyn, *Phase-matched generation of coherent soft x-rays*, Science **280**, 1412 (1998).

[143] C. H. Keitel and P. L. Knight, *Monte carlo classical simulations of ionization and harmonic generation in the relativistic domain*, Phys. Rev. A **51**, 1420 (1995).

[144] M. J. DeWitt and R. J. Levis, *Calculating the keldysh adiabaticity parameter for atomic, diatomic, and polyatomic molecules*, J. Chem. Phys. **108**, 7739 (1998).

[145] R. Shakeshaft, R. M. Potvliege, M. Dörr, and W. E. Cooke, *Multiphoton processes in an intense laser field. iv. the static-field limit*, Phys. Rev. A **42**, 1656 (1990).

[146] A. Scrinzi, M. Geissler, and T. Brabec, *Ionization above the coulomb barrier*, Phys. Rev. Lett. **83**, 706 (1999).

[147] S. Augst, D. D. Meyerhofer, D. Strickland, and S. L. Chin, *Laser ionization of noble gases by coulomb-barrier suppression*, J. Opt. Soc. Am. B **8**, 858 (1991).

[148] P. B. Corkum, N. H. Burnett, and F. Brunel, *Above-threshold ionization in the long-wavelength limit*, Phys. Rev. Lett. **62**, 1259 (1989).

[149] M. Lewenstein, P. Salières, and A. L'Huillier, *Phase of the atomic polarization in high-order harmonic generation*, Phys. Rev. A **52**, 4747 (1995).

[150] J. L. Krause and a. K. C. K. Kenneth J. Schafer, *High-order harmonic generation from atoms and ions in the high intensity regime*, Phys. Rev. Lett. **68**, 3535 (1992).

[151] P. Salières, B. Carré, L. Le Déroff, F. Grasbon, G. G. Paulus, H. Walther, R. Kopold, W. Becker, D. B. Milošević, A. Sanpera, et al., *Feynman's path-integral approach for intense-laser-atom interactions*, Science **292**, 902 (2001).

[152] P. Tzallas, D. Charalambidis, N. A. Papadogiannis, K. Witte, and G. D. Tsakiris, *Direct observation of attosecond light bunching*, Nature **426**, 267 (2003).

[153] A. Baltuška, T. Udem, M. Uiberacker, M. Hentschel, E. Goulielmakis, C. Gohle, R. Holzwarth, V. S. Yakovlev, A. Scrinzi, T. W. Hänsch, et al., *Attosecond control of electronic processes by intense light fields*, Nature **421**, 611 (2003).

[154] T. Pfeifer, L. Gallmann, M. J. Abel, D. M. Neumark, and S. R. Leone, *Single attosecond pulse generation in the multicycle-driver regime by adding a weak second-harmonic field*, Opt. Lett. **31**, 975 (2006).

[155] T. Kreibich, M. Lein, V. Engel, and E. K. U. Gross, *Even-harmonic generation due to beyond-born-oppenheimer dynamics*, Phys. Rev. Lett. **87**, 103901 (2001).

[156] V. P. Gavrilenko and E. Oks, *A significant enhancement of high-order harmonic generation by using a dipole gas*, J. Phys. B **33**, 1629 (2000).

[157] H. Stapelfeldt and T. Seideman, *Colloquium: Aligning molecules with strong laser pulses*, Rev. Mod. Phys. **75**, 543 (2003).

[158] Z. Chang, A. Rundquist, H. Wang, M. M. Murnane, and H. C. Kapteyn, *Generation of coherent soft x rays at 2.7 nm using high harmonics*, Phys. Rev. Lett. **79**, 2967 (1997).

[159] M. Schnürer, C. Spielmann, P. Wobrauschek, C. Streli, N. H. Burnett, C. Kan, K. Ferencz, R. Koppitsch, Z. Cheng, T. Brabec, et al., *Coherent 0.5-kev x-ray emission from helium driven by a sub-10-fs laser*, Phys. Rev. Lett. **80**, 3236 (1998).

[160] Z. Chang, A. Rundquist, H. Wang, I. Christov, M. M. Murnane, and H. C. Kapteyn, *Generation of coherent, femtosecond, x-ray pulses in the 'water window'*, IEEE J. Sel. Topics Quantum Electron. **4**, 266 (1998).

[161] C. Kan, C. E. Capjack, R. Rankin, and N. H. Burnett, *Spectral and temporal structure in high harmonic emission from ionizing atomic gases*, Phys. Rev. A **52**, R4336 (1995).

[162] E. A. J. Marcatili and R. A. Schmeltzer, *Hollow metallic and dielectric waveguides for long distance optical transmission and lasers*, The Bell System Techn. J. **43**, 1783 (1964).

[163] C. G. Durfee III, A. Rundquist, S. Backus, C. Herne, M. M. Murnane, and H. C. Kapteyn, *Phase matching of high-order harmonics in hollow waveguides*, Phys. Rev. Lett. **83**, 2187 (1999).

[164] B. L. Henke, E. M. Gullikson, and J. C. Davis, *X-ray interactions - photoabsorption, scattering, transmission, and reflection at E=50-30,000 eV, Z=1-92*, At. Data Nucl. Data Tables **54**, 181 (1993).

[165] I. P. Christov, H. C. Kapteyn, and M. M. Murnane, *Dispersion-controlled hollow core fiber for phase matched harmonic generation*, Opt. Express **3**, 360 (1998).

[166] A. L'Huillier, M. Lewenstein, P. Saliéres, P. Balcou, M. Y. Ivanov, J. Larsson, and C. G. Wahlström, *High-order harmonic-generation cutoff*, Phys. Rev. A **48**, R3433 (1993).

[167] A. Bouhal, P. Salières, P. Breger, P. Agostini, G. Hamoniaux, A. Mysyrowicz, A. Antonetti, R. Constantinescu, and H. G. Muller, *Temporal dependence of high-order harmonics in the presence of strong ionization*, Phys. Rev. A **1** (58).

[168] P. Salières, A. L'Huillier, and M. Lewenstein, *Coherence control of high-order harmonics*, Phys. Rev. Lett. **74**, 3776 (1995).

[169] G. A. Reider, *Xuv attosecond pulses: generation and measurement*, J. Phys. D: Appl. Phys. **37**, R37 (2004).

[170] M. Bellini, C. Lyngå, A. Tozzi, M. B. Gaarde, T. W. Hänsch, A. L'Huillier, and C.-G. Wahlström, *Temporal coherence of ultrashort high-order harmonic pulses*, Phys. Rev. Lett. **81**, 297 (1998).

[171] C. Lyngå, M. B. Gaarde, C. Delfin, M. Bellini, T. W. Hänsch, A. L'Huillier, and C.-G. Wahlström, *Temporal coherence of high-order harmonics*, Phys. Rev. A **60**, 4823 (1999).

[172] M. B. Gaarde, F. Salin, E. Constant, P. Balcou, K. J. Schafer, K. C. Kulander, and A. L'Huillier, *Spatiotemporal separation of high harmonic radiation into two quantum path components*, Phys. Rev. A **59**, 1367 (1999).

[173] E. Benedetti, J.-P. Caumes, G. Sansone, S. Stagira, C. Vozzi, and M. Nisoli, *Frequency chirp of long electron quantum paths in high-order harmonic generation*, Opt. Express **14**, 2242 (2006).

[174] R. A. Bartels, A. Paul, H. G. ans Henry C. Kapteyn, M. M. Murnane, S. Backus, I. P. Christov, Y. Liu, D. Attwood, and C. Jacobsen, *Generation of spatially coherent light at extreme ultraviolet wavelengths*, Science **297**, 376 (2002).

[175] D. G. Lee, J. J. Park, J. H. Sung, and C. H. Nam, *Wave-front phase measurements of high-order harmonic beams by use of point-diffraction interferometry*, Opt. Lett. **28**, 480 (2003).

[176] T. Ditmire, E. T. Gumbrell, R. A. Smith, J. W. G. Tisch, D. D. Meyerhofer, and M. H. R. Hutchinson, *Spatial coherence measurement of soft x-ray radiation produced by high order harmonic generation*, Phys. Rev. Lett. **77**, 4756 (1996).

[177] P. Balcou, A. S. Dederichs, M. B. Gaarde, and A. L'Huillier, *Quantum-path analysis and phase matching of high-order harmonic generation and high-order frequency mixing processes in strong laser fields*, J. Phys. B **32**, 2973 (1999).

[178] M. B. Gaarde, *Time-frequency representations of high order harmonics*, Opt. Express **8**, 529 (2001).

[179] C. Corsi, A. Pirri, E. Sali, A. Tortora, and M. Bellini, *Direct interferometric measurement of the atomic dipole phase in high-order harmonic generation*, Phys. Rev. Lett. **97**, 023901 (2006).

[180] E. Seres and C. Spielmann, in *CLEO/Europe-EQEC 2005 Conference Digest* (2005), vol. 29B of *Europhysics Conference Abstracts*, ISBN 0-7803-8974-3.

[181] C. Spielmann, C. Kan, N. H. Burnett, T. Brabec, M. Geissler, A. Scrinzi, M. Schnürer, and F. Krausz, *Near-keV coherent x-ray generatin with sub-10-fs lasers*, IEEE J. Sel. Topics Quantum Electron. **4**, 249 (1998).

[182] E. A. Gibson, A. Paul, N. Wagner, R. Tobey, D. Gaudiosi, S. Backus, I. P. Christov, A. Aquila, E. M. Gullikson, D. T. Attwood, et al., *Coherent soft x-ray generation in the water window with quasi-phase matching*, Science **302**, 95 (2003).

[183] E. Seres, J. Seres, F. Krausz, and C. Spielmann, *Generation of coherent soft-x-ray radiation extending far beyond the titanium L edge*, Phys. Rev. Lett. **92**, 163002 (2004).

[184] J. Seres, E. Seres, A. J. Verhoef, G. Tempea, C. Streli, P. Wobrauschek, V. Yakovlev, A. Scrinzi, C. Spielmann, and F. Krausz, *Source of coherent kiloelectronvolt x-rays*, Nature **433**, 596 (2005).

[185] Y. Kobayashi, T. Ohno, T. Sekikawa, Y. Nabekawa, and S. Watanabe, *Pulse width measurement of high-order harmonics by autocorrelation*, Appl. Phys. B **70**, 389 (2000).

[186] N. A. Papadogiannis, L. A. A. Nikolopoulos, D. Charalambidis, G. D. Tsakiris, P. Tzallas, and K. Witte, *Two-photon ionization of he through a superposition of higher harmonics*, Phys. Rev. Lett. **90**, 133902 (2003).

[187] N. Miyamoto, M. Kamei, D. Yoshitomi, T. Kanai, T. Sekikawa, T. Nakajima, and S. Watanabe, *Observation of two-photon above-threshold ionization of rare gases by xuv harmonic photons*, Phys. Rev. Lett. **93**, 083903 (2004).

[188] T. Sekikawa, A. Kosuge, T. Kanai, and S. Watanabe, *Nonlinear optics in the extreme ultraviolet*, Nature **432**, 605 (2004).

[189] H. Hasegawa, E. J. Takahashi, Y. Nabekawa, K. L. Ishikawa, and K. Midorikawa, *Multiphoton ionization of he by using intense high-order harmonics in the soft-x-ray region*, Phys. Rev. A **71**, 023407 (2005).

[190] M. Schnürer, Z. Cheng, M. Hentschel, G. Tempea, P. Kálmán, T. Brabec, , and F. Krausz, *Absorption-limited generation of coherent ultrashort soft-x-ray pulses*, Phys. Rev. Lett. **83**, 722 (1999).

[191] Y. Mairesse, A. de Bohan, L. J. Frasinski, H. Merdji, L. C. Dinu, P. Monchicourt, P. Breger, M. Kovacěv, T. Auguste, B. Carré, et al., *Optimization of attosecond pulse generation*, Phys. Rev. Lett. **93**, 163901 (2004).

[192] R. J. Jones, K. D. Moll, M. J. Thorpe, and J. Ye, *Phase-coherent frequency combs in the vacuum ultraviolet via high-harmonic generation inside a femtosecond enhancement cavity*, Phys. Rev. Lett. **94**, 193201 (2005).

[193] C. Gohle, T. Udem, M. Herrmann, J. Rauschenberger, R. Holzwarth, H. A. Schuessler, F. Krausz, and T. W. Hänsch, *A frequency comb in the extreme ultraviolet*, Nature **436**, 234 (2005).

[194] T. Brixner and G. Gerber, *Quantum control of gas-phase and liquid-phase femtochemistry*, Chem. Phys. Chem. **4**, 418 (2003).

[195] D. Meshulach and Y. Silberberg, *Coherent quantum control of two-photon transitions by a femtosecond laser pulse*, Nature **396**, 239 (1998).

[196] M. E. Fermann, V. da Silva, D. A. Smith, Y. Silberberg, and A. M. Weiner, *Shaping of ultrashort optical pulses by using an integrated acousto–optic tunable filter*, Opt. Lett. **18**, 1505 (1993).

[197] E. Zeek, K. Maginnis, S. Backus, U. Russek, M. Murnane, G. Mourou, H. Kapteyn, and G. Vdovin, *Pulse compression by use of deformable mirrors*, Opt. Lett. **24**, 493 (1999).

[198] F. Verluise, V. Laude, Z. Cheng, C. Spielmann, and P. Tournois, *Amplitude and phase control of ultrashort pulses by use of an acousto-optic programmable dispersive filter: pulse compression and shaping*, Opt. Lett. **25**, 575 (2000).

[199] A. Paulus, C. Winterfeldt, T. Pfeifer, D. Walter, G. Gerber, and C. Spielmann, *Novel time-of-flight electron spectrometer optimized for time-resolved soft-x-ray photoelectron spectroscopy*, Rev. Sci. Instr. **77**, 043105 (2006).

[200] D. J. Tannor, R. Kosloff, and S. A. Rice, *Coherent pulse sequence induced control of selectivity of reactions: Exact quantum mechanical calculations*, J. Chem. Phys. **85**, 5805 (1986).

[201] D. J. Tannor and S. A. Rice, *Control of selectivity of chemical reaction via control of wave packet evolution*, J. Chem. Phys. **83**, 5013 (1985).

[202] P. Brumer and M. Shapiro, *Control of unimolecular reactions using coherent light*, Chem. Phys. Lett. **126**, 477 (1986).

[203] M. Shapiro and P. Brumer, *On the origin of pulse shaping control of molecular dynamics*, J. Phys. Chem. A **105**, 2897 (2001).

[204] U. Gaubatz, P. Rudecki, M. Becker, S. Schiemann, M. Külz, and K. Bergmann, *Population switching between vibrational levels in molecular beams*, Chem. Phys. Lett. **149**, 463 (1988).

[205] K. Bergmann, H. Theuer, and B. W. Shore, *Coherent population transfer among quantum states of atoms and molecules*, Rev. Mod. Phys. **70**, 1003 (1998).

[206] K. J. Schafer, M. B. Gaarde, A. Heinrich, J. Biegert, and U. Keller, *Strong field quantum path control using attosecond pulse trains*, Phys. Rev. Lett. **92**, 023003 (2004).

[207] J. Biegert, A. Heinrich, C. P. Hauri, W. Kornelis, P. Schlup, M. P. Anscombe, M. B. Gaarde, K. J. Schafer, and U. Keller, *Control of high-order harmonic emission using attosecond pulse trains*, J. Mod. Opt. **53**, 87 (2006).

[208] D. G. Lee, J. H. Kim, K. H. Hong, and C. H. Nam, *Coherent control of high-order harmonics with chirped femtosecond laser pulses*, Phys. Rev. Lett. **87**, 243902 (2001).

[209] Z. Chang, A. Rundquist, H. Wang, I. Christov, H. C. Kapteyn, and M. M. Murnane, *Temporal phase control of soft-x-ray harmonic emission*, Phys. Rev. A **58**, R30 (1998).

[210] C. Altucci, R. Bruzzese, C. de Lisio, M. Nisoli, S. Stagira, S. De Silvestri, O. Svelto, A. Boscolo, P. Ceccherini, L. Poletto, et al., *Tunable soft-x-ray radiation by high-order harmonic generation*, Phys. Rev. A **61**, 021801(R) (1999).

[211] H. T. Kim, D. G. Lee, K. H. Hong, J. H. Kim, I. W. Choi, and C. H. Nam, *Continuously tunable high-order harmonics from atoms in an intense femtosecond laser field*, Phys. Rev. A **67**, 051801 (2003).

[212] J. Mauritsson, P. Johnsson, R. López-Martens, K. Varjú, W. Kornelis, J. Biegert, U. Keller, M. B. Gaarde, K. J. Schafer, and A. L'Huillier, *Measurement and control of the frequency chirp rate of high-order harmonic pulses*, Phys. Rev. A **70**, 021801(R) (2004).

[213] M. Murakami, J. Mauritsson, A. L'Huillier, K. J. Schafer, and M. B. Gaarde, *Calculation and manipulation of the chirp rates of high-order harmonics*, Phys. Rev. A **71**, 013410 (2005).

[214] F. Brandi, D. Neshev, and W. Ubachs, *High-order harmonic generation yielding tunable extreme-ultraviolet radiation of high spectral purity*, Phys. Rev. Lett. **91**, 163901 (2003).

[215] R. López-Martens, K. Varjú, P. Johnsson, J. Mauritsson, Y. Mairesse, P. Salières, M. B. Gaarde, K. J. Schafer, A. Persson, S. Svanberg, et al., *Amplitude and phase control of attosecond light pulses*, Phys. Rev. Lett. **94**, 033001 (2005).

[216] H. Muller, *Reconstruction of attosecond harmonic beating by interference of two-photon transitions*, Appl. Phys. B **74**, S17 (2002).

[217] R. López-Martens, J. Mauritsson, P. Johnsson, K. Varjú, A. L'Huillier, W. Kornelis, J. Biegert, U. Keller, M. Gaarde, and K. Schafer, *Characterization of high-order harmonic radiation on femtosecond and attosecond time scales*, Appl. Phys. B **78**, 835 (2004).

[218] K. T. Kim, C. M. Kim, M.-G. Baik, G. Umesh, and C. H. Nam, *Single sub-50-attosecond pulse generation from chirp-compensated harmonic radiation usin material dispersion*, Phys. Rev. A **69**, 051805(R) (2004).

[219] A.-S. Morlens, P. Balcou, P. Zeitoun, C. Valentin, V. Laude, and S. Kazamias, *Compression of attosecond harmonic pulses by extreme-ultraviolet chirped mirrors*, Opt. Lett. **30**, 1554 (2005).

[220] F. A. Weihe and P. H. Bucksbaum, *Measurement of the polarization state of high harmonics generated in gases*, J. Opt. Soc. Am. B **13**, 157 (1996).

[221] A. Flettner, J. König, M. B. Mason, T. Pfeifer, U. Weichmann, and G. Gerber, *Atomic and molecular high-harmonic generation: A comparison of ellipticity dependence based on the three-step model*, J. Mod. Opt. **50**, 529 (2003).

[222] P. B. Corkum, N. H. Burnett, and M. Y. Ivanov, *Subfemtosecond pulses*, Opt. Lett. **19**, 1870 (1994).

[223] M. Ivanov, P. B. Corkum, T. Zuo, and A. Bandrauk, *Routes to control of intense-field atomic polarizability*, Phys. Rev. Lett. **74**, 2933 (1995).

[224] C. Altucci, C. Delfin, L. Roos, M. B. Gaarde, A. L'Huillier, I. Mercer, T. Starczewski, and C.-G. Wahlstróm, *Frequency-resolved time-gated high-order harmonics*, Phys. Rev. A **58**, 3934 (1998).

[225] V. Strelkov, A. Zaïr, O. Tcherbakoff, R. López-Martens, E. Cormier, E. Mével, and E. Constant, *Generation of attosecond pulses with ellipticity-modulated fundamental*, Appl. Phys. B **78**, 879 (2004).

[226] A. Zair, O. Tcherbakoff, E. Mevel, E. Constant, R. Lopez-Martens, J. Mauritsson, P. Johnsson, and A. L'Huillier, *Time-resolved measurements of high order harmonics confined by polarization gating*, Appl. Phys. B **78**, 869 (2004).

[227] D. Oron, Y. Silberberg, N. Dudovich, and D. M. Villeneuve, *Efficient polarization gating of high-order harmonic generation by polarization-shaped ultrashort pulses*, Phys. Rev. A **72**, 063816 (2005).

[228] T. Brixner and G. Gerber, *Femtosecond polarization pulse shaping*, Opt. Lett. **26**, 557 (2001).

[229] T. Brixner, G. Krampert, T. Pfeifer, R. Selle, G. Gerber, M.Wollenhaupt, O. Graefe, C. Horn, D. Liese, and T. Baumert, *Quantum control by ultrafast polarization shaping*, Phys. Rev. Lett. **92**, 208301 (2004).

[230] Z. Chang, *Chirp of the single attosecond pulse generated by a polarization gating*, Phys. Rev. A **71**, 023813 (2005).

[231] R. López-Martens, J. Mauritsson, P. Johnsson, A. L'Huillier, O. Tcherbakoff, A. Zaïr, E. Mével, and E. Constant, *Time-resolved ellipticity gating of high-order harmonic emission*, Phys. Rev. A **69**, 053811 (2004).

[232] C. A. Froud, E. T. F. Rogers, D. C. Hanna, W. S. Brocklesby, M. Praeger, A. M. de Paula, J. J. Baumberg, and J. G. Frey, *Soft-x-ray wavelength shift induced by ionization effects in a capillary*, Opt. Lett. **31**, 374 (2006).

[233] L. Roos, M. B. Gaarde, and A. L'Huillier, *Tailoring harmonic radiation to different applications using a genetic algorithm*, J. Phys. B **34**, 5041 (2001).

[234] A. B. H. Yedder, C. Le Bris, O. Atabek, S. Chelkowski, and A. D. Bandrauk, *Optimal control of attosecond pulse synthesis from high-order harmonic generation*, Phys. Rev. A **69**, 041802(R) (2004).

[235] M. Nisoli, S. D. Silvestri, and O. Svelto, *Generation of high energy 10 fs pulses by a new pulse compression technique*, Appl. Phys. Lett. **68**, 2793 (1996).

[236] T. Pfeifer, U. Weichmann, S. Zipfel, and G. Gerber, *Compression and shaping of a self-phase-modulated laser pulse with a deformable mirror device*, J. Mod. Opt. **50**, 705 (2003).

[237] Y. Tamaki, Y. Nagata, M. Obara, and K. Midorikawa, *Phase-matched high-order-harmonic generation in a gas-filled hollow fiber*, Phys. Rev. A **59**, 4041 (1999).

[238] D. B. Milošević and W. Becker, *Role of long quantum orbits in high-order harmonic generation*, Phys. Rev. A **66**, 063417 (2002).

[239] E. S. Toma, P. Antoine, A. de Bohan, and H. G. Muller, *Resonance-enhanced high-harmonic generation*, J. Phys. B: At. Mol. Opt. Phys. **32**, 5843 (1999).

[240] I. P. Christov, R. Bartels, H. C. Kapteyn, and M. M. Murnane, *Attosecond time-scale intra-atomic phase matching of high harmonic generation*, Phys. Rev. Lett. **86**, 5458 (2001).

[241] S. Kazamias, F. Weihe, D. Douillet, C. Valentin, T. Planchon, S. Sebban, G. Grillon, F. Augé, D. Hulin, and P. Balcou, *High order harmonic generation optimization with an apertured laser beam*, Eur. Phys. J. D **21**, 353 (2002).

[242] J. R. Sutherland, E. L. Christensen, N. D. Powers, S. E. Rhynard, J. C. Painter, and J. Peatross, *High harmonic generation in a semi-infinite gas cell*, Opt. Express **12**, 4430 (2004).

[243] D. Homoelle and A. L. Gaeta, *Nonlinear propagation dynamics of an ultrashort pulse in a hollow waveguide*, Opt. Lett. **25**, 761 (2000).

[244] G. Tempea and T. Brabec, *Theory of self-focusing in a hollow waveguide*, Opt. Lett. **23**, 762 (1998).

[245] Y. Kobajashi, Y. Igasaki, N. Yoshida, H. T. N. Fukuchi, T. Hara, and M. H. Wu, in *Diffractive/Holographic Technologies and Spatial Light Modulators VII* (2000), vol. 3951 of *Proc. SPIE*.

[246] D. Walter, T. Pfeifer, C. Winterfeldt, R. Kemmer, R. Spitzenpfeil, G. Gerber, and C. Spielmann, *Adaptive spatial control of fiber modes and their excitation for high-harmonic generation*, Opt. Express **14**, 3433 (2006).

[247] R. M. Jenkins and R. W. J. Devereux, *Effect of field regeneration on the TEM00 transmission characteristics of a circular-section waveguide*, Appl. Opt. **31**, 5086 (1992).

[248] R. M. Koehl, T. Hattori, and K. A. Nelson, *Automated spatial and temporal shaping of femtosecond pulses*, Opt. Commun. **157**, 57 (1998).

[249] R. Kemmer, *Adaptive räumliche und zeitliche Formung von ultrakurzen Laserpulsen*, Diplomarbeit, Universität Würzburg, Physikalisches Institut (2005).

[250] A. Paul, R. A. Bartels, R. Tobey, H. Green, S. Weiman, I. P. Christov, M. M. Murnane, H. C. Kapteyn, and S. Backus, *Quasi-phase-matched generation of coherent extreme-ultraviolet light*, Nature **421**, 51 (2003).

[251] P. L. Shkolnikov, A. E. Kaplan, and A. Lago, *Phase-matching optimization of large-scale nonlinear frequency upconversion in neutral and ionized gases*, J. Opt. Soc. Am. B **13**, 412 (1996).

[252] C. Altucci, T. Starczewski, E. Mevel, and C.-G. Wahlström, *Influence of atomic density in high-order harmonic generation*, J. Opt. Soc. Am. B **13**, 148 (1996).

[253] A. Flettner, T. Pfeifer, D. Walter, C. Winterfeldt, C. Spielmann, and G. Gerber, *High-harmonic generation and plasma radiation from water microdroplets*, Appl. Phys. B **77**, 747 (2003).

[254] V. V. Strelkov, V. T. Platonenko, and A. Becker, *High-harmonic generation in a dense medium*, Phys. Rev. A **71**, 053808 (2005).

[255] J. R. Davies and J. T. Mendonça, *Basic physics of laser propagation in hollow waveguides*, Phys. Rev. E **62**, 7168 (2000).

[256] C. Delfin, C. Altucci, F. De Filippo, C. de Lisio, M. B. Gaarde, A. L'Huillier, L. Roos, and C.-G. Wahlström, *Influence of the medium length on high-order harmonic generation*, J. Phys. B: At. Mol. Opt. Phys. **32**, 5397 (1999).

[257] Y. Tamaki, J. Itatani, M. Obara, and K. Midorikawa, *Optimization of conversion efficiency and spatial quality of high-order harmonic generation*, Phys. Rev. A **62**, 063802 (2000).

[258] S. Kazamias, D. Douillet, C. Valentin, F. Weihe, F. Augé, T. Lefrou, G. Grillon, S. Sebban, and P. Balcou, *Observation of high-contrast coherence fringes in high-order harmonic generation*, Phys. Rev. A **68**, 033819 (2003).

[259] S. Kazamias, D. Douillet, F. Weihe, C. Valentin, A. Rousse, S. Sebban, G. G. F. Augé, D. Hulin, and P. Balcou, *Global optimization of high harmonic generation*, Phys. Rev. Lett. **90**, 193901 (2003).

[260] Y. Liang, A. Talebpuor, C. Y. Chien, S. Augst, and S. L. Chin, *Comparison of high harmonic conversion efficiency in atomic and diatomic molecular gases*, J. Phys. B **30**, 1369 (1997).

[261] C. Altucci, R. Velotta, E. Heesel, E. Springate, J. P. Marangos, C. Vozzi, E. Benedetti, F. Calegari, G. Sansone, S. Stagira, et al., *High-order harmonic generation in alkanes*, Phys. Rev. A **73**, 043411 (2006).

[262] T. D. Donnelly, T. Ditmire, K. Neuman, M. D. Perry, and R. W. Falcone, *High-order harmonic generation in atom clusters*, Phys. Rev. Lett. **76**, 2472 (1996).

[263] P. A. Norreys, M. Zepf, S. Moustaizis, A. P. Fews, J. Zhang, P. Lee, M. Bakarezos, C. N. Danson, A. Dyson, P. Gibbon, et al., *Efficient extreme uv harmonics generated from picosecond laser pulse interactions with solid targets*, Phys. Rev. Lett. **76**, 1832 (1996).

[264] P. Moreno, L. Plaja, and L. Roso, *Ultrahigh harmonic generation from diatomic molecular ions in highly excited vibrational states*, Phys. Rev. A **55**, R1593 (1997).

[265] M. Lein, *Mechanisms of ultrahigh-order harmonic generation*, Phys. Rev. A **72**, 053816 (2005).

[266] A. D. Bandrauk, S. Chelkowski, H. Yu, and E. Constant, *Enhanced harmonic generation in extended molecular systems by two-color excitation*, Phys. Rev. A **56**, R2537 (1997).

[267] T. Pfeifer, D. Walter, G. Gerber, M. Y. Emelin, M. Y. Ryabikin, M. D. Chernobrovtseva, and A. M. Sergeev, *Transient enhancement of high-harmonic generation in expanding molecules*, Phys. Rev. A **70**, 013805 (2004).

[268] S. A. Korff and G. Breit, *Optical dispersion*, Rev. Mod. Phys. **4**, 471 (1932).

[269] CXRO at Lawrence Berkeley National Laboratory, *X-Ray Interactions with Matter*, http://www-cxro.lbl.gov/opticalconstants (1995–2004).

[270] S. E. Harris, J. E. Field, and A. Kasapi, *Dispersive properties of electromagnetically induced transparency*, Phys. Rev. A **46**, R29 (1992).

[271] M. D. Lukin, *Colloquium: Trapping and manipulating photon states in atomic ensembles*, Rev. Mod. Phys. **75**, 457 (2003).

[272] L. V. Hau, S. E. Harris, Z. Dutton, and C. H. Behroozi, *Light speed reduction to 17 metres per second in an ultracold atomic gas*, Nature **397**, 594 (1999).

[273] M. M. Kash, V. A. Sautenkov, A. S. Zibrov, L. Hollberg, G. R. Welch, M. D. Lukin, Y. Rostovtsev, E. S. Fry, and M. O. Scully, *Ultraslow group velocity and enhanced nonlinear optical effects in a coherently driven hot atomic gas*, Phys. Rev. Lett. **82**, 5229 (1999).

[274] E. McCullough, M. Shapiro, and P. Brumer, *Coherent control of refractive indices*, Phys. Rev. A **61**, 041801(R) (2000).

[275] R. Haight and P. F. Seidler, *High resolution atomic core level spectroscopy with laser harmonics*, Appl. Phys. Lett. **65**, 517 (1994).

[276] M. Wieland, R. Früke, T. Wilhein, C. Spielmann, M. Pohl, and U. Kleineberg, *Submicron extreme ultraviolet imaging using high-harmonic radiation*, Appl. Phys. Lett. **81**, 2520 (2002).

[277] R. Früke, J. Kutzner, T. Witting, H. Zacharias, and T. Wilhein, *Euv scanning transmission microscope operating with high-harmonic and laser plasma radiation*, Europhys. Lett. **72**, 915 (2005).

[278] T. Remetter, P. Johnsson, J. Mauritsson, K. Varjú, Y. Ni, F. Lépine, E. Gustafsson, M. Kling, J. Khan, R. López-Martens, et al., *Attosecond electron wave packet interferometry*, Nature Physics **2**, 323 (2006).

[279] M. Bauer, C. Lei, K. Read, R. Tobey, J. Gland, M. M. Murnane, and H. C. Kapteyn, *Direct observation of surface chemistry using ultrafast soft-x-ray pulses*, Phys. Rev. Lett. **87**, 025501 (2001).

[280] P. Siffalovic, M. Drescher, M. Spieweck, T. Wiesenthal, Y. C. Lim, R. Weidner, A. Lizarov, and U. Heinzmann, *Laser-based apparatus for extended ultraviolet femtosecond time-resolved photoemission spectroscopy*, Rev. Sci. Instr. **72**, 30 (2001).

[281] G. Tsimilis, C. Benesch, J. Kutzner, and H. Zacharias, *Laser based soft-x-ray pulses for photoelectron spectroscopy of surfaces*, J. Opt. Soc. Am. B **20**, 2003 (2003).

[282] G. Tsimilis, J. Kutzner, and H. Zacharias, *Photoemission study of clean and c(4x2)-2co-covered pt(111) using high-harmonic radiation*, Appl. Phys. A **76**, 743 (2003).

[283] T. Shimizu, T. Sekikawa, T. Kanai, S. Watanabe, and M. Itoh, *Time-resolved auger decay in CsBr using high harmonics*, Phys. Rev. Lett. **91**, 017401 (2003).

[284] M. Lein, N. Hay, R. Velotta, J. P. Marangos, and P. L. Knight, *Interference effects in high-order harmonic generation with molecules*, Phys. Rev. A **66**, 023805 (2002).

[285] M. Lein, P. P. Corso, J. P. Marangos, and P. L. Knight, *Orientation dependence of high-order harmonic generation in molecules*, Phys. Rev. A **67**, 023819 (2003).

[286] T. Kanai, S. Minemoto, and H. Sakai, *Quantum interference during high-order harmonic generation from aligned molecules*, Nature **435**, 470 (2005).

[287] R. Berlasso, C. Dallera, F. Borgatti, C. Vozzi, G. Sansone, S. Stagira, M. Nisoli, G. Ghiringhelli, P. Villoresi, L. Poletto, et al., *High-order laser harmonics and synchrotron study of transition metals m2,3 edges*, Phys. Rev. B **73**, 115101 (2006).

[288] T. Pfeifer, *Adaptive Control of Coherent Soft X-Rays*, Dissertation, Universität Würzburg, Physikalisches Institut (2004).

[289] T. Pfeifer, C. Spielmann, and G. Gerber, *Femtosecond x-ray science*, Rep. Prog. Phys. **69**, 443 (2006).

[290] K. Oguri, Y. Okano, T. Nishikawa, and H. Nakano, *Transient observation of extended x-rayi absorption fine structure i laser-melted Si by using femtosecond laser-produced-plasma soft x ray*, Appl. Phys. Lett. **87**, 011503 (2005).

[291] E. Goulielmakis, M. Uiberacker, R. Kienberger, A. Baltuška, V. Yakovlev, A. Scrinzi, T. Westerwalbesloh, U. Kleineberg, U. Heinzmann, M. Drescher, et al., *Direct measurement of light waves*, Science **305**, 1267 (2004).

[292] J.-C. M. Diels, J. J. Fontaine, I. C. McMichael, and F. Simoni, *Control and measurement of ultrashort pulse shapes (in amplitude and phase) with femtosecond accuracy*, Appl. Opt. **24**, 1270 (1985).

[293] D. J. Kane and R. Trebino, *Characterization of arbitrary femtosecond pulses using frequency-resolved optical gating*, IEEE J. Quantum Electron. **29**, 571 (1993).

[294] R. Trebino, K. W. Delong, D. N. Fittinghoff, J. N. Sweetser, M. A. Krummbügel, and B. A. Richman, *Measuring ultrashort laser pulses in the time-frequency domain using frequency-resolved optical gating*, Rev. Sci. Instrum. **68**, 3277 (1997).

[295] J.-C. Diels and W. Rudolph, *Ultrashort laser pulse phenomena* (Academic Press, San Diego, 1995), ISBN 0-12-215492-4.

[296] S. Linden, H. Giessen, and J. Kuhl, *XFROG - A new method for amplitude and phase characterization of weak ultrashort pulses*, phys. stat. sol. (b) **206**, 119 (1998).

[297] P. O'Shea, M. Kimmel, X. Gu, and R. Trebino, *Highly simplifid device for ultrahort-pulse measurement*, Opt. Lett. **26**, 932 (2001).

[298] E. Hecht, *Optics* (Addison-Wesley, 1998), 3rd ed., ISBN 0-201-30425-2.

[299] L. Lepetit, G. Chériaux, and M. Joffre, *Linear techniques of phase measurement by femtosecond spectral interferometry for applications in spectroscopy*, J. Opt. Soc. Am. B **12**, 2467 (1995).

[300] D. N. Fittinghoff, J. L. Bowie, J. N. Sweetser, R. T. Jennings, M. A. Krumbügel, K. W. DeLong, and R. Trebino, *Measurement of the intensity and phase of ultraweak, ultrashort laser pulses*, Opt. Lett. **21**, 884 (1996).

[301] C. Iaconis and I. Walmsley, *Spectral phase interferometryfor direct electric-field reconstructionof ultrashort optical pulse*, Opt. Lett. **23**, 792 (1998).

[302] C. Iaconis and I. A. Walmsley, *Self-referencing spectral interferometry for measuring ultrashort optical pulses*, IEEE J. Quantum Electron. **35**, 501 (1999).

[303] M. E. Anderson, L. E. E. de Araujo, E. M. Kosik, and I. A. Walmsley, *The effects of noise on ultrashort-optical-pulse measurements using SPIDER*, Appl. Phys. B **70**, S85 (2000).

[304] C. Dorrer and I. A. Walmsley, *Accuracy criterion for ultrashort pulse characterization techniques: application to spectral phase interferometry for direct electric field reconstruction*, J. Opt. Soc. Am. B **19**, 1019 (2002).

[305] A. Hofmann, *Bestimmung des elektrischen Feldes ultrakurzer Laserpulse mit SPIDER, Teil1: Theorie*, Projektpraktikumsbericht, Physikalisches Institut, EP1, Universität Würzburg (2005).

[306] S. Mark, *Bestimmung des elektrischen Feldes ultrakurzer Laserpulse mit SPIDER, Teil2: Experiment*, Projektpraktikumsbericht, Physikalisches Institut, EP1, Universität Würzburg (2005).

[307] P. Baum, S. Lochbrunner, and E. Riedle, *Zero-additional-phase SPIDER: full characterization of visible and sub-20-fs ultraviolet pulses*, Opt. Lett. **29**, 210 (2004).

[308] A. S. Wyatt, I. A. Walmsley, G. Stibenz, and G. Steinmeyer, *Sub-10 fs pulse characterization using spatially encoded arrangement for spectral phase interferometry for direct electric field reconstruction*, Opt. Lett. **31**, 1914 (2006).

[309] A. D. Bandrauk, S. Chelkowski, and N. H. Shon, *Measuring the electric field of few-cycle laser pulses by attosecond cross correlation*, Phys. Rev. Lett. **89**, 283903 (2002).

[310] J. Itatani, F. Quéré, G. L. Yudin, M. Y. Ivanov, F. Krausz, and P. B. Corkum, *Attosecond streak camera*, Phys. Rev. Lett. **88**, 173903 (2002).

[311] J. Mauritsson, R. López-Martens, A. L'Huillier, and K. J. Schafer, *Ponderomotive shearing for spectral interferometry of extreme-ultraviolet pulses*, Opt. Lett. **28**, 2393 (2003).

[312] F. Quéré, J. Itatani, G. L. Yudin, and P. B. Corkum, *Attosecond spectral shearing interferometry*, Phys. Rev. Lett. **90**, 073902 (2003).

[313] Y. Mairesse, O. Gobert, P. Breger, H. Merdji, P. Meynadier, P. Monchicourt, M. Perdrix, P. Salières, and B. Carré, *High harmonic XUV spectral phase interferometry for direct electric-field reconstruction*, Phys. Rev. Lett. **94**, 173903 (2005).

[314] J. M. Schins, P. Breger, P. Agostini, R. C. Constantinescu, H. G. Muller, G. Grillon, A. Antonetti, and A. Mysyrowicz, *Observation of laser-assisted auger decay in argon*, Phys. Rev. Lett. **73**, 2180 (1994).

[315] T. E. Glover, R. W. Schoenlein, A. H. Chin, and C. V. Shank, *Observation of laser assisted photoelectric effect and femtosecond high order harmonic radiation*, Phys. Rev. Lett. **76**, 2468 (1996).

[316] J. M. Schins, P. Breger, P. Agostini, R. C. Constantinescu, H. G. Muller, A. Bouhal, G. Grillon, A. Antonetti, and A. Mysyrowicz, *Cross-correlation measurements of femtosecond extreme-ultraviolet high-order harmonics*, J. Opt. Soc. Am. B **13**, 197 (1996).

[317] A. Bouhal, R. Evans, G. Grillon, A. Mysyrowicz, P. Breger, P. Agostini, R. C. Constantinescu, H. G. Muller, and D. von der Linde, *Cross-correlation measurement of femtosecond noncollinear high-order harmonics*, J. Opt. Soc. Am. B **14**, 950 (1997).

[318] T. Sekikawa, T. Kanai, and S. Watanabe, *Frequency-resolved optical gating of femtosecond pulses in the extreme ultraviolet*, Phys. Rev. Lett. **91**, 103902 (2003).

[319] Y. Mairesse and F. Quéré, *Frequency-resolved optical gating for complete reconstruction of attosecond bursts*, Phys. Rev. A **71**, 011401(R) (2005).

[320] F. Quéré, Y. Mairesse, and J. Itatani, *Temporal characterization of attosecond xuv fields*, J. Mod. Opt. **52**, 339 (2005).

[321] G. Sansone, E. Benedetti, J.-P. Caumes, S. Stagira, C. Vozzi, M. Pascolini, L. Poletto, P. Villoresi, S. D. Silvestri, and M. Nisoli, *Measurement of harmonic phase differences by interference of attosecond light pulses*, Phys. Rev. Lett. **94**, 193903 (2005).

[322] K. Oguri, T. Nishikawa, T. Ozaki, and H. Nakano, *Sampling measurement of soft-x-ray-pulse shapes by femtosecond sequential ionization of kr+ in an intense laser field*, Opt. Lett. **29**, 1279 (2004).

[323] N. M. Kroll and K. M. Watson, *Charged-particle scattering in the presence of a strong electromagnetic wave*, Phys. Rev. A **8**, 804 (1973).

[324] E. Yablonovitch, *Energy conservation in the picosecond and subpicosecond photoelectric effect*, Phys. Rev. Lett. **60**, 795 (1988).

[325] P. Agostini, P. Breger, A. L'Huillier, H. G. Muller, G. Petite, A. Antonetti, and A. Migus, *Giant stark shifts in multiphoton ionization*, Phys. Rev. Lett. **63**, 2208 (1989).

[326] R. R. Freeman and P. H. Bucksbaum, *Investigations of above-threshold ionization using subpicosecond laser pulses*, J. Phys. B: At. Mol. Opt. Phys. **24**, 325 (1991).

[327] E. S. Toma, H. G. Muller, P. M. Paul, P. Breger, M. Cheret, P. Agostini, C. Le Blanc, G. Mullot, and G. Cheriaux, *Ponderomotive streaking of the ionization potential as a method for measuring pulse durations in the xuv domain with fs resolution*, Phys. Rev. A **62**, 061801(R) (2000).

[328] J. Peatross, J. L. Chaloupka, and D. D. Meyerhofer, *High-order harmonic generation with an annular laser beam*, Opt. Lett. **19**, 942 (1994).

[329] E. Goulielmakis, G. Nersisyan, N. Papadogiannis, D. Charalambidis, G. Tsakiris, and K. Witte, *A dispersionless michelson interferometer for the characterization of attosecond pulses*, Appl. Phys. B **74**, 197 (2002).

[330] N. A. Papadogiannis, G. Nersisyan, E. Goulielmakis, T. P. Rakitzis, E. Hertz, D. Charalambidis, G. D. Tsakiris, and K. Witte, *Temporal characterization of short-pulse third-harmonic generation in an atomic gas by a transmission-grating michelson interferometer*, Opt. Lett. **27**, 1561 (2002).

[331] D. Charalambidis, N. A. Papadogiannis, E. Goulielmakis, G. Nersysian, G. D. Tsakiris, and K. Witte, *A transmission grating interferometer for the temporal characterization of harmonics*, J. Mod. Opt. **50**, 387 (2003).

[332] Y. Kobayashi, T. Sekikawa, Y. Nabekawa, and S. Watanabe, *27-fs extreme ultraviolet pulse generation by high-order harmonics*, Opt. Lett. **23**, 64 (1998).

[333] N. A. Papadogiannis, L. A. A. Nikolopoulos, D. Charalambidis, G. D. Tsakiris, P. Tzallas, and K. Witte, *On the feasibility of performing non-linear autocorrelation with attosecond pulse trains*, Appl. Phys. B **76**, 721 (2003).

[334] L. A. A. Nikolopoulos, E. P. Benis, P. Tzallas, D. Charalambidis, K. Witte, and G. D. Tsakiris, *Second order autocorrelation of an xuv attosecond pulse train*, Phys. Rev. Lett. **94**, 113905 (2005).

[335] Y. Nabekawa, T. Shimizu, T. Okino, K. Furusawa, H. Hasegawa, K. Yamanouchi, , and K. Midorikawa, *Conclusive evidence of an attosecond pulse train observed with the mode-resolved autocorrelation technique*, Phys. Rev. Lett. **96**, 083901 (2006).

[336] T. Okino, T. Shimizu, K. Furusawa, H. Hasegawa, Y. Nabekawa, K. Yamanouchi, and K. Midorikawa, in *CLEO/QELS 2006 post-deadline paper* (2006).

[337] T. Sekikawa, T. Katsura, S. Miura, and S. Watanabe, *Measurement of the intensity-dependent atomic dipole phase of a high harmonic by frequency-resolved optical gating*, Phys. Rev. Lett. **88**, 193902 (2002).

[338] J. Norin, J. Mauritsson, A. Johansson, M. K. Raarup, S. Buil, A. Persson, O. Dühr, M. B. Gaarde, K. J. Schafer, U. Keller, et al., *Time-frequency characterization of femtosecond extreme ultraviolet pulses*, Phys. Rev. Lett. **88**, 193901 (2002).

[339] A. Kosuge, T. Sekikawa, X. Zhou, T. Kanai, and S. Watanabe, in *CLEO/QELS 2006 post-deadline paper* (2006).

[340] M. Wollenhaupt, A. Assion, D. Liese, C. Sarpe-Tudoran, T. Baumert, S. Zamith, M. A. Bouchene, B. Girard, A. Flettner, U. Weichmann, et al., *Interferences of ultrashort free electron wave packets*, Phys. Rev. Lett. **89**, 173001 (2002).

[341] T. C. Weinacht, J. Ahn, and P. H. Bucksbaum, *Measurement of the amplitude and phase of a sculpted rydberg wave packet*, Phys. Rev. Lett. **80**, 5508 (1998).

[342] P. Tournois, *Acousto-optic programmable dispersive filter for adaptive compensation of group delay time dispersion in laser systems*, Opt. Commun. **140**, 245 (1997).

[343] W. Kornelis, C. P. Hauri, A. Heinrich, F. W. Helbing, M. P. Anscombe, P. Schlup, J. W. G. Tisch, J. Biegert, and U. Keller, *Frequency-sheared, time-delayed extreme-ultraviolet pulses produced by high-harmonic generation in argon*, Opt. Lett. **30**, 1731 (2005).

[344] P. H. Bucksbaum, M. Bashkansky, and T. J. McIlrath, *Scattering of electrons by intense coherent light*, Phys. Rev. Lett. **58**, 349 (1987).

[345] M. D. Davidson, J. Wals, H. G. Muller, and H. B. van Linden van den Heuvell, *Observation of full ponderomotive shift for the photodetachment threshold in a strong laser field*, Phys. Rev. Lett. **71**, 2192 (1993).

[346] K. Varjú, Y. Mairesse, B. Carré, M. B. Gaarde, P. Johnsson, S. Kazamias, R. López-Martens, J. Mauritsson, K. J. Schafer, P. Balcou, et al., *Frequency chirp of harmonic and attosecond pulses*, J. Mod. Opt. **52**, 379 (2005).

[347] R. López-Martens, J. Mauritsson, A. Johansson, J. Norin, and A. L'Huillier, *Time-frequency characterization of high-order harmonic pulses*, Eur. Phys. J. D **26**, 105 (2003).

[348] L. C. Dinu, H. G. Muller, S. Kazamias, G. Mullot, F. Augé, P. Balcou, P. M. Paul, M. Kovacev, P. Breger, and P. Agostini, *Measurement of the subcycle timing of attosecond xuv bursts in high-harmonic generation*, Phys. Rev. Lett. **91**, 063901 (2003).

[349] S. A. Aseyev, Y. Ni, L. J. Frasinski, H. G. Muller, and M. J. J. Vrakking, *Attosecond angle-resolved photoelectron spectroscopy*, Phys. Rev. Lett. **91**, 223902 (2003).

[350] K. Varjú, Y. Mairesse, P. Agostini, P. Breger, B. Carre, L. J. Frasinski, E. Gustafsson, P. Johnsson, J. Mauritsson, H. Merdji, et al., *Reconstruction of attosecond pulse trains using an adiabatic phase expansion*, Phys. Rev. Lett. **95**, 243901 (2005).

[351] K. T. Kim, M. N. Park, K. S. Kang, T. Imran, J. Park, and C. H. Nam, in *CLEO/QELS 2006 post-deadline paper* (2006).

[352] E. Papalazarou, M. Kovačev, P. Tzallas, E. P. Benis, C. Kalpouzos, G. D. Tsakiris, and D. Charalambidis, *Spectral phase distribution retrieval through coherent control of harmonic generation*, Phys. Rev. Lett. **96**, 163901 (2006).

[353] E. M. Kosik, L. Corner, A. S. Wyatt, E. Cormier, I. A. Walmsley, and L. F. DiMauro, *Complete characterization of attosecond pulses*, J. Mod. Opt. **52**, 361 (2005).

[354] A. Paulus, *Entwicklung und Bau eines Elektronenflugzeitspektrometers*, Diplomarbeit, Universität Würzburg, Physikalisches Institut (2004).

[355] D. C. McGilvery and D. Dahl, *Simion*, Scientific Instrument Services, Inc. (1977).

[356] L. Nugent-Glandorf, M. Scheer, M. Krishnamurthy, J. W. Odom, and S. R. Leone, *Photoelectron spectroscopic determination of the energy bandwidths of high-order harmonics (7th–55th) produced by an ultrafast laser in neon*, Phys. Rev. A **62**, 023812 (2000).

[357] J. B. West and J. Morton, *Absolute photoionization cross-section tables for xenon in the VUV and the soft x-ray regions*, Atom. Data Nucl. Data Tables **22**, 103 (1978).

[358] J. Sugar and A. Musgrove, *Energy levels of krypton, Kr I through Kr XXXVI*, J. Phys. Chem. Ref. Data **20**, 859 (1991).

[359] NIST, *Nist atomic spectra database levels data, kr i* (2006), URL `http://physics.nist.gov/PhysRefData/ASD/levels_form.html`.

[360] A. Derevianko, W. R. Johnson, and K. T. Cheng, *Non-dipole effects in photoelectron angular distributions for rare gas atoms*, Atom. Data Nucl. Data Tables **73**, 153 (1999).

[361] E. Cormier, D. Garzella, P. Breger, P. Agostini, G. Chériaux, and C. Leblanc, *Above-threshold ionization contrast and channel closure in argon*, J. Phys. B: At. Mol. Opt. Phys. **34**, L9 (2001).

[362] A.-S. Morlens, R. López-Martens, O. Boyko, P. Zeitoun, P. Balcou, K. Varjú, E. Gustafsson, T. Remetter, A. L'Huillier, S. Kazamias, et al., *Desgin and characterization of extreme-ultraviolet broadband mirrors for attosecond science*, Opt. Lett. **31**, 1558 (2006).

[363] H. Mashiko, A. Suda, and K. Midorikawa, *Focusing multiple high-order harmonics in the extreme-ultraviolet and soft-x-ray regions by a platinum-coated ellipsoidal mirror*, Appl. Opt. **45**, 573 (2006).

[364] J. Xiao, Z. Sun, X. Zhang, Y. Wang, W. Zhang, Z. Wang, R. Li, and Z. Xu, *Optimization of single attosecond x-ray pulses by genetic algorithm control of the chirp and initial phase of 5 fs laser pulses*, J. Opt. Soc. Am. B **23**, 771 (2006).

[365] C. Rose-Petruck, R. Jimenez, T. Guo, A. Cavalleri, C. W. Siders, F. Ráksi, B. J. A. Squier, K. R. Wilson, and C. P. J. Barty, *Picosecond-milliångström lattice dynamics by ultrafast x-ray diffraction*, Nature **398**, 310 (1999).

[366] S. Düsterer, H. Schwoerer, W. Ziegler, C. Ziener, and R. Sauerbrey, *Optimization of euv radiation yield from laser-produced plasma*, Appl. Phys. B **73**, 693 (2001).

[367] S. J. McNaught, J. Fan, E. Parra, and H. M. Milchberg, *A pump-probe investigation of laser-droplet plasma dynamics*, Appl. Phys. Lett. **79**, 4100 (2001).

[368] M. Lein, N. Hay, R. Velotta, J. P. Marangos, and P. L. Knight, *Role of the intramolecular phase in high-harmonic generation*, Phys. Rev. Lett. **88**, 183903 (2002).

[369] R. Velotta, N. Hay, M. B. Mason, M. Castillejo, and J. P. Marangos, *High-order harmonic generation in aligned molecules*, Phys. Rev. Lett. **87**, 183901 (2001).

[370] A. Flettner, J. König, M. B. Mason, T. Pfeifer, U. Weichmann, R. Düren, and G. Gerber, *Ellipticity dependence of atomic and molecular high harmonic generation*, Europ. Phys. J. D **21**, 115 (2002).

[371] M. Y. Emelin, M. Y. Ryabikin, A. M. Sergeev, M. D. Chernobrovtseva, T. Pfeifer, D. Walter, and G. Gerber, *Attosecond burst and high-harmonic generation in molecular ionization by ultrashort laser pulses*, JETP Lett. **77**, 212 (2003).

[372] M. Protopapas, C. H. Keitel, and P. L. Knight, *Atomic physics with super-high intensity lasers*, Rep. Prog. Phys. **60**, 389 (1997).

[373] K. Z. Hatsagortsyan and C. H. Keitel, *X-ray amplification by laser controlled coherent bremsstrahlung*, Phys. Rev. Lett. **86**, 2277 (2001).

[374] T. Ditmire, T. Donnelly, A. M. Rubenchik, R. W. Falcone, , and M. D. Perry, *Interaction of intense laser pulses with atomic clusters*, Phys. Rev. A **53**, 3379 (1996).

[375] S. Düsterer, H. Schwoerer, W. Ziegler, D. Salzmann, and R. Sauerbreay, *Effects of a prepulse on laser-induced EUV radiation conversion efficiency*, Appl. Phys. B **76**, 17 (2003).

[376] C. Rajyaguru, T. Higashiguchi, M. Koga, W. Sasaki, and S. Kubodera, *Systematic optimization of the extreme ultraviolet yield from a quasi-mass-limited water-jet target*, Appl. Phys. B **79**, 669 (2004).

[377] Y. T. Li, J. Zhang, Z. M. Sheng, H. Teng, T. J. Liang, X. Y. Peng, X. Lu, Y. J. Li, and X. W. Tang, *Spatial distribution of high-energy electron emission from water plasmas produced by femtosecond laser pulses*, Phys. Rev. Lett. **90**, 165002 (2003).

[378] J. Zheng, Z.-M. Sheng, X.-Y. Peng, and J. Zhang, *Energetic electrons and protons generated from the interaction of ultrashort laser pulses with microdroplet plasmas*, Phys. Plasmas **12**, 113105 (2005).

[379] R. Zürl and H. Graener, *High-harmonic generation of mid-ir pulses in simple liquids*, Appl. Phys. B **66**, 213 (1998).

[380] C. Favre, V. Boutou, S. C. Hill, W. Zimmer, M. Krenz, H. Lambrecht, J. Yu, R. K. Chang, L. Woeste, and J. P. Wolf, *White-light nanosource with directional emission*, Phys. Rev. Lett. **89**, 035002 (2002).

[381] J. H. Eickmans, W.-F. Hsieh, and R. K. Chang, *Laser-induced explosion of h_2o droplets: spatially resolved spectra*, Opt. Lett. **12**, 22 (1987).

[382] A. N. Zaidel', V. K. Prokof'ev, S. M. Raiskii, V. A. Slavnyi, and E. Y. Shreider, *Tables of Spectral Lines* (Ifi/Plenum, New York-London, 1970).

[383] NIST, *Nist atomic spectra database* (1999), URL `http://physics.nist.gov/cgi-bin/AtData/main_asd`.

[384] J. Noack and A. Vogel, *Laser-induced plasma formation in water at nanosecond to femtosecond time scales: Calculation of thresholds, absorption coefficients, and energy density*, IEEE J. Quantum Electron. **35**, 1156 (1999).

[385] F. Courvoisier, V. Boutou, C. Favre, S. C. Hill, and J.-P. Wolf, *Plasma formation dynamics within a water microdroplet on femtosecond time scales*, Opt. Lett. **28**, 206 (2003).

Curriculum vitae

Dipl.-Phys. Carsten Winterfeldt
Nopitschstraße 4 A, 97074 Würzburg

geb. 14. Dezember 1977 in Würzburg,
verheiratet

Akademische Ausbildung

seit 2003	Doktorarbeit als Stipendiat der Studienstiftung des deutschen Volkes am Lehrstuhl für Experimentelle Physik I, Prof. Dr. Gustav Gerber, Universität Würzburg
	Thema: "Generation and control of high-harmonic radiation"
2001–2002	Auslandsstudium an der University of Texas at Austin, Department of Physics
	Abschluss: Master of Arts (M.A.)
	Titel der Thesis: "'Optical Parametric Amplifier for Nonlinear Optical Spectroscopy"' (Prof. Dr. Michael C. Downer)
1998–2002	Studium der Physik an der Universität Würzburg als Stipendiat nach dem Bayerischen Begabtenförderungsgesetz 12/2003: Wilhelm-Conrad-Röntgen-Studienpreis des Physikalischen Instituts der Universität Würzburg 12/2002: Diplom (Physik) 08/2000: Vordiplom
1997	Abitur am Reuchlin-Gymnasium Ingolstadt

Kirchenmusik

2001/2003	Ausbildung zum nebenberuflichen Kirchenmusiker (D-/C-Prüfung)
seit 1994	Organistentätigkeit in Ingolstadt und Würzburg

Würzburg, November 15, 2006